UNIVERSITÉ DE
NEUCHÂTEL

SEISMO-HYDROMECHANICAL INTERACTION DURING IN-SITU HYDRAULIC FRACTURING EXPERIMENTS

A thesis submitted to attain the degree of
DOCTOR OF SCIENCES of UNIVERSITY OF NEUCHÂTEL
(Dr. sc. nat. UniNE)

presented by
NATHAN OLIVER DUTLER

M.Sc. in Earth Science with a major in Geophysics,
ETH Zurich

born on 12.04.1988

citizen of
Sevelen SG

accepted on the recommendation of

Prof. Dr. Benoît Valley (thesis director)
Prof. Dr. Florian Amann, Germany
Prof. Dr. Philippe Renard
Prof. Dr. Günter Zimmermann, Germany

Defended on April 23rd, 2020

Imagination is more important than knowledge

A. Einstein

Acknowledgements

First, I thank my supervisor Prof. Benoît Valley for the opportunity to work in such an interesting topic and interdisciplinary project team for the last few years. I am thankful to my supervisors, Prof. Benoît Valley and Prof. Florian Amann, for their assistance and contributions during my PhD and all the fruitful discussions. I thank Prof. Phillippe Renard for the constructive discussions and support during my PhD and especially during the development of openhytest. Furthermore, I thank Prof. Günter Zimmermann for serving as external referee on my doctoral committee.

Special gratitudes goes to Dr. Valentin Gischig and Dr. Reza Jalali. We had so many interesting discussions and your inputs were always very supportive and helpful the last three and a half years of my PhD. A very special thank goes to the Grimsel data acquisition team, which was the research group I worked all the time, for the hydraulic fracturing experiment: Dr. Joesph Doetsch, Dr. Valentin Gischig, Prof. Benoît Valley, Prof. Florian Amann, Dr. Reza Jalali, Dr. Hannes Krietsch, Linus Villiger, Bernard Brixel and Dr. Clément Roques. It was a pleasure to work with you in the field. And for sure, the after-field work leisure time was always well invested. It was a very valuable experience and the interdisciplinary group allowed me discuss our observations in many different details. Without the support of the in-site NAGRA technicians René Dorrer and Michael Treuthardt this project would not show the same quality. Similarly, I thank Gerd Klee (MesySolexpert) and Karam Konter (Solexpert) for conducting the high-pressure fluid injections and the supportive pump supply.

I am very thankful to Dr. Morteza Nejati for incredible important support and instruction during the writing of my first paper. It was a time intensive paper with many valuable discussions. I like to thank my doctoral colleague Bernard Brixel and Dr. Reza Jalali, who worked with me in Grimsel for the hydraulic characterisation prior and after the main HF experiment. Bernard, I enjoyed all the discussions and lunch breaks with you during the writing time of the thesis. I thank Prof. Brice Lecampion for his support during the design of the injection protocol. I thank Prof. Jörg Renner for the valuable discussions and the inputs on the analysis of periodic pumping tests. Further, I thank Patrick Schmidt and Boris Galvin for the discussions and projects on the numerical analysis of the hydraulic fracturing experiments.

I would like to thank all my colleagues and friends at the Center for Hydrogeology and Geothermics at University of Neuchâtel and the Earth Science Department at ETH Zurich for all the great times we had at conferences and lunch breaks. Further, I thank all my former colleagues, and friends for all the support through the last three and a half years. I excuse me, that I can not name all of

you in here. Last but not least, I thank my parents and my sister for their constant support since the beginning.

Abstract

Hydraulic fracturing is a common technique used in a variety of fields like civil and mining engineering, oil & gas and geothermal industry. It can be used to enhance the permeability of low permeable rocks, to increase the connectivity of natural fractures, to modify the rock mass strength, or to measure the Earth's stress field. In the context of deep geothermal energy exploitation, a heat exchanger needs to be created at depth with characteristics favorable for heat extraction i.e. sufficient permeability and heat exchanger area. The creation of the heat exchanger for geothermal heat extraction remains a critical element with high associated risks including poor reservoir performance and induced seismicity. Hence the need for a better understanding of the coupled seismic-hydromechanical processes during stimulation operations. The execution of experiments on the intermediate-scale has the advantage of a better control on the processes associated with induced seismicity and reservoir performance compared to full-scale and allow to use comprehensive real time monitoring of pore pressure, rock mass deformation and seismicity. This scale is closer to the full-scale stimulation than laboratory scale, where seismo-hydromechanical interactions are generally focused on single fractures.

The decameter-scale In-situ Stimulation and Circulation (ISC) project took place between 2015 and 2018 at the Grimsel Test Site (GTS), Switzerland. The GTS is located in the Central Swiss Alps, beneath the mountains of the Grimsel Pass. Overall, the moderately crystalline fractured rock mass shows a pervasive foliation and was intersected by six major sub-vertical shear zones. For each of the two assumed stimulation endmembers, hydraulic shearing and hydraulic fracturing, six experiments were conducted. Prior to the experiments, the test volume was characterized in great detail with respect to geology, geophysics, hydrogeology and in-situ stress field. This doctoral thesis aims at better understanding tensile fracture growth. It includes study of fracture toughness and fracture process zone on laboratory scale and the investigation of the seismo-hydromechanical coupled processes during in-situ hydraulic fracturing experiments.

The tested intact Grimsel Granodiorite samples indicate that the resistance against material failure is significantly higher across the foliation plane than along it. The results from Digital Image Correlation (DIC) confirm the development of a semi-elliptical fracture process zone (FPZ) with an average length to width ratio of about two for both principal directions. This agrees well with the available results in the literature. The experimental results of the length of the FPZ give supporting evidence to the fact that a nonlinear cohesion stress distribution provides an accurate cohesive model that agrees well with the experimental results. Additionally, the conformity of the ratio of the FPZ length in two principal directions with the theoretical predictions gives supporting evidence to the proportionality of the FPZ length with respect to the square of fracture toughness to tensile strength.

At the decametric scale during the in-situ experiment, the hydromechanical coupled responses of the rock mass and its fractures were captured by a comprehensive monitoring system installed along the tunnels and within dedicated boreholes. At the borehole scale, these processes involved newly created tensile fractures intersecting the injection interval while at the cross-hole scale, the natural network of fractures dominated the propagation process. The six HF experiments can be divided into two groups based on their injection location (i.e., south or north to a brittle ductile shear zone), their similarity of injection pressures and their response to deformation and pressure propagation. The experiments executed north of the shear zone, show smaller injection pressures and larger backflow during bleed-off phases. In addition, we observe re-orientation of the seismic cloud as the fracture propagated away from the wellbore. The re-orientation during propagation is interpreted to be related to a strong stress heterogeneity and the intersection of natural fractures striking different from the propagating hydraulic fracture. This leads in the details to complex geometry departing from theoretical mode I fracture geometries. The seismic activity was limited to about 10 m radial distance from the injection point. In contrast, strain and pressure signals reach further into the rock mass indicating that the process zone around the injection point is larger than the zone illuminated by seismic signals. Furthermore, strain signals indicate not just single fracture openings but also the propagation of multiple fractures.

Various methods to estimate the fracture opening and fracture contact pressure were applied and compared from single injection borehole observations with the strain gauge in distance from the injection point. The results show, that the fracture opening pressure was also observed at the strain gauge, associated with a strong increase of fracture transmissivity. The combination of injection pressure and strain observation allows to define an aperture-stress relationship with a general trend toward decreasing normal fracture stiffness during fracture opening. The fracture contact pressure can be estimated, but hydromechanical superposition of pump shut-in and corresponding pressure loss and interaction of the connected surrounding fractures make this task very challenging and error-prone.

The pore pressure data set differentiate two distinct responses based on lag time and amplitudes. This allow to distinguish a near- and far-field response. The near-field response is due to pressure diffusion and the far-field response is due to stress perturbation. The far-field pore pressure response is consistent for all experiments, indicating the dominant failure mechanism. This change in the far-field are very sensitive and can be used as a complementary method to seismic monitoring during hydraulic stimulations. The exceptional hydromechanical dataset allow to test numerical stimulations and can help to improve injection strategies, the monitoring design and the numerical modelling.

Résumé

La fracturation hydraulique est une technique utilisée pour diverses applications dans les domaines du génie civil et minier, l'industrie pétrolière et gazière et de la géothermies. Elle peut être utilisée pour améliorer la perméabilité des roches peu perméables, pour augmenter la connectivité des fractures naturelles, pour modifier la résistance de la masse rocheuse ou pour mesurer le champ de contrainte in-situ. Dans le contexte de l'exploitation d'énergie géothermique profonde, un échangeur de chaleur doit être créé en profondeur avec des caractéristiques favorables à l'extraction de la chaleur, c'est-à-dire une perméabilité et une surface d'échange de chaleur suffisantes. La création de l'échangeur de chaleur par stimulation reste un élément critique avec de forts risques associés, notamment le risque d'une mauvaise performance du réservoir et/ou de génération de sismicité induite. D'où la nécessité de mieux comprendre les processus couplés sismo-hydromécaniques lors des opérations de stimulation. Ceci peut être réalisé avec des expériences à l'échelle intermédiaire, réduite par rapport aux applications industrielles, ce qui présente l'avantage de mieux contrôler les processus associés à la sismicité induite et à la performance des réservoirs et permet de déployer des systèmes de mesure en temps réel de la pression interstitielle, de la déformation de la masse rocheuse et de la sismicité. Cette échelle est plus proche de la stimulation à grande échelle que l'échelle de laboratoire, où les interactions sismo-hydromécaniques sont généralement concentrées sur des fractures uniques.

Le projet de stimulation et de circulation in-situ décamétrique (« In-situ Stimulation and Circulation », ISC) s'est déroulé entre 2015 et 2018 dans le laboratoire souterrain du Grimsel (GTS), en Suisse. Le GTS est situé dans les Alpes de Suisse centrale, sous les montagnes du col du Grimsel. Le massif est constitué de roches cristallines modérément fracturées, présente une foliation persistante et est recoupée par six grandes zones de cisaillement sub-verticales. Deux mécanismes de stimulation idéaux sont présupposés: le cisaillement hydraulique (HS) et la fracturation hydraulique (HF). Douze injections favorisant l'un ou l'autre de ces mécanismes, c'est-à-dire six pour chacun, ont été menées. Avant les expériences, le volume expérimental a été caractérisé de façon très détaillée en ce qui concerne la géologie, la géophysique, l'hydrogéologie et le champ de contrainte in-situ. Cette thèse de doctorat vise à mieux comprendre la croissance des fractures en tension créée lors de ces expériences. Elle comprend l'étude de la ténacité des fractures et de la zone plastique à l'échelle du laboratoire et l'étude des processus couplés sismo-hydromécaniques lors des expériences de fracturation hydraulique in-situ.

Les échantillons de granodiorite du Grimsel testés indiquent que la résistance à la rupture du matériau est plus faible le long du plan de foliation que lorsque la fracture recoupe le plan foliation perpen-

diculairement. Les résultats de la corrélation d'images numériques (DIC) confirment le développement d'une zone plastique (« fracture process zone », FPZ) semi-elliptique avec un rapport moyen longueur/largeur d'environ deux pour les deux directions principales. Cela correspond bien aux résultats de la littérature. Les résultats expérimentaux de la longueur de la FPZ valide l'hypothèse d'une distribution non linéaire des contraintes de cohésion. En outre, la concordance avec les prédictions théoriques du rapport de la longueur de la FPZ dans deux directions principales atteste de la proportionnalité de la longueur de la FPZ au carré du rapport de la ténacité et de la résistance à la traction.

À l'échelle décamétrique pendant l'expérience in-situ, les réponses hydromécaniques couplées du massif et des fractures ont été mesurées par un système de surveillance complet installé le long des tunnels et dans des forages dédiés. À la paroi du forage d'injection, des fractures en tension coupant l'intervalle d'injection ont été nouvellement créées, alors qu'à l'échelle inter-puit, le réseau naturel de fractures a dominé le processus de propagation. Les six expériences HF peuvent être divisées en deux groupes en fonction de leur lieu d'injection (c'est-à-dire au sud ou au nord d'une zone de cisaillement ductile et fragile), des similarités des pressions d'injection et de leur réponse en déformation et propagation de la pression. Les expériences réalisées au nord de la zone de cisaillement, montrent des pressions d'injection plus faibles et une récupération plus importante du fluide injecté pendant les phases de purge. De plus, nous observons une réorientation du nuage sismique lorsque la fracture se propage en s'éloignant du puits de forage. La réorientation au cours de la propagation est interprétée comme étant liée à une forte hétérogénéité des contraintes et à l'intersection de fractures naturelles orientées obliquement à la direction de propagation de la fracture hydraulique. Cela conduit dans les détails à une géométrie complexe qui s'écarte des géométries de fractures théoriques en mode I. L'activité sismique a été limitée à une distance radiale d'environ 10 m du point d'injection. En revanche, les signaux de déformation et de pression s'étendent plus loin dans la masse rocheuse, ce qui indique que la zone activée autour du point d'injection est plus grande que la zone illuminée par les signaux sismiques. En outre, les signaux de déformation indiquent non seulement des ouvertures de fractures uniques, mais aussi la propagation de fractures multiples.

Différentes méthodes d'estimation de l'ouverture de la fracture et de la pression de contact de la fracture ont été appliquées et comparées à partir d'observations au forage d'injection et avec une jauge de déformation positionnée dans un forage d'observation. Les résultats montrent que la pression d'ouverture de la fracture a également été observée au niveau de la jauge de déformation et est associée à une forte augmentation de la transmissivité de la fracture. La combinaison de la pression d'injection et de l'observation de la déformation permet de définir une relation ouverture-contrainte avec une tendance générale à la diminution de la rigidité normale de la fracture lors de son ouverture. La pression de contact de la fracture peut être estimée, mais la superposition des effets hydromécanique liés à l'arrêt de la pompe, à l'inertie et aux pertes de pression et à l'interaction avec les fractures environnantes connectées rend cette tâche difficile et sujette aux incertitudes. L'ensemble des données de pression dans le massif mettent en évidence deux réponses distinctes par leurs temps de réponse et leurs amplitudes. Cela permet de distinguer une réponse en champ proche et une réponse en champ

lointain. La réponse en champ proche est due à la diffusion de la pression et la réponse en champ lointain est due à la perturbation des contraintes. La réponse en pression en champ lointain est consistante pour toutes les expériences, et dépend du mécanisme de rupture dominant. Ces changements en champ lointain sont très sensibles et pourrait être utilisés comme une méthode complémentaire à la surveillance sismique pendant les stimulations hydrauliques. L'ensemble unique de données hydromécaniques collecté lors de ces expériences est disponible pour valider des approches de simulations numériques et peut contribuer à améliorer les stratégies d'injection, la conception de la surveillance et la stimulation de systèmes géothermiques profonds.

Zusammenfassung

Hydraulisches Aufbrechen (hydraulic fracturing (HF)) ist eine gängige Technik, die in einer Vielzahl von Bereichen wie Bau, Bergbau, Geothermie, Öl- und Gasindustrie eingesetzt wird. Sie kann verwendet werden, um die Durchlässigkeit von schwach durchlässigem Gestein zu verbessern, die Verbindung von natürlichen Brüchen zu erhöhen, die Festigkeit von Gesteinsmassen zu modifizieren oder das Spannungsfeld der Erde zu messen. Im Zusammenhang mit der tiefen geothermischen Energiegewinnung muss in der Tiefe ein Wärmetauscher mit günstigen Eigenschaften für die Wärmeausbeutung geschaffen werden, d.h. mit ausreichender Durchlässigkeit und Fläche, damit das Fluid die Wärme aufnehmen kann. Die Schaffung des Wärmetauschers für die geothermische Wärmegewinnung bleibt eine kritische Komponente mit grossem Risiko bezüglich schlechter Reservoirleistung und induzierter Seismizität. Das Beobachten von seismo-hydromechanisch gekoppelten Prozessen während Stimulationen erlaubt es neue Erkenntnisse zu gewinnen. Dazu eignen sich Experimenten auf der mittleren Skala, um die kritischen Prozesse wie induzierte Seismizität und Reservoirleistung besser zu kontrollieren mithilfe einer umfassenden Echtzeitüberwachung des Porendrucks, der Gesteinsverformung und der Seismizität. Auf dieser Skala ist ein Vergleich zur Stimulation im Vollmassstab naheliegender als auf dem Labormassstab, bei dem die seismo-hydromechanischen Wechselwirkungen im Allgemeinen auf einzelne Brüche beschränkt sind.

Das In-situ-Stimulations- und Zirkulationsprojekt (ISC) wurde zwischen 2015 und 2018 durchgeführt. Das Projekt war beheimated auf dem Testgelände Grimsel (GTS), Schweiz. Das GTS befindet sich in den Zentralschweizer Alpen, unterhalb des Grimselpasses in der Nähe des Räterichbodensees. Das massige, kristalline Grimsel-Granodiorit-Gestein weist eine durchdringende Folierung auf und wurde von sechs grossen subvertikalen Scherzonen durchschnitten. Vorgängig zu den Stimulationen wurde das Testvolumen sehr detailliert charakterisiert. Die beiden Hauptexperimente hatten zum Ziel die beiden Stimulationsendglieder, hydraulische Scherung und hydraulisches Aufbrechen, mit je sechs Experimenten zu untersuchen. Diese Doktorarbeit untersucht das Wachstum von Zugbrüchen. Sie umfasst die Untersuchung der Bruchzähigkeit und der Bruchprozesszone im Labormassstab sowie die Untersuchung der seismo-hydromechanisch gekoppelten Prozesse während der in-situ hydraulischen Bruchversuche.

Die getesteten intakten Grimsel-Granodiorit-Proben zeigen, dass der Widerstand gegen Materialversagen in der Richtung senkrecht zur Foliationsebene signifikant höher ist als in der Richtung der Foliationsebene. Die Ergebnisse der digitalen Bildkorrelation bestätigen die Entwicklung einer halbelliptischen Bruchprozesszone (BPZ) mit einem durchschnittlichen Verhältnis von Länge zu

Breite von etwa zwei für beide Hauptrichtungen, was wiederum gut mit den in der Literatur verfügbaren Ergebnissen übereinstimmt. Im Weiteren sind die experimentellen Ergebnisse zur Länge der BPZ ein unterstützender Beweis für eine nichtlineare Kohäsionsspannungsverteilung. Des weiteren untermauern die Verhältnisse der BPZ-Länge in den beiden Hauptrichtungen, die theoretischen Vorhersagen, dass die Proportionalität der BPZ-Länge in Bezug steht zum Quadrat der Bruchzähigkeit zur Zugfestigkeit.

Während des in-situ-Experiments wurden die hydromechanisch gekoppelten Reaktionen des Gesteinsmaterials und seiner Brüche auf einer 20 Meter Skala durch ein umfassendes Überwachungssystem erfasst, das entlang der Tunnel und in speziellen Bohrlöchern installiert wurde. Auf der Bohrlochskala waren diese Prozesse mit neu geschaffenen Zugbrüchen verbunden, die das Injektionsintervall schneiden, während auf der Reservoir Skala das natürliche Netzwerk der Brüche den Ausbreitungsprozess dominierte. Die sechs HF-Experimente können in zwei Gruppen unterteilt werden, und zwar aufgrund ihres Injektionsortes (d.h. südlich oder nördlich der spröd-duktilen Scherzone) ergeben sich Ähnlichkeiten bei den Injektionsdrücken, der Gesteinsverformung und der Druckausbreitung. Die Experimente nördlich der Scherzone zeigen kleinere Injektionsdrücke und einen größeren Rückfluss während der Druckentlastungsphasen. Darüber hinaus beobachten wir eine Neuorientierung der seismischen Wolke, während sich der Bruch vom Bohrloch weg ausbreitet. Die Neuorientierung während der Ausbreitung wird durch eine starken Spannungsheterogenität und der Überschneidung natürlicher Brüche interpretiert, die sich in der Orientierung von dem sich ausbreitenden hydraulischen Bruch unterscheiden. Dies führt im Detail zu einer komplexen Geometrie, die von der theoretischen Rissbildungsgeometrie unter Zug abweicht. Die seismische Aktivität war auf etwa 10 m radialen Abstand vom Injektionspunkt begrenzt. Im Gegensatz dazu reichen Dehnungs- und Drucksignale weiter in das Gestein hinein, was darauf hinweist, dass die Prozesszone um den Injektionspunkt größer ist als die von den seismischen Signalen angezeigten Zone. Darüber hinaus weisen Dehnungssignale nicht nur auf einzelne Bruchöffnungen, sondern auch auf die Ausbreitung von Mehrfachbrüchen hin. Es wurden verschiedene Methoden zur Abschätzung der Bruchöffnung und des Bruchkontaktdrucks angewandt. Beobachtungen von Injektionsdrücken und Dehnungsmessstreifen mit einem Abstand zum Injektionspunkt wurden verglichen und die Ergebnisse zeigen eine starke Erhöhung der Bruchöffnung beim Dehnungsmessstreifen während der gemessene Injektionsdruck über dem Bruchkontaktdruck liegt. Diese Kombination von Injektionsdruck und Dehnungsbeobachtung erlaubt es, eine Bruchöffnungs-Spannungs-Beziehung zu definieren. Diese zeigt einen allgemeinen Trend zur Abnahme der Bruchsteifigkeit während der Bruchöffnung. Die Abschätzung des schliessenden Bruches (Bruchanpressdruckes) ist schwierig und fehleranfällig, da dieses Signal hydromechanisch überlagert wird durch den augenblicklichen Druckverlust beim Pumpstopp und der einhergehenden Wechselwirkung der verbundenen umgebenden Brüche.

Der Porendruckdatensatz unterscheidet zwei verschiedene Reaktionen auf Grundlage des Zeitabstandes zwischen den Drucksignalen und der Amplitude. Dies ermöglicht die Unterscheidung einer Nah- und einer Fernfeldreaktion. Die Nahfeldreaktion ist auf die Druckdiffusion und die Fernfeldreaktion auf die Spannungsstörung zurückzuführen. Die Fernfeld-Porendruckreaktion ist bei allen

Experimenten konsistent, was auf den dominierenden Versagensmechanismus hinweist. Diese Veränderungen sind im Fernfeld sehr empfindlich und können als ergänzende Methode zur seismischen Überwachung während hydraulischen Stimulationen verwendet werden. Der aussergewöhnliche hydromechanische Datensatz erlaubt es, numerische Stimulationen zu testen und kann dazu beitragen die Injektionsstrategien, das Monitoring-Design und die numerischen Modelle zu verbessern.

Table of contents

1 Introduction 1

1.1 Heat reservoir: Earth . . . 1
1.2 Engineered or enhanced geothermal system (EGS) . . . 2
1.3 Reservoir creation . . . 3
1.4 Hydromechanical experiments at different scales . . . 7
1.5 Objectives of the thesis . . . 10
1.6 Thesis organization . . . 10

2 The In-situ Stimulation and Circulation (ISC) project 13

2.1 Context of the ISC project . . . 13
2.2 The ISC project . . . 13
  2.2.1 Pre-stimulation phase . . . 14
  2.2.2 Stimulation phase . . . 15
  2.2.3 Post-stimulation phase . . . 15
2.3 The hydraulic fracturing experiment . . . 16
  2.3.1 A mathematical approach . . . 16
  2.3.2 Semi-analytical solutions for fracture design . . . 18
  2.3.3 Injection metrics . . . 23
  2.3.4 Injection Protocol . . . 24

3 The fracture process zone in anisotropic rocks 27

3.1 Introduction . . . 28
3.2 Fracture toughness and strength . . . 29
  3.2.1 Fracture toughness measurement . . . 29
  3.2.2 Anisotropy of fracture toughness . . . 30
  3.2.3 Anisotropy of strength . . . 31
3.3 Fracture process zone . . . 32
  3.3.1 Characteristics of process zone . . . 32
  3.3.2 Experimental methods to evaluate FPZ . . . 34
  3.3.3 Lessons learned from past experiments . . . 36

3.3.4 FPZ evaluation using DIC . . . 38
3.4 Experimental setup . . . 39
3.4.1 The rock samples . . . 39
3.4.2 Fracture toughness and strength measurement . . . 40
3.4.3 Digital image correlation . . . 41
3.5 Experimental results on toughness and strength . . . 43
3.5.1 Fracture toughness anisotropy . . . 43
3.5.2 Post-mortem fracture surface analyses . . . 46
3.5.3 Strength anisotropy . . . 47
3.6 Experimental results on the FPZ . . . 49
3.6.1 Identification of the FPZ . . . 49
3.6.2 Shape of the fracture process zone . . . 52
3.6.3 Size of the fracture process zone . . . 52
3.7 Link between toughness, strength and the FPZ size . . . 57
3.8 Conclusions . . . 61

4 Hydraulic fracture propagation in a heterogeneous stress field 63
4.1 Introduction . . . 64
4.1.1 Intermediate scale experiments . . . 65
4.1.2 Complex hydro-mechanical response . . . 66
4.1.3 Seismic response and seismic cloud . . . 67
4.1.4 Our contribution . . . 67
4.2 Site and rock mass characterization . . . 68
4.2.1 Site description . . . 68
4.2.2 Geological characterization . . . 68
4.3 Field setup and monitoring . . . 73
4.3.1 Hydraulic fracturing equipment . . . 73
4.3.2 Monitoring systems . . . 74
4.4 Overview of the HF experiments . . . 75
4.4.1 Injection protocol . . . 75
4.4.2 Diagnostic injection parameters . . . 77
4.4.3 Transmissivity values from pre- and post-HF hydraulic tests . . . 81
4.4.4 Borehole fracture trace . . . 82
4.4.5 Microseismicity . . . 83
4.4.6 Fracture geometry . . . 84
4.4.7 Hydromechanical observations . . . 86
4.5 Comparison between stress characterization and HF experiments . . . 90
4.5.1 Injection pressure observations . . . 90
4.5.2 Fracture geometry . . . 91

4.5.3 Fracture propagation 94

4.6 Discussion 96

4.6.1 Hydraulic and mechanical response to hydraulic fracturing 96

4.6.2 Borehole trace and fracture tortuosity 97

4.6.3 Seismic response and fracture geometry 97

4.6.4 Permeability creation by HF 98

4.6.5 Stress heterogeneity 99

4.7 Conclusions 101

5 Hydromechanical insight of fracture closure 105

5.1 Introduction 106

5.1.1 Background on transient pressure analysis (TPA) 107

5.1.2 Hydromechanics 108

5.1.3 Research objectives 109

5.2 Rock mass characterization and experimental setup 109

5.2.1 Rock mass characterization 109

5.2.2 Experimental setup 111

5.2.3 Injection protocol 112

5.3 Methods 113

5.3.1 DFIT 114

5.3.2 Pressure-controlled step tests 115

5.4 Results and Interpretations 115

5.4.1 DFIT 115

5.4.2 Pressure-controlled step tests 119

5.4.3 Comparison of methods 122

5.5 Discussion 124

5.5.1 Transient pressure effects: geology and fluid rheology 124

5.5.2 Best estimate of the minimum principal stress magnitude 124

5.5.3 Implication for the stress field 126

5.6 Conclusions 129

6 The poroelastic far-field response 133

6.1 Introduction 134

6.2 Method 135

6.3 Results and Discussion 142

7 Periodic injection 151

7.1 Introduction 151

7.2 Experimental details 152

7.2.1 Injection and monitoring record 152

7.2.2 Pumping procedure . . . 152
7.2.3 Processing . . . 153
7.3 Preliminary results . . . 154
7.3.1 Lock-in amplifier vs. sliding FFT . . . 155
7.3.2 Observations from experiment HF8 . . . 155
7.3.3 Interference analysis . . . 157
7.3.4 Injectivity analysis . . . 159
7.4 Preliminary conclusions . . . 159
7.5 Outlook . . . 160
7.6 Digital lock-in amplifier . . . 161

8 Synthesis, conclusions and recommendations 163
8.1 Conclusions . . . 163
8.2 Perspectives and recommendations for future research . . . 168

References 171

Appendix A Supplemement: Hydraulic fracture propagation in a heterogeneous stress field 195
A.1 Pressure vs. Flow-rate analysis . . . 195
A.2 Transmissivity values . . . 199
A.3 Detailed observation of tilt, strain and pressure . . . 199
A.4 Summary of the MF injection pressure and seismic characteristics . . . 204
A.5 Fracture orientation determination from borehole logging and seismic plane analyses 205
A.6 Experimental summary cards . . . 207

Appendix B Observations of fracture propagation during decameter-scale hydraulic fracturing experiments 221
B.1 Introduction . . . 222
B.2 Geological site description . . . 223
B.3 Hydraulic fracturing . . . 225
B.3.1 HF procedure . . . 226
B.3.2 Variations along INJ1 and INJ2 . . . 226
B.3.3 Break down analysis . . . 228
B.4 Fracture geometry . . . 228
B.4.1 HF3 . . . 230
B.4.2 HF2 . . . 231
B.4.3 Outlook . . . 231
B.5 Conclusion . . . 232

Appendix C Observation of a repeated step-wise fracture growth during hydraulic fracturing experiment at the Grimsel Test Site 233
C.1 Introduction . . . 234
C.2 Study site characterization and monitoring . . . 235
C.3 Results . . . 237
  C.3.1 Hydraulic observations . . . 237
  C.3.2 Mechanical observations . . . 238
  C.3.3 Seismic observations . . . 239
C.4 Discussion seismo-hydromechanics . . . 239
  C.4.1 Multiple fracture extension . . . 239
  C.4.2 Stick-split mechanism . . . 242
  C.4.3 Hydraulic clapping mechanism . . . 245
C.5 Conclusion . . . 247

Appendix D Abstracts of related co-authored publications and reports 249
D.1 The seismo-hydromechanical behavior during deep geothermal reservoir stimulations: open questions tackled in a decameter-scale in situ stimulation experiment . . . 249
D.2 Comprehensive geological data of a fractured crystalline rock mass analog for hydraulic stimulation experiments . . . 250
D.3 Grimsel ISC Experiment description . . . 251
D.4 Stress measurements for an in-situ stimulation experiment: Integration of induced seismicity, stress relief and hydraulic methods in crystalline rock . . . 251
D.5 Running up the scales towards engineered geothermal systems: hydraulic stimulation and fluid circulation experiments in underground laboratories . . . 252
D.6 Influence of reservoir geology on seismic response during decameter scale hydraulic stimulations in crystalline rock . . . 253
D.7 On the Variability in Pressure Propagation during Hydraulic Stimulation based on Seismic Velocity Observations . . . 254
D.8 In-situ observation of helium and argon release during fluid-pressure-triggered rock deformation . . . 255

Chapter 1

Introduction

1.1 Heat reservoir: Earth

Earth is continuously generating approximately 46 ± 3 TW of thermal power (Jaupart et al., 2015), mainly by radiogenic heat production and primordial heat from its original formation. Earth's internal heat flow to the surface is mainly controlled by mantle convection (80%), which controls the heat transport from the mantle-core-boundary towards the crust. It is the driving force of the movement of the lithospheric plates. The remaining heat flow originates from the crust by radioactive decay of heavy nuclei ^{238}U, ^{235}U, ^{232}T and ^{40}K (Jaupart et al., 2015) and with about 1% by volcanic activity, earthquakes and orogeny (Turcotte and Schubert, 2014). Therefore, 99% of Earth's heat loss towards the surface is driven by conduction through the crust. The heat flow of the thicker continental crust is attributed to the radiogenic heat production, in contrast the thinner oceanic crust show a characteristic heat flow and age pattern, due to plate tectonic. Where the main driving force of heat flow is freezing the asthenosphere to the oceanic crust and cooling the both the oceanic mantel lithosphere and the oceanic crust. The specific mean heat flux for continental and oceanic crust is 70.9 and 105.4 $\mathrm{mW/m^2}$ (Davies and Davies, 2010). The highest heat fluxes are from the youngest rock at mid-ocean ridge spreading centers and the lowest heat fluxes can be found in the oldest rocks the so called cratons (Davies and Davies, 2010). The Earth's cooling process is very slow 99% of the Earth is hotter than 1000°C and 99% of the last percent is still hotter than 100°C. Human mankind has the technology and possibility to access the heat stored underground. Each kilometer we dig into the Earth's crust, the average temperature rises continuously by 30° C/km in average. The earth is therefore extremely suitable as a thermal source for energy generation.

However, currently, the technology needed for geothermal power production is largely limited to distinct geological conditions, namely volcanic area, where heat sources, temperature and heat flow are driven by strong advective heat transport (Saar, 2011). In non-volcanic area, developing deep geothermal comes with challenges. Particularly, the upfront economic challenge is the high cost and commercial risks associated with drilling deep geothermal wells to produce energy and longer development time compared to solar or wind energy. The advantages are the high availability and independence from weather conditions compared to other renewable sources. It has the advantage that it is naturally stored in the underground and can be directly accessed when needed through geothermal wells. Direct usage of geothermal energy involves space heating, greenhouse heating, aquaculture, agricultural drying, bathhouses, industrial uses, and cooling. For the use of geothermal production for electrical power generation, the first law of thermodynamics applies with energy transfer/conversion either by directly running turbines with the overheated geothermal fluid or by transferring first the heat to a secondary fluid with low boiling point that is used to drive a turbine. With the right target temperature, pressure and circulation fluid, it can produce carbon dioxide neutral electricity and is ideally for baseload power (i.e. 24/7). It can play a significant role as the world moves toward a low-carbon economy by reducing greenhouse gas emission and phasing out fossil-fueled thermal and probably nuclear plants. In many countries, it is an integral part of the strategy to achieve energy independence and reduce reliance on fossil fuels (Zarrouk and McLean, 2019).

1.2 Engineered or enhanced geothermal system (EGS)

Hot rock masses are found everywhere at sufficient depth in the continental crust, but often have natural permeability less than 10^{-16} m^2 (Achtziger-Zupančič et al., 2017; Manning and Ingebritsen, 1999; Saar and Manga, 2004). This is insufficient to allow large volume fluid circulation to advectively extract heat energy economically, such that permeability has to be artificially enhanced. Production flow rates above $50\,\mathrm{l/s}$ for water should be achieved in order to ensure an economical operation of an EGS (Evans et al., 2014). To get such flow, one needs to increase the permeability or do use a more favourable fluid or both. For example, due to its lower viscosity, CO_2 will be able to circulate with larger flow rates than water. It has been shown that CO_2 can utilize lower temperatures and permeabilities for economical power generation (Randolph and Saar, 2011). The first 'engineered geothermal system' was developed at Fenton Hill, USA under the project name Hot Dry Rock (HDR) followed by Rosemanowes Quarry (UK), Falkenberg (D), Le Mayet (F), Urach (D), Ogachi (J), Fjällbacka (Sw) and Soultz-sous-Forets (F) (more in Breede et al., 2013; Tester et al., 2007). Later, the term HDR was replaced by Engineered or Enhanced Geothermal Systems (EGS) to reflect the correct basic idea of artificial enhancement of the permeability in a rock mass in order to produce a suitable heat exchanger that allows fluid circulation between two or more wells Cummings and Morris (1979). The EGS-technique has the advantage that it can be used independent of the geological setting (e.g. sedimentary rock: Gross Schönebeck, Germany; igneous rock: Krafla, Iceland; metamorphic rock: Lardello, Italy).

In regions with standard geothermal gradient of about $30^\circ\,\mathrm{C/km}$, a well needs to be drilled at least 5 to 6 km depth into crystalline hard rock to reach the target formation temperature above 180° C. Sometimes it is required to use high pressure or chemical stimulations achieving a sustainable heat exchanger. This critical stage has often unpredictable outcomes due to insufficient knowledge about the underground conditions and the physical mechanism involved. Everywhere in the Earth exists compressive stress, where the magnitude of stress depends on the depth, pore pressure and the geological processes. These geological processes exist at various temporal and spatial scales. The relative stress magnitudes allow to differentiate between normal, reverse and strike-slip faulting regimes. The Earth does not have a homogeneous crust, different geological formations and structures are present. Fractures with the right orientation for shear failure, which are stable as long as there is not an additional amount of pore or fracture fluid pressure are active fractures, which are near to creep or catastrophic failure. These active fractures in the crust is referred to as 'critically stressed' and are traditionally presented by a Mohr diagram (more details can be found in Zoback, 2007). Hydraulic stimulation into the critical stressed earth crust produces earthquakes, where felt earthquakes (i.e. M_w 3.2 earthquake Basel EGS (Häring et al., 2008) or M_w 5.5 earthquake Pohang EGS (South Korea) (Grigoli et al., 2018; Kim et al., 2018)) led to the abandonment of some projects (Basel EGS project (Häring et al., 2008)). Recently, it was found out that the Pohang earthquake was very likely triggered by the geothermal reservoir development activities (Lee et al., 2019). Other technical problems are wellbore integrity (Newberry EGS (Cladouhos et al., 2015)), gas inflow potentially leading to borehole blow-out (St. Gallen hydrothermal project (Diehl et al., 2017; Obermann et al., 2015)) or too low production flow rates. During hydraulic stimulation, difficulties due to near-wellbore tortuosity (Bunger and Lecampion, 2017), and complex fracture network interaction (e.g. basic conditions for network versus localized fracture growth) are reported (see Bunger and Lecampion, 2017, for more references). Promising results were found in well explored areas like Soultz-sous-Fôret (Genter et al., 2010) and Rittershofen (Baujard et al., 2017).

It is a challenging task to generate a reservoir with enough fracture area, which allows heat extraction through a big swept volume. Especially, as the fracture network needs to intersect the production and injection well to establish a circulation between the two. Therefore, transmissivity/injectivity needs to be in a range such that an efficient heat exchange between circulation fluid and rock can be generated. Thus, the production time can be above 20 years, which is important for the return of investment. The circulation of fluid from well to well is one of the main differences between EGS and oil & gas applications.

1.3 Reservoir creation

Hydraulic stimulation aims at creating connected permeability in a defined volume which I will refer to as the reservoir. Two different paradigms are commonly known: 1) hydraulic fracturing as the initiation and propagation of mode I fractures, and 2) hydraulic stimulation, i.e., the reactivation of pre-existing fractures that support shear stress, which promotes shear failure with associated irreversible dilation. These end-members are not mutually exclusive and a combination is possible: McClure and Horne (2014) suggested combined hydraulic stimulation mechanisms such as primary hydraulic fracturing with shear stimulation leak off or mixed-mechanism stimulation (Fig. 1.1). Hydraulic fracturing is the common concept used in reservoir stimulation in the oil and gas industry (King and

Corporation, 2012; Sutton et al., 2010), while the hydraulic shearing concept became important for the understanding of enhanced geothermal reservoirs (i.e. Rosemanowes test site (Pine and Batchelor, 1984) and at Soultz-sous-Forêts test site (Evans et al., 2005)).

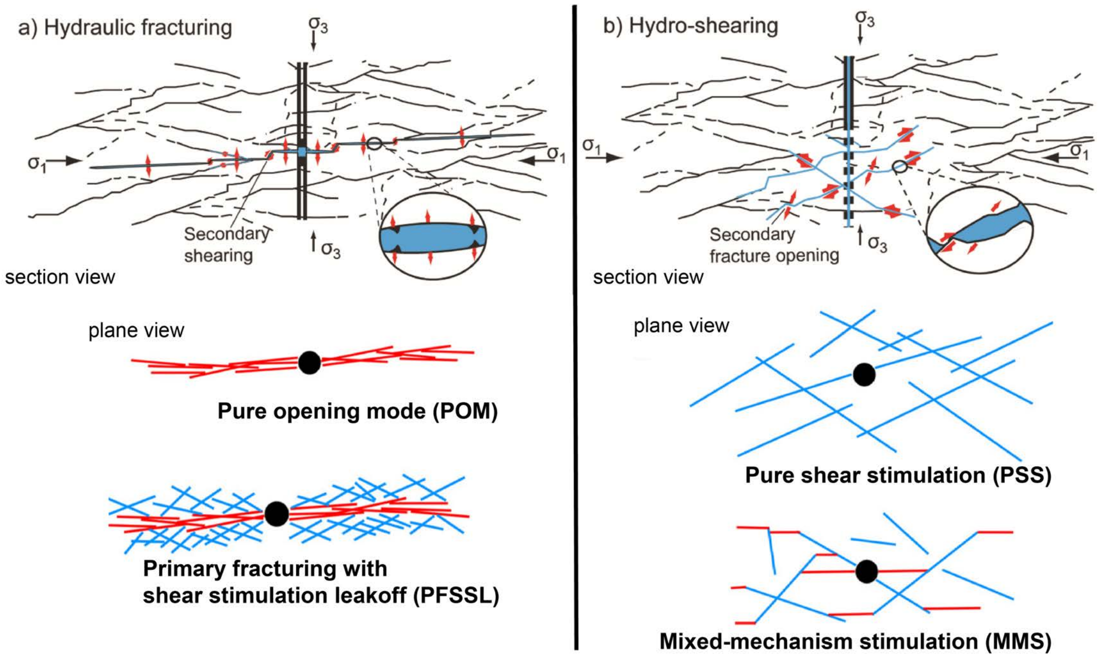

Fig. 1.1 a) Hydraulic fracturing opens new or pre-existing tensile fractures from a small packed interval. The fluid is injected at pressure above σ_3. The plane view indicates two conceptual models with new fractures as red lines and preexisting fractures are represented by blue lines. The two mechanism are: pure opening mode (POM) and primary fracturing with shear stimulation leakoff (PFSSL). b) Hydro-shearing target to reactivate natural pre-existing fractures approvingly oriented for shearing. The fluid is injected at pressure remaining lower than σ_3. The plane view indicates two conceptual models with new fractures as red lines and preexisting fractures are represented by blue lines. The two mechanism are: pure shear stimulation (PSS) and mixed-mechanism stimulation (MMS). Adapted Figure after Gischig and Preisig (2015); McClure and Horne (2014).

The evolution of deep geothermal reservoir concepts is presented by conceptual end-members (Fig. 1.2). Keep in mind, that from a historical perspective, the terms were sometimes used differently. Stimulations in the context of EGS often take place along open borehole sections of several hundred meters (Brown et al., 2012). In early times, the conventual hydraulic fracturing after Sneddon and Elliott (1946) was used for designing the Hot Dry Rock (HDR) concept, assuming a single vertical and penny-shaped fracture. The HDR concept (Fig. 1.2a) is a fully engineered, petrothermal reservoir with the minimum principal stress in direction normal to the hydraulic fracture. The 21 years of HDR research at Fenton Hill (Brown, 2009) showed that an HDR reservoir is saturated and confined (Fig. 1.2b). By confined, the author at the time meant "that except for a small—and slowly decreasing-pressure-dependent diffusion of fluid from its boundaries, the reservoir of pressurized fluid is totally contained" (Brown, 2009). Nowadays, we would typically refer this as a closed-system. This is taken into account with the color shift in Fig. 1.2 a) and b) from reddish to greyish color for the crystalline rock mass. Both concepts, HDR and HWR assume an intact rock without fractures, where the fluid loss is small during stimulation and circulation.

Hydrothermal systems are associated with existing aquifers, where natural fractures and structural weak zones in the reservoir dominate the in-situ fluid transport. They are known under the name hot fractured rock (HFR, Fig. 1.2c) (Wyborn et al., 2005) or fractured hydrothermally altered geothermal reservoir (HFR, Fig. 1.2d) (Genter et al., 2010, 2003). Both types of reservoir can be enhanced by hydraulic, thermal or chemical stimulations (the acronym for the enhancement of the geothermal system is also EGS, Fig. 1.2e). The acronym EGS is often used indifferently for enhanced & engineered geothermal systems with enhanced or engineered being used practically as synonyms. We propose here, based on the literature study and evolution of reservoir stimulation concepts to differentiate enhanced from engineered geothermal systems. For instance the Soultz-sous-Forêts project showed a dominant hydraulic shearing mechanism for permeability creation (Evans et al., 2014). The hydrothermal concepts do have an in-situ flow path extension typically in the direction of the major principal stress magnitude. The interconnected joint structure control the pressure during stimulation and circulation, which is a critical task as the in-situ flow and the injected fluid can not be controlled due to the open hydrothermal nature of these structures.

To counteract this uncertainty, there is another concept that is more oriented towards the early HDR concept (Fig. 1.2f). It is often observed that after a short distance away from the injection interval the hydraulic fracture is not breaking open intact crystalline rock against the inherent tensile strength, rather than opening sealed natural fractures. The conventional theory of HF ignores the presence of flaws in the crystalline rock (Brown et al., 2012). Such stimulation treatments are usually controlled by the most permeable fractures that are often critically stressed (Barton et al., 1995), and hydraulic shearing becomes the dominant mechanism for permeability creation, at least several tens of meters distance away from the injection interval (Evans et al., 2014). These highlight a widespread problem of enhanced geothermal system projects: permeability in the near-field around the borehole can be adequately enhanced, but not necessarily in the far-field. In order to develop geothermal reservoirs with more success, more control on the permeability enhancement processes must be gained. This requires to apply more engineering in the reservoir development protocols. One possibility to impose more engineering and gain control is to reduce stimulation intervals with multi-packer systems to control the flow zonally. We call such approach engineered geothermal system (EGS, Fig. 1.2f) concept including multi-stage hydraulic stimulation (e.g. Meier et al., 2015) and we differentiate it from "enhanced geothermal system" where preexisting flow zones dominate the reservoir response during stimulation. The reduced length of the open intervals will probably allow to initiate and propagate tensile fractures, which may become an important mechanism in the near field of the wellbore to connect the wellbore to the pre-existing fracture network and to increase the swept reservoir volume. It is still debated how far a hydraulic fracture or a mixed fracturing (shearing and fracturing in combination) can grow in length. Additionally, the amount of injection fluid for stimulation can be controlled and the fluid viscosity can be enhanced to decrease the fluid leak-off. To avoid large formation break down pressure during the first stimulation cycle, the borehole intervals can be notched. Depending on the fracture characteristics in the near-field of the borehole, it could be necessary to add proppants (e.g. sand) to the injection fluid to keep the fracture open. Another, possibility is to apply a backpressure to the interval during circulation. In any case, our ability to understand and develop any of these deep systems depends greatly on in-situ flow paths, the in-situ stress field and a-priori knowledge of the fracture systems.

Key parameters like tensile strength and Mode I fracture toughness value for the intact rock mass can be investigated on lab scale (Ouchterlony, 1988; Perras and Diederichs, 2014). Complexity arises due to rock heterogeneity and rock anisotropy, both can strongly affect hydraulic fracture propagation together with stress field perturbations (Bunger and Lecampion, 2017). Furthermore, the natural fractures can play an important role, depending on fracture density, fracture orientation, fracture length and fracture connectivity. Successful hydraulic fracturing with the aim to increase the connectivity between two boreholes depends directly on the rock and fracture characteristics and the stress conditions. Therefore, the hydromechanical coupling plays a central aspect. Guglielmi et al. (2014, 2015) performed in-situ experiments to study the fault zone response using a straddle packer system that allowed measuring the 3-dimensional relative displacement at the injection point. These tests were performed in sedimentary rocks at shallow depth, while no such measurements have been performed on faults in crystalline rocks. The coupled hydromechanical effects of fractures and faults under high-pressure fluid injection in crystalline rock were extensively studied on dm lab-scale (Bandis et al., 1983; Cornet and Valette, 1984; Evans et al., 1992; Rutqvist and Stephansson, 2003; Zangerl et al., 2008). The opening/closure behaviour is associated with effective normal stress change and can be described as highly non-linear. In addition, the shearing causes irreversible increase in permeability and even for single fractures scale, the uncertainty are big due to fracture transmissivity sensitivity to small fracture aperture changes (Louis et al., 1977; Rutqvist and Stephansson, 2003).

The fluid metric and the injection flow-rate or the injection pressure can be controlled by the reservoir engineer. The conventional injection scheme with continuous or step rate test are often applied and can either allow to create new HF or shear pre-existing structures depending on the injection location. It is debated if alternative injection schemes like cyclic injections (called fatigue fracturing or harmonic pulse testing) can reduce the maximum possible earthquake magnitudes (Zang et al., 2017). It is shown that the break down pressure on laboratory scale can be reduced by 20% for some rocks, but has no effect for others (Patel et al., 2017; Stephansson et al., 2019). The fatigue hydraulic fracturing was applied at the Äspö Hard Rock Laboratory, Sweden (Zang et al., 2017, 2019; Zimmermann et al., 2019) and the Pohang site (Hofmann et al., 2019). The authors assume that the cyclic fluid interaction can reach the fracture tip, such that extended branching of the fractures appear. Others used cyclic or pulsating injection schemes as monitoring tool to estimate hydraulic

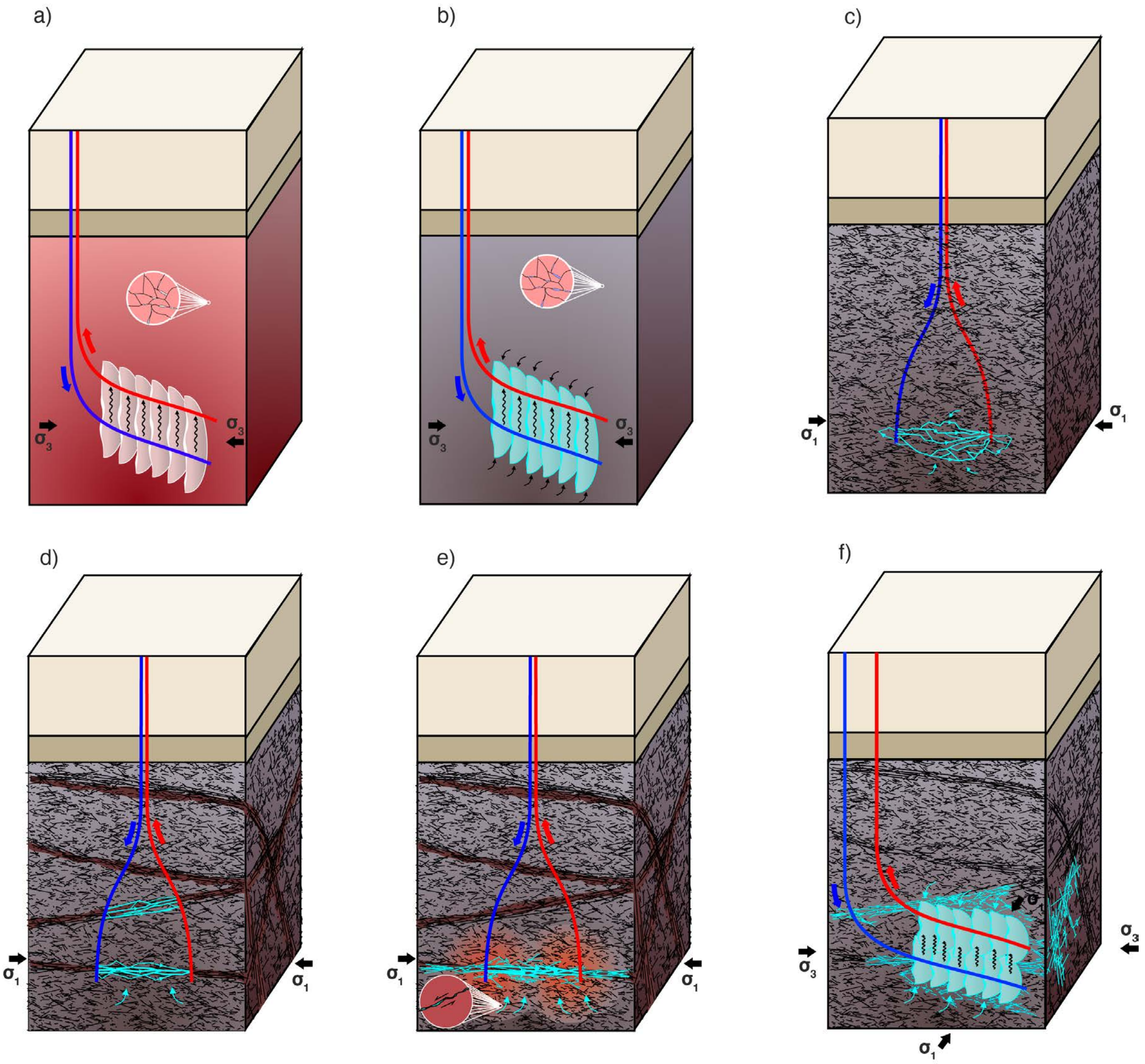

Fig. 1.2 The evolution and classification of the deep geothermal reservoir concepts: a) Hot dry rock (HDR), b) hot wet rock (HWR), c) hot fractured rock (HFR), d) fractured hydrothermally altered geothermal reservoir (HFR), e) enhanced geothermal reservoir (EGS) and f) engineered geothermal reservoir (EGS; e.g. multistage fractured geothermal reservoirs).

and poroelastic rock and reservoir properties (Fokker et al., 2018; Hasanov et al., 2019; Renner and Messar, 2006).

1.4 Hydromechanical experiments at different scales

Large scale hydraulic fracturing has in general the goal to enhance the bulk permeability, induce new fracture paths or connect new fractures to a preexisting natural fracture network. From the oil & gas industry comprehensive and good quality data available to the scientific community are sparse and rarely published. Hence, data are acquired from German continental deep drilling program (Baisch and Harjes, 2003; Emmermann and Lauterjung, 1997; Jost et al., 1998; Zoback and Harjes, 1997) or deep geothermal boreholes (Albright and Pearson, 1982; Asanuma et al., 2005; Evans et al., 2005; Häring et al., 2008; Moeck et al., 2015). During the hydraulic fracturing job, flow rate and injection pressure from the stimulated interval are measured. Other monitoring systems are recommended and sometimes mandatory. Different systems are available to record microseismic (Das and Zoback, 2011; Rutledge and Phillips, 2003; Sasaki, 1998; van der Baan et al., 2013; Warpinski, 2009), tilt (Lecampion et al., 2005; Warpinski et al., 1997; Wright et al., 1998) and strain data (Karrenbach et al., 2017). These data allow to gain fracture maps, source mechanics (van der Baan et al., 2013; Warpinski et al., 2013) and energy balance between injected fluids and seismic energy release (Boroumand and W. Eaton, 2012; van der Baan et al., 2013; Warpinski et al., 2013; Zoback et al., 2012).The seismo-hydromechanical processes during hydraulic fracturing growth cannot be resolved during large scale hydraulic fracturing jobs. Especially the interaction between the hydraulic fracture growth and the natural fracture network are referred to complexity in the HF jargon, which is a major limiting factor to increase the understanding of permeability creation process. This limitation is directly associated with the limited access of the underground, due to a given number of boreholes and monitoring costs for a high spatial resolution.

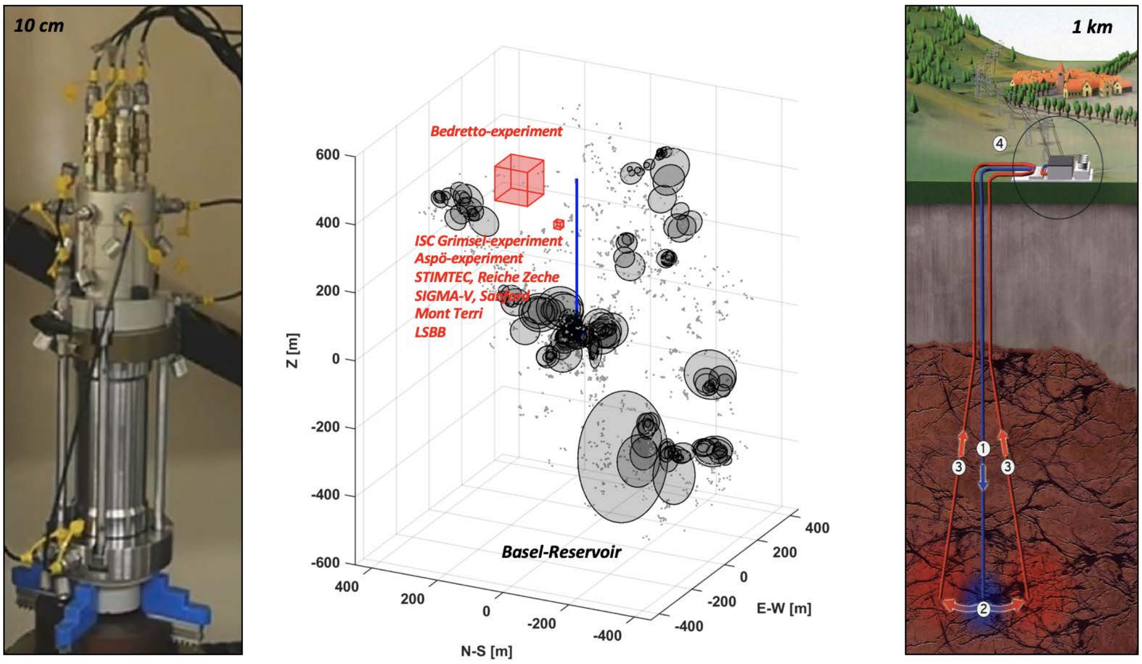

Fig. 1.3 Compares the representative elementary volume (REV) from laboratory to field scale including in-situ experimental sites (red squares) compared to the Basel-Reservoir (Figure adapted from Gischig et al., 2019).

On the laboratory scale, very well controlled small scale experiments on samples in laboratory settings were performed (Bennour et al., 2015; Casas et al., 2006; Chen et al., 2015; Ishida et al., 2012, 2004, 2000; Jaeger, 1963; Jeffrey and Bunger, 2007; Johnson and Cleary, 1991; Yushi et al., 2017; Zoback et al., 1977). The samples have typically a shape of a hollow cylinder or perforated prisms. The samples are loaded and injected until a fracture is initiated and propagated. Different studies are carried out to study fracture propagation (Jeffrey and Bunger, 2007), fracture branching (Athavale and Miskimins, 2008), testing different fluids (Bennour et al., 2015; Ishida et al., 2004) and acoustic emission versus aseismic slip (Ishida et al., 2012; Molenda et al., 2015). An additional aim of this well-controlled laboratory investigation is to benchmark numerical hydraulic fracturing codes. The drawback of laboratory scale is that samples are in general relative homogeneous compared to field scale and oversimplify the hydraulic fracturing process. The upscaling to field scale is affected by large uncertainties (i.e. geological model, heterogeneities and in-situ stress field).

The intermediate scale bridge the gap between reservoir scale and laboratory scale. It allows to develop well-controlled in-situ experiments in the underground laboratory. The access of the rock mass allow characterisation before and after hydraulic stimulation and spatial dense monitoring system can be installed to study seimo-hydromechanical processes. The first kind of these experiments took place at the Nevada test site in soft volcanic tuff (Warpinski, 1985). The mine back after injection experiment showed multiple fracture strands and complex fracture shapes due to pressure and fluid distribution. The Northpark mines hydraulic fracturing experiment (Jeffrey et al., 2009) was developed to investigate fracture growth in naturally fractured rock and to compare the fracture geometry from microseismic and tilt monitoring. The latest projects are Äspö Hard Rock Laboratory, Sweden, (Zang et al., 2017), Grimsel Test Site, Switzerland, (Amann et al., 2018), Reiche Zeche STIMTEC, Germany, (Dresen et al., 2019), Mizunami Underground Research Laboratory, Japan, (Ishida et al., 2019), Bedretto Underground Research Laboratory for Geoenergies, Switzerland, (Gischig et al., 2019) and Stanford Underground Research Facility, USA, (Kneafsey et al., 2018). These kind of experiments is downscaling the overall geometry inclusive some physical parameters. Varying the boundary conditions allow to investigate different physical processes appearing on the reservoir scale. Some limitation still exist, like the limiting size of the representative experimental volume (REV), which scales with the fluid volume, which will be injected without risk damaging the surrounding laboratory. This reduction is significant compared to the reservoir scale (around 4 orders of magnitude) and makes it safer with respect to induced seismicity. Other parameters, such as fracture spacing, fracture length, number of fracture sets, fracture aperture, rock mechanical parameters and the in-situ stress field are not scalable. The laboratory-scale experiments investigate the behavior of single fractures, but is limited on this single fractures, where the intermediate in-situ scale gives more and more insights into the complex hydromechanical coupled processes related to different fracture networks approaching by the increasing REV.

1.5 Objectives of the thesis

The main scope of this thesis is to gain insights on the involved physical processes during hydraulic stimulation within a decameter-scaled crystalline rock mass. The hydromechanical data set allow us to study fundamental processes involving transient pressure propagation, permanent and transient rock mass deformation, seismics, fracturing mechanisms and the interaction with the involved natural fracture system and stress field. This thesis contributes to the hydraulic fracturing experiment during pre-, main and post-stimulation phase addressing the following questions:

- How does the anisotropy of the rock mass influence rock mass properties (i.e. fracture toughness and tensile strength)? Does anisotropy also influence the fracture process zone?
- How does the injection metrics (e.g. injection flow rate and fluid viscosity) influence fracture propagation, micro-seismicity and fracture geometry (e.g. length, fracture trajectory and aperture history) and how does the injection protocol influence fracture propagation and associated micro-seismicity? How do hydraulic fractures interact with pre-existing natural fractures?
- How are aperture-stress relations linked with observations from the diagnostic fracture injection test analysis and pressure-controlled step tests? Does the stress tensor indicate any changes due to main geological structures?
- How does the poro-elastic effect look during the HF experiment? What are the main structures influencing poro-elastic effects?
- What are hydraulic and poroelastic rock properties from oscillating high-pressure injections?

In addition, the in-situ HF experiment provides a novel reference 3D data set at exceptional high spatial resolution.

1.6 Thesis organization

The thesis consists of a main part and the appendix. The main part contains the general introduction to this thesis motivating the key questions (Chapter 1), the introduction to the In-situ Stimulation and Circulation project inclusive design and preparation work to the HF experiment (Chapter 2) and the five manuscripts that either are already published in scientific journals or a mature draft close to submission at the time of compilation of this thesis. The first manuscript (Chapter 3) deal with rock mechanical properties linking Mode I fracture toughness, tensile strength and fracture process zone in anisotropic rocks like Grimsel Gneiss, the host rock of the ISC project. The other manuscripts deal with the overall seismo-hydromechanical rock mass response during the in-situ hydraulic fracturing experiment (Chapter 4), hydromechanical insights of fracture closure (Chapter 5), the poro-elastic effects during in-situ hydraulic fracturing experiments (Chapter 6) and hydraulic and poro-elastic response to the oscillating high-pressure injection (Chapter 7).

The appendix contains the supplementary materials for Chapter 4 and two related first author conference proceeding paper which were submitted to the 52nd US Rock Mechanics / Geomechanics Symposium (2018) and the World Geothermal Congress (2021). The first contribution deals with the observation of fracture propagation during the in-situ hydraulic fracturing experiment (Appendix B) and the second contribution investigates the repeated step-wise fracture growth during a hydraulic fracturing experiment (Appendix C). The abstract of the seven co-authored journal publications, that have been published or submitted to a journal are provided, as well as the abstract of the ISC experimental description (Appendix D).

Chapter 2

The In-situ Stimulation and Circulation (ISC) project

2.1 Context of the ISC project

In Switzerland, the popular vote accepted the ’Swiss Energy Strategy 2050’ in May 2017. It requires the phasing out of the nuclear power plants and their replacement by mostly local and renewable ressources. The Swiss Energy Strategy 2050 foresees roughly 4.4 TWh of electricity per year produced via geothermal energy by 2050. These are 20 power plants with 25 MWe capacity. As no power plant with this capacity is working in Switzerland until today, this demanding strategy needs to encourage scientific and engineering developments in the understanding of reservoir creation to limit the seismic activity during fracture creation and dilation (a detailled analysis of the deep geothermal resources can be found in Bauer et al., 2015). The Swiss Competence Centre of Energy Research – Supply of Energy (SCCER-SoE) with the aim to carry out innovative and sustainable research in geo-energy and hydropower is a conssequence of the Swiss Coordinated Energy Research action plan. The SCCER-SoE conducts various experiments on different scales from centimetres (rock deformation laboratory) to two decametres, which is called "In-situ Stimulation and Circulation" (ISC) experiment in a Deep Underground Laboratory (DUG-Lab). The follow-up project is on a scale of hectometer, which is called "Bedretto Underground Laboratory for Geoenergy" research (BULG). The experimental work is supported by numerical modelling studies to understand the stimulation process over different scales and how the rock mechanical parameters can be upscaled for a future EGS (km scale).

2.2 The ISC project

The ISC experiment was carried out at the Grimsel Test Site (GTS) (Fig. 2.1), Switzerland, between 2015 and 2018. The GTS is situated beneath the mountains of the Grimsel Pass connecting the Valais with the Bernese Oberland and lies 480 m below the surface (Figure 2.1). It is owned by the National

Cooperative for the Disposal of Radioactive Waste (NAGRA) and is originally host of experiments relevant to nuclear waste repository. The rock type at the GTS is representative for crystalline basement under the Swiss Molasses Basement, which is main target for EGS in Switzerland. The main goal of the project was to gain insights from fundamental hydromechanical processes involved during hydraulic stimulation. The decameter scaled test volume consists of a slightly fractured rock mass with two prominent shear/fault zones. The shear zones intersecting the underground laboratory extend more than 480 m and outcrop in the mountainous surface. The ISC experiment is located in the southern part of the GTS between two tunnels called VE and AU-tunnel. The comprehensive, interdisciplinary project was divided into three parts.

Fig. 2.1 Location of the GTS next to the Grimsel pass and the ISC test volume is located in the southern part of the GTS.

2.2.1 Pre-stimulation phase

The pre-stimulation phase took place between 2015 and February 2017. This phase in turn can be divided into three tasks: borehole drilling, sensor installation and rock mass characterization. A total of 15 boreholes were drilled into the rock mass. Simultaneously, geological mapping was done in the three access tunnels and the newly drilled boreholes using geophysical borehole logging tools. All the boreholes were cored and allowed laboratory testing of the rock mass (e.g. Chapter 3 and Dambly et al., 2019; Dutler et al., 2018a; Nejati et al., 2019a; Selvadurai et al., 2019; Wenning et al., 2018). The primary geological model was updated by a step-be-step basis for further planning of the stimulation experiment. Additionally, the rock mass was geophysically characterized by tunnel-tunnel seismic tomography and ground penetrating radar measurements (Doetsch et al., 2017). The finalised geological model was published (Krietsch et al., 2018) and can be used to interpret the stimulation experiments. The in-situ stress was characterized by hydraulic and stress relief methods (Krietsch et al., 2019). The hydrogeological characterisation involved single well, interference tests (Brixel et al., 2020a,b; Jalali et al., 2018b), tracer tests (Kittilä et al., 2019) and hydraulic tomography to characterize the main flow paths (Klepikova et al., 2020). The monitoring systems were installed along the tunnel and in the drilled boreholes based on the comprehensive characterization phase. The monitoring system consists of pore pressure, temperature, rock mass deformation and microseismic monitoring and allow high temporal and spatial resolution of seismo-hydromechanical processes during stimulation (Doetsch et al., 2018b).

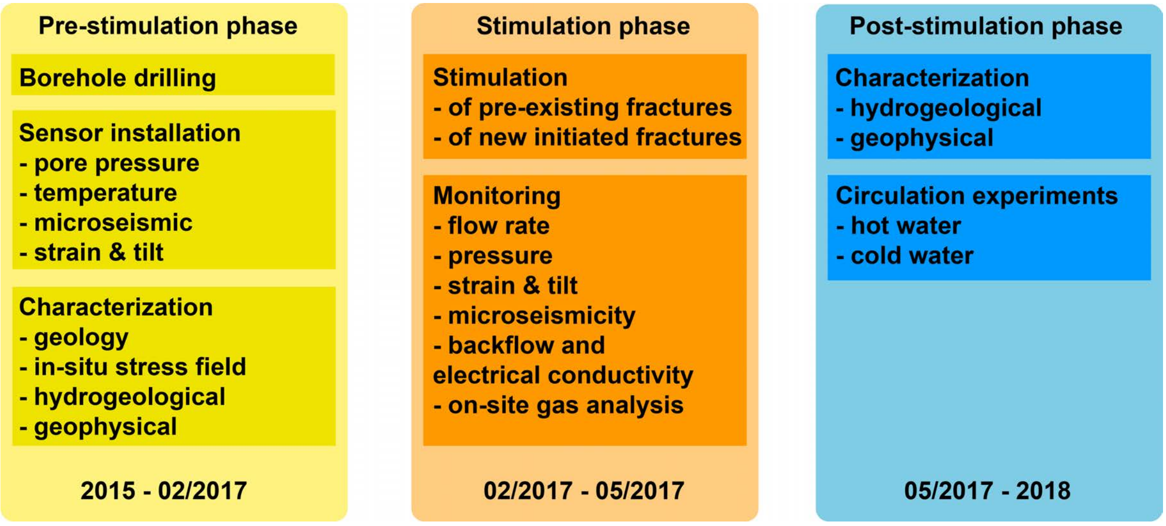

Fig. 2.2 Visualization of the three phases of the ISC project.

2.2.2 Stimulation phase

The main stimulation phase took place between February and May 2017. A total of six hydro-shearing (HS) and six hydraulic fracturing (HF) experiments were conducted within the test volume. During the experiments, the comprehensive monitoring systems recorded a unique dataset which allow to study fundamental processes related to seismo-hydromechanical coupled processes during hydraulic stimulation (Dutler et al., 2019; Krietsch et al., 2020; Villiger et al., 2020). During the experiments, the pre-existing structures were successfully reactivated yielding in enhanced transmissivity and rock mass deformation. The hydraulic fracturing was placed in intact rock to create new flow paths and enhance the fracture connectivity. Both stimulation types were successfully tested and lead to partly similar and partly different outcomes. The seism o-hydromechanical observations from the HF experiments are presented in Chapter 4 (Dutler et al., 2019), 5 (Dutler et al., view), 6, 7 and in the Appendix (Dutler et al., 2018b, 2020).

2.2.3 Post-stimulation phase

The post-stimulation phase of the ISC project took place between May 2017 and 2018. During this last phase the test volume was again hydraulically and geophysically characterized. The transmissivity enhancement and improved fracture connectivity were quantified by single well tests, thermal and dye/salt tracer tests. The ground penetrating radar surveys were done to visualise the highly transmissive fluid paths. The very last phase contains the circulation experiment to study the rock mass effects during cold water and hot water circulation. Unfortunately, the difficulties with the fluid cooling and the time restrictions did not allow to successfully investigate cooling effects on the rock mass.

2.3 The hydraulic fracturing experiment

In the following section, I introduce a general mathematical approach for a steady state fluid-driven fracture propagation. Depending on boundary conditions and fracture geometries different semi-analytical solutions exist. In industry, these solutions are often used for fracture design, so did I. I calibrated the solutions against the hydraulic fracturing records from the stress characterisation phase and used it to design the injection protocol.

2.3.1 A mathematical approach

A general approach formulates the governing equation using a planar crack. Consider hydraulic fracture propagating in an infinite elastic medium. An incompressible fluid of viscosity μ is injected at the centre of the fracture at constant injection rate Q_0. Therefore, the fluid is injected from a point source. The fluid reaches the tip of the crack. The fracture propagates continuously in mobile equilibrium. So far, the problem is similar to a plane-strain semi-infinite fracture propagating in a homogeneous solid with constant velocity. It is assumed that the lubrication theory is applicable and the hydraulic fracture is characterised by two distinct fronts moving with time t: crack edge $C_c(t)$ and fluid front $C_f(t)$, which is contained in $C_c(t)$. $C_f(t)$ defines the fluid-filled fracture domain $A_f(t) \in A_c(t)$. A fluid driven fracture shows a negligible lag such that the two fronts, crack edge and fluid front, effectively coalesce to a single front. Under the assumption that fluid leak-off into the host rock is negligible and the Linear Elastic Fracture Mechanics (LEFM) is valid the problem can be described for a steady propagation of semi-infinite fluid-driven fracture (Detournay, 2016).

The fluid lag λ is described as the distance between x_f and x_c (compare Figure 2.3). It is a priori unknown. Two fundamental equations govern the fracture opening $w(\boldsymbol{x},t)$ and the fluid pressure $p_w(\boldsymbol{x},t)$: nonlinear Reynolds lubrication equation and the nonlocal elasticity equation. For simplicity, the following material parameters are introduced:

$$E' = \frac{E}{1-\nu}, \quad K' = 4(\frac{2}{\pi})^{1/2} K_{Ic}, \quad \mu' = 12\mu \tag{2.1}$$

E' is known as the plane-strain modulus with E Young's modulus and ν Poisson's ratio of the rock mass. K' is toughness with K_{Ic} fracture toughness, which is the measure of energy required to create new fracture surfaces and μ' is viscosity with μ fluid viscosity. The fluid pressure p_f corresponds to the sum of net pressure p and minimum in-situ stress σ_0. $\mathbf{x}'$ is the integration variable. We assume that the orientation of the minimum principal stress is uniform, such that the fracture propagates in pure tensional mode. The elasticity equation can be expressed as hypersingular integral equation

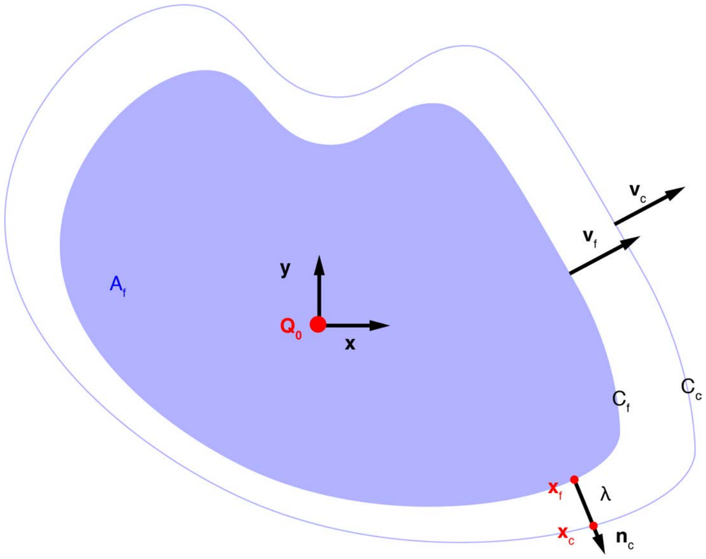

Fig. 2.3 Planar hydraulic fracture with two distinct moving fronts: crack edge $C_c(t)$ and fluid front $C_f(t)$. Figure adapted from Detournay (2016).

(Crouch et al., 1983; Hills et al., 1996). It equilibrates the net pressure in the fracture with the normal stress induced by continuous normal dislocation.

$$p(\mathbf{x},t) = \quad p_f(\mathbf{x},t) - \sigma_0(\mathbf{x}) = -\frac{E'}{8\pi}\int_{A_c(t)} \frac{w(\mathbf{x}',t)dA_c(\mathbf{x}')}{|\mathbf{x}-\mathbf{x}'|^3} \qquad \mathbf{x} \in A_c(t) \tag{2.2}$$

The Reynolds Equation 2.3 is a specific approximation of the Navier-Stokes-Equation neglecting the inertial terms due to slow flow of the fracture fluid. It is assumed to be laminar. The nonlinear Reynolds Equation 2.3 describes the change of normal opening in the fracture during continuous fluid injection $Q(t)\delta(\mathbf{x})$ and the gradient of fluid flux $\mathbf{q}$.

$$\frac{\partial w}{\partial t} = \quad \frac{1}{\mu'}\nabla(w^3\nabla p_f) + Q(t)\delta(\mathbf{x}), \quad \mathbf{x} \in A_f(t) \tag{2.3}$$

Poiseuille's law relates the fluid flux $\mathbf{q}$ with the fracture normal opening, the fluid pressure gradient in the fracture and the fluid viscosity, together.

$$\mathbf{q} = \quad -\frac{w^3}{\mu'}\nabla p_f \tag{2.4}$$

Combining equation 2.3 and 2.4 leads to the continuity equation 2.5.

$$\frac{\partial w}{\partial t} + \nabla\mathbf{q} = \quad Q(t)\delta(\mathbf{x}) \tag{2.5}$$

$\delta(\mathbf{x})$ correspond to the Dirac function with $\boldsymbol{x}$ as space vector. The positions vector $\boldsymbol{x}$ has the injection point conveniently at the origin. The boundary conditions on the crack moving front are:

$$w(\mathbf{x_c},t)=0, \quad K_I(\mathbf{x_c},t)=K_{Ic}, \quad \mathbf{x_c}\in C_c(t) \tag{2.6}$$

The second condition reflects that the stress intensity factor K_I, is everywhere equal to toughness (Irwin, 1957). The dissipated energy during creation of new surfaces in the solid is exactly equal to the energy flowing from the infinitesimal advance of the front to the crack tip. The outward normal to the crack front $\boldsymbol{n_c(x_c)}$ and the velocity $\boldsymbol{v_c(x_c)}$ of the crack front, with $v_c = \boldsymbol{n_c(x_c)}\cdot\boldsymbol{v_c(x_c)}$ is normal to the crack front. Writing $K_I = K_{Ic}$ implies continuous propagation everywhere along the crack front, therefore $v_c(\boldsymbol{x_c}) \geq 0$. The boundary conditions on the fluid moving front are:

$$p_f(\mathbf{x_f},t)=0, \quad \mathbf{v_f}(\mathbf{x_f})=\frac{\mathbf{q}}{w(\mathbf{x_f})}, \quad \mathbf{x_f}\in C_f(t) \tag{2.7}$$

The second condition express the local filling front at the crack moving front, $\boldsymbol{v_f}\cdot w$ is equal to the flux $\boldsymbol{q(x_f)}$. It is recommended to read the review on mechanics of hydraulic fracture (Detournay, 2016) for further discussion and asymptotic solutions.

Different scaling is necessary to investigate the parametric space. This shows that the regime of propagation evolve with time. For a penny-shaped fracture three asymptotes exist with early, intermediate and late time. The early time asymptote describes the fracture initiation process, where a big fluid lag is present. Keep in mind, that this solution lasts for milliseconds or less. In our case, the intermediate and late time asymptotes are of interest. The intermediate time describes an asymptote which has no fluid lag. It is called the viscosity dominated solution. The late time solution is called toughness dominated asymptote and is characterized by uniform pressure in the crack. The dimensionless toughness K is a monotonically increasing function of time and describes the transition between viscosity and toughness dominated solution (Fig. 2.4).

2.3.2 Semi-analytical solutions for fracture design

The interest to estimate the hydraulic fracture growth was driven by petroleum industry. Various analytical and semi-analytical have been implemented for fracture design and propagation models. Figure 2.5a) presents the PKN (Nordgren, 1972; Perkins and L. R. Kern, 1961) solution, which is a 2D solution assuming a constant height and is valid for long fractures compared to height (L $\gg$ h). This is a 2D plane strain solution with an elliptical vertical cross-section of the fracture. The second 2D plane strain solution (Figure 2.5b) has an elliptical horizontal cross-section of the fracture with cusp-shape fracture tip. It is known as KGD model (Geertsma and De Klerk, 1969; Khristianovic and Zheltov, 1955) and assumes a constant height. It is valid for fractures width length to height ratio near unity or less (L$\sim$h). The pseudo-three-dimensional (P3D) model (Figure 2.5c) was introduce by

$$K = K' \times \left(\frac{t^2}{E'^3\mu'^5Q^3}\right)^{\frac{1}{18}}$$

K'	fracture toughness value
t	time
E'	plane-strain modulus
μ'	fluid viscosity
Q	flow rate

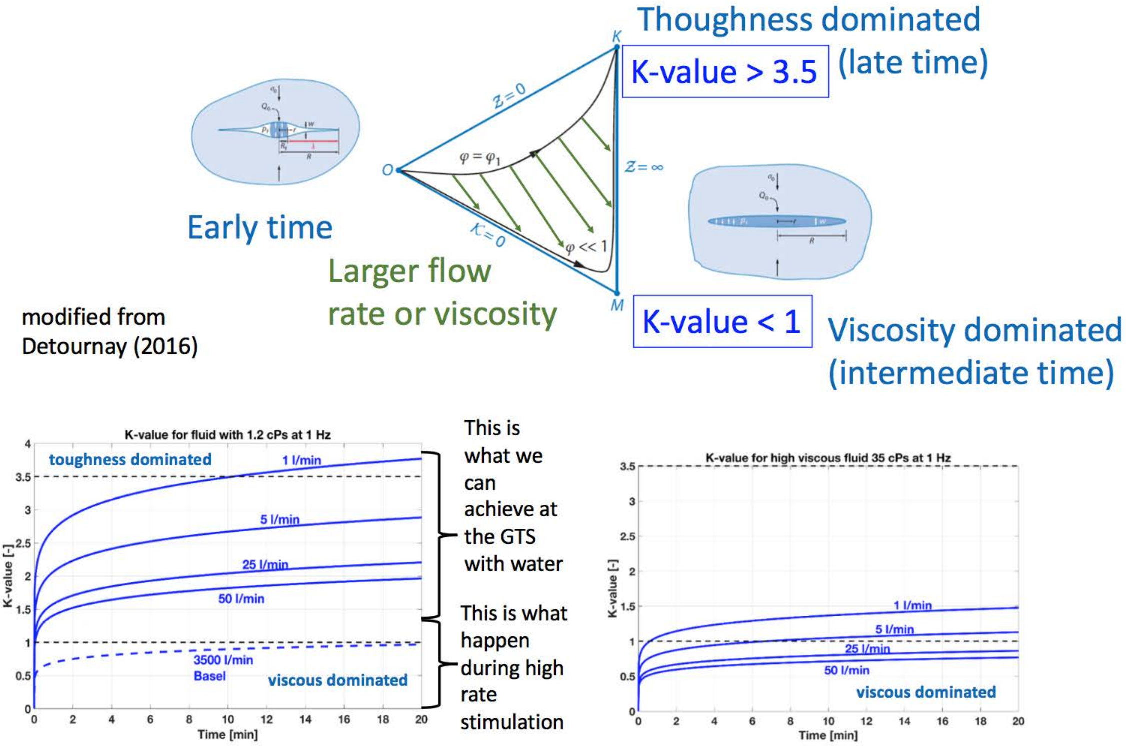

Fig. 2.4 The solution space for the propagation of penny-shaped hydraulic fractures at three different times.

Morales and Abou-Sayed (1989) and Settari and Cleary (1984) and the radial or penny-shaped model (Figure 2.5d) was introduced by Abé et al. (1976).

Prior to the hydraulic fracturing experiment, my goal was to understand the semi-analytical solutions used in industry. Therefore, I developed a comparison study to reproduce the observations of the fracture length from the hydraulic fractures during the stress characterisation phase. For this I used the PKN, KGD, P3D, penny-shaped model and a model for fracture toughness equilibration from Keith Evans (personal communication). The goal was to get a good estimate between the fracture length from the seismic cloud and the injection volume (Fig. 2.6). The other parameters, net pressure and normal fracture opening were considered as unimportant. All the models overestimated the length of the fracture except the penny-shaped model, which was able to reproduce the observed lengths with the given injection volume. That's why I considered to use only this solution to estimate the radius for the main experiment, which was calculated to be around 30 m (Fig. 2.7). In the following, we introduce the fracture toughness solution and the asymptotic approximation for a penny-shaped

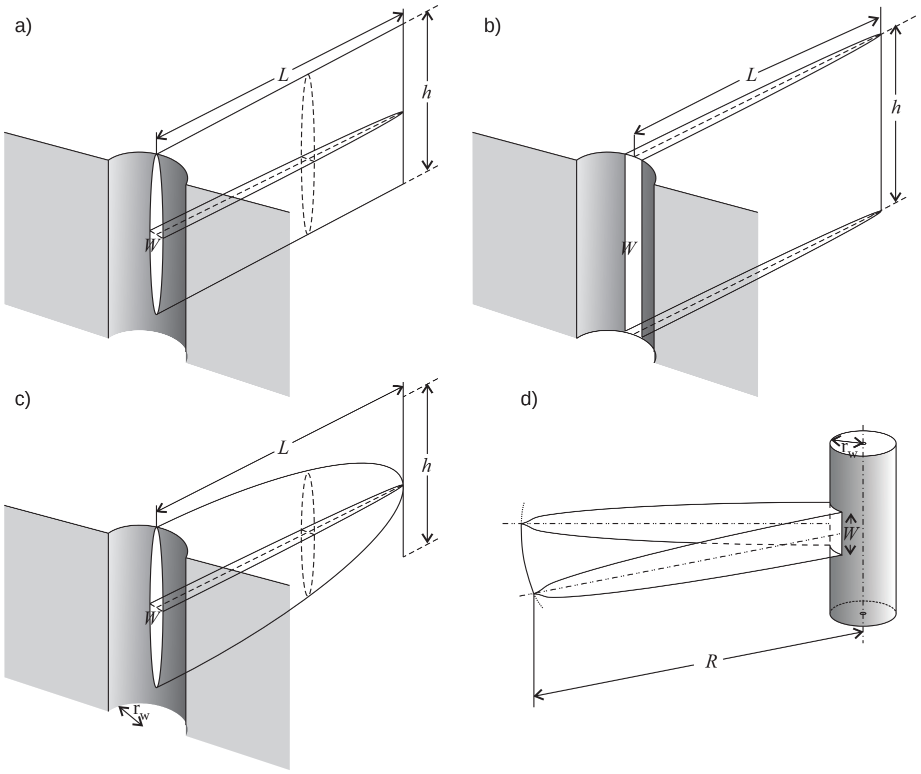

Fig. 2.5 Layout of the hydraulic fracture with the the indication of the geometric parameters for a) the PKN model, b) the KGD model, c) the Pseudo-3D (P3D) model and d) the radial or penny-shaped model.

fracture. The in here asymptotic approximation is referred to as the large-toughness asymptotic solution in Savitski and Detournay (2002).

Fracture Toughness Solution (FTS)

The fracture toughness solution is derived from a penny shaped-crack (PSC) using an elasticity and a fracture toughness equation (Keith Evans, pers. comm.) as followed:

$$E = \frac{16(1-\mu^2)R^3 p_{net}}{3Qt} \tag{2.8}$$

$$K_{Ic} = p_{net}\left(\frac{R}{\pi}\right)^{0.5} \tag{2.9}$$

The elasticity equation 2.8 is solved for the net pressure p_{net} and fracture toughness equation 2.9 is solved for the fracture radius R of the penny-shaped crack. The assumed injected volume is 1 m^3 and the Poisson's ratio is $\nu = 0.25$. The net pressure (equation 2.10) can be calculated for a range of

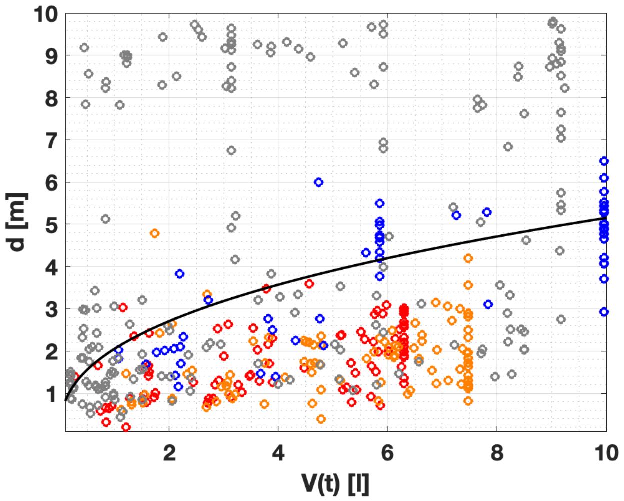

Fig. 2.6 The points indicate the radial distance from the injection point to the seismic events at a specific injection time/volume. The injection volume is corrected for the backflow. The black solid line indicates the approximative toughness solution for a penny-shaped fracture. The colored points indicate the three different data sets compared during the study (MF1: red, MF2: orange and MF3: blue). The input parameters for the solutions are given in Fig. 2.7

fluid volume ($V = Q \cdot t$). Including the net pressure in equation 2.11 allow to solve for the radius of the crack depending on the injected volume. No explicit formulation is used for the fracture width. Hence, the presented solution is independent of the fracture width. All values are given in SI units.

$$p_{net} = \left(\frac{16(1-\nu^2)K_{Ic}^6\pi^3}{3QtE}\right)^{(1/5)} \tag{2.10}$$

$$R = \pi\left(\frac{K_{Ic}}{p_{net}}\right)^2 \tag{2.11}$$

This solution is presented in Fig. 2.7 as FTS for PSC. The injection pressure p_w consists of the calculated net pressure p_{net} and the normal stress on the crack Sh.

Asymptotic solution

Bunger and Detournay (2007) introduced a parametric space (Figure 2.4) with early (O), intermediate (M) and late time (K) asymptotes for a penny-shaped crack propagating fluid-driven in impermeable elastic medium. The sketches in Figure 2.4 illustrate a solution with large lag (O-vertex) and zero lag in the (MK-edge), where it has zero lag for the viscosity dominated solution. The lag between fracture front and fluid front increases towards the toughness dominated solution. A constant injection rate lead to a tip velocity, which decreases as the fracture growths. On the basis of the penny-shaped hydraulic fracture, the asymptotic solution of storage-toughness K following Savitski and Detournay

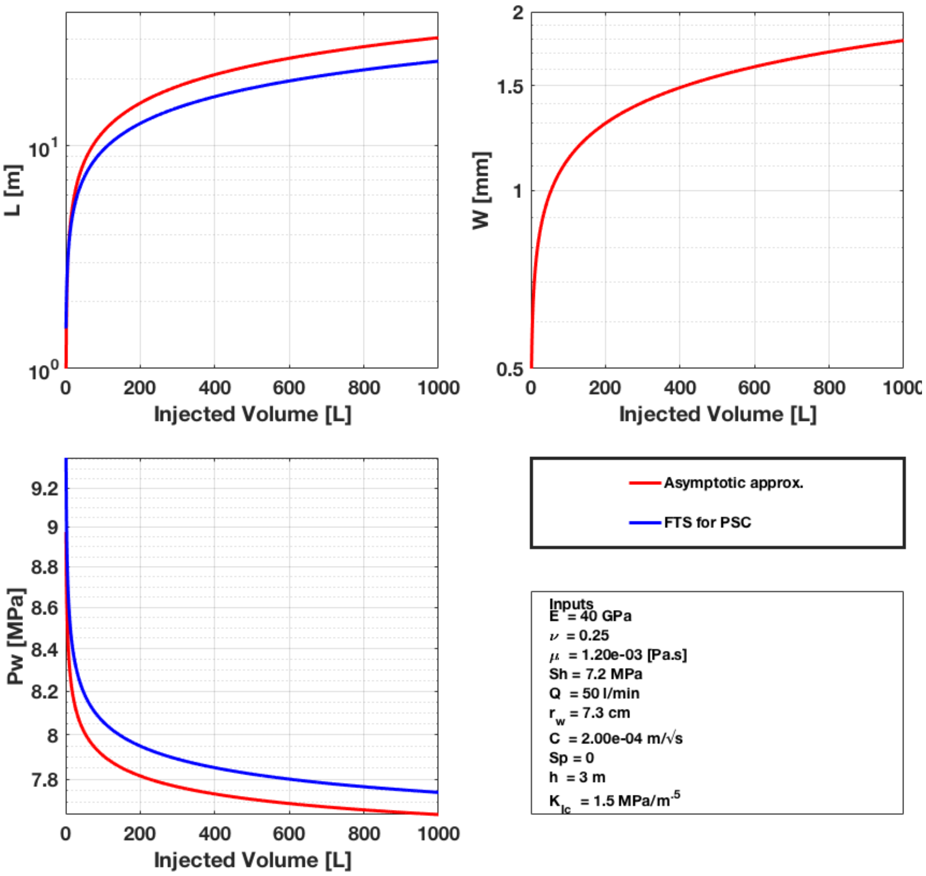

Fig. 2.7 The asymptotic approximation is given by the toughness solution for a penny-shaped fracture and the fracture toughness solution (FTS) is given by a penny-shaped crack using an elasticity and fracture toughness equation. The injected volume is presented against the length (L) of the crack, the aperture at the borehole (W) and the injection pressure (Pw).

(2002) is introduced. Hence, we introduce three time-dependent scales: L(t) for the fracture radius, p(t) for the net pressure and W(t) for the fracture opening.

$$W(\rho,t) = W(t)\Omega(\rho,P(t)) \tag{2.12}$$

$$P_{net}(\rho,t) = p(t)\sum(\rho,P(t)) \tag{2.13}$$

$$R(t) = L(t)\gamma(P(t)) \tag{2.14}$$

The dimensionless radial coordinate is defined as $\rho = r/R(t)$ $(0 \leq \rho \leq 1)$. P(t) is a dimensionless history parameter, which depends monotonically on t.

The non-dimensional toughness value (or K-value) is calculated as followed:

$$K = \quad K' \cdot (\frac{t^2}{E'^3 \mu'^5 Q^3})^{\frac{1}{18}} \tag{2.15}$$

The general solutions are represented in terms of infinite series of base functions and coefficients. In addition the general and particular solution have to satisfy the elasticity equation. Depending on the calculated K-value (Equation 2.15) the toughness (M) or viscous (K) solution is applicable. For both solutions a self-similar asymptote exists, which is presented in Figure 2.4. The toughness values depend on time, such that it changes with time from a pure viscous to a more toughness dominated regime. In the rest of this section, we introduce the approximation by the the toughness dominated edge for $K \geq 3.5$. It lead to the following equations:

$$\begin{aligned}
L = &\quad L_k \cdot \gamma_k && (2.16)\\
W = &\quad W_k \cdot \Omega_k && (2.17)\\
Pw = &\quad P_k \cdot \Sigma_k && (2.18)\\
L_k = &\quad (\frac{V^2 E'^2}{K'^2})^2 && (2.19)\\
W_k = &\quad (\frac{K'^4 V}{E'^4})^2 && (2.20)\\
P_k = &\quad (\frac{K'^6}{E'V})^2 && (2.21)\\
& && (2.22)
\end{aligned}$$

V is the volume calculated by $V = Q \cdot t$. Length L, width W and pressure Pw at the well for the toughness asymptotes are calculated by the non-dimensional solutions (γ_k, Ω_k, Σ_k) times the characteristic length L_k, width W_k and pressure P_k. The equations for the non-dimensional solutions (γ_k, Ω_k, Σ_k) for the zero and first order can be found in Savitski and Detournay (2002, Eq. 74-93).

Both presented solutions, the FTS for PSC and asymptotic toughness solution, are similar. Both solutions depends linear on the time, such that the solutions can easily be solved for injected volume. The radius is around 30 m for an injection of 1 m^3 of fluid (see Fig. 2.7). The K-vertex solution indicates the biggest radius compared to the other vertex and was used to estimate the maximum possible radius. The K-vertex solution was simplified by Dontsov (2016). This solution is presented as black solid line in Fig. 2.6 and is calculated as followed:

$$d(V) = \quad 0.8546 \cdot (\frac{V * E'}{K'})^{2/5} \tag{2.23}$$

2.3.3 Injection metrics

A penny-shaped fracture shape was able to reproduce the observations from the stress characterization and the hydraulic fracturing results in terms of fracture net pressure and fracture length. Therefore, we use the same solution to design the HF experiment. The injection flow-rate was kept between 0.5

and 5 l/min during the stress characterization phase, reaching a total volume of $\sim$10 l. For the HF experiments, we limited the volume of injection for each experiments to 1 m^3. The solution space presented in Fig. 2.4 show an early time, intermediate and late time solution. Depending on the dimensionless K-value the solution always starts in the early time edge and follows a path towards the intermediate and/or late time solution depending on the injection metrics. The early and late time solution have a lag in between the fluid and fracture front. These two fronts only overlap during the intermediate (viscous dominated) solution. Taking a closer look on the dimensionless K shows that the fracture toughness and Young's modulus are defined by the rock mass. The time, flow rate and fluid viscosity are free parameters and can be changed. The maximum given volume allow only certain values for time and flow rate. The injection over hours will not generate the same normalized hydraulic power (is defined as injection pressure times injection flow rate), thus we limit the timing to maximum 20 min. The flow rate is limited due to the pumps, having the opportunity reaching a maximum flow rate of 100 l/min. For water injection, the flow rate between 1 and 50 l/min have K values above 2 and are not able to reach the viscous dominated region (Fig. 2.4). As there are limitations due to pump supply and pressure level during injection, we decided to start with a short formation break down cycle followed by two refrac cycles with step-rate increase all 2-3 minutes. The main interest of the project was to investigate the rock mass, fracture pressure and seismic response depending on the injection location. Therefore, for comparison of the responses due the geological heterogeneities, we decided to keep the protocols a) simple and b) similar. To compare our injection experiments with real cases (like Basel), we decided to modify the fluid viscosity for three HF experiments with a viscosity 35 times higher than water. This allows us to reach the viscous dominated region with flow rates of only 10 l/min during 20 minutes. We used a Xanthan-salt-water (XSW) mixture to reach this target. The rheological behaviour of Xanthan-salt-water shows a high degree of pseudo-plasticity. In short, the viscosity decreases with higher shear rate and increases in low shear rate regions. This allow us to pump it with the same pumps used for water applications. In addition, the leak-off into micro-cracks and wrong oriented fractures should decrease.

2.3.4 Injection Protocol

The injection protocol is presented as flow chart and injection/pressure protocol (Fig. 2.8). The injection protocol is divided into different tasks linked in the flow chart. At the beginning, a pulse test is performed to test interval integrity and proper packer sealing. The breakdown cycle at a flow-rate of 5 l/min lead to a rapid increase of pressure in the injection chamber and initiates a new fracture into the formation. Depending on the fluid, the protocol has always two refrac cycles and an additional flushing cycle if XSW was injected. At the end, a pressure-controlled step test was conducted to evaluate the post-stimulation injectivity around the injection interval and the stress acting normal to the hydraulic fracture (jacking pressure).

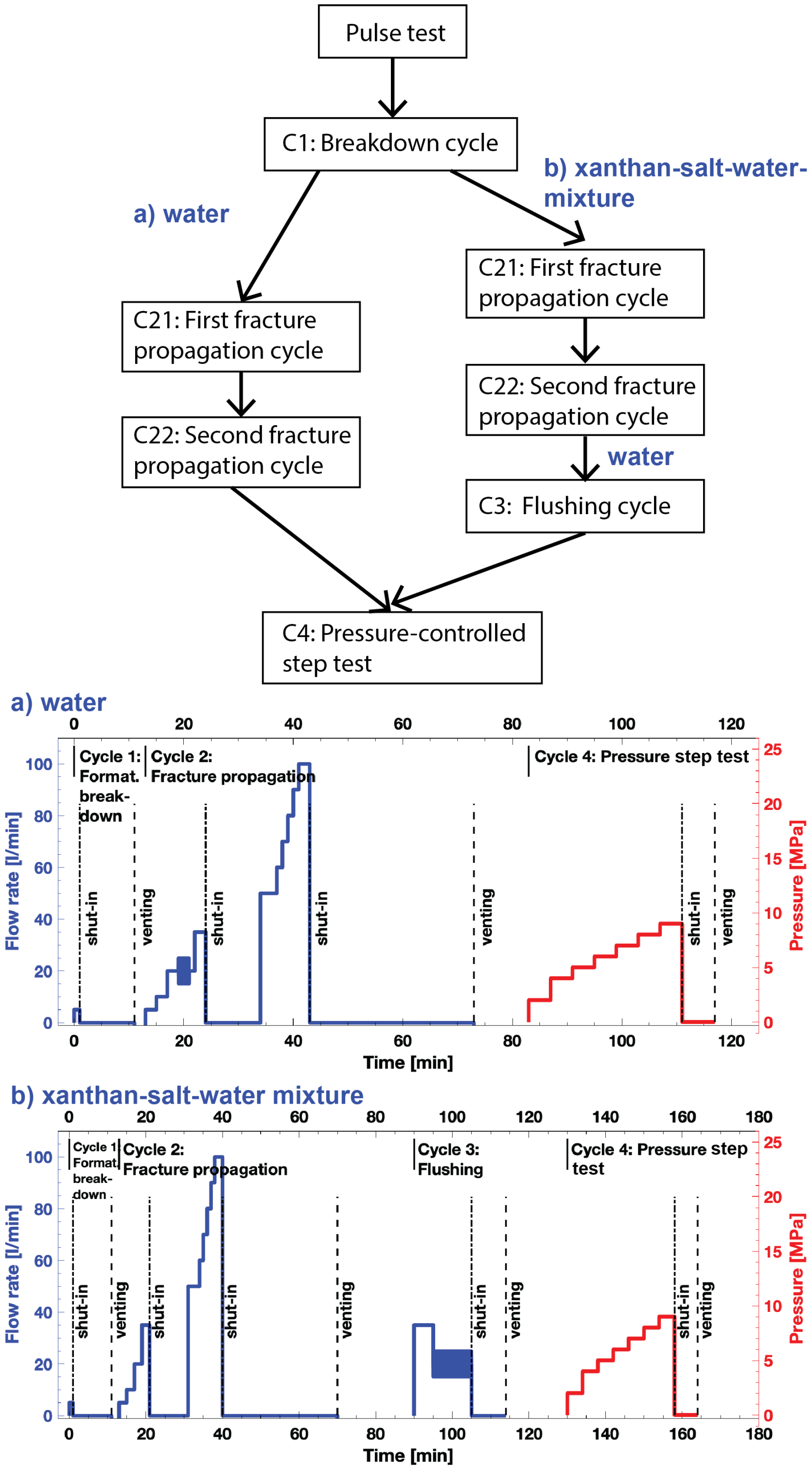

Fig. 2.8 The flow path diagram illustrate the different injection schemes depending on the fluid metric. The injection protocols show a blue solid line for rate controlled injection and a red solid line for pressure controlled injection.

Chapter 3

On the link between fracture toughness, tensile strength, and fracture process zone in anisotropic rocks

The test series were designed by N.D. The laboratory of G.M. was used to test the prepared rock samples incl. DIC. The experiments were executed and analysed by N.D.. N.D. did the data curation, visualisation and the writing of the first draft with the help of M.N. The writing – review and editing was done by B.V., F.A. and G.M.

Please cite this chapter as: Dutler, N., Nejati, M., Valley, B., Amann, F., Molinari, G., On the link between fracture toughness, tensile strength, and fracture process zone in anisotropic rocks, Engineering Fracture Mechanics (2018), doi: https://doi.org/10.1016/j.engfracmech.2018.08.017

Abstract

This paper presents experimental results on the anisotropy of the fracture toughness, Brazilian tensile strength, and the fracture process zone (FPZ) in granodiorite samples. The fracture toughness is measured using semi-circular bending tests, while Brazilian disk tests were conducted to measure the tensile strength indirectly. Digital image correlation (DIC) was employed to obtain full-field surface deformation associated with the fracture propagation and identify the FPZ. An averaging scheme is proposed to determine the length and width of the FPZ from the strain field. The DIC results confirm a semi-elliptical FPZ developing ahead of the crack tip, with an average length-to-width ratio of approximately two. The results also indicate that the theoretical models such as Irwin and strip-yield with uniform traction, which are based on plastic deformation near the crack tip, underestimate the extent of the inelastic zone, while the strip-yield model with a linear cohesion stress distribution overestimate the length of the process zone. The anisotropy ratio of the FPZ length obtained from the models, however, agrees very well with the ratio obtained from the DIC measurements. This

evidence supports the basis of the theoretical models that predict the FPZ length to be proportional to the square of fracture toughness over tensile strength.

3.1 Introduction

The mechanics of crack growth in rocks is an important field of research with direct applications in many geoscience and geoengineering fields including geothermal energy production, mining, tunneling, earthquake seismology, and reservoir geomechanics. In order to analyse the mechanics of fracturing in rocks, mechanical properties such as elasticity constants, strength and fracture toughness have to be accurately measured. An example of the importance of the anisotropy in rock mass response to external loading was recently demonstrated in an in-situ stimulation and circulation project in the deep underground laboratory at the Grimsel Test Site in Switzerland (Amann et al., 2018; Gischig et al., 2018; Jalali et al., 2018b). Elasticity parameters characterize the elastic deformation of rock due to the applied load, while strength is the critical tensile or compressive stress at which the rock fails. Closely related to the strength is a parameter called fracture toughness which is a measure of the resistance of rock against crack growth. Fracture toughness is a key intrinsic material property used in analyzing brittle fracture growth.

Due to the texture or layered structure developed during the formation or metamorphic process (e.g. foliation, bedding), a large class of rocks have anisotropic mechanical properties such as elasticity, strength and fracture toughness. The anisotropy of fracture toughness implies the directional-dependency of the rock resistance against crack growth. In the context of linear elastic fracture mechanics, the fracture toughness is closely related to the concept of the fracture energy G_f defined by Griffith. The Griffith theory of fracture growth postulates that the strain energy released due to the fracture growth is consumed to create the fracture surfaces. The process of creating fracture surfaces may involve dissipation of energy by heat, wave propagation, inelastic deformation near the fracture surfaces and bonds breakage between the fracture surface (Hoagland et al., 1973; Olgaard and Brace, 1983).

The growth of crack in rocks is accompanied by significant inelastic deformation near the crack tip. This highly damaged region adjacent to the crack tip is called fracture process zone (FPZ) within which the material undergoes micro-damaging. In the fracture process zone, micro-cracks close or open depending on their orientation with respect to the direction of the applied load, and crack growth in fact occurs by connecting the micro-cracks at a critical load. The fracture toughness K_{Ic} gives the intensity of stress at this critical state. One of the reasons for the anisotropy of the fracture toughness and tensile strength is the preferential direction of pre-existing micro-cracks, which seems to be mostly aligned with the textural orientation of rock such as foliation or bedding. Therefore, the interaction of newly developed micro-cracks with the pre-existing ones, in terms of density, size and orientation, is central in understanding the anisotropy of the fracture toughness (Anders et al., 2014).

The anisotropic elasticity of foliated and sedimentary rocks can be efficiently modeled through a transversely isotropic constitutive behavior which includes five elastic constants in the model. This approximation relies on the fact that there is an isotropic plane normal to which a different Young's modulus is to be expected. The isotropy plane is often assumed to be the foliation or bedding plane of the rock. Apart from the elasticity, strength and toughness are also expected to be anisotropic and dependent on the direction of the applied load with respect to the plane of anisotropy. Most of the studies conducted on the anisotropy of fracture toughness focus on the anisotropic ratio and its correlation with the micro-crack structure of rock (see a review in Section 3.2). However, a key ingredient of fracturing is the fracture process zone (FPZ), and the development and characteristics of this zone in anisotropic rocks have not been investigated so far. Most of research on FPZ development is focused on concrete, and occasionally on some isotropic rocks. It is well known that the FPZ has a central role in linking the fracture toughness and strength.

This work investigates the anisotropy of the tensile strength and mode I fracture toughness in granodiorite samples from Grimsel Test Site (GTS) in Switzerland. Digital image correlation (DIC) is employed to observe the development of fracture process zone near the crack tip. An averaging method is used to calculate the width of the FPZ from strain and displacement fields. The size and shape of the FPZ calculated from the DIC results are then used to evaluate the anisotropy of the FPZ. The results show that the FPZ develops as a semi-elliptical localized region, with the ratio of length to width being about two in both principal directions (isotropic shape). However, the actual values of the length and width show slight anisotropy, with the size of the FPZ being bigger for cracks oriented along the foliation compared to the ones oriented normal to the foliation plane. It is also shown that the theoretical models such as Irwin and strip-yield with uniform traction underestimate the extent of the inelastic zone, while the strip-yield model with a linear cohesion stress distribution overestimate the length of the process zone. However, the ratio of the FPZ lengths at principal directions fits the theoretical models very well. This indicates that the length of the FPZ is indeed proportional to the square of fracture toughness over strength.

3.2 Fracture toughness and strength

3.2.1 Fracture toughness measurement

Several methods of measuring mode I fracture toughness exist in literature. Reviews on various methods with their attributes, advantages and drawbacks are given in Whittaker et al. (1992) and Bearman (1999). To obtain precise, accurate and consistent results, the International Society for Rock Mechanics (ISRM) recommends four test procedures: (1) Chevron bend (CB) (Ouchterlony, 1988); (2) Short rod (SR) (Ouchterlony, 1988); (3) Cracked chevron notched Brazilian disc (CCNBD) (Fowell, 1995); and (4) Notched semi-circular bend (SCB) (Kuruppu et al., 2014). These standards indicate the requirements for the samples in terms of their preparation, dimensions, and test procedure in terms of loading type and rate. Formulae are also provided to calculate the fracture toughness from the failure load and geometrical factors.

Despite standardized testing, the results from CB, SR and CCNBD exhibit a deviation in the range of 20-30%. This deviation is often explained by size effects, anisotropy of the rock and inaccuracy of the dimensionless parameters used in the calculation. Among these methods, the CCNBD show a consistently lower variation (Dwivedi et al., 2000). Iqbal and Mohanty (2007) compared CB and CCNBD methods on three different rock types with two-hundred specimens and concluded that the methods are very comparable when the correct equation for fracture toughness calculation was used and the specimen size was selected carefully. Kataoka et al. (2015b) compared CB and SCB method using Kimachi sandstone and obtained almost the same values. In term of size effects, the recommended ISRM procedure for a specific method allows to minimize the variation of fracture toughness values among the different methods.

The effect of rock anisotropy on fracture toughness has been investigated in a number of studies. Krishnan et al. (1998) and Ke et al. (2008) studied the fracture toughness anisotropy of sandstone and marble using Cracked Straight Through Brazilian Disc (CSTBD) specimens. Kataoka and Obara (2012) and Kataoka et al. (2015a) used the SCB method to study two end-member configurations (named as short-transvers and arrester) of anisotropy in rocks under water-vapor pressure. The CCNBD method was used by Nasseri and Mohanty (2008) to measure the fracture toughness of different granitic rocks and sandstones at different orientations. Chandler et al. (2016) and Chandler et al. (2017) used a SR method to study Mancos shale in three configurations arrester, divider and short-transverse, at different temperatures. The SCB method was used by Funatsu et al. (2012) to study the relationship between fracture toughness and loading axis with respect to the bedding planes using sandstone.

In this study, the notched semi-circular bend configuration is used for investigating the fracture toughness anisotropy in Grimsel Granodiorite. The advantages of using SCB specimens are (1) it requires small samples, (2) sample preparation is easy due to minimal machining, and (3) only the failure load is required to determine the fracture toughness (Kuruppu et al., 2014). The effect of anisotropy can also be studied in a straightforward fashion by using SCB samples. Using this method, it is necessary to use slow loading rates so that the dynamic effects can be ignored.

3.2.2 Anisotropy of fracture toughness

Table 3.1 summarizes the findings on the anisotropic fracture toughness in different types of rocks. An important result is the identification of the central role of micro-structure orientation and grain size in the anisotropy of the fracture toughness. The fracture toughness is closely linked to the presence of micro-cracks and their orientation. It is in fact reported that micro-crack structure in crystalline rock is more important than the grain size and orientation when it comes to the fracture toughness (Nasseri and Mohanty, 2008).

A correlation between the orientation of foliation/bedding and the maximum of P-wave velocity was observed in granite and shale (Chandler et al., 2016; Nasseri and Mohanty, 2008). The highest P-wave velocity is measured parallel to foliation/bedding while the minimum value was obtained in

Table 3.1 A summary of findings on the fracture toughness of anisotropic rocks

Rock type	Methodology	Important Results	Reference
Sandstone Marble	Notched Brazilian disk specimen Microscopic analysis Mixed mode I/II experiments	• Mixed-mode I/II fracture envelops were developed. • The effect of anisotropy on fracture toughness can be significant.	Ke et al. (2008); Krishnan et al. (1998)
Granite	Cracked chevron notched Brazilian disk specimen Microscopic analysis Acoustic Emission 3D X-ray and CT scans	• Micro-crack density and length are major contributors to the value of fracture toughness. • Fracture toughness is inversely proportional to micro-crack density and length. • There is a correlation between fracture toughness and fracture roughness. • FPZ from acoustic emission and optical measurement are in good agreement. • The seismic velocities is closely linked to the micro-crack density and its orientation. • A decreasing anisotropy was observed with the increase of the loading rate.	Dai et al. (2013); Nasseri et al. (2010); Nasseri and Mohanty (2008); Nasseri et al. (2005, 2006, 2011, 2009)
Granite	Notched semi-circular bend specimen Acoustic emission Ultrasonic measurements Microscopic analysis 3D X-ray CT scans	• Orientation of micro-cracks can be estimated by measurement of wave velocity. • Both elastic wave velocity and fracture toughness exhibit anisotropy. • Fracture toughness is dependent on the micro-structure of rock. • K_{Ic} decreases with increasing water vapor pressure.	Kataoka et al. (2015a)
Shale	Notched semi-circular bend specimen Microscopic analysis	• The influence of calcite-filled veins on propagation path is investigated. • The propagation is strongly influenced by the approach angle of the induced fracture to the veins and the thickness of the veins.	Lee et al. (2015)
Shale	Short rod specimen Ultrasonic measurements Microscopic analysis	• Strong fracture toughness anisotropy was observed in shale. • K_{Ic} changes very little up to 120° at which temperature it starts to increase slightly. • When the original crack is oriented normal to the bedding, there is a strong tendency to deviate towards the bedding.	Chandler et al. (2016, 2017)

the direction normal to the foliation/bedding. This fact indicates that the micro-cracks are dominantly oriented along the foliation/bedding. The reason for lower measured values of fracture toughness along foliation and bedding seems to be the higher density of micro-cracks in those directions. The process of fracture growth is explained by the gradual initiation and growth of (existing) micro-cracks, and their coalescence to form larger cracks. Therefore, higher density and larger micro-cracks facilitates the growth of fracture in certain directions.

The presence of a correlation between fracture toughness and fracture surface roughness of Stanstead and Barre granite was suggested by Nasseri et al. (2010, 2009). Their study shows a significant increase of K_{Ic} and fracture roughness between directions parallel to and normal to petrofabric orientation. In addition, the rock with a coarser micro-structural fabric shows a rougher fracture surface. The results generally confirm an essential link among petrofabric anisotropy, fracture toughness, fracture roughness, and evolution and extent of associated induced cracks along specific directions in the fracture process zone. Similar results have been shown for shale, where the fracture growing normal to the direction of bedding seems to be tortuous and kinked, inducing a rougher fracture surface (Chandler et al., 2016).

3.2.3 Anisotropy of strength

The tensile strength of brittle materials can be obtained by direct or indirect methods. A simple indirect method is the Brazilian tensile test in which a thin circular disk is loaded diametrically up to failure (see reviews by Li and Wong (2013) and Perras and Diederichs (2014)). This diametrical compression induces a tensile stress normal to the direction of applied load, and it is expected that the specimen failure initiates at the point of maximum tensile stress, i.e. at the center of disk. The elasticity solution that calculates the stress at the center of disk is based on a homogeneous, isotropic and linearly elastic material behavior (ASTM, 2008; Bieniawski and Bernede, 1979; Hondros, 1959), and requires only the peak load and sample dimensions to calculate the tensile strength. With the introduction of anisotropic elasticity, the solution is not only a function of loading and geometry dimensions, but also the elastic constants of the anisotropic material. The explicit representation of stress in a Brazilian disk with transversely isotropic material has been given by Chen et al. (1998); Exadaktylos and Kaklis (2001) and Claesson and Bohloli (2002). These studies are based on the Lekhnitskiy's anisotropic elasticity solution (Lekhnitskiy, 1969), and show that the elasticity solution of Brazilian disk depends on two material parameters.

The early work of Barla and Innaurato (1973) investigated the suitability of Brazilian and ring tests for the measurement of tensile strength. Using finite element simulations, they concluded that the anisotropy has a significant influence on the stress at the center of disk, and therefore the tensile strength measurement based on an isotropic elasticity solution may be significantly inaccurate. They also found that the failure may occur along the bedding or foliation, and not always along the loading direction, which raises serious doubts on the nature of failure process. Many experimental results on anisotropic rocks show that the micro-structure orientation can significantly influence the strength of rock, with the strength along the bedding or foliation is significantly lower than perpendicular to it (Khanlari et al., 2015; Tavallali and Vervoort, 2010; Vervoort et al., 2014; Wild et al., 2015). It has also been shown that when the foliation or bedding is oblique to the direction of applied load, a significant shearing component develops at the plane of failure, which raises doubts on the suitability of the results to be considered as tensile strength.

3.3 Fracture process zone

This section provides a review on the previous work related to the development of the FPZ in quasi-brittle materials.

3.3.1 Characteristics of process zone

Linear elastic fracture mechanics describe a square-root singular stress state adjacent to the tip of a sharp crack. However, no material is able to resist an infinite amount of stress, and therefore the material undergoes an inelastic deformation in the vicinity of the crack tip. This inelastic region is of different nature depending on the material type. Metals often exhibit yielding and plasticity, often accompanied with strain hardening, due to the distortional component of stress. For this reason, the inelastic region near the tip in metals is called the plastic zone. On the other hand, brittle materials often exhibit damage due to initiation and propagation of micro-cracks, which is accompanied with strain softening and mainly driven by normal components of stress. For this reason, the inelastic region in brittle materials is often called fracture process zone (FPZ). In materials such as rock and concrete, the size of the FPZ can be large enough to introduce significant nonlinearity (softening) near the failure point. These materials derive their toughness from subcritical cracking that precedes the ultimate failure. This is the reason to name this types of materials as "quasi-brittle" rather than "brittle". Both plastic and fracture process zones are regions where considerable energy dissipation occurs. The fracture energy and toughness will therefore depend on the strength of the degree of nonlinearity and the size and shape of these zones.

The FPZ develops as a transition zone between the macro-crack which has strong discontinuity and the remote region which is assumed to be continuous in micro-scale. In fact, the process of fracture growth is described by the transition of the material behavior in the FPZ from micro-scale continuum to micro-scale discontinuum due to initiation and propagation of micro-cracks. These micro-cracks inside the FPZ then coalesce to form a macro-scale discontinuity represented as fracture surfaces. In other words, the FPZ acts as a bridging zone between cracked region and uncracked region. This transition process dissipates strain energy to create new micro-cracks and damage zones. Therefore, more efficient energy dissipation mechanisms in the FPZ, and bigger sizes of process zone lead to higher energy dissipation which can be regarded as higher resistance of the materials against failure and fracturing. This is the reason why the fracture energy is significantly influenced by the FPZ characteristics. The stages of the development of the micro-crack damage zone around a crack tip in rock have been described in Hoagland et al. (1973).

There have been mainly two models to estimate the size of plastic zone under mode I loading: The Irwin approach, and the strip-yield model. Irwin (1961) estimated the plastic zone size by equating the normal stress along crack plane to the yield stress. This first approximation was then improved by considering the stress redistribution along the crack plane, giving a simple formula of $L_{\mathrm{I}}^{p} = (K_{\mathrm{I}}/\sigma_u)^2/\pi$, where L_{I}^{p} is the size of plastic zone in the crack plane, K_{I} is the mode I stress intensity factor and σ_u is the yield strength. The strip-yield model was proposed independently by Barenblatt (1959) and Dugdale (1960), and considers the inelastic zone in front of the crack tip as a part of a larger crack extending to the end of inelastic zone and having a uniform cohesion stress equal to a yield strength applied on its boundary. The method uses superposition principle to give an approximation of inelastic zone which vanishes the stress singularity, and gives a simple approximation of $L_{\mathrm{S}}^{p} = \pi(K_{\mathrm{I}}/\sigma_u)^2/8$. Irwin and strip-yield models predicts close values for the size of the plastic zone for small values of K_{I}/σ_u. For brittle material, one can simply replace the yield strength σ_u by the tensile strength σ_t to estimate the size of the FPZ. The size of a fully developed FPZ on the onset of fracture propagation ($K_{\mathrm{I}} = K_{\mathrm{Ic}}$) is given by $L_{\mathrm{I}} = (K_{\mathrm{Ic}}/\sigma_t)^2/\pi$ and $L_{\mathrm{S_u}} = \pi(K_{\mathrm{Ic}}/\sigma_t)^2/8$ based on Irwin and strip-yield models. These estimations assume a uniform stress being applied along the length of the FPZ, and therefore they are not expected to give very accurate predictions of FPZ length since the inelastic deformation has the nature of micro-damaging rather than plasticity in quasi-brittle materials. Taking into account a linear reduction of traction with proximity to the tip, Labuz et al. (1985) modified the strip-yield model to adjust for the micro-damaging of the rock material in the FPZ. This approximation gives a longer FPZ length with the relation $L_{\mathrm{S_l}} = 9\pi(K_{\mathrm{Ic}}/\sigma_t)^2/32$. Since both K_{Ic} and σ_t are considered material properties, the size of the FPZ is also expected to be a material property.

Models describing the shape of the inelastic zone are based on determining the boundary of a region within which a component or invariant of elastic stress exceeds the yield stress. Unlike the metals in which a distortion-based criterion like Von Mises governs best the plastic behaviour, the nonlinear micro-crack zone in quasi-brittle materials is mainly developed due to the tensile stress. The most well-known criterion to describe the shape and size of the FPZ is the maximum normal stress introduced by Schmidt (1980). According to this criterion, the FPZ is formed in the region where the local maximum principal stress exceeds the tensile strength of the material. This model uses the elastic stress field near the tip and solve for the boundary of the region where maximum principal stress reaches the strength. This model, however, does not account for the redistribution of stress outside the FPZ while inelastic deformation occurs inside the FPZ, and therefore underestimate the size of the FPZ. As will be explained later, most of the experiments suggest a band-shaped (semi-elliptical) process zone for quasi-brittle materials which does not match the butterfly shape suggested by Schmidt (1980). The main reason might be that the the Young's modulus reduces mainly in the direction normal to the fracture plane in the process zone, and the reduction of strength within the process zone due to micro-cracking may lead to elongation of the process zone. One therefore should account for the the reduction of elastic properties and strength, perhaps using an anisotropic damage model, in order to provide a better model for the shape of the FPZ in quasi-brittle materials.

The FPZ size and shape are expected to depend only on the loading mode of the crack and the material properties and not on the specimen configuration. However, this is only true when the material properties such as K_{Ic} and σ_t do not exhibit specimen size and configuration dependence. For example, K_{Ic} is dependent on the size of specimen for smaller specimens mainly for two reasons: (i) the LEFM theory is unable to give good approximation of stress field when the FPZ is large compared to the crack size, (ii) even if one still considers the LEFM theory for crack with large nonlinear zones, the FPZ is likely to develop outside the singular dominant region, where only singular terms of the crack elastic solution are not sufficient to characterise the stress field. In other words, when the FPZ is large enough compared to the size of the crack and crack ligaments, higher order terms of the elastic solution also play a role in stress characterisation near the crack tip, and influence the FPZ development (Aliha et al., 2010; Smith et al., 2001). This is why the FPZ is also specimen size dependent for small specimens. Experimental observations also indicate that the boundary of specimen can influence the size of the FPZ and prevent the FPZ to develop fully (Zietlow and Labuz, 1998). The significant size of the FPZ compared to the specimen size is the main reason for the size dependency of strength and fracture toughness. This is why the FPZ plays an important role in determining a characteristic length of the micro-structure that reflects size effects. The fracture energy is closely related to the FPZ size and this implies that the existence of a FPZ may be the intrinsic cause for size effects. The applicability of linear elastic fracture mechanics for analyzing cracked structures is therefore determined by how big the FPZ is compared to the size of the specimen.

3.3.2 Experimental methods to evaluate FPZ

The importance of the FPZ in understanding the size effect phenomenon in quasi-brittle materials has encouraged many researchers to experimentally observe the development of the FPZ. The observation of fracture process zone is difficult because of the small scale at which micro-structural events occur.

The experimental techniques used to determine the FPZ in quasi-brittle materials can be divided into three categories:

- **Visual and image-based** methods such as optical and photoelectron microscopy, moiré interferometry, and digital image correlation (DIC): These methods rely on the analysis of images obtained from the surfaces of cracked specimens. The region of inelastic deformation is then identified by analyzing the changes in the surfaces due to highly localized strain near the tip of fractures (Chengyong et al., 1990; Guo et al., 1993). DIC has been particularly popular recently due to simplicity, availability and the fact that it can provide a very accurate full-field measurement of strain field (Lin and Labuz, 2013; Lin et al., 2014; Wu et al., 2011). The resolution of the full-field data obtained from the DIC is considerably high, often below 1 μm .
- **Acoustic-based** methods such as acoustic emission and ultrasonic probing: These methods utilize the information obtained from active and passive seismic waves traveling within the cracked specimens. Acoustic emission analyses the micro-seismic events generated by the inelastic mechanisms like micro-cracking and traces the location of micro-seimic event (Backers et al., 2005; Lin et al., 2009; Zietlow and Labuz, 1998). Ultrasonic probing, on the other hand, analyses the attenuation of active ultrasonic waves when they travel through a region of high inelastic deformation (Labuz et al., 1987; Swanson and Spetzler, 1984; Zang and Wagner, 2000).
- **Mechanical property-based** methods such as microhardness and nanoindentation: These methods are based on using nano- or micro-indentors to perform small scale load tests around the tip of cracks. A change in hardness is expected inside the FPZ since the material has undergone inelastic deformation. The boundary of the FPZ can then simply identified based on the change in hardness. Plastic deformation in metals is often accompanied with an increase in nanomechanical properties whereas damaged zones in quasi-brittle materials have a reduction in nanomechanical properties (Brooks, 2013; Brooks et al., 2012, 2013).

A noteworthy review of the works done using most of these techniques is given in Brooks et al. (2013). Among methods mentioned above, the AE and DIC seem to have attracted a lot of attention. The ability of AE to trace the inelastic deformation not only on the surface but also inside the cracked specimens has made this method very powerful for characterising the FPZ. The main drawback of this method is high possible errors in determining the events' locations due to the uncertainty in the velocity model. Alam et al. Alam et al. (2015, 2014) used both the AE and DIC simultaneously and concluded that material damaging can change the velocity model significantly, and the location inaccuracy in their experiments is in the range of 5 mm. Therefore, an accurate determination of the FPZ size can be difficult to achieve with the AE. The DIC, on the other hand, provides very accurate full-field displacement and strain measurement on the surfaces of the cracked specimens. When performed using high-speed camera, the DIC is able to trace the mechanisms of fracture growth at the peak load very accurately.

3.3.3 Lessons learned from past experiments

On the basis of the results obtained from different experimental techniques used to characterise the FPZ in quasi-brittle materials, we can summarize the current knowledge as following:

1. There is a general consensus among the researchers that a positive correlation exists between the grain size (aggregate size in concrete) and the width of the FPZ. This means that the larger the grain size, the bigger the FPZ width in quasi-brittle materials (Brooks, 2013; Brooks et al., 2012; Chengyong et al., 1990; Otsuka and Date, 2000; Skarzyński and Tejchman, 2013). Zietlow and Labuz Zietlow and Labuz (1998) measured the width of the FPZ for four different rock types and suggested that there exists a linear relation between the FPZ width and the logarithm of the grain size. The reason for this trend is perhaps due to a relation between the grain size and micro-crack density. Finer grained materials develop more micro-cracks in their damage zones than coarse-grained materials. In other words, the finer-grained materials dissipate energy more efficiently with respect to space, and therefore can develop a smaller damage zone before fracture (Brooks, 2013).

2. There seems to be an inverse correlation between the grain size and fracture toughness/tensile strength. Finer grain materials dissipate energy more efficiently in their smaller FPZ than coarse-grained materials in their larger FPZ, and thus attain higher strength properties (Brooks, 2013; Nasseri et al., 2005). The experiments also show that as the grain size decreases, micro-crack density increases, which means that finer-grained materials have more micro-cracks in their damage zones than coarse grained materials (Brooks, 2013). However, this is a strong statement and needs more supporting evidence.

3. Results from different experiments agree that the micro-crack density increases exponentially within the FPZ by approaching the fracture or fault (Backers et al., 2005; Faulkner et al., 2011; Janssen et al., 2001; Nasseri et al., 2006; Scholz et al., 1993; Vermilye and Scholz, 1998). Microhardness and nanoindentation experiments also confirm that the regions of increased micro-cracking aligns with regions of reduced nanomechanical properties (Brooks et al., 2013). This indicates the reduction of mechanical properties is due to the micro-cracking (Brooks, 2013). Micro-cracks were also found to be mainly orientated parallel to the fracture (Nasseri et al., 2006).

4. Many experimental data show that the process zone is of a semi-elliptical (narrow-band) shape (Backers et al., 2005; Chengyong et al., 1990; Otsuka and Date, 2000; Skaråyåski et al., 2011; Swanson and Spetzler, 1984; Wu et al., 2011; Zietlow and Labuz, 1998). This structure conforms well with the assumption of cohesion-based process zone along the crack plane in the strip-yield (Dugdale-Barenblatt) model. In fact, it has been shown that the narrow-band shape of the FPZ is in a good agreement with the Dugdale-Barenblatt model (Chengyong et al., 1990; Nasseri et al., 2006; Scholz et al., 1993; Vermilye and Scholz, 1998). Micro-structure analyses

by Nasseri et al. (2006) also show that micro-cracks in the FPZ are mainly oriented parallel to the fracture, which justify the formation of a band-shaped FPZ. From the results on sandstone, Backers et al. Backers et al. (2005) also observed a semi-elliptical FPZ with a length and width of about 20 mm and 10 mm. The width of the FPZ is often regarded as the characteristic length of micro-structure, and has been introduced into non-local and strain-gradient damage models to describe the width of localized zones. This often leads to capturing a deterministic size effect of quasi-brittle materials. The length seems to also depend on the rate and the significance of material softening. The arising question is in fact if there is any relation between the width and the length of the FPZ.

5. The FPZ size seems to be dependent on the specimen size for smaller samples. This is due to the proximity of specimen boundary to the crack tip. Experimental data on concrete suggests an increase of the FPZ length with the increase of the sample size (Otsuka and Date, 2000; Wu et al., 2011). In fact, the main sample size parameter influencing the FPZ length is the ligament size, which is the distance between the crack tip and the closest boundary. The trend shows that the FPZ length becomes smaller as the ligament size decreases. This is due to the boundary constraint in front of the crack tip, that does not allow the FPZ to fully develop. Despite the strong dependency of length on size, the width seems to hardly show any dependency on the specimen size (Dong et al., 2017a; Otsuka and Date, 2000; Skaråyåski et al., 2011).

6. Near the peak load, the length of the FPZ exhibits more load-dependency than its width. Experimental results from both AE and DIC show that the FPZ width almost stabilizes at about $70-80\%$ of the pre-peak load whereas its length exhibit a significant load-dependency starting at 80% of pre-peak and continuing over the post-peak period (Alam et al., 2014; Skarzyński et al., 2013; Skarzyński and Tejchman, 2013). This indicates that the formation of macro-cracks (micro-crack coalescence) which occurs near the peak-load does not significantly influence the width of the FPZ while it has a strong influence on the length (see results of Wu et al. (2011)). The increase of load generally causes the activation of more micro-cracks. However, it seems that near the peak load, the main energy dissipation mechanism is the coalescence of previously activated micro-cracks. Since the micro-cracks are oriented in the direction of the main crack as mentioned previously, the width is not influenced by micro-crack coalescence, while the length significantly depends on that because damage and degradation continues extending the FPZ in the direction of main crack.

7. The FPZ size identified by AE is much larger than the one obtained by microscopy (Backers et al., 2005; Janssen et al., 2001; Otsuka and Date, 2000; Zang and Wagner, 2000). This may be because there is generally a high uncertainly in locating acoustic emissions due to uncertainty in the velocity model resulted from rock anisotropy and heterogeneity. Another reason for this behaviour may be the fact that the AE is able to locate all the local failures within the body while the microscopic analyses are only surface measurements.

8. Results form AE measurements show that both tensile and shearing events are captured even when the macro-crack is subjected to pure mode I (Alam et al., 2015; Backers et al., 2005; Nasseri et al., 2006). This can be explained by taking into account the fact that in essence micro-cracks are randomly oriented, and some are more susceptible to shear than tensile failure, and therefore one should not expect only tensile failure in mode I loading of original main crack. In addition, under mode I loading, the shear stress is zero only along the crack ligament, and significant shear stresses are present at other directions. These results generally suggest that both tensile and shearing failures occur in the micro-scale irrespective of the type of the loading applied on the original macro-crack.

9. Experiments on the FPZ characterization under mixed-mode loading condition show that the FPZ slightly rotate from the crack plane, and both crack opening and sliding occur at the crack mouth (Dong et al., 2017b; Lin et al., 2014).

3.3.4 FPZ evaluation using DIC

DIC is a relatively new method in experimental mechanics, whose popularity was favored by the advancements in imaging and digital image processing techniques. The DIC uses consecutive imaging of the surface of a deforming body, whose surface is covered in a random speckle pattern, and calculates the surface position and displacements by correlating the patterns in space and time. Through high resolution and high speed cameras, and through the availability of robust numerical algorithms for cross correlation, the DIC is nowadays a powerful technique in experimental mechanics, and is able to provide high resolution and precise measurements of surface displacements and strains. For this reason, DIC has been widely used recently for investigating the inception and the evolution of the strain localization in quasi-brittle materials. However, when using DIC for evaluating localized deformation in the FPZ, the calculated displacements and strains can be sensitive to length resolution, search patch size of images and filter size used for smoothing purposes.

The following methods have been used to determine the FPZ from DIC:

- The most simple method is based on the jump of displacement across the crack plane (Corr et al., 2007; Dong et al., 2017a,b; Lin and Labuz, 2013; Lin et al., 2014; Wu et al., 2011). Based on this scheme, the distance between the two ends of the displacement jump at either sides of crack plane denotes the FPZ width, while the distance from the tip up to the point along the crack ligament at which displacement jump vanishes denotes the FPZ length. It is noteworthy that the evolution of the displacement jump by load shows three different stages: (1) Elastic phase in which no considerable jump is recognizable, (2) formation of the FPZ with moderate displacement gradient, and (3) very high gradient of displacement which occurs at the moment of instability and macro-crack initiation. The width of the FPZ shall be measured towards the end of the second phase which is expected to be near the peak load on the force-displacement curve. At any stage after this point, the opening of macro-crack surfaces known as the crack tip opening displacement has to be deduced from the distance between the two ends of the displacement jump in order to obtain a valid FPZ width. The crack mouth opening and its variation along the FPZ can also be evaluated using this method. Most of studies show a somewhat linear reduction of opening along the FPZ.

- The second method is based on strain contours and using a critical strain as a threshold to define the FPZ (Alam et al., 2014; Enfedaque et al., 2015; Skaråyåski et al., 2011). Although strains are good indicators of localised zones, one needs to address the following issues when using this method: (1) How the accuracy of calculated strains in the FPZ is influenced by subset size, subset distance and filter size. (2) What value is suitable for the critical strain and which component or invariant of strain tensor shall be used.
- Skarzynski et al. Skarzyński et al. (2013); Skarzyński and Tejchman (2013) discussed the objectivity of the DIC measurements at localized zones, and suggested a third method. It uses the error function to fit the displacement jump, and the normal distribution function to fit the strain variation along a path crossing the crack plane. Their results show that the FPZ size obtained from the displacement is different from the one obtained from the strain. The average of the fitting parameters for the displacement and strain with different search patch sizes is suggested to be used to define the width of the FPZ. Their suggested method also calculates different values for the size of the FPZ when using different software.

3.4 Experimental setup

3.4.1 The rock samples

In order to conduct the fracture toughness and strength tests, all samples were obtained from the cores extracted from the Grimsel Test Site (GTS) in the central Swiss Alps, Switzerland, which is part of the Aare massif. The rocks found in the rock laboratory consists of granitic to granodioritic composition. The material originates from the borehole FBS16.003, which was drilled during the In-situ Stimulation and Circulation (ISC) experiment in this rock laboratory (Amann et al., 2018; Krietsch et al., 2018). The borehole has a length of 44 m, a diameter of 87 mm, azimuth of 219.9° and dip of 37.3°. The foliation (175/75°) in the axial plane of the core dips with approximate 11°, which makes the foliation plane almost parallel to the axis of the cores. The specimens are cut from the borehole interval 38 to 39 m for Brazilian tensile tests and 43 to 44 m for the fracture toughness tests. All the specimens were dried for 24 h at 105° C three days before testing.

The lithology of the tested material consists of the so-called Grimsel Granodiorite which has a magmatic fabric, which is coarse-grained, massive and slightly porphyritic (Keusen et al., 1989; Schaltegger, U., 1989; Schneeberger et al., 2017). The rock is mainly composed of phyllosilicates, feldspar and quartz, with the volumetric ratios of 28% kalifeldspar and 36% plagioclase and 36% quartz, which is close to the mineralogical transition between granodioritic and granitic composition.

The quartz occurs in mm sized grains, while the orthoclase shows a few mm sized grains with Carlsbad-Twins and the plagioclase occurs from a few 10 microns to mm sized grains. Biotite occurs as predominant phyllosilicate and defines a strong foliation. During Alpine orogeny, strong textural overprinting of the rock occurred. The maximum pressure and temperature conditions are of greenshist conditions with $450° \pm 30°$ C and around 6 ± 1 kbar pressure (Challandes et al., 2008). The plagioclase is saussuritised and mainly persists as albite and epidote. The biotite is partly displaced by chloride during hydrothermal fluid circulation. The planar minerals are adjusted to the Alpine foliation, such that the naming by geological terminology is a Gneiss. The presence of aligned phylosilicates implies that grain boundaries are preferentialy aligned with the schistosity. The grain boundaries are initiation points for the micro-fracturing process. In the reminder of the paper, we will associate them with pre-existing micro-cracks and refer to them simply as micro-cracks.

A specific model of anisotropic elasticity is the transversely isotropic constitutive law, which is suitable for predicting the deformational behaviour of many types of rocks including the Grimsel Granodiorite. The transversely isotropic model defines a so-called isotropy plane, which is assumed to coincide with the apparent foliation plane, and postulates that every plane transverse to it also defines a symmetry plane. Dambly et al. (2018) investigated the orientation of the isotropy plane in Grimsel Granodiorite and concluded that the isotropy plane coincides with the foliation plane with a good accuracy. Hereafter, the foliation plane is used to refer to the isotropy plane in a transversely isotropic model. Five elastic constants characterize the elasticity of the transversely isotropic material in principal coordinates: Two Young's moduli, E and E', are defined within and normal to the isotropy plane, respectively; two ratios, ν and ν', represent the Poisson's ratios within and normal to the isotropy plane, respectively; and a transverse shear modulus, G', which defines the shear modulus in the direction transverse to the isotropy plane. Through the well-known Saint-Venant relation, an approximation for G'_{sv} can be obtained through the other elastic constants: $1/G'_{sv} = 1/E + 1/E' + 2\nu'/E'$. In reality, G' is an independent constant and can deviate from the approximated G'_{sv}. The in-plane shear modulus, G, is dependent of E and ν and is given by the relation $G = E/[2(1+\nu)]$. Table 3.2 lists the five elastic constants averaged from different tests and measured for the Grimsel Granodiorite samples (Dambly et al., 2018; Nejati et al., 2019a).

Table 3.2 The five elastic constants measured for Grimsel Granodiorite from uniaxial compression tests.

E	E'	G'	ν	ν'
42 GPa	21 GPa	17 GPa	0.2	0.1

3.4.2 Fracture toughness and strength measurement

Figure 3.1 shows schematically the geometrical configuration of the Brazilian and SCB samples used for tensile strength and fracture toughness measurements. The isotropy plane makes angle φ with the load axis in both SCB and BD tests. The geometrical details of the samples are given in Table 3.3.

The fracture toughness tests were conducted using four configurations $\varphi = 0°, 45°, 60°, 90°$, while only two configurations of $\varphi = 0°, 90°$ were tested for tensile strength measurements.

The prepared samples for fracture toughness were tested in a Zwick/Roell Z005 AllroundLine uniaxial press with maximum applicable force of 5 kN and linear variable displacement transducer (LVDT). A three-point-bending fixture with central loading stamp of 10 mm diameter was employed. To start the test, the specimen was preloaded with 1 N. Thereafter, the Zwick universal testing machine was driven by a displacement criterion of 0.1 mm/min. After the load drop of 80% due to breaking, the Zwick universal testing machine stops the loading.

The Brazilian tensile strength specimens were tested in a Zwick/Roell 1474 RetroLine universal testing machine capable of reaching a maximum force of 100 kN. A curved loading jaw was used to distribute the load over a portion of disk's circumference and avoid point load. To start the test, the specimen was preloaded with 5 N. Thereafter, the Zwick universal testing machine was driven by a displacement criterion of 0.05 mm/min. For both SCB and Brazilian disk tests, the load and the LVDT displacement were recorded by the digital acquisition system 1 (DAS 1). Both machines have a load resolution of 10 N and data were acquired with a rate of 100 Hz.

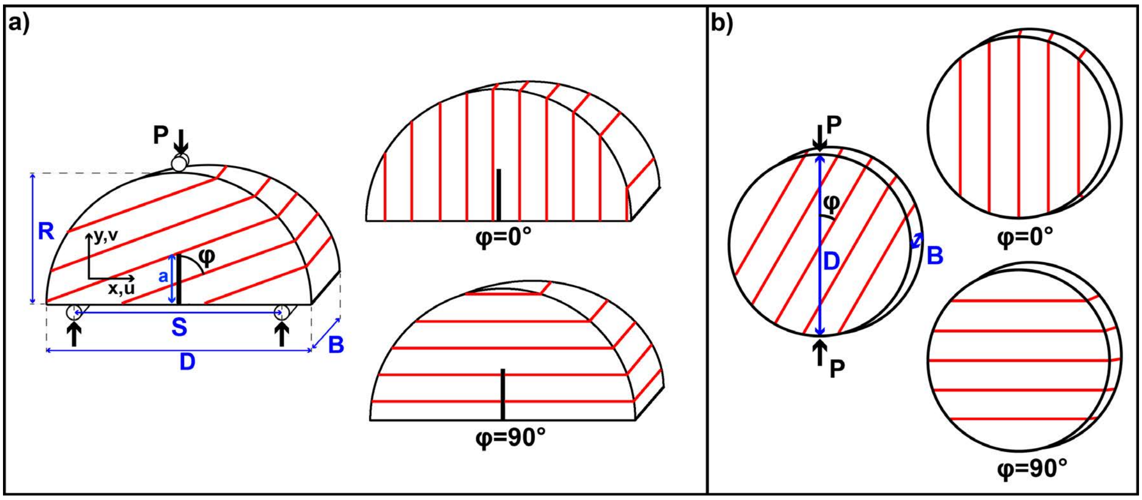

Fig. 3.1 Schematics of (a) Semi-circular bending and (b) Brazilian disk specimens, with their two end members $\varphi = 0°, 90°$ where φ is the angle between isotropy plane and the loading direction. A picture of the Brazilian disk with the apparent direction of isotropy plane (foliation) is also shown.

3.4.3 Digital image correlation

One side of the samples were coloured white and then were sparkled by an air brush to generate a random speckle pattern. We used a VIC-3D Digital Image Correlation System, which consists of two Prosilica GT 3400 9.2 Megapixel B/ W cameras, with 80 mm focal length and capturing images with a sampling rate of 4 fps. The cameras were connected to the second digital acquisition system 2 (DAS

Table 3.3 Geometrical dimensions of specimens used for semi-circular bending (SCB) and Brazilian tensile (BD) tests.

Parameter	SCB		BD
	Values [mm]	**Dimensionless values**	**Values [mm]**
Diameter (D)	82.9		83.3
Thickness (B)	37-39	$B/D \approx 0.46$	37.3-40.3
Radius (R)	39.4-41.7		
Span length (S)	58.4	$S/D = 0.7$	
Crack length (a)	17-20	$\alpha = a/R = 0.41$-0.5	

2). The two acquisition systems were synchronized by acquiring the force signal from the load cell with both the universal testing machine and the ADC converter of the DIC equipment. A reference image was recorded before deformation and a series of images was recorded during the tests. The resolution of this method depends directly on the speckle pattern on the specimen. Well-distributed and fine speckles allow to decrease bias and noise.

The DIC system was calibrated using a reference target reaching a calibration score (as defined in the software VIC-3D 7) of 0.018 pixels. The system setup, with the aforementioned choice of lenses, results in an average resolution of $\tilde{4}0$ pixels per millimeter. The subset size for the correlation process was chosen as a square with edge size of 35 to 47 pixels with a step size of one third of the edge size between subset centers, to deliver an average uncertainty throughout the area of interest of 0.01 pixels. This assumption was verified in the post-processing phase, and the average uncertainty for a representative test of 0.01 pixel was obtained. The DIC-system was started at the same time as the Zwick universal testing machine and stopped after total failure.

The series of images for each test were post-processed with VIC-3D 7 software (Correlated Solutions, Inc., 2016). The squared subset was correlated using Gaussian weight with an optimized 8-tap interpolation and normalized squared difference criterion. For consistency threshold, confidence margin and maximum margin was set to 0.05 pixels in the VIC-3D software. The strain calculation in VIC-3D depends on the step size and on the filter size. Smaller step sizes increase the calculation time, which is accepted. A sensitivity analysis was performed to investigate the effect of the FPZ width varying resolution edge size, search patch size and filter size at different pre-peak load. The FPZ width was compared from the u-displacement jump and the width of the ε_{xx}-strain field. It was found that keeping the step size at one third of the subset size and having a filter size between 5 and 9 points can reliably identify the FPZ (details given in section 3.6.1). Since noise level increases at such small filter sizes, an averaging scheme was used to reduce the effect of noise. MATLAB (The MathWorks Inc., 2017) was used for subsequent visualisation and further calculations.

3.5 Experimental results on toughness and strength

3.5.1 Fracture toughness anisotropy

Table 3.4 presents the geometrical details, the failure load as well as the calculated values of fracture toughness for 23 samples tested at different directions with respect to foliation (φ). Figure 3.2a illustrates these data with respect to the normalized crack length, and Figure 3.2b shows the variation of normalized fracture toughness values against the angle φ. The normalization is performed with respect to the mean value of fracture toughness at the configuration $\varphi = 90°$ which corresponds to 1.66 MPa$\sqrt{m}$. The mean values are shown by black asterisks in Figure 3.2b.

Table 3.4 Values of the fracture toughness measured for different angles between foliation and initial crack (φ).

φ	**Sample ID**	α	**B [mm]**	Y_I	P_m **[N]**	K_Ic **[MPa$\sqrt{m}$]**	**Average K_Ic**
0°	FT01	0.506	39.4	5.79	1410	0.65	0.73± 0.09
	FT02	0.487	39.3	5.53	1810	0.77	
	FT05	0.417	39.1	4.78	2550	0.88	
	FT06	0.429	38.3	4.88	2200	0.82	
	FT15	0.495	39.2	5.64	1410	0.63	
	FT16	0.503	39.4	5.74	1420	0.65	
	FT21	0.412	37.3	4.73	2040	0.72	
45°	FT11	0.421	36.9	4.81	2760	1.03	0.99± 0.06
	FT12	0.415	36.7	4.76	2520	0.92	
	FT13	0.501	38.5	5.72	2100	0.97	
	FT17	0.429	37.3	4.89	2360	0.90	
	FT18	0.428	36.9	4.88	2830	1.08	
	FT25	0.514	38.1	5.89	2070	1.01	
60°	FT27	0.514	37.5	5.89	2410	1.21	1.30± 0.10
	FT28	0.484	37.6	5.50	3170	1.40	
90°	FT03	0.491	38.3	5.59	4010	1.80	1.66± 0.15
	FT04	0.495	38.3	5.64	3360	1.54	
	FT08	0.484	39.1	5.50	3510	1.50	
	FT09	0.491	36.3	5.59	4000	1.89	
	FT19	0.456	37.8	5.17	3540	1.47	
	FT20	0.427	37.6	4.87	4810	1.79	
	FT23	0.481	38.5	5.46	4020	1.72	
	FT24	0.514	38.1	5.89	3180	1.58	

The mode I fracture toughness is calculated based on the normalized stress intensity factor Y_I and the maximum load P_m as (Kuruppu et al., 2014)

$$K_\mathrm{Ic} = Y_\mathrm{I} \frac{P_m \sqrt{\pi a}}{DB} \tag{3.1}$$

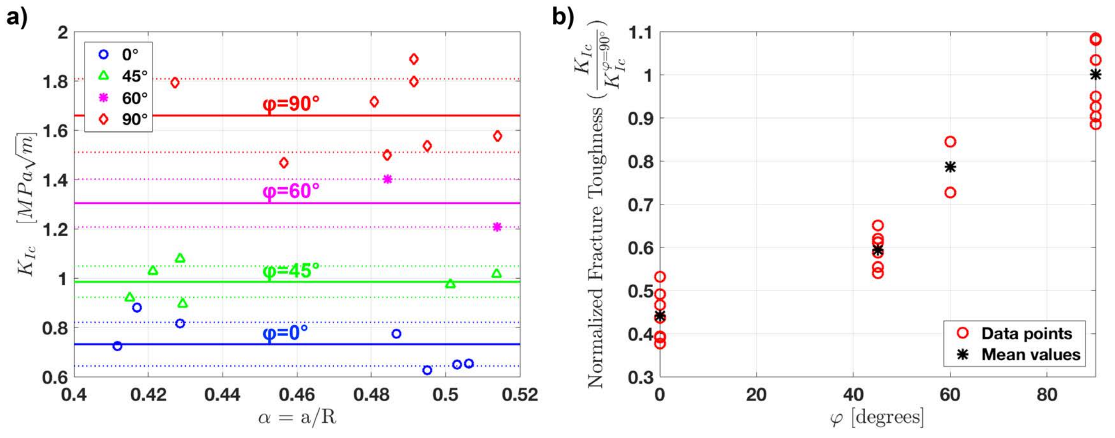

Fig. 3.2 a) The variation of fracture toughness against the dimensionless notch ratio α for different angles between the foliation and the crack orientation. The solid and dotted lines indicate mean and standard deviation (SD), respectively. b) The variation of normalized fracture toughness to the mean value at $\varphi = 90^\circ$ against the angle between foliation and direction of initial crack φ.

where

$$Y_\text{I} = -1.297 + 9.516\frac{S}{D} - (0.47 + 16.457\frac{S}{D})\alpha + (1.071 + 34.401\frac{S}{D})\alpha^2 \qquad (3.2)$$

Here, a is the crack length, and B and D are the specimen thickness and diameter. The normalized stress intensity factor Y_I is a geometrical factor obtained from a fit to finite element (FE) results, and is valid only for isotropic materials (Kuruppu et al., 2014). In anisotropic cases, in addition to geometrical configuration, the material constants also influence the stress intensity factor solution. Several finite element analyses were performed to evaluate how strongly an anisotropic material model influences the stress intensity factor solution Y_I. The specimen was modeled and analyzed with the commercial finite element code ABAQUS. The finite element mesh and boundary condition are shown in Figure 3.3. An anisotropic elasticity model was used to define the transversely isotropic properties given in Table 3.2. The contour integral module of ABAQUS uses cylindrical domains to calculate the interaction integrals and subsequently the stress intensity factors (ABAQUS/CAE, 2014). The domain integral method to calculate the stress intensity factors has been successfully used for isotropic materials (Nejati et al., 2015; Shih and Asaro, 1988), as well as anisotropic elasticity models (Banks-sills et al., 2005, 2007; Wang et al., 1980). Upon the calculation of the stress intensity factors, the normalized stress intensity factors Y_I and Y_II are obtained from

$$Y_\text{I} = \frac{K_\text{I}BD}{P\sqrt{\pi a}}, \qquad Y_\text{II} = \frac{K_\text{II}BD}{P\sqrt{\pi a}} \qquad (3.3)$$

using the geometrical and loading values employed in the finite element model. The finite element results for isotropic as well as anisotropic material models are compared in Table 3.5. The values obtained from Eq. (3.2) are also given for comparison. It is seen that the influence of anisotropy on the values of the normalized stress intensity factors is minimal.

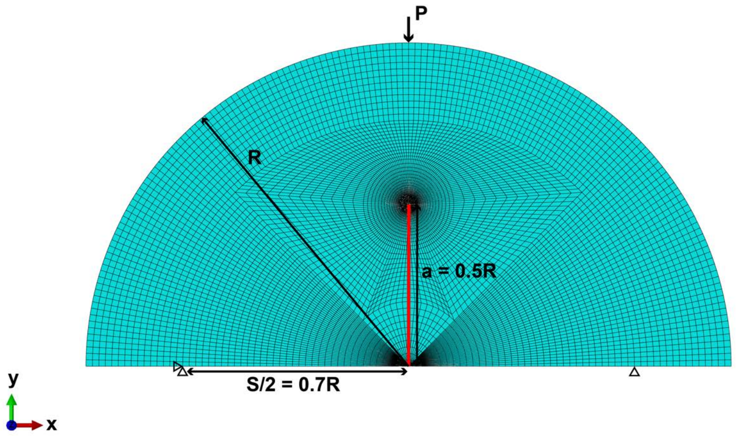

Fig. 3.3 The finite element mesh and the boundary condition used for the finite element analyses of the SCB specimen.

Table 3.5 Comparison of normalized stress intensity factors obtained from isotropic and anisotropic solutions.

	Y_{I}			Y_{II}
φ	**Eq. (3.2)**	**Isotropic (FE)**	**Anisotropic (FE)**	**Anisotropic (FE)**
0°	5.657	5.557	5.619	0
45°			5.658	-0.640
90°			5.527	0

The results indicate the following: (1) Y_{I} obtained from the formula given in Kuruppu et al. (2014) overestimate the fracture toughness by only 2%. (2) The influence of the anisotropy on the stress intensity solution Y_{I} is negligible. (3) Although the cases $\varphi = 0°, 90°$ still induce pure mode I using an anisotropic elasticity model, the configurations $\varphi = 45°$ yield a mixed-mode I/II type with $K_{\mathrm{II}}/K_{\mathrm{I}} \approx 0.1$. This indicate that the results obtained for $\varphi = 45°, 60°$ are not in fact pure mode I fracture toughness. Note that the influence of the anisotropy on the stress intensity factor solution can be more significant in other samples, configurations and anisotropy ratios.

Analyzing the fracture toughness results, the following remarks are noted:

- The values of fracture toughness are not influenced by the dimensionless notch length. It is known that for small samples, the fracture toughness can be significantly influenced by the ligament size. These results therefore seem to imply that the samples are large enough to be suitable for fracture toughness measurement of the type of rock under study.

- The ratio of the maximum fracture toughness to its minimum is 2.27, which indicates a strong anisotropy in fracture toughness. The fracture toughness is the largest for crack propagating normal to the foliation, and is the minimum when the crack grows along the foliation.
- Although the configurations $\varphi = 0^\circ$ and $\varphi = 90^\circ$ correspond to pure mode I crack deformation, the configurations $\varphi = 45^\circ$ and $\varphi = 60^\circ$ involve mixed mode I/II crack growth. This is due to the elasticity anisotropy.
- Normalizing the values of the standard deviation with respect to the actual values of the fracture toughness gives $0.73 \pm 12\%$, $0.99 \pm 6\%$ and $1.66 \pm 9\%$ for $\phi = 0^\circ, 45^\circ, 90^\circ$, respectively. The comparison of the standard deviations shows no significant variation of the scatter from one configuration to another. The reason for this small difference in scatter can be attributed to the heterogeneity and large grain size of the rock under study. Any conclusion on the difference of the scatter of the results between different configurations requires a bigger data set where the effect of heterogeneity between different configurations is minimized.

3.5.2 Post-mortem fracture surface analyses

Post-mortem analyses of fracture surfaces help to understand the fracturing processes in different configurations. Such analyses may also be used to validate the accuracy of test conditions for mode I fracture toughness measurement as explained by Kuruppu et al. (2014). According to these guidelines, a deviation of more than $0.05D$ (equivalent to 4.1 mm in our samples) of the cracked ligament from the notch plane makes the test invalid, with the resulting value being not representative of mode I fracture toughness. Figure 3.4 illustrates the fracture trace, both front and back views, together with the mineral analyses of fracture surfaces of all different configurations. The fracture trace is described in terms of two length parameters: maximum offset indicates the maximum distance between the fracture path and the line connecting the start and end points of the generated fracture; and kink distance is the distance between the end point of generated fracture from the loading point. The type of the minerals in the new fracture surface are also analyzed macroscopically.

In the case of fracture growth along foliation ($\varphi = 0^\circ$), the fracture path shows very small values of kink distance (about 1 mm) and maximum offset (about 2 mm). The analysis of fracture surfaces show a high content of sheet silicates such as biotite and chlorite, indicating the fracture is aligned with the biotite-rich plane. Epidote, feldspar and quartz were also observed in the new fracture surfaces, with apparent average grain size of smaller than 4 mm. When the fracture growth is normal to foliation ($\varphi = 90^\circ$), the kink distance is still very low (about 2 mm), while the maximum offset (about 6 mm) is higher compared to results of $\varphi = 0^\circ$. The fracture seems to break through patches of stiffer quartz and feldspar rich layers, and this may be the reason why the fracture surfaces are rougher compared to the case $\varphi = 0^\circ$.

The fracture traces for $\varphi = 45^\circ$ show much higher kink distance, about 4-6 mm, compared to the other two configurations. These values are at the border or slightly higher than the limits set based on the guideline ($0.05D = 4.1$ mm), and therefore these test may not be considered as valid pure mode I fracture toughness tests. The maximum offset is about 4 mm which is more than $\varphi = 0°$ and less than $\varphi = 90°$. The highly kinked fracture path may indicate the presence of mode II loading, which is in agreement with what was noted in Section 3.5.1. However, one should also note that the crack kinking in anisotropic rocks can be present even for pure mode I loading condition since apart from the loading, the directional-dependency of the strength can also influence the fracture growth direction (Saouma et al., 1987). The fracture traces sometimes shortly align with the foliation plane and breaks sometimes through stiffer layers containing quartz or feldspar.

The following remarks are noted: (1) The fracture roughness is much higher in the case of $\varphi = 90°$ compared to $\varphi = 0°$, which seems to be the influence of aligned micro-cracks along the foliation. As the angle between foliation and the initial crack, φ, increases, the maximum offset also raises, which is consistent with rougher fracture surfaces. (2) The largest kink distance is observed in the cases of $\varphi = 45°, 60°$. These cases show clear deviation from the original crack direction, which seems to be due to a mixed mode I/II crack loading. (3) As φ increases, the content of philosilicate minerals (e.g. biotite) on the fracture plane decreases. The fracture plane for $\varphi = 45°$ shows a higher content of feldspar and quartz compared to the one from $\varphi = 0°$ but less than $\varphi = 90°$.

3.5.3 Strength anisotropy

This section presents the indirect tensile strength measurements using Brazilian disk tests. Table 3.6 lists the thickness, failure load and the calculated strength of six Brazilian disk specimens in two configurations $\varphi = 0°$ and $\varphi = 90°$. In order to calculate the strength, finite element analyses were performed to obtain the tensile stress at the center disk using the elastic constants of transversely isotropic elasticity model given in Table 3.2. It is evident that the strength is strongly anisotropic, with the value in the direction normal to the foliation being 2.61 times the one along the foliation. This indicates the principal role of micro-cracks dominantly aligned with the foliation on the strength of rock.

Table 3.6 The tensile strength measurements using Brazilian disk tests. The tensile stress at the center of disk was obtained using finite element solution of a transversely isotropic model based on elastic constants reported in Table 3.2.

φ	**B [mm]**	P_m **[kN]**	σ_t **[MPa]**	**Average** σ_t **[MPa]**	**Ratio**
0°	39.5	32.39	5.50	5.63±0.11	2.61
	38.6	34.3	5.68		
	40.3	36	5.71		
90°	38.9	74.2	16.07	14.69±2.00	
	38.0	55.9	12.39		
	37.3	69.1	15.60		

Many previous studies have employed the isotropic solution to calculate the strength from Brazilian disk. Table 3.7 presents the values of strength calculated based on an isotropic elasticity behavior

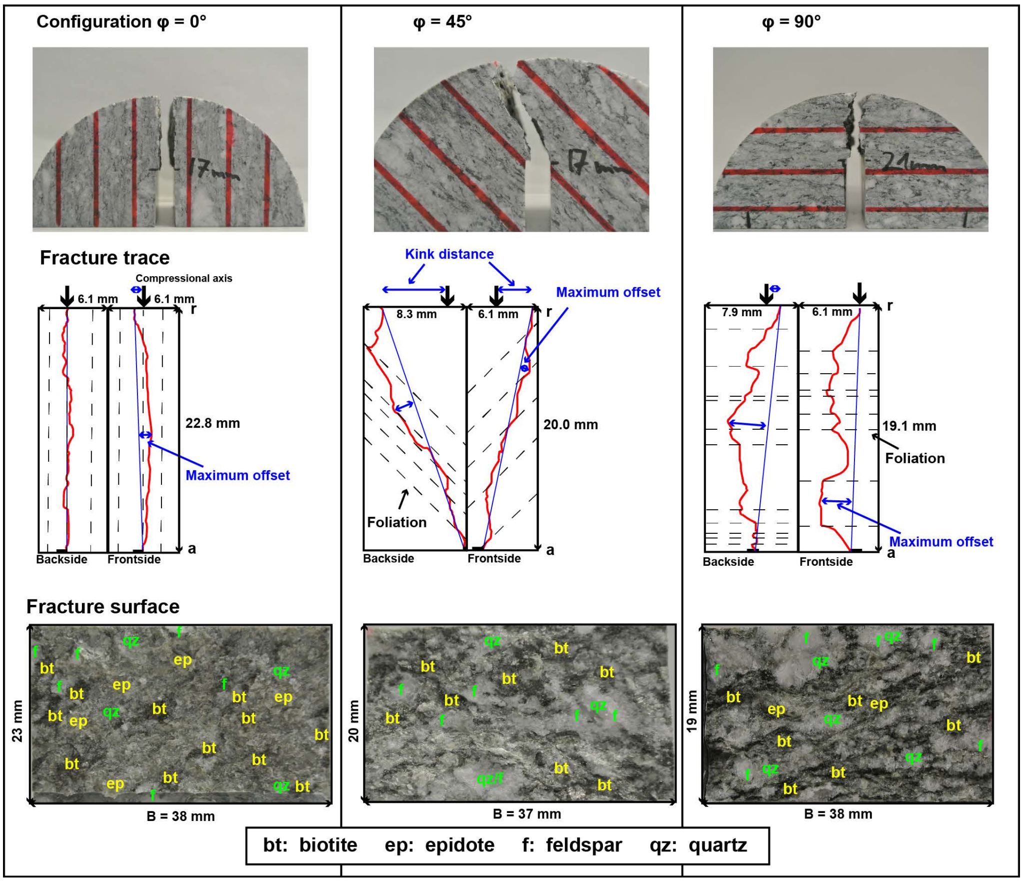

Fig. 3.4 The visual analyses of fracture traces and surfaces for three angles between initial crack and foliation: $\varphi = 0°, 45°, 90°$.

in comparison with the ones obtained from the finite element solution of anisotropic model. It is clear that an isotropic assumption introduces a large error, 20% in the direction of foliation and 9% in the direction normal to foliation, in the calculation of strength. In addition, an anisotropy ratio of 2.01 is obtained from isotropic model, which is significantly lower than the anisotropic prediction. It is expected that the error stemming from the isotropic solution will increase with increasing elastic anisotropy.

Table 3.7 Comparison of average Brazilian disk tensile strength obtained from isotropic and transversely isotropic elasticity solutions.

φ	σ_t [MPa]	σ_t^{iso} [MPa]	$\lvert\sigma_t - \sigma_t^{\mathrm{iso}}\rvert/\sigma_t$ [%]
0°	5.63	6.73	20
90°	14.69	13.33	9

The failure mechanism in two main directions also shows significant differences. The failure normal to the direction of foliation exhibits a more sudden and instantaneous behavior than the one along the foliation. In fact, the analyses of strains obtained from DIC measurement show the development of a band of failure along the foliation before the final rupture. This may indicate that the fracturing process is mainly due to the gradual activation of micro-cracks, which are mainly aligned with foliation, followed by their coalescence to form a macro-crack that splits the specimen. On the other hand, when the direction of final rupture is normal to the foliation, the existing micro-cracks cannot simply connect to form the fracture, and a more complex mechanism is required in the failure process perhaps including the development of new micro-cracks to connect the existing ones. Overall, the results emphasize the role of existing set of micro-cracks in the fracturing of granite, as it has also been observed in previous studies (Nasseri et al., 2005).

3.6 Experimental results on the FPZ

As discussed in the review given in Section 3.3, the characterization of the FPZ in quasi-brittle materials including rocks is of great importance, and is in fact a difficult task to conduct. Three suggested method to identify the FPZ from DIC results were also discussed. Due to the highly localized strain in the FPZ, the strain values should be used with caution when the FPZ is identified from strain results. Also, due to the small size of the FPZ, highly accurate DIC measurements are required. Therefore, an accurate determination of the FPZ requires highly accurate DIC results with appropriate smoothing methods to obtain strain in highly localized zones. This section introduces an averaging method to obtain reliable values for the size of the FPZ, and discusses anisotropy of the FPZ in anisotropic rocks. The calculated values are then compared to the values estimated by models based on linear elastic fracture mechanics.

3.6.1 Identification of the FPZ

The DIC method provides a full-field representation of in-plane surface displacements. The spatial gradient of the displacement field is then evaluated to obtain the strain field. Due to noises involved in the displacement measurements, smoothing techniques are used to obtain the derivatives. The subset size is defined as a squared window used to compare two different speckle-pattern and the step size is the spacing between the subset centers. In our case the measurement needs to cover a region of 8 cm × 6 cm and the recording resolution is 3384 pixels × 2704 pixels. The average accuracy allowed is set to 0.01 pixels. During the measurements, an average resolution of 40 pixels/mm was employed. The choice of the subset size between 35 to 41 pixels corresponds to 1×1 mm^2. The recommended step size is one-third of the subset size i.e. 13 pixels which is equivalent to $1/3$ mm. This means that a 41×41 pixel area is tracked at every 13 pixels. The filter size is defined as the length of the displacement values at subset centers, which smooths the strain field with increasing number of displacement points. The strain field depends directly on the step size and the filter size of the strain tensor.

In this paper we use an averaging window to obtain the width of the FPZ, and compare this value with the one calculated from the jump in displacement. This averaging is required since small filters are insufficient to remove sufficient noise from the strain results. This methodology is based on a window containing ten paths with intervals of 0.5 mm crossing the crack ligament near the top. Averaging the strain and displacement then removes the local noises, and facilitate observing the localized zone even with very small filter sizes. There are mainly two parameters influencing the smoothing of strain measurements: step size and filter size. The shape and the length of the FPZ is also obtained using the variation of the maximum principal strain ε_1 along a path ahead of the crack tip. The length is evaluated based on the distance in which the maximum principal strain is highly localized. The shape can also be determined based on the values of the maximum principal strain.

Figure 3.5 shows the variation of the FPZ width against the step and filter size at different load levels with respect to the peak (failure) load. The results in both Figures 3.5a and 3.5b are obtained from the subset size of 39 pixels to deliver an average uncertainty of displacement resolution throughout the area of interest of 0.01 pixel. In Figure 3.5a the filter size is kept constant at the minimum possible value (five points), while in Figure 3.5b, the step size of thirteen pixels is used. The displacement values are not influenced by the step size and filter size since these parameters are only involved in the post-processing stage to obtain strains from displacements. These two plots suggest two main trends:

- As long as the filter size is chosen to be a small value, the calculated value for the width of localized zone is not influenced by the value of step size, and the width obtained from strains and displacement are in very good agreement. This suggest that given an appropriate choice of filter size, the step size recommended by the software (one-third of the subset size, thirteen pixels in our case) can be reliably used.
- At the constant step size, as the filter size approaches its minimum (five points), the width obtained from strain approaches the one obtained from displacement. Moreover, the calculated width from strain increases linearly for filter sizes above ten points. This suggests that high values of filter size increases the size of the region in which a strain smoothing procedure is applied, and therefore if the smoothing region is greater than the half of the FPZ width, the sharp displacement jump at the middle of the FPZ widens the strain profile, which leads to inaccurate measurement of the FPZ width from the strains.

An example to clarify the influence of the filter and step sizes is arranged as follows. Consider the width of the FPZ is 5.5 mm for the sample under study in Figure 3.5. A sharp gradient of displacement is expected to be present at the middle of this region due to a possible macro-crack being developed there. In this case, the distance from the sharp displacement gradient to the boundary of the FPZ is 2.75 mm. Any smoothing scheme used on a distance larger than 2.75 mm inaccurately propagates the large gradient at the center of the FPZ beyond the actual boundary of the FPZ. The choices of thirteen pixels and five points respectively for step and filter sizes results in a smoothing distance of sixty-five pixels which is equivalent to about 1.625 mm, far below 2.75 mm. However, any filter size above eight points would make the smoothing distance to extend above 2.6 mm which is almost equal to the half of the FPZ width. Figure 3.5b shows that the calculated width of the FPZ start to increase linearly above the filter size of about eight. This indicates that for such big filter sizes, the smoothing distance is larger than half of the FPZ, and therefore the calculated values of FPZ width are inaccurate, and the result of smoothing procedure.

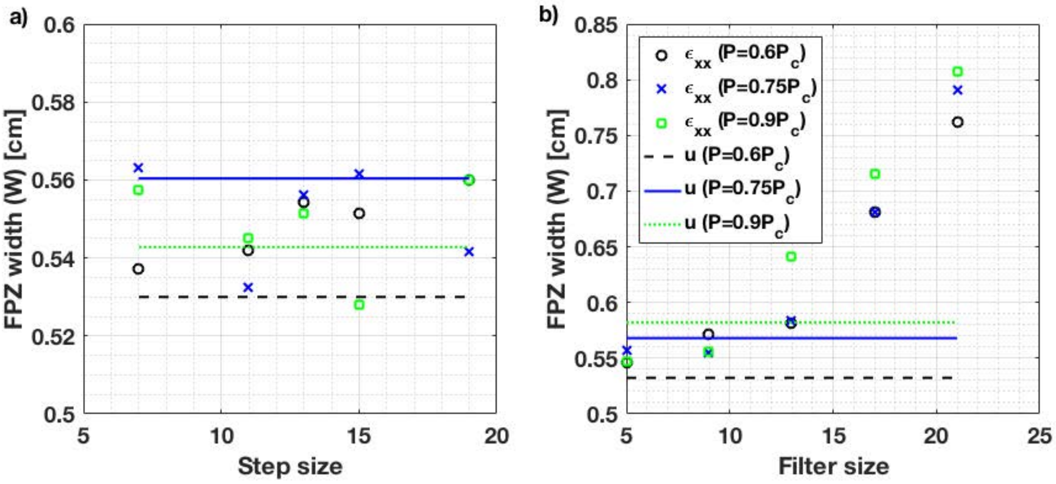

Fig. 3.5 (a) The variation of the FPZ width obtained from localised strain ε_{xx} and displacement jump u against (a) step size and (b) filter size, for three load levels of 60%, 75% and 90% of pre-peak load for a configuration $\varphi = 0^\circ$. The subset size for all measurements is thirty-nine pixels. In (a) and (b) the filter size and step size are five points, and thirteen pixels, respectively.

According to this sensitivity analyses, it was concluded that a step size of thirteen pixels and filter size of five can provide accurate enough strain field for the evaluation of the FPZ size from strain localization. In fact, these parameters assure that the size of the FPZ obtained from strains are in very good agreement with the one obtained from displacement. It is noteworthy that the results in Figure 3.5 also show that the FPZ width is not dependent on the load level above 60% of the peak-load. This observation agrees with similar findings in previous studies (Alam et al., 2014; Skarzyński et al., 2013; Skarzyński and Tejchman, 2013; Wu et al., 2011). Note that the variation of the FPZ width obtained from displacements and strains at different loads is small (about 0.3 mm) compared to the actual value of the FPZ width which is about 5.5 mm.

3.6.2 Shape of the fracture process zone

Figure 3.6 shows the region with highly localized maximum principal strains ahead of the crack tip in the samples tested in two configurations $\varphi = 0°, 90°$. When the crack is oriented along foliation ($\varphi = 0°$), almost all samples show the development of a semi-elliptical FPZ region. Although this is also the dominant shape in configuration $\varphi = 90°$, the FPZ seems to show an angular deviation from the notch plane in some samples. The angular deviation of the FPZ can be attributed to the influence of micro-cracks oriented along the foliation, resulting in the tendency to the change the direction of crack growth. This is the reason for having a more tortious crack path observed in the post-mortem analyses. The semi-elliptical FPZ shape observed in our experiments agrees well with the results reported in many previous researches on the FPZ shape of quasi-brittle materials (Backers et al., 2005; Chengyong et al., 1990; Otsuka and Date, 2000; Skaråyåski et al., 2011; Swanson and Spetzler, 1984; Wu et al., 2011; Zietlow and Labuz, 1998). These results emphasize that butterfly-shaped FPZ obtained from analytical models are not accurate estimations of localized zones in quasi-brittle materials.

The overall conclusion from Figure 3.6 is that the FPZ seems to be developed in a semi-elliptical region ahead of the crack tip. This finding is in very good agreement with the previous studies and also matches the strip-yield (Dugdale-Barenblatt) model. Figure 3.6 shows a schematic representation of a semi-elliptical FPZ with the width of W and the length of L. These two length parameters seem to be independent, and are expected to be only material properties provided that the boundary of the FPZ is fully formed (no load dependency of the FPZ boundary) and the crack ligament is large enough (no boundary influence).

3.6.3 Size of the fracture process zone

Figure 3.7 schematically shows the identification of the FPZ width from the strain localization and displacement jump in two specimens from different configurations. These results show the agreement of the FPZ width obtained from strains and displacements. All three components of strain show localization in the process zone, with the component normal to the crack plane, ε_{xx}, being an order of magnitude greater that the other two strain components. The width of the FPZ is picked using an zone of averaging (ZOA) at 70% of pre-peak load.

It is noteworthy that according to the values of tensile strength and Young's moduli, a critical tensile strain of about 320 and 350 micro strains are obtained for the principal directions normal and parallel to the foliation. From the ε_{xx} plots in Figure 3.7, it is seen that such values of critical strain are exceeded at a loading stage between 50% to 70% of the peak load. This loading level is in a very good agreement with the general belief that the development of inelastic deformation of quasi-brittle materials start at about 60-70% of the peak load (Whittaker et al., 1992).

Figure 3.8 shows the variation of maximum principal strain ε_1, along twelve paths oriented at different angles with respect to the crack plane. Localization of the maximum principal strain is a good indicator of the inelastic region i.e. the FPZ. Therefore, the plots in Figure 3.8 can be used to

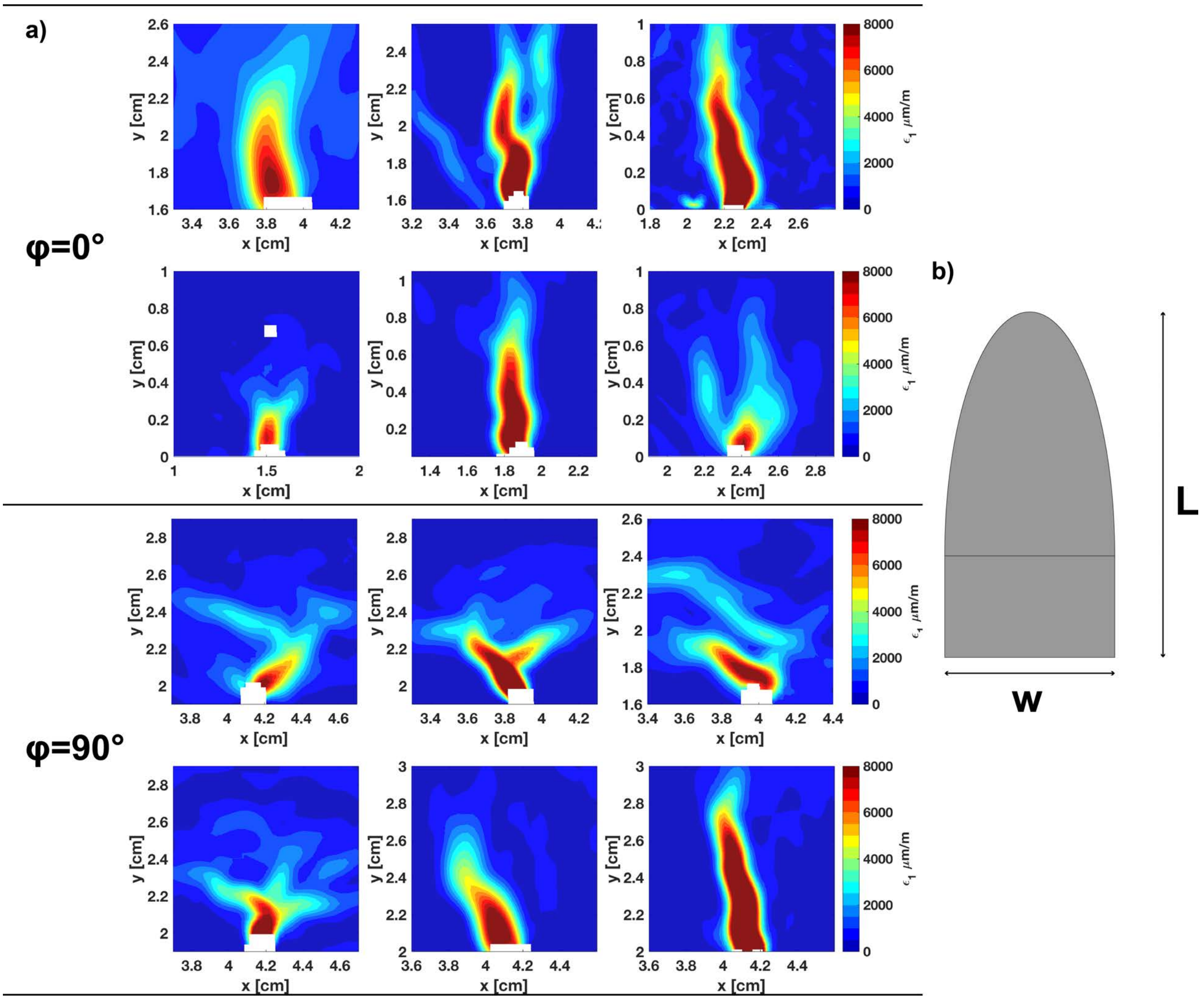

Fig. 3.6 a) The contours of maximum principal strain showing the FPZ shape at peak load for the configurations $\varphi = 0°, 90°$. b) The FPZ is idealized schematically as a semi-elliptical region with the width of W and the length of L.

define the boundary of the FPZ, whereby the length, width and shape of the FPZ are determined. At the peak load, the maximum principal strain reaches as high as 0.01 near the center of the FPZ (see Figure 3.8d). This high strain reduces dramatically when approaching the FPZ boundary, with localized deformation vanishing completely along the FPZ boundary. The shapes of the strains along different paths at different loads have similar trends and show an onion skin structure, where the load increases the strain in the nonlinear region, but does not influences the strain values around the FPZ. This clearly shows the localization of strain in the FPZ by increasing load. It is seen from both contours and plots that the FPZ is bigger in the configuration $\varphi = 0°$ than $\varphi = 90°$, with the length to width ratio in both cases being $L/W \approx 2$.

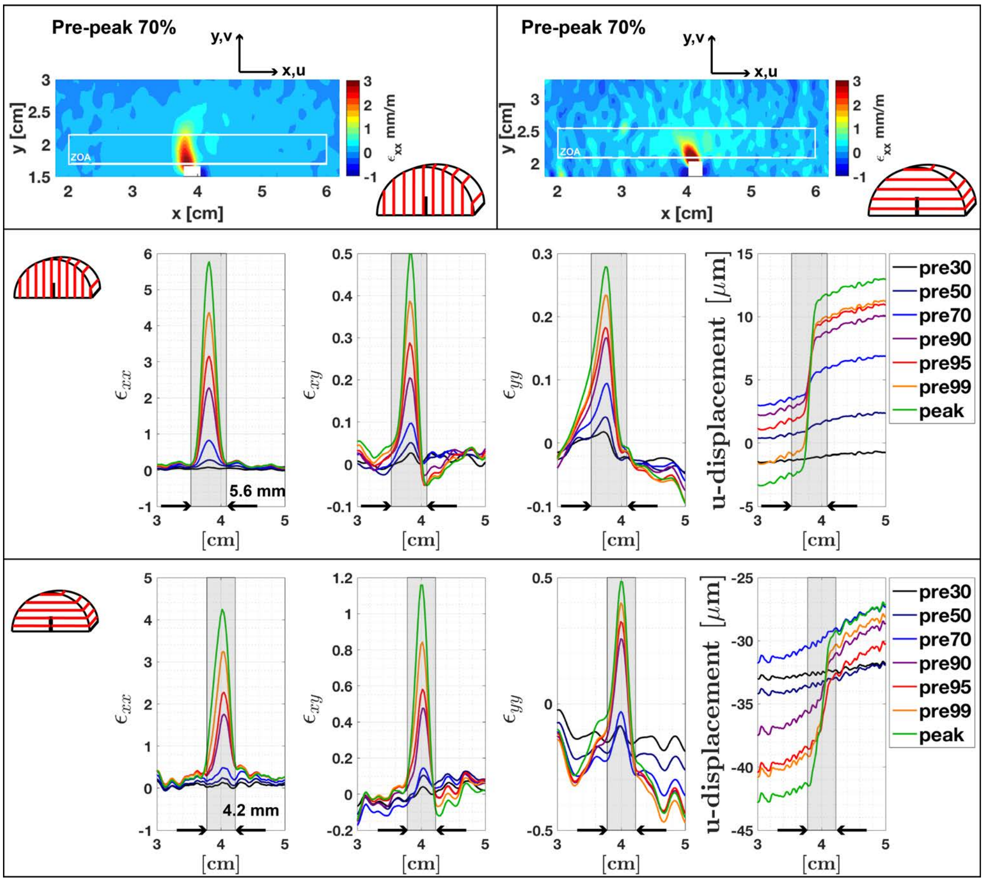

Fig. 3.7 The calculation of the FPZ width based on localization of strain components ε_{xx}, ε_{xy}, ε_{yy}, given in millistrain (mm/m) and the jump of displacement u for two end-member configurations of $\varphi = 0^\circ, 90^\circ$ at seven different loading stages prior to the peak load. The width of the FPZ corresponds to the width of the shaded region and measures $w = 5.6$ mm for φ=0° and $w = 4.2$ mm for φ=90°. The width of the FPZ is picked using a zone of averaging (ZOA) at 70% of pre-peak load. According to the coordinate system shown, negative values of displacement imply movements to the left.

Figure 3.8 also shows that once the boundary of the FPZ is fully formed at about 70% to 90% of the peak load, the size of the FPZ is not load dependent anymore. However, this does not mean crack extension already starts at this load level or a cohesion-less crack is developed. The activation and coalescence of the micro-cracks can still continue within the FPZ, after the FPZ, or the region in which the energy dissipation occurs, has reached its ultimate size. Fakhimi et al. (2017) reported the formation of cohesion-less crack surfaces before the peak load in their experiments. However, we can not confirm such traction-free surfaces being created before the peak load in our tests. This is because (1) the DIC measurement is only surface measurement and does not give any information with regard to the strains along the crack front, and (2) there is no tool to obtain tractions within the FPZ and high values of strain do not necessarily imply a cohesion-free surface.

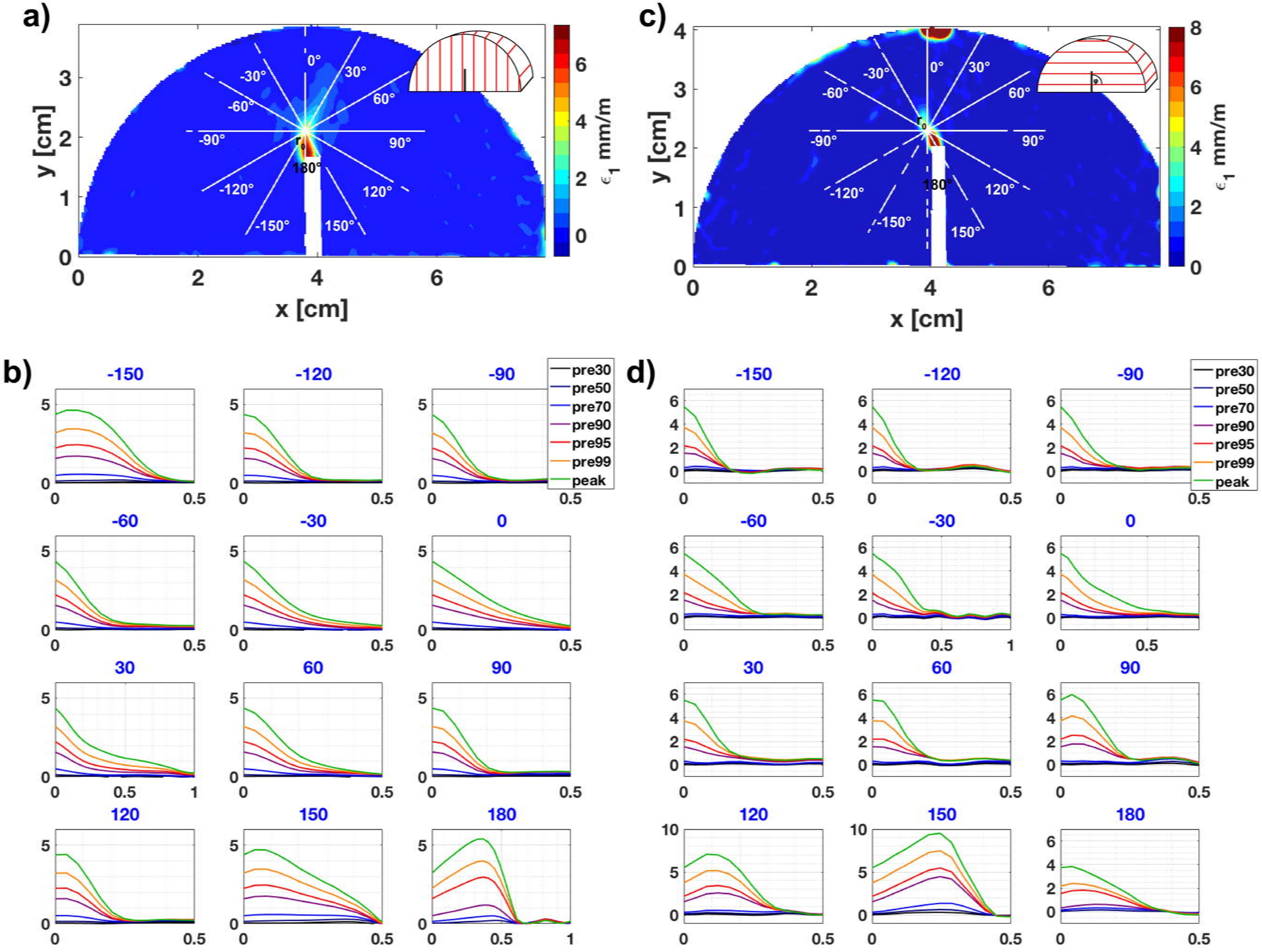

Fig. 3.8 (a,c) The contours of maxmimum principal strain ε_1 at peak load for two configurations $\varphi = 0°, 90°$. (b,d) The variation of ε_1 is given in millistrain (mm/m) along different radial paths originated from the point r_0 (white lines in (a) and (c)) for different pre-peak load levels from 30% up to the peak load. The blue colored numbers in the titles of the plots in (b) and (d) indicate the specific radial path shown in (a) and (c). The unit of the x-axis in (b) and (d) is cm.

Figure 3.9 presents the measured values of the width (W) and the length (L) of the FPZ in two configurations $\varphi = 0°, 90°$. As it was previously mentioned, the boundary of the FPZ is developed earlier for $\varphi = 0°$ than $\varphi = 90°$. The data points for $\varphi = 90°$ correspond to 90% pre-peak load, whereas the data point for $\varphi = 0°$ are at 70% of the peak load. The results for twelve samples are given in this Figure as data points, with the mean values and the standard deviation (SD) are shown by red solid lines and dotted blue lines, respectively. For crack propagating along the foliation $\varphi = 0°$, the mean values of the six tests measure $w = 5.4$ mm in width and $L = 10.84$ mm in length. For the configuration $\varphi = 90°$, the mean values for the width and the length of the FPZ are 4.7 mm and 8.8 mm, respectively. The following remarks shall be noted:

- In both configurations $\varphi = 0°$ and $\varphi = 90°$, the average length to width ratio is $L/W \approx 2$.
- The fracture process zone is larger in size when the crack grows along the foliation compared to the case it propagates normal to the foliation. The ratio of the FPZ size in two directions is $L^{\varphi=0°}/L^{\varphi=90°} \approx W^{\varphi=0°}/W^{\varphi=90°} \approx 1.2$. This indicates that the fracture process zone is anisotropic in terms of size.
- The reason for a bigger FPZ along the foliation may be the preferred direction of micro-crack in such direction. Since the micro-cracks are oriented in the direction of crack growth, their activation and propagation can lead to a wider process zone.
- There is a negative correlation between the length and the width of the FPZ in both configurations. Both plots show that, the higher the FPZ width, the lower the FPZ length. One can explain this trend by considering that the energy dissipated via micro-cracking is a material property which drives the resistance of the material toward crack propagation. If one assumes that this energy is constant for a configuration, any increase in the FPZ length must be accompanied with a reduction in the FPZ width.
- The scatter of the FPZ width and length data can be attributed to the heterogeneous nature of rock. The mean values of the data are therefore considered as the representative values for these parameters.

It is noteworthy that the full development of the FPZ in rocks is a necessary condition for a reliable fracture toughness test. In both rocks and metals, the crack length and ligament are crucially important in order to allow the nonlinear zone to develop fully so that a representative fracture toughness can be measured. The specimen thickness requirement, however, seems to be of less importance in rock material compared to the metals. The reason is that the FPZ development in rocks is mainly due to tensile stresses, whereas the nonlinear plastic zone in metals mainly develops due to shear stresses. Therefore, while the size of the plastic zone depends significantly on the specimen thickness and out-of-plane stress, the FPZ size seems to be rather independent of whether the plane-stress or plane-strain condition holds (Schmidt, 1980). Many experimental results obtained from different specimen types show that the measured fracture toughness is somewhat independent of the specimen thickness

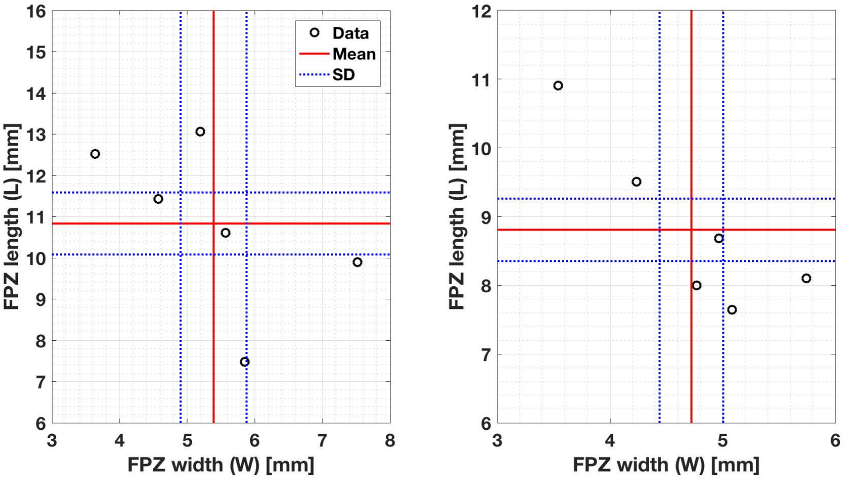

Fig. 3.9 The measured values for the FPZ width (W) and length (L) for two cases of $\varphi = 0°$ and $\varphi = 90°$. The mean values of the six tests are shown by red line, while the blue pointed line show the standard deviation. The results are taken from the fully formed FPZ, i.e. at 70% of pre-peak load for $\varphi = 0°$ and 90% of pre-peak load for $\varphi = 90°$.

(Haberfield and Johnston, 1990; Khan and Al-Shayea, 2000; Kobayashi et al., 1986; Laqueche et al., 1986; Lim et al., 1994; Schmidt and Lutz, 1979; Singh and Sun, 1990). Therefore, the FPZ size obtained from the surface can technically show how the inelastic zone is developed within the solid, since a uniform FPZ is expected along the crack front.

Figure 3.10 compares our results on the FPZ width and length with the results reported in previous research. Tarokh et al. (2017) and Otsuka and Date (2000) used concrete specimens with aggregate sizes up to 10 mm and obtained the FPZ length and width for various sample sizes. Backers (2004) used sandstone specimens with grain sizes between 0.1 mm and 0.5 mm. Tarokh et al. (2017) obtained the results from DIC experiments while Backers (2004) and Otsuka and Date (2000) conducted acoustic emission tests. This figure shows that the length to width ratio of the FPZ mainly varies between two and four. In addition, the size of the process zone increases with increasing the sample size, where the ratio L/W increases from two for small samples to about six for larger ones. Overall, the results characterize the FPZ of the quasi-brittle materials as a rather narrow semi-elliptical region.

3.7 Link between toughness, strength and the FPZ size

This section compares the experimental results on the FPZ size with the prediction of theoretical models. Let us consider a plane stress problem where one of the symmetry planes of the material is parallel to the symmetry plane of the model (normal to z-axis). According to the generalized Hooke's law, the stress-strain relationship of an elastic anisotropic material within the plane follow

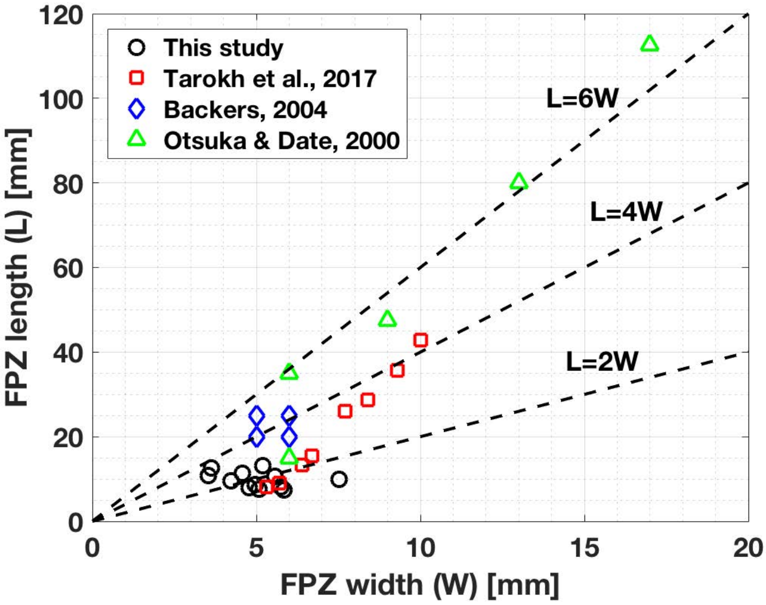

Fig. 3.10 The comparison of the width and length of the FPZ obtained from this study with the results given in three previous studies.

$$\begin{bmatrix} \varepsilon_x \\ \varepsilon_y \\ 2\varepsilon_{xy} \end{bmatrix} = \begin{bmatrix} S_{11} & S_{12} & S_{16} \\ S_{21} & S_{22} & S_{26} \\ S_{61} & S_{62} & S_{66} \end{bmatrix} \begin{bmatrix} \sigma_x \\ \sigma_y \\ \tau_{xy} \end{bmatrix} \tag{3.4}$$

where $S_{ij}, i, j = 1,2,6$ are the components for the compliance matrix. Considering a crack in the plane oriented along the x-axis, the stress field adjacent to the crack tip under mode I loading is given by Sih et al. (1965):

$$\begin{aligned} \vec{\sigma}_x &= \frac{K_{\mathrm{I}}}{\sqrt{2\pi r}} \Re \left[\frac{\mu_1 \mu_2}{\mu_1 - \mu_2} \left(\frac{\mu_2}{\sqrt{\cos\theta + \mu_2 \sin\theta}} - \frac{\mu_1}{\sqrt{\cos\theta + \mu_1 \sin\theta}} \right) \right] \\ \vec{\sigma}_y &= \frac{K_{\mathrm{I}}}{\sqrt{2\pi r}} \Re \left[\frac{1}{\mu_1 - \mu_2} \left(\frac{\mu_1}{\sqrt{\cos\theta + \mu_2 \sin\theta}} - \frac{\mu_2}{\sqrt{\cos\theta + \mu_1 \sin\theta}} \right) \right] \\ \vec{\tau}_{xy} &= \frac{K_{\mathrm{I}}}{\sqrt{2\pi r}} \Re \left[\frac{\mu_1 \mu_2}{\mu_1 - \mu_2} \left(\frac{1}{\sqrt{\cos\theta + \mu_1 \sin\theta}} - \frac{1}{\sqrt{\cos\theta + \mu_2 \sin\theta}} \right) \right] \end{aligned} \tag{3.5}$$

Here, r and θ are the polar coordinates of the point near the tip in the crack tip local coordinate system, $\Re$ denotes the real part of complex numbers, and μ_1 and μ_2 are the roots of the characteristic equation, and are dependent on the component of the the compliance matrix:

$$S_{11}\mu^4 - 2S_{16}\mu^3 + \left(2S_{12} + S_{66}\right)\mu^2 - 2S_{26}\mu + S_{22} = 0 \tag{3.6}$$

This characteristic equation always has complex or pure imaginary roots which appear in conjugate pairs as μ_1, $\bar{\mu}_1$ and μ_2, $\bar{\mu}_2$. Let us now consider the stress variation along the crack ligament ($\theta = 0$):

$$\sigma_x = \frac{K_\mathrm{I}}{\sqrt{2\pi r}} \Re \left[-\mu_1 \mu_2 \right], \qquad \sigma_y = \frac{K_\mathrm{I}}{\sqrt{2\pi r}}, \qquad \tau_{xy} = 0 \tag{3.7}$$

This equation shows the shear stress is zero along such path, and the stress component σ_y does not explicitly depend on the material properties. On the other hand, according to the solution by Sih et al. (1965), the stress intensity factor for a central crack in an infinite anisotropic medium with remote stress of σ applied normal to the crack is given by $K_\mathrm{I} = \sigma\sqrt{\pi a}$. This formula is identical to the one obtained for isotropic materials, which indicates that for a central crack, the material constants of the anisotropic medium do not influence σ_y along the crack ligament.

As it was mentioned in Section 3.3.1, the two main models used for the estimation of the size of the inelastic zone are the Irwin approach, and the strip-yield model with uniform and linear closing stresses along the FPZ. Both models use the stress component σ_y along the crack ligament to obtain estimations of the inelastic zone. Since this component of stress is not influenced by the material constants according to Eq. (3.7), both models can be readily extended to anisotropic materials without any modification. Table 3.8 presents the size of the process zone obtained from these two models in comparison with the experimental results. The theoretical prediction are based on the average measurements of fracture toughness and strength given in Tables 3.4 and 3.6. It is evident from the results that the Irwin model and the strip-yield model with uniform closing stress underestimate the length of the FPZ, whereas the strip-yield model with a linear closing stress overestimate the FPZ length.

Table 3.8 The comparison of the FPZ length obtained from the experimental results with the theoretical models. Length values are in *mm*.

φ	Theoretical Models			Experiment
	Irwin	Strip-yield uniform traction	Strip-yield linear traction	
	$L_\mathrm{I} = \frac{1}{\pi}\left(\frac{K_\mathrm{Ic}}{\sigma_t}\right)^2$	$L_{\mathrm{S_u}} = \frac{\pi}{8}\left(\frac{K_\mathrm{Ic}}{\sigma_t}\right)^2$	$L_{\mathrm{S_l}} = \frac{9\pi}{32}\left(\frac{K_\mathrm{Ic}}{\sigma_t}\right)^2$	
0°	5.4	6.6	14.9	10.8
90°	4.1	5	11.3	8.8
Ratio		1.32		1.23

These results give an interesting insight about the type of the micro-damaging that occurs in the FPZ. Since the experimental results give values in between the predictions of the strip-yield model with uniform and linear closing (cohesion) stress distribution, it is expected the cohesion stress in reality distributes nonlinearly with higher gradient near the crack tip as shown in Figure 3.11. This means that the gradient of the micro-damaging and reduction of strength is much higher near the tip than towards the end of the process zone. These experimental results give supporting evidence to the fact that a non-linear distribution is more realistic than uniform or linear variation of the cohesion.

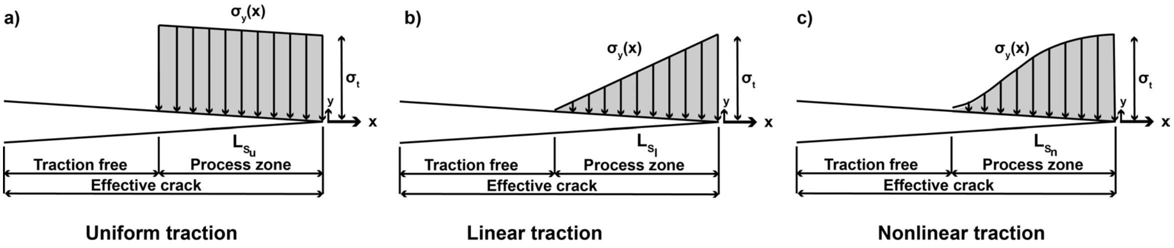

Fig. 3.11 Schematic of models with uniform, linear and nonlinear distributions of cohesion stress along the FPZ. A cohesive model based the nonlinear distribution matches the experimental results better than the uniform and linear types.

Let us now compare the ratio of the process zone obtained for the principal directions. Both models predict the same ratio of the FPZ length at two configurations $\varphi = 0^\circ$ and $\varphi = 90^\circ$ from:

$$\frac{L^{\varphi=0^\circ}}{L^{\varphi=90^\circ}} = \left(\frac{K_{\mathrm{Ic}}^{\varphi=0^\circ}}{K_{\mathrm{Ic}}^{\varphi=90^\circ}}\right)^2 \times \left(\frac{\sigma_t^{\varphi=90^\circ}}{\sigma_t^{\varphi=0^\circ}}\right)^2 \tag{3.8}$$

Using the measured values of fracture toughness and strength, one can predict the ratio of the FPZ length at two principal directions, and compares it with the experimental results of the FPZ size:

$$\left(\frac{L^{\varphi=0^\circ}}{L^{\varphi=90^\circ}}\right)_{\text{Model}} = 1.32, \qquad \left(\frac{L^{\varphi=0^\circ}}{L^{\varphi=90^\circ}}\right)_{\text{Experiment}} = 1.23 \tag{3.9}$$

Eq. (3.9) shows that there is a very good agreement between the results obtained directly from the experiments, and the ones calculated from the models predicting the size of the process zone. This gives supporing evidence that the FPZ length is in fact proportional to the square of the fracture toughness to strength ratio: $L \propto \left(K_{\mathrm{Ic}}/\sigma_t\right)^2$. The proportional constant depends on the details of the damaging processes in the FPZ.

It is worth noting that the large FPZ size obtained for granodiorite samples in this study demonstrates the development of a large nonlinear zone ahead of the crack tip. One important implication of this finding is that the LEFM concept may not be applicable to small samples since a large portion of the sample deforms nonlinearly. The tests conducted in this research follow the size requirements of the ISRM suggested method (Kuruppu et al., 2014): $D \geq 2(K_{Ic}/\sigma_t)^2$. Based on the measured strength and fracture toughness values, the requirement for the minimum diameter of the samples are $D = 34$ mm for $\phi = 0^\circ$ and $D = 26$ mm for $\phi = 90^\circ$, which is significantly lower than the diameter of the samples $D = 82.9$ mm. The suggested size requirement assures the full development of the FPZ in order to obtain reliable values of the fracture toughness. This raises an important question: Is the LEFM valid for the entire range of sizes that are acceptable based on the size requirement of the ISRM suggested method? Further research is welcome to answer this question.

In addition, such big FPZ size also questions one-parameter fracture propagation criteria to be applicable for such rocks. These criteria are formulated based on only singular terms of the crack tip asymptotic fields, and the higher order terms are ignored based on an assumption of small process zones. However, many experimental studies have demonstrated the significance of the higher order terms to be included in the fracture growth criteria for rocks with large process zones (Aliha et al., 2010, 2012; Ayatollahi and Aliha, 2008; Smith et al., 2001). Ayatollahi and Akbardoost (2012), and Akbardoost and Ayatollahi (2014) explained the dependency of the fracture toughness on the specimen size using a multi-parameter fracture criterion.

It is important to emphasize that the tensile strength results in this research are obtained indirectly from the Brazilian disk test. Experimental results show that the Brazilian test overestimates the true tensile strength, perhaps due to the applied compressive stress parallel to the loading axis in the BD test. Nevertheless, the Brazilian tensile strength still gives reasonable estimates of the true tensile strength of rock (Perras and Diederichs, 2014). We should note that the tensile strength of the rock material in the FPZ may also in essence differ from the true tensile strength of rock. This is because the rock material in the process zone is under a biaxial state of the stress and not a uniaxial one. In fact, the stress component parallel to the crack, called T-stress, is negative for the SCB specimen configuration used in this study (Ayatollahi and Aliha, 2007). Hence, the nature of the failures in the SCB and BD are in fact similar in the sense that a compressive stress is applied parallel to the failure plane. In this case, strength obtained from the BD test may be more representative of the failure in the FPZ rather than the true tensile strength obtained from direct tests.

3.8 Conclusions

- Experimental results of Grimsel Granodiorite samples show anisotropy ratios of 2.27 and 2.61 for fracture toughness and Brazilian tensile strength, respectively. This indicates that the resistance against material failure is significantly higher in the direction normal to the foliation plane compared to the direction of the foliation plane.

- The post-mortem analyses shows significant difference of fracture path and surface characteristics between the two principal directions. The fracture surface shows higher roughness and more deviation from the expected path in the direction normal to the foliation compared to the direction along the foliation.

- The averaging scheme proposed for the measurement of the FPZ from DIC results calculates the width of the FPZ accurately, whereby the results from the strain and displacement fields match very well.

- The DIC results confirms the development of a semi-elliptical fracture process zone with an average length to width ratio of about two for both principal directions. These results agree well with the available results in the literature which suggest a ratio between two to four.

- The boundary of the FPZ fully forms at about 70% of the pre-peak load for crack oriented along the foliation plane, while about 90% of pre-peak load is required for crack oriented normal to the foliation. Above these load levels and before the crack extension occurs, micro-crack activation and coalescence is constrained within the boundary of the FPZ.

- Theoretical models of Irwin and strip-yield with uniform cohesion stress distribution underestimate the length of the FPZ. These models are based on the plastic deformation near the crack tip, and one can expect they underestimate the length of the FPZ for quasi-brittle materials in which the inelastic deformation is strongly dominated by damage rather than plasticity. On the other hand, it is found the strip-yield model with a linear cohesion stress distribution overestimate the length of the process zone. The experimental results give supporting evidence to the fact that a nonlinear cohesion stress distribution provides a more accurate cohesive model that agrees better with the experimental results.

- The ratio of the FPZ length in two principal directions agrees very well with the theoretical predictions. This gives supporting evidence to the proportionality of the FPZ length with respect to the square of fracture toughness to tensile strength: $L \propto \left(K_{\mathrm{Ic}}/\sigma_t\right)^2$, where the proportionality constant can be obtained from theoretical models or experiments.

Acknowledgement

The ISC is a project of the Deep Underground Laboratory at ETH Zurich, established by the Swiss Competence Center for Energy Research - Supply of Electricity (SCCER-SoE) with the support of the Swiss Commission for Technology and Innovation (CTI). Funding for the ISC project was provided by the ETH Foundation with grants from Shell and EWZ and by the Swiss Federal Office of Energy through a P&D grant. Nathan Dutler is supported by SNF grant no. 200021_165677. The DIC system from the Composite Materials and Adaptive Structures laboratory was acquired through the SNF R'Equip grant no. 206021_150729. The authors like to thank Claudio Madonna for using the Rock Deformation Laboratory and Nils Knornschild, Thomas Mörgeli and Thomas Good for their help for equipments, sample preparation and testing.

Chapter 4

Hydraulic fracture propagation in a heterogeneous stress field in a crystalline rock mass

The monitoring setup was designed by V.G., J.D. M.J. and F.A. The injection protocol and operation planning were designed by N.D. and B.V. All the authors were part of the data acquisition team during the HF experiments of the ISC project, where F.A. was the project administrator. The formal analysis, data curation and data visualization inclusive writing the original draft preparation was done by N.D with help of B.V. The writing—review and editing was done by V.G., L.V. H.K. J.D. B.B. M.J. and F.A. The supervision and funding acquisition for this work was done by B.V.

Please cite this chapter as: Dutler, N., Valley, B., Gischig, V., Villiger, L., Krietsch, H., Doetsch, J., Brixel, B., Jalali, M., and Amann, F.: Hydraulic fracture propagation in a heterogeneous stress field in a crystalline rock mass, Solid Earth, 10, 1877–1904, https://doi.org/10.5194/se-10-1877-2019, 2019.

Abstract

As part of the In-situ Stimulation and Circulation (ISC) experiment, hydraulic fracturing (HF) tests were conducted in a moderately fractured crystalline rock mass at the Grimsel Test Site (GTS), Switzerland. The aim of these injection tests was to improve our understanding of processes associated with high-pressure fluid injection. A total of six HF experiments were performed in two inclined boreholes, where the surrounding rock mass was accessed with twelve observation boreholes, which allow high-resolution monitoring of fracture fluid pressure, strain and micro-seismicity in an exceptionally well-characterized rock mass. A

similar injection protocol was used for all six experiments to investigate the complexity of the fracture propagation processes. At the borehole scale, these processes involved newly created tensile fractures intersecting the injection interval while at the cross-hole scale, the natural network of fractures dominated the propagation process. The six HF experiments can be divided into two groups based on their injection location (i.e., south or north to a brittle ductile shear zone), their similarity of injection pressures and their response to deformation and pressure propagation. The injection tests performed in the south connect upon propagation to the brittle ductile shear zone. Thus, the shear zone acts as a dominant drain and a constant pressure boundary. The experiments executed north of the shear zone, show smaller injection pressures and larger backflow during bleed-off phases. From a seismic perspective, the injection tests show high variability in seismic response independent of the location of injection. For two injection experiments, we observe re-orientation of the seismic cloud as the fracture propagated away from the wellbore. In both cases, the main propagation direction is normal to the minimum principal stress direction. The re-orientation during propagation is interpreted to be related to a strong stress heterogeneity and the intersection of natural fractures striking different than the propagating hydraulic fracture. The seismic activity was limited to about 10 m radial distance from the injection point. In contrast, strain and pressure signals reach further into the rock mass indicating that the process zone around the injection point is larger than the zone illuminated by seismic signals. Furthermore, strain signals indicate not just single fracture openings but also the propagation of multiple fractures. Transmissivities of injection intervals increase about 2-4 orders of magnitudes.

4.1 Introduction

Hydraulic fracturing (HF) is a technology based on the initiation and propagation of tensile cracks in rock from a wellbore using high-pressure fluid injections. It is used to promote fluid flow through newly-created permeable fractures with the goal to extract energy (heat or hydrocarbons) from the subsurface in formations with insufficient natural permeability (Economides and Nolte, 2000). Massive hydraulic fracturing technology is often used in the oil and gas industry (Economides and Nolte, 2000) and in applications in the context of enhanced geothermal projects (Brown et al., 2012). Other applications of HF involve the preconditioning of ore bodies with low fracture density (e.g. to induced block caving; Jeffrey et al., 2013; van As and Jeffrey, 2000) and various applied industrial projects, for which a detailed understanding of the stress state is needed (e.g. to optimize the design of an underground facility or pressure tunnels in hydropower; Haimson and Cornet, 2003; Hubbert and Willis, 1957). Furthermore, fluid driven fracturing also occurs naturally, for instance in kilometer-long dikes that transfer magma from deep underground chambers to the Earth's surface or as sills between two older horizontal layers (Lister and Kerr, 1991; Rubin, 1995; Spence and Sharp, 1985).

The context of our study is the exploitation of geothermal energy using an approach known as Enhanced Geothermal Systems (EGS). A central aspect of the EGS technology are stimulation operations to develop the reservoir permeability prior to heat exploitation, because the crustal permeability is generally insufficient at depth (Manning and Ingebritsen, 1999). Stimulation approaches include hydraulic stimulation, thermal stimulation and chemical stimulation. For hydraulic stimulation, two prevalent processes for permeability creation can be distinguished: 1) hydraulic fracturing (HF) as the initiation and propagation of tensile fractures and 2) hydraulic shearing (HS), i.e., the reactivation of pre-existing fractures that support shear stress, which promotes shear failure with associated irreversible dilation. These end-members are not mutually exclusive and a combination is possible: McClure et al. (2014) (McClure and Horne, 2014) suggested combined hydraulic stimulation mechanisms such as primary hydraulic fracturing with shear stimulation leak off or mixed-mechanism stimulation. Stimulations in the context of EGS often take place along open borehole sections of several hundred meters (Brown et al., 2012). Such stimulation treatments are usually controlled by the most permeable fractures that are often critically stressed (Barton et al., 1995), and hydraulic shearing becomes the dominant mechanism for permeability creation, at least several tens of meters distance away from the injection interval (Evans et al., 2014). Since this usually does not result in the desired permeability increase, the stimulation intervals can be reduced with packers and thus the injection flow can be controlled zonally. In proposed EGS concepts that includes multi-stage hydraulic stimulation of multiple shorter borehole intervals (e.g. Meier et al., 2015), the initiation and propagation of tensile fractures may become an important mechanism in the near field of the wellbore to connect the wellbore to the pre-existing fracture network and to increase the swept reservoir volume.

Thus, the motivation of this work is to better understand hydraulic fracture initiation and propagation in crystalline rock, as well as the influence of pre-existing geological features and stress heterogeneities on the HF processes. To this end, we performed a series of six extensively monitored HF experiments in the underground laboratory of the Grimsel Test Site in May 2017 (Amann et al., 2018). The first experiments series – six hydraulic shearing tests targeting pre-existing fractures – were performed a few months earlier in February 2017 and are presented by Krietsch et al. (2020). Both experiment series were accompanied by monitoring of induced seismicity, the results of which are presented by Villiger et al. (2020).

4.1.1 Intermediate scale experiments

There are only a few examples of in-situ HF experiments performed in crystalline rock at the deca- to hectometer scale, for example the experiments performed at the Nevada test site (Warpinski, 1985), at Northpark mine (Jeffrey et al., 2009) and in the Aspö Hard Rock Laboratory (López-Comino et al., 2017; Zang et al., 2017). New experiments are being executed or planned at the Homestake mine (EGS collab project; Kneafsey et al., 2018), at the Bedretto

Underground Laboratory for Geoenergy research (BULG; Hertrich and Maurer, 2019) and at the Reiche Zeche Underground Laboratory (STIMTEC; Dresen et al., 2019). All experiments differ in terms of the in-situ geological and stress conditions, and also in terms of injection protocols and monitoring concepts.

The Northpark experiment was executed with relatively large injection volumes and rates (max. 16 m^3 and 320 l/min), and included a mine-back of the stimulated volume. However, microseismic monitoring was very limited. Thus, seismic events could not be detected in the immediate vicinity of the stimulated fractures. The results of the study illustrate that 1) the stress state is decisive of the overall geometry of the stimulated volume and that 2) the pre-existing fracture network defines the development of the newly created flow paths (Jeffrey et al., 2009). The Nevada test site experiment also included mine-back of the rock volume and highlighted the complexity and tortuosity of the flow path of a hydraulic fracture (Warpinski, 1985; Warren and Smith, 1985). At Aspö, one of the focus was testing the hypothesis that using alternative injection strategies, as for example repeated progressively increasing and cyclic pressurization, may help reducing the number and magnitudes of seismic events. Zimmermann et al. (2019) show results that tend to support this hypothesis, where the cyclic fracturing net pressure seems to lead to a lower seismicity but increases the permeability, although the number of tests is not statistically sufficient. They also show that the maximum magnitude in each fracture phase appears to be correlated to the injected volume in agreement with McGarr (2014) assumption.

4.1.2 Complex hydro-mechanical response

A central aspect of our study focuses on the complex hydromechanical coupling occurring during fracture initiation and propagation, for which fluid pressure and deformation data are key parameters. The pressure response at the injection point has been used to quantify pressure-sensitive permeability changes (Louis et al., 1977) or for stress estimations (Doe and Korbin, 1987; Evans and Meier, 1995; Rutqvist and Stephansson, 1996). Rutqvist (1995) and Rutqvist et al. (1998) combined hydraulic jacking tests with numerical modeling to determine the in-situ normal stiffness of natural fractures or faults in crystalline rock. Hydraulic jacking tests were conducted by a step-wise increase in injection interval pressure. It was concluded that during hydraulic injection into a single fracture in granite, the storativity depends solely on the fracture's normal compliance. Moreover, it depends in turn on the stiffness of both the rock mass and the fracture. Numerical analysis of these tests showed that the flowrate at each pressure step is strongly dependent on the aperture and normal stiffness of the fracture in the vicinity of the injection interval (Rutqvist and Stephansson, 2003). The borehole injection pressure and the injection rate allow the direct estimate of the injectivity of the injection interval, which is again related to the fracture and rock compliance in the stimulated interval.

4.1.3 Seismic response and seismic cloud

Induced seismicity accompanies hydraulic stimulation and can be detrimental to deep geothermal projects when magnitudes of induced earthquakes are perceptible to the public (Ellsworth, 2013; Evans et al., 2012). However, in many industrial projects in the context of both hydrocarbon and heat extraction, including this study, it is an indispensable tool that is used to map the stimulated fracture system (Maxwell et al., 2010; Niitsuma et al., 1999; Warpinski et al., 2013). When the hydraulic fractures propagate beyond the vicinity of the injection point, they will inevitably interact with natural fractures to some degree. Induced microseismicity (on a small scale also called acoustic emissions) occur as located brittle-failure processes during high-pressure fluid injection and can be used to approximate the geometry of a single hydraulic fracture or a fracture network. Nolen-Hoeksema and Ruff (2001) proposed three mechanisms that may produce seismicity during hydrofracturing: 1) Tensile failure at the fracture tip, 2) the stress concentration at the fracture tip causing shear slip along suitably oriented pre-existing fractures and, 3) fluid leak off into pre-existing fractures rising the fracture fluid pressure inducing slip if they support sufficient shear stress. The tensile failure at the tip is typically aseismic or at least radiates a small amount of energy. Mechanism two and three are often seen as the main processes leading to induced seismicity during hydraulic fracturing (e.g. Martínez-Garzón et al., 2013; Rutledge et al., 2004; Warpinski and Branagan, 1989). Thus, induced seismicity does not represent the propagating fracture itself, but is indicative of the hydraulic fracture propagation as it tracks the propagating fracture. Many experiments on different scales in laboratory and under in-situ conditions showed that the seismicity cloud has a tendency to be oriented normal to the minimum principal stress (σ_3) direction (Evans et al., 2005; Häring et al., 2008; Hubbert and Willis, 1957; Rutledge et al., 2004). Majer and Doe (1986) concluded from the occurrence rate, spatial and temporal distribution of the microseismic events, that the hydro-fracture growth pattern does not follow an often-assumed single and symmetric fracture path. In fact, the one "hydraulic fracture" is actually made of multiple fractures.

4.1.4 Our contribution

A detailed characterization of the stress state as well as a geological, hydrological and geophysical characterization of the experimental rock volume took place before the main injection experiments were executed. The in-situ hydraulic fracturing experiment presented here along with detailed pressure, deformation and seismic monitoring were designed to address the following research questions:

- What is the injection pressure response at the injection interval and at pressure observation intervals in the rock volume?
- What is the rock deformation response to high pressure fluid injection?

- How does permeability increase in response to HF processes?
- How does the microseismic cloud propagate and what is the best description of the fracture geometry? Does the borehole trace of the hydraulic fracture match the late-time geometry? How does the outcome vary related to the volume of injected fluid?
- How can we describe the stress state during fracture propagation? Does it change?

4.2 Site and rock mass characterization

Our detailed rock mass characterization included geological mapping, hydrological and geophysical testing, as well as in-situ stress measurements.

4.2.1 Site description

The experiment took place in the Grimsel Test Site (GTS), which is operated by the Swiss National Cooperative for the Disposal of Radioactive Waste (NAGRA). The GTS is situated $\sim$450 m below the Western flank of the Haslital valley. The ISC test volume is located in the southern part of the Grimsel Test Site and is accessible by the AU and VE tunnels (Fig. 4.1). Prior to the ISC experiments, two injection boreholes (INJ1 and INJ2) were drilled from the AU cavern, which were used for the actual high-pressure fluid injections. In addition, another ten boreholes were drilled to access the rock mass for monitoring purposes: Three boreholes (PRP) were used to monitor fluid pressure, another three boreholes (FBS) were used for strain measurement. The remaining four boreholes (GEO) were used for geophysical measurements during injections such as monitoring the seismic activity or to perform active seismic tests. Three additional boreholes (SBH) were drilled prior to the stimulation experiment during the stress characterization campaign in 2015. A detailed description of the installation of permanent downhole instrumentation systems is provided in a technical description of the ISC Experiment (Doetsch et al., 2018b).

4.2.2 Geological characterization

The ISC test volume is situated slightly south of the boundary between Central Aare Granite (towards north) and Grimsel Granodiorite (towards south). Alpine deformation and metamorphism overprinted both lithologies, resulting in a pervasive foliation oriented 157/75° (dip direction/dip given in xxx/xx°) (Keusen et al., 1989). See Wenning et al. (2018) for a detailed description of the rock mass in the GTS vicinity and its deformation history, including a comprehensive reference list. Tunnel mapping in the AU, VE and AU-UP gallery was conducted to identify the main structures. The 15 boreholes drilled as part of the ISC project were logged with an optical televiewer to provide quantitative and qualitative information on the lithology, foliation, and

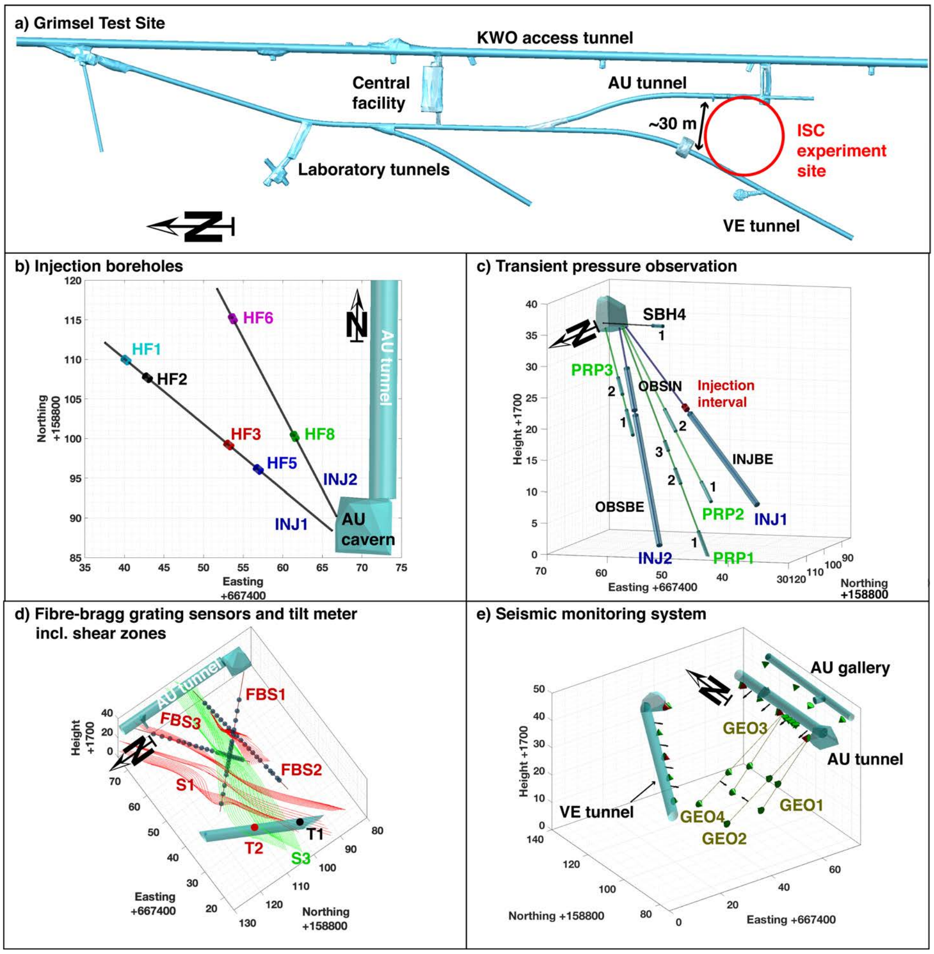

Fig. 4.1 a) The ISC experiment site is indicated in the south of the Grimsel test site laboratory facility. b) The AU cavern, the AU tunnel and the injection interval locations in the two injection boreholes are shown and numbered. c) Transient pressure observation intervals in 6 different boreholes. d) Rock mass monitoring systems like Fiber-Bragg Grating (FBG) sensors are indicated by blue circles in the three FBS boreholes and tilt meter are indicated by T1 and T2. The two different shear-zones S1 and S3 are indicated by red respective green. e) The seismic monitoring system consists of accelerometers (red cones) and acoustic emission sensors (green cones) with eight sensors placed in four geophysical monitoring boreholes. Coordinates on figure b) to e) are referenced to the Swiss metric coordinate system (CH1903).

fractures. Based on these data the main pre-existing shear zones have been interpolated within a 3D geological model (Fig. 4.2b).

The moderately fractured rock mass is crosscut by two sets of shear-zones that differ in terms of deformation history and orientation. The first set (referred to as S1.0, S1.1, S1.2, and S1.3) included four ductile shear zones that are characterized by a strong increase in the degree of foliation and mylonitization. All four shear zones have an ENE-WSW strike and dip towards SE. These shear zones experienced retrograde brittle deformation and thus contain few discrete brittle fractures. The second set (referred to as S3.1 and S3.2) contains two brittle-ductile shear zones. The S3 brittle-ductile shear-zones consist of a densely fractured zone (>10 fractures per meter) in between two biotite-rich meta-basic dykes.

The three lower hemisphere equal-area pole stereonet with Kamb contour plots presenting each fracture as a pole point within the host rock and the associated shear zone S1 and brittle-ductile shear zone S3 (Fig. 4.2a). The pole points for the host rock and the S1 shear zone indicates a fracture system with a consistent horizontal NNW orientation with a tendency of higher variation in the host rock. The fractures of the ductile-brittle S3 shear zone indicate two different fracture systems (Fig. 4.2a).

Figure 2d) shows the fracture frequency, corrected into volumetric fracture density (p32) to account for sampling biases (see Brixel et al., 2020a, for the correction), for the two injection boreholes, which indicates a moderately fractured rock mass. The fracture frequency in the INJ boreholes is 0-3 fractures per meter, with higher frequency towards the shear zones. All obtained geological data and the interpolated 3D model were published by Krietsch et al. (2018).

Stress characterization

Details of the stress characterization campaign are given by Krietsch et al. (2019). Impression packers and microseismic monitoring were used to map hydraulic fracture orientation, which revealed consistent E-W, sub-vertical fracture extension. The averaged stress field in relatively unperturbed rock (i.e. with little fracture density) about 8 m from the S3 shear zones (Fig. 4.1c) and the perturbed stress field are summarized in Table 4.1. Hence, the minimum principal stress magnitude, measured in the sub-horizontal borehole SBH4 approaching the S3 shear-zone at the borehole bottom, reduces towards the S3 shear zone (Krietsch et al., 2019). This study will show that the perturbed stress state can be extended from the S3 brittle-ductile shear zone towards the S1 shear zone. The two main changes compared to the perturbed stress field are 1) a primary 30° clockwise rotation accompanied with a decrease of the major principal stress dip and 2) a permutation of the intermediate and minimum stress axis.

Table 4.1 Summary of the unperturbed and perturbed stress state

Stress state	Magnitude			Dip direction/dip		
	σ_1 [MPa]	σ_2 [MPa]	σ_3 [MPa]	dd_1/d_1	dd_2/d_2	dd_3/d_3
unperturbed	14.4	10.2	8.6	104/39°	259/48°	004/13°
perturbed	13.1	8.2	6.5	134/14°	026/50°	235/36°

Figure 4.2c) presents the Mohr-Coulomb circle for the unperturbed stress state considering the observed hydrostatic formation pressure of 0.3 MPa. Four different failure limits are presented between 7 and 10 MPa overpressure, assuming a friction coefficient of 0.8 and no cohesion.

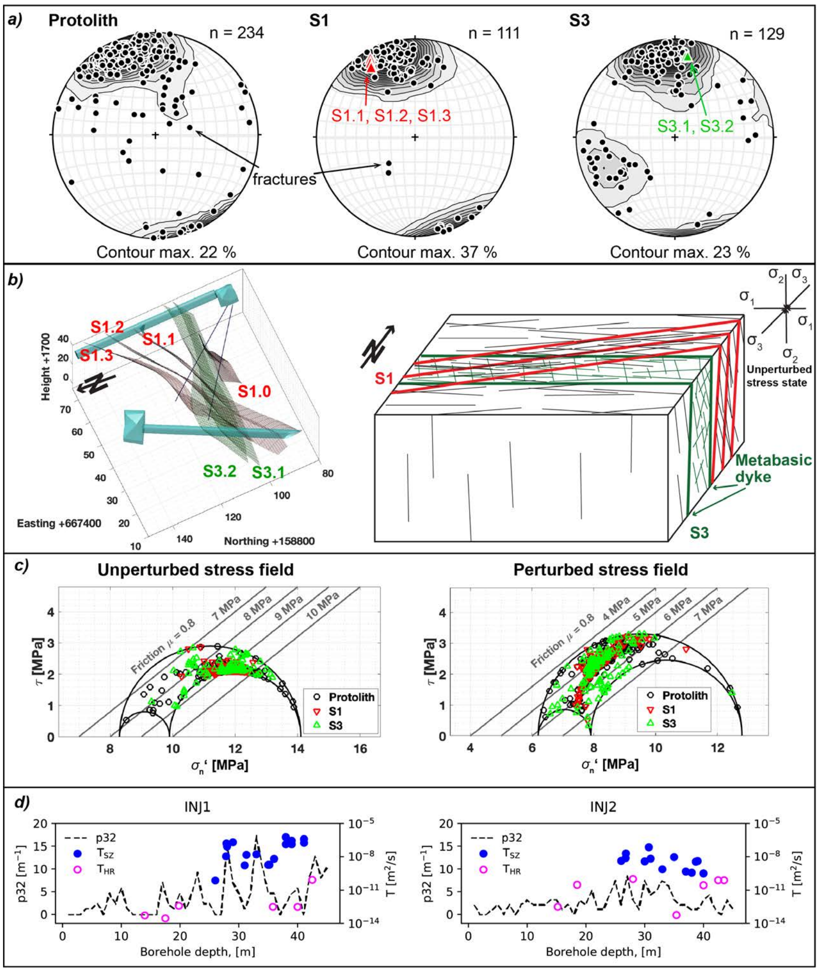

Fig. 4.2 a) Kamb contour plots of fracture orientation projected on a lower hemisphere equal-area pole stereonet for the intact rock (host rock), the ductile shear zone S1 and the brittle-ductile shear zone S3. b) Geological model and block model for the ductile shear zones S1 respective the brittle-ductile shear zone S3. The models indicate the different fracture systems associated with the two shear zones. c) Mohr–Coulomb diagram representing the unperturbed and perturbed stress field estimate by Krietsch et al. (2019) (including hydrostatic pressure of 0.3 MPa). The failure limits assuming a friction coefficient of 0.8. The identified and allocated fractures from borehole logging in all 15 boreholes are presented to indicate possible failure at a specific pore pressure (grey solid lines). d) The black dashed line indicates the volumetric fracture intensity calculated over 1 m intervals for both injection boreholes INJ1 and INJ2. The magenta open and blue filled points indicate the position of well tests with the resulting transmissivities from fractured (T_{SZ}) and intact rock (T_{HR}).

Fractures and faults mapped from all 15 boreholes are sorted in three categories based on their relation to the main S1 or S3 structures and presented to estimate their criticality due to the fluid pressure increase. Structures favorably oriented for failure will fail with overpressures ranging from 8 to 10 MPa. All the HF experiments are located around the S3 shear zone, which influences the stress field as observed during the stress characterization campaign. To investigate this effect a Mohr-Coulomb circle for the perturbed stress state is presented and the failure limits are indicated for 4 to 7 MPa overpressure. The perturbed stress field would allow shearing of structures above 4.5 MPa overpressure, which is significantly below the observations from the unperturbed stress state. It is not clear, which of the two observed stress states describe the injection into the rock volume approaching the S3 and S1 shear zones best. The experiments executed in borehole SBH4 approaching the S3.1 shear zone indicate the change towards the perturbed stress state.

Hydraulic characterization

Multiple field tests were performed to characterize hydraulic conditions at and near the injection borehole pair, including dilution tests, single-hole and cross-hole hydraulic tests. The transport properties of the conductive fractures were characterized using salt and DNA tracer tests (Jalali et al., 2018b). An overview of the hydrogeological baseline conditions for the ISC project is presented by Brixel et al. (2020a). Hydrogeological conditions prior to the hydraulic fracturing experiment may be summarized as follows:

- The transmissivity of the intact injection intervals (defined here as intact lithology by the absence of visually detected brittle deformation on cores and borehole image logs) was estimated through hydraulic pressure pulse tests and range from 10^{-13} to $10^{-11}\mathrm{m}^2/\mathrm{s}$ (pink circles in Fig. 4.2d). In injection intervals intersected by shear zones, constant rate injections (CRI) or pulse injections (PI) indicate higher transmissivity values in the order of 10^{-6} to 10^{-13} m^2/s (blue dots in Fig. 4.2d). The geometric average transmissivity of the host rock is estimated to be 10^{-11} m^2/s.
- The estimated transmissivities are in good correlation with the fracture intensity in the injection borehole INJ1 (Figure 4.2d, left), although the spatial resolution of our hydraulic measurements do not permit to capture all fracture intensity peaks. These measurements are also dependent on the natural heterogeneities, particularly related to the S1 shear zones. More details on these complex relations can be found in Brixel et al. (2020a).
- Within the brittle fractured zone between the two S3 shear zones an average discharge into the GTS tunnel of $\sim$60 ml/min was measured prior to the injection experiments.
- Based on the characterization tests conducted, the fractured zone between and along the two S3 metabasic dykes provide the most conductive, natural flow pathways between the two injection boreholes. This observation agrees well with the existence of two different fracture systems in the S3 shear zone: (i) one set following the main NE-SW alpine foliation orientation and (ii) one set abutting on the two S3 dykes at high angles, which we identified as the alpine tension gashes commonly mapped between dyke swarms throughout the Grimsel Test Site (Figure 4.2a, right). This rock volume contains open fractures with high transmissivity (i.e. extension fractures), whereby the transport of

solutes, salt and DNA tracers between the two injection boreholes show a preferential pathway towards the gallery rather than towards the INJ1 borehole for the case of injection into INJ2 (Jalali et al., 2018b).

4.3 Field setup and monitoring

Hydraulic fracturing experiments conducted within this study were accompanied by an extensive monitoring program including measurements of rock deformation, fracture fluid pressure and microseismicity. In the following sections, we introduce the hydraulic fracturing equipment and the monitoring systems.

4.3.1 Hydraulic fracturing equipment

The HF interval was isolated using a hydraulic double-packer system with a 1 m long pressurization interval. Two different triplex pumps (brand SPECK Pumpen) were used to deliver 1) a pressure up to 30 MPa at a flowrate up to 35 l/min and 2) a flowrate up to 100 l/min at a maximal pressure of 10 MPa. The first pump was used to breakdown the formation and for the first propagation cycle. Then, the pump was switched to reach flowrates up to 100 l/min. A second double-packer system was installed to monitor the fluid pressure response in the monitoring interval in the second injection borehole that was not used for active stimulation. A data acquisition system recorded the pressure in the open intervals of the INJ boreholes, the flowrate in the injection interval and the packer pressure in the injection and monitoring intervals with a sampling rate of 20 Hz. Fluid pressure was also monitored in the intervals beneath the injection and monitoring intervals with a sampling rate of 1 Hz. The injected fluid and the backflow were measured with different flowmeters depending on expected flowrates with a sampling rate of 20 Hz. Figure 4.1b) presents the position of the six injection intervals along the two injection boreholes INJ1 and INJ2. As a visual aid, we used consistent color throughout the paper to display data from a specific HF experiment. The execution times and the intervals for all experiments are summarized in Table 4.2.

Table 4.2 Overview of the executed experiment and borehole location, depth of testing interval and observation depth interval.

Experiment	**Date**	**Start time**	**End time**	**Injection borhole**	**Interval start [m]**	**Interval end [m]**	**Observation borehole**	**Interval start [m]**	**Interval end [m]**
HF1	15.05.2017 16.05.2017	13:30 07:30	16:30 11:00	INJ1	40.0	41.0	INJ2	19.6	27.3
HF3	16.05.2017	13:45	16:00	INJ1	19.8	20.8	INJ2	8.3	17.0
HF2	17.05.2017	08:00	11:00	INJ1	35.8	36.8	INJ2	8.3	17.0
HF5	17.05.2017	11:30	14:00	INJ1	14.0	15.0	INJ2	8.3	17.0
HF6	18.05.2017	08:00	12:15	INJ2	38.4	39.4	INJ1	23.9	32.9
HF8	18.05.2017	13:00	15:30	INJ2	15.2	16.2	INJ1	23.9	32.9

4.3.2 Monitoring systems

The pressure monitoring system was designed to observe transient pressure response at specific locations to track pressure propagation throughout the rock mass, either through natural fractures or newly created ones. Customized grout packer systems were installed in the PRP monitoring boreholes. The open intervals were packed and separated with hydro-mechanical packers supplement with resin. The uppermost interval was filled with grout to ensure low compressibility of the system. Open hole sections are shown as blue cylinders in Figure 4.1d. The sections PRP1-1, PRP2-1 and PRP3-1 are positioned within shear zone S1 and all the other intervals are positioned within shear zone S3. The pressure sensors (PAA33-X Keller) were connected to the Solexpert data acquisition system running the Solexpert GM-HF software with a maximum sampling rate of 20 Hz. The possible pressure range of the pressure sensors was 10 MPa with a resolution < 1 kPa. The raw pressure data from HF stimulations are presented in the paper without any filtering.

The rock mass deformation monitoring system consists of 60 fibre-bragg grating (FBG) sensors (Type os3600 by Micron Optics Inc) in the three FBS boreholes. The FBG sensors have a base length of 1 m. 20 FBG sensors were installed along each FBS borehole to characterize the strain field in both intact and fractured rock. The sensors (including strain and temperature) are pre-strained to about 2000 microstrain such that also shortening can be recorded. The sensors were connected to an interrogator of type si255 (Hyperion Platform by Micron Optics Inc.) that can record with a sampling rate of 1 kHz, an accuracy of 0.85 microstrains and wavelength repeatability of 0.1 microstrains. The strain data presented here is not temperature corrected as it is not required for our isothermal injections. Extensional strain is negative.

Two tiltmeters (Type A711-2 by Jewell Instruments) were installed in the VE tunnel to characterize the deformation with respect to the stimulation volume. The location of each tiltmeter is presented in Figure 4.1c. The tiltmeters measure the deviation from horizontal tilt in axial (X) and normal (Y) direction to the tunnel with a resolution of 0.05 µradians after filtering with a 100 Hz low pass filter. The two horizontal tilt axis and the temperature were digitized and recorded by the data acquisition system with a sampling rate of 100 Hz. The initial value was subtracted to display the change of tilt during the HF experiment. Then, a positive tilt in x-axis implies a dip of the tunnel wall towards NNE. A positive dip in the y-axis indicates a dip of the tunnel floor towards WNW.

The seismic monitoring network consists of a total of 26 uncalibrated piezo-electric acoustic emission (AE) sensors (type GMuG Ma-Bls-7-70m) and 5 calibrated accelerometers (type Wilcoxon 736 T) (Figure 4.1e). The AE sensors have a bandwidth of 1 to 100 kHz and their highest sensitivity at 70 kHz. Eight of the AE receivers were deployed in four geophysical boreholes (GEO) in close proximity (3 – 25 m) to the injection intervals. The accelerometers have a bandwidth of 5 to 25'000 Hz with a sensitivity of 100 mV/g. The seismic data were recorded continuously throughout the experiments at a sampling rate of 200 kHz, using a 32-channel acquisition system. AE and accelerometer receiver signals were high-pass hardware filtered at 1 kHz and 50 Hz, respectively.

Based on the picked P-wave onsets, the seismic event locations were calculated using a homogeneous but transversely isotropic P-wave velocity model. For more details on the seismic monitoring and event localization, see Doetsch et al. (2018a); Gischig et al. (2018); Villiger et al. (2020). The experimental summary cards in the Supplement (Fig. A.7 to A.12) present the located seismic events and their radial distance to the injection interval. Time synchronization of all data acquisition units used for the HF injection tests was ensured using a network time protocol server.

4.4 Overview of the HF experiments

4.4.1 Injection protocol

The HF injection experiment was executed between May 15. and May 18., 2017. The injection protocol showing the injected flowrate (blue line) and the injection pressure (red line) for each HF experiment are presented in Figure 4.3. The grey shaded regions in the plots correspond to the phases of fluid injection. Prior to the first injection phase of each experiment, a pulse injection was executed to test interval integrity and packer sealing. The actual hydraulic fracturing experiment started with a rate-controlled fluid injection at approximately 5 $\mathrm{l/min}$ for ten seconds to initiate a hydraulic fracture. This formation breakdown cycle (or short: frac cycle) is indicated by the letter F in the injection protocols and consists of the fluid-injection, the pressure observation during shut-in time and fluid recovery during bleed-off time.

The two following refrac cycles RF1 and RF2 had the aim to propagate the hydraulic fracture. During these cycles, we used either water with a viscosity of 1 cP (10^{-3} Pa.s) (Fig. 4.3 a-d, experiments HF1, HF2, and HF3) or a shear-thinning fluid (xanthan-salt-water mixture or XSW) with a viscosity of $\sim$35 cPs (Figure 4.3 e-g, HF5, HF6 and HF8). The refrac cycle RF1 starts with a flowrate of 5 $\mathrm{l/min}$ which was progressively increased to 10 and 20 $\mathrm{l/min}$. Each step lasted for approximately 2 minutes or less. For the experiment with water, we performed a cyclic injection during the 20 $\mathrm{l/min}$ step. The cyclic injection consisted of a sinusoidal variation of flowrate with a period of 2.5 to 20 s and an amplitude of $\pm$ 15 $\mathrm{l/min}$. Following the 20 $\mathrm{l/min}$ injection step we increased to 35 $\mathrm{l/min}$ for 3 minutes. Then, the system was shut-in to change to the bigger pump and injection was resumed without bleed-off with a second propagation cycle called RF2.

The refrac cycle RF2 begins with a rapid increase in the flowrate to 35 $\mathrm{l/min}$ and then increased to 50 $\mathrm{l/min}$. Both flow steps were maintained for 2 min. Afterward, each step was held for 1

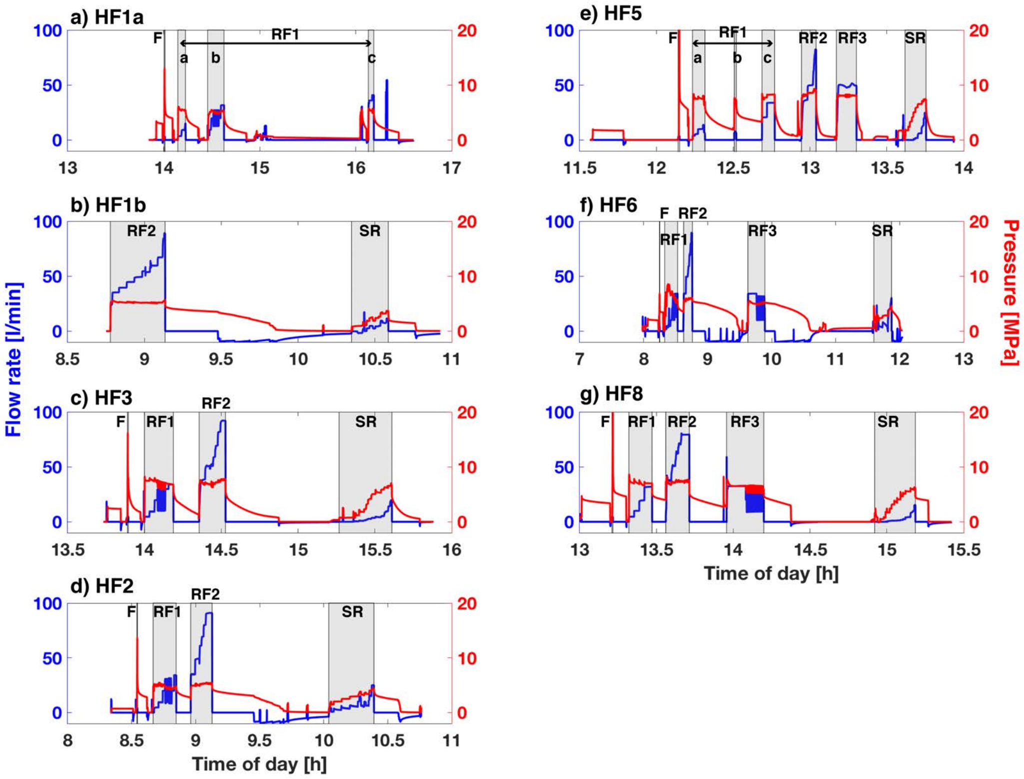

Fig. 4.3 The injection protocol of the different HF experiments is presented showing the flowrate (blue line) and the injection pressure (red line). The grey shaded sections correspond to fluid injection into the interval. Experiment HF1 was divided into two protocols due to water supply problems during the first day. The protocols a-g) follow the temporal execution in the field. For the experiments a-d) the injection fluid was water during the fracture propagation cycles (RF1-RF2) and for the experiments e-g) the injection fluid was xanthan-salt-water mixture.

min starting from 60 l/min and going up to 70, 80, 90 and 100 l/min. The system was then shut-in for several minutes to half an hour to observe the hydro-mechanical response in the system. Finally, the system was opened to allow bleed-off. The fluid recovery rate was monitored. For the HF experiments with XSW fluid (HF5, HF6, and HF8), we added a third refrac cycle RF3 with clean water with the aim of flushing out the XSW fluid. The water was injected at 35 l/min. This cycle was also an opportunity to test different cyclic injection schemes. The fluid injection was again followed by shut-in and bleed-off phases. For all experiments, the last cycle was a pressure-controlled step test (SR) to evaluate the post-stimulation injectivity of the created hydraulic fracture and to estimate the stress acting normal to the hydraulic fracture (jacking pressure) based on Doe and Korbin (1987). For the executed injection protocols, the following remarks are noted:

- Logistic problem affected the execution of HF1 experiment. The issue was an insufficient water supply. This led to several repetitions of the refrac cycle RF1. The second refrac cycle (RF2) was then executed a day later with a new installed water-supply pump delivering the necessary flowrates. Furthermore, the seismic monitoring system recorded an increased quantity of electronic interferences due to a faulty shielding of the power line between the frequency control unit and pump motor. Therefore, a seismic evaluation was not possible.
- At a flowrate of 5 l/min during the first refrac cycle of experiment HF5, a short-cut occurred to one of the open seismic monitoring boreholes (GEO1, Fig. 4.1e). For this reason, we had to interrupt RF1 and resume multiple times. This is why RF1 is subdivided in part a, b, c on Figure 4.3. Thereafter, the pump was changed to allow flowrates above 35 l/min, but the flowrate was limited to a maximum of 80 l/min and short duration due to the short-cut to the GEO1 borehole. The flushing cycle RF3 was executed with a flowrate of 50 l/min.
- The low magnitude of breakdown pressure during the frac cycle of HF6 is an indication for a pre-existing sealed fracture in the open interval. The stimulation interval was mistakenly placed 3 meters further down in the borehole at a pre-existing fracture.
- During all refrac cycles, we never exceeded an injection pressure of 10 MPa.
- Experiment HF3, HF5, and HF8 show a similar fast pressure decay during the shut-in time for the refrac cycles. The same experiments show very small fluid recovery (fluid recovery is shown as negative flowrate in Fig. 4.3) after the refrac cycle RF2 compared to the experiments HF1, HF2, and HF6.

4.4.2 Diagnostic injection parameters

Table 4.3 summarizes key observations from the injection protocol (labeling after to Fig. 4.3). The measurement of breakdown pressure, fracture reopening and instantaneous shut-in pressure (ISIP) followed the ISRM standard presented by Haimson and Cornet (2003). The breakdown pressure represents the peak pressure during injection cycle F. The instantaneous shut-in pressure (ISIP) was obtained during each cycle using the tangent method, i.e. the departure from a linear pressure decrease vs. time occurring right after shut-in (Amadei and Stephansson, 1997). The apparent re-opening pressure (P_r) was picked when the pressure change-time step-relationship starts being non-linear (Bredehoeft et al., 1976). The jacking pressure was measured during the pressure-controlled step test SR (more in the Supplement A.1). The cumulative injected water corresponds to the injected volume, V_i, indicated for each cycle and the entire experiment. The backflow was measured at the injection interval during venting. Thus, the fluid recovery V_r is only the recovery from the injection interval, however, fluid also escaped from two of the monitoring borehole (GEO) during HF5 and HF8

Table 4.3 Overview of fracture breakdown pressure (P_c) and fracture reopening pressure (P_r) and additional hydraulic test parameters (injected fluid: water (W) or Xanthan-salt-water mixture (XSW); V_i, injected volume; V_r, recovered volume) and located AE event numbers.

Stage No.	Test-Stage	Fluid	P_c & P_r [MPa]	ISIP [MPa]	V_i [l]	V_r [l]	No. of located AE
1	HF1-F	W	14.9	6.6	1.7	0.6	N/A
2	HF1-RF1	W	5.7	4.5	447.4	18.2	N/A
3	HF1-RF2	W	4.9	4.8	1066.9	337.2	N/A
4	HF1-SR	W	-	3.0	48.4	31.0	N/A
					1564.4	**24.7 %**	
5	HF2-F	W	13.95	5.5	2.8	2.3	10
6	HF2-RF1	W	4.6	5.6	170.5	-	208
7	HF2-RF2	W	4.5	4.65	646.9	226.6	313
8	HF2-SR	W	-	3.9	141.8	46.0	0
					962.0	**28.6 %**	**531**
9	HF3-F	W	16.3	7.7	1.7	1.7	0
10	HF3-RF1	W	8.0	5.6	214.4	-	26
11	HF3-RF2	W	6.7	5.7	621.1	12.7	49
12	HF3-SR	W	-	4.7	71.4	1.9	0
					908.6	**1.8 %**	**75**
13	HF5-F	W	20.5	7.9	1.9	1.0	6
14	HF5-RF1	XSW	6.9	6.0	188.6	-	13
15	HF5-RF2	XSW	6.8	6.3	274.3	0.1	0
16	HF5-RF3	W	7.25	5.9	376.8	0.2	0
17	HF5-SR	W	-	5.8	32.1	0.1	0
					873.7	**0.2 %**	**19**
18	HF6-F	W	(7.0)	5.9	2.1	1.2	0
19	HF6-RF1	XSW	6.3	4.95	171.1	-	0
20	HF6-RF2	XSW	5.3	5.5	467.4	310.8	26
21	HF6-RF3	W	5.3	5.2	435.6	323.5	5
22	HF6-SR	W	-	3.8	143.6	75.6	0
					1219.8	**58.3 %**	**31**
23	HF8-F	W	21.2	7.5	2.3	0.9	3
24	HF8-RF1	XSW	7.3	5.1	165.7	-	163
25	HF8-RF2	XSW	6.3	5.25	561.7	-	18
26	HF8-RF3	W	7.1	4.7	386.3	8.7	8
27	HF8-SR	W	-	4.7	31.5	11.3	0
					1147.5	**1.8 %**	**192**

experiments and from the fractured zones during all experiments. These outflows were also monitored to validate the overall fluid balance over each experiment. Cycle RF1 for HF1a and HF5 correspond of multiple refrac cycles. Thus, the re-opening pressure and the ISIP were averaged and the fluid injection respective recovery is presented in a cumulative number.

Figure 4.4a presents the flowrate (q_{inj}) vs the interval pressure (p_{inj}) at pseudo steady-state for the second refrac cycle RF2 and the pressure-controlled step test for each HF experiment. For any injection step, the injection conditions (either controlled flowrate or constant pressure) were maintained until a stable state was reached, i.e. quasi constant pressure for rate-controlled injections or quasi constant flowrate for pressure-controlled injections, while we acknowledge that true steady state conditions are never reached in practice, we took the latest data point prior starting the next step of our injection. A major observation is that there is a clear difference between HF experiments executed south of the S3 shear zone (HF3, HF5 and HF8) and north of the S3 shear zone (HF1, HF2 and HF6). HF1 and HF2 were located in the S1 shear zone and reached a pressure limiting behavior at an injection pressure of 5.4 MPa for flowrates larger than 35 $\mathrm{l/min}$ (Figure 4.4a). During these two experiments, only two propagation cycles (RF1 and RF2) were executed. Considering experiment HF6, the pressure limiting behavior occurred at a higher pressure of 6 MPa.

HF3, HF5, and HF8 were located south of the S3 shear zone. In general, all experiments executed on this side of the S3 shear zone had higher injection pressure. HF3 and HF8 showed

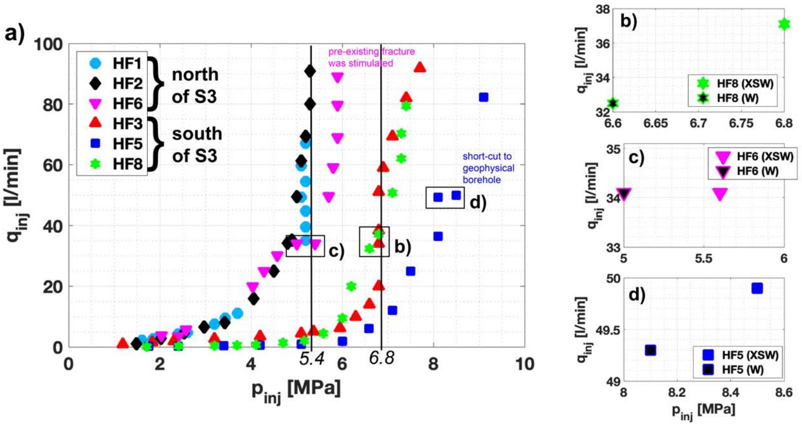

Fig. 4.4 a) Presents the injection flowrate q_{inj} vs interval pressure p_{inj} at pseudo steady-state from the second refrac cycle RF2 and pressure-controlled step test SR (similar to Fig. A.1 in the Supplement) for all HF experiments. The black solid lines indicate a limiting pressure behaviour for HF1/HF2 and HF3. (b-d) Highlights the pressure drop when changing from XSW to water with similar flow rate.

similarly, a slight increase after reaching a flowrate of 10 l/min. The injection pressure reached a limiting pressure of 7.8 MPa. The injection fluid for HF3 was water and for HF8 XSW followed by an additional flushing cycle using water. Experiment HF5 showed the highest increase in injection pressure for increasing flowrate with a maximum injection pressure above 9 MPa. The pressure dropped around 0.5 MPa at the same flowrate (35 l/min or 50 l/min) using XSW during the refrac cycle RF2 and the flushing cycle (RF3) using water for experiment HF6 and HF5. The effect is smaller for HF8 with a pressure drop of only 0.2 MPa. Therefore, we can infer that the viscosity effect (i.e., the change of XSW to water) results in a decrease of injection pressure, but further investigation is necessary to reliably quantify the effect. For the sake of clarity, the flowrate and pressures from the flushing cycle associated with the pressure drop are presented in Figure 4.4 (b-d).

The limiting pressure is smaller compared to the hydraulic tensile strength calculated from the difference between breakdown and reopening pressure (Bredehoeft et al., 1976) ranging between 8.3 and 9.6 MPa. The tensile strength measured by Dutler et al. (2018a) ranges between 5.6 and 14.7 MPa for the transversely isotropic host rock. Therefore, the hydraulic tensile strength depends on the orientation of the isotropic plane. The limiting pressure ranges between 5.4 MPa (HF1 and HF2) and 6.8 MPa (HF3), and is interpreted as reflecting conditions when the fracture surfaces have fully lifted off near the wellbore. However, it is questionable if the hydraulic fractures still extend (creating new surfaces) at this pressure.

The difference from HF6 to the two other injection experiments (HF1 and HF2) may be related to two reasons: 1) The HF6 interval contains a pre-existing fracture that may not be perpendicular to the minimum principal stress. 2) The injection fluid in HF6 is XSW. Thus, the pressure reaches higher values as pressure dissipation is affected by the high fluid viscosity.

During the flushing cycle of this fracture (RF3), a pressure decrease was observed, reflecting a viscosity effect.

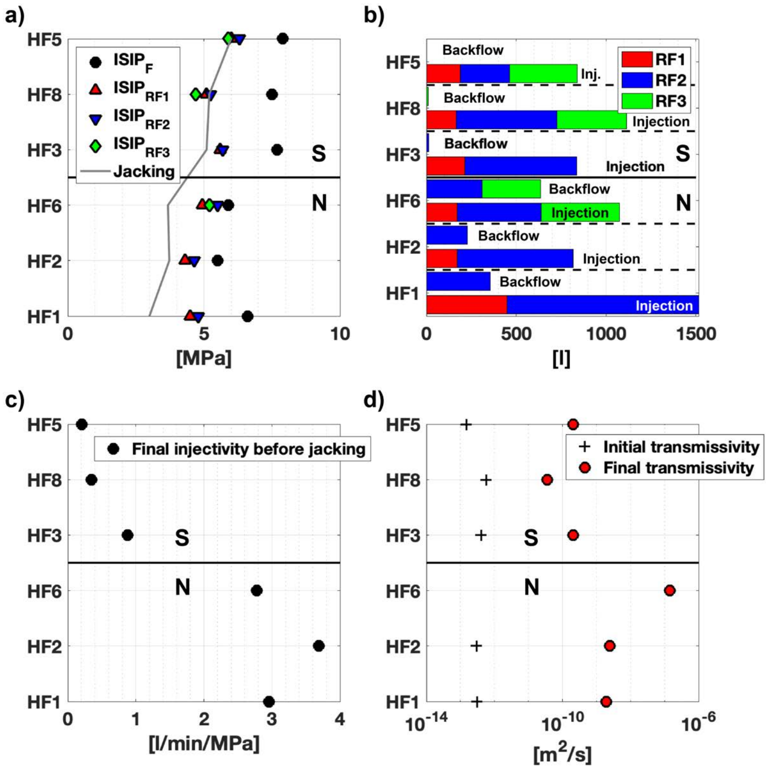

Fig. 4.5 The black solid line on all plots indicate the S3 shear-zone, which divide the experiments in north (N) and south (S) with a pseudo-distance ordering the HF experiments on the y-axis from top of the borehole (HF5) to the end (HF1). a) Presents ISIP from frac / refrac cycle and the best estimate of jacking pressure (JP). b) The injected and backflow volume are presented for the 3 main refrac cycles for each experiment. No recovery phase took place after RF1. c) Presents the final matrix injectivity from the pressure-controlled step test. d) The initial transmissivity was measured from pulse injection prior to the HF experiment and the final transmissivity was measured via constant head injection several weeks after the experiment.

Fig. 4.5 presents four subplots summarizing (a) the ISIP and JP, (b) the injected volume and backflow, (c) the final injectivities before jacking derived from the analyses of the SR cycles and (d) the initial and final transmissivity derived from hydraulic experiments performed prior and after the HF experiment. Fig. 4.5a compares the ISIP obtained during the frac / refrac cycles with the jacking pressure. The ISIP varies between 5.5 and 7.9 MPa for the frac cycle and decreases with ongoing refracturing. For all experiments, the ISIP stabilizes around 5 MPa and show slightly higher values between 4.5 and 6.5 MPa for experiments executed south of S3 (above the black solid line) and values between 4.0 to 6.0 MPa for experiments executed north of the S3 shear zone. South of the S3 shear zone, the jacking pressure reaches values between

5.1 and 6.0 MPa, which is comparable with the ISIP from the refrac cycles. In contrast, the jacking pressure north of S3 range between 3.0 and 3.7 MPa for the experiments executed. This reflects 1 to 2 MPa smaller values than using the ISIP from the refrac cycle (Fig. 4.5a).

The injection volume and the recovery volume from the injection intervals for the main fracture propagation cycles RF1/RF2 and the flushing cycle RF3 are presented in Fig. 4.5b. The injection volume for each cycle is similar for all experiments except HF1. For HF1 the injection protocol was stopped after refrac RF1 and continued the following day. After the first propagation cycle, no fluid recovery took place. Both, the second fracture propagation cycle RF2 and the flushing cycle RF3 do show minor or no backflow from the injection interval for the experiments executed south of S3 (> 2%). In contrast, for the experiments executed north of S3, the recovered fluid from the injection point reaches values between 15.0% and 23.5%. Experiment HF6 reached the largest volume recovery of all experiments: during the flushing cycle RF3 a recovery of 74.3% was observed. The final injectivity before jacking is presented in Figure 4.5c and ranges between 2.77 and 3.69 $\mathrm{l/min/MPa}$ north of S3 and between 0.21 and 0.88 $\mathrm{l/min/MPa}$ south of S3. Approaching the S3 shear zone from the south, injectivity values increase. The experiments located further down in the borehole show highest injectivity values, which correlates directly with an increase of fracture density in the shear zone S1.

4.4.3 Transmissivity values from pre- and post-HF hydraulic tests

The change in transmissivity at the injection interval was investigated by packer testing before and after the HF experiment in borehole INJ1 and INJ2. Prior to the HF experiment, pulse injection (PI) and after the HF experiment, constant head injection (CHI) tests were performed. To estimate the equivalent hydraulic parameters (transmissivity and storativity), the PI tests were inverted with n-dimensional Statistical Inverse Graphical Hydraulic Test Simulator, nSIGHTS (Roberts, 2006) and the CHI tests were analyzed using the Jacob and Lohman (1952) solution. For both methods the radius of influence is different and therefore the numbers are only an indication of permeability enhancement and not for direct comparison. The initial magnitude of local transmissivity estimates ranges between $10^{-13} - 8 * 10^{-13}$ $\mathrm{m^2/s}$. Final transmissivities post to the HF experiment, from CHI tests reach values between $1.9 * 10^{-9} - 3.6 * 10^{-11}$ $\mathrm{m^2/s}$. HF6 is an exception as it took place at a pre-existing fracture, for which transmissivity was not measured before the HF experiment. The final transmissivity for HF6 is highest in magnitude for all HF experiments with $1.5 * 10^{-7}$ $\mathrm{m^2/s}$. There is a trend of one magnitude higher transmissivities after HF for experiments on the northern side of the S3 shear zone (more in the Supplement A.2).

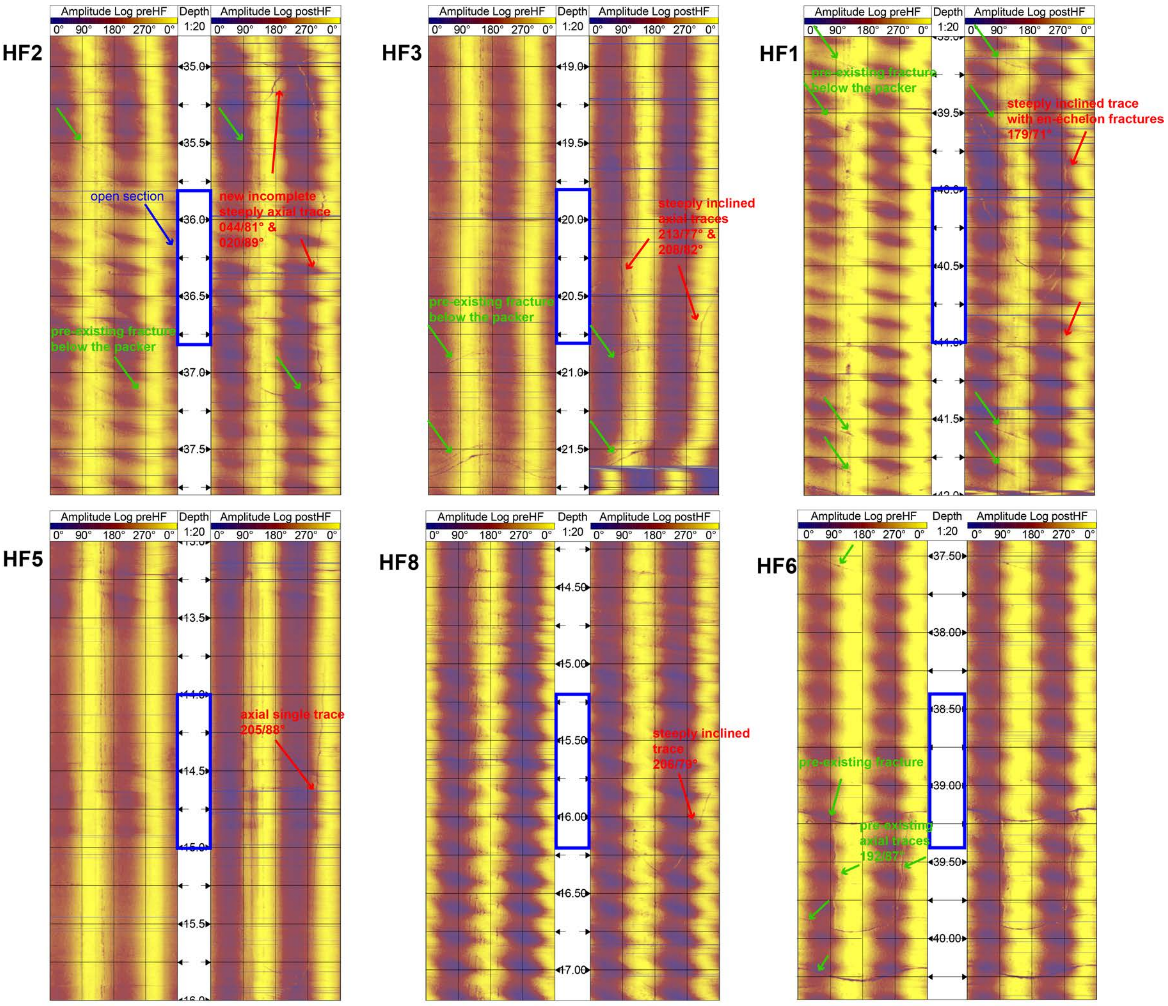

Fig. 4.6 Pre- and post-testing acoustic borehole televiewer (ATV) logs of the borehole INJ1 and INJ2. The blue highlighted sections in the center indicate the open intervals which do not show any fractures prior to testing except for HF6, which was stimulated at the wrong position. The pre-existing fractures are indicated with green arrows. The areas below and above the blue section show the location of the straddle packers. Five of six experiments show new features in the post-testing images which indicates an induced fracture.

4.4.4 Borehole fracture trace

Prior to the HF experiments, analysis of drill cores, optical and acoustic televiewer have been carried out to select appropriate test intervals. Suitable test intervals for hydraulic fracturing were selected if no pre-existing fractures were visible. Figure 4.6 presents the amplitude log from the acoustic borehole televiewer for the six HF intervals for pre- and post-testing. The travel-time log is not presented as no changes were recognized. The blue highlighted section in the center indicates the injection interval, which does not show any fractures prior to testing, except for HF6. The areas below and above the blue section show the location of the straddle packer of 1 m length. The pre-existing fractures are indicated in green and located at the straddle-packer emplacement. The new fracture trace is indicated by a red arrow. The dip and dip direction were determined by fitting a sinusoidal trace using the WellCAD software by Advance Logic Technology. Based on the probe orientation measurements, the true orientations of the induced fractures were computed. Travel time data accuracy which allows at best to resolve radius changes of 0.15 mm does not allow to quantify wellbore deformation associated with the presence of the newly created fracture trace, but changes in signal amplitude are sufficient to identify the newly created features during the HF experiments. The borehole traces are either axial to the borehole or have a steep angle to the borehole axis not exceeding 20°. An exception is found in the post-log of HF1, which indicates new en-échelon structures for one side of the fracture trace and mostly likely a packer induced fracture trace towards the bottom of the HF interval. This structure is a result of the deviated borehole with respect to the perturbed stress tensor (Table 4.1). We recognized that for all HF experiments many of the new fractures extend below the straddle-packer and stop at a pre-existing fracture.

4.4.5 Microseismicity

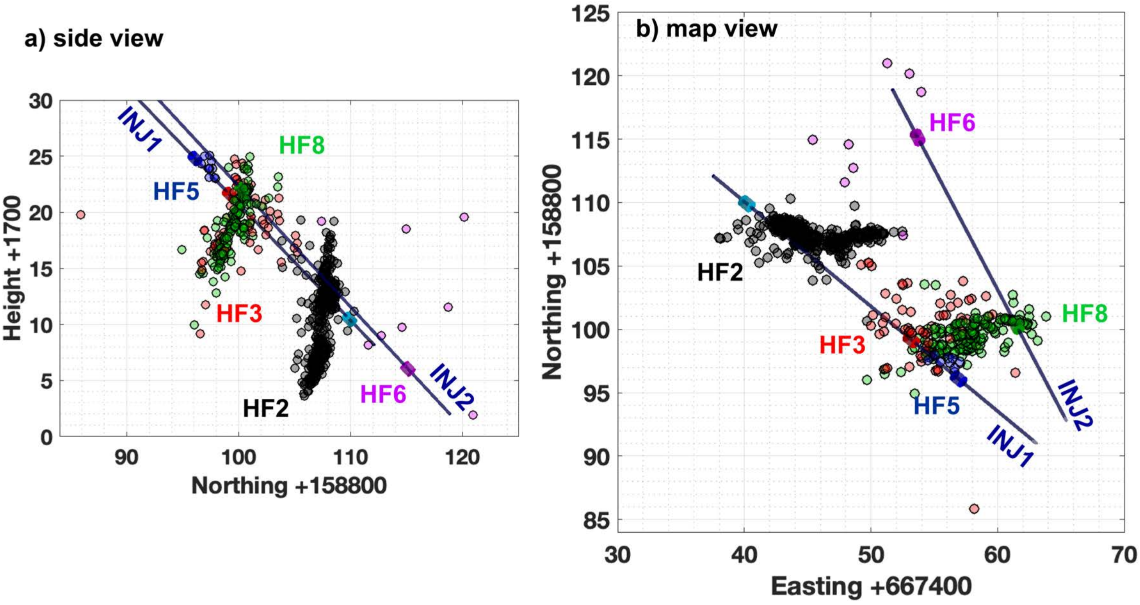

Fig. 4.7 Seismicity clouds in side view a) and map view b) inclusive 3D cylinders presenting the open injection intervals in the two injection boreholes. Each experiment has the same color for seismicity points, the 3D cylinders and the labels.

During the HF experiments, we detected in total 6986 microseismic events, from which 730 events were located. P-wave arrivals were picked manually and located using an absolute location procedure including a joint hypocenter determination (JHD) and a homogeneous, transversely isotropic velocity model (P-wave velocity along the axis of symmetry 5195 m/s, along the axis of isotropy 4865 m/s). The relative uncertainty of location considering picking uncertainties lies in the range of ±1.5 m, absolute location uncertainties range from below 0.5 m in a depth interval from 15 to 30 m in INJ1 to 1.5 m towards the mouth and bottom of INJ1 and INJ2. Details to the analyzed induced seismicity are presented in Villiger et al. (2020). The number of located events for each frac / refrac cycle are indicated in the last row of Table 4.2. In the Supplement A.6, each experiment is presented showing the injection protocol with flowrate and injection pressure, the located seismic events for each frac / refrac cycle in plane and profile view and the cumulative injected volume, cumulative backflow and the distance between injection point and located seismic events. Figure 4.7a presents the seismic clouds for five of the six hydraulic fracturing experiments (experiment-wise color-coded).

The number of located seismic events for experiment HF5 and HF6 is very small. Most seismic activity is observed during experiment HF2 and HF8. Note that the location of the injection intervals with respect to the seismic sensors cannot explain the large difference in detected and located seismic events. During all experiments, the seismic events are located more often below the injection point than above. Also, seismicity propagates predominantly towards east.

A peculiar seismic pattern was observed during HF2 (see Fig. A.9 in the Supplement): seismicity radiates away from the injection point up to a distance of about 5 m during the first part of refrac cycle (RF1), and then propagates to about 10 m away from injection. However, during the second refrac cycle (RF2), seismicity resumes 10 m away from the injection point and develops towards the injection point. This behavior is atypical since migration away from the injection point is typically expected and observed.

Seismicity occurred during all frac / refrac cycles for HF8. Most of the seismic events were observed during the first refrac cycle. The events were located around the borehole with a maximal radial distance of only 10 m. Only three events were located further away during the same cycle. Refrac cycle RF2 and RF3 show less seismic activity compared to RF1, which occurs further away from the injection point.

During the two refrac cycles of HF3, 75 located seismic events occurred. These located seismic events show a dispersed pattern. Most of the seismic events appear below 10 m radial distance from the injection point. Generally, minor seismicity is related with the refrac cycle RF3 and no seismicity is associated with the pressure-controlled step cycle SR for all experiments except HF6.

4.4.6 Fracture geometry

The seismic event locations are shown in a stereographic projection centered on the injection point in Figure 4.8. Here, each seismic event is represented by the intersection of a unit sphere centered on the middle of the injection interval and a line connecting this middle point and the location of the seismic event. With this method, each seismic event is presented as a point

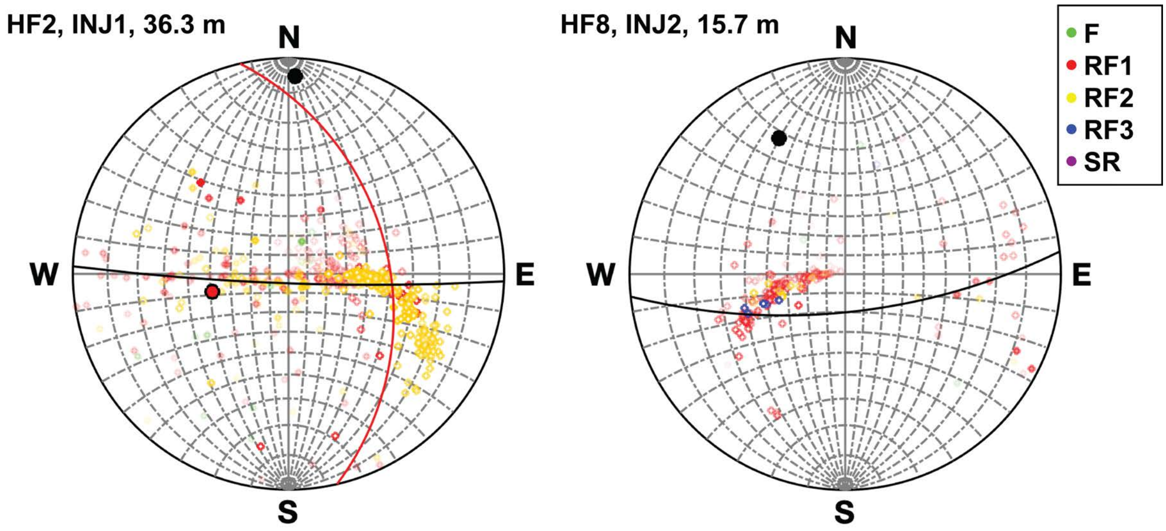

Fig. 4.8 The center of the lower stereographic projection corresponds to the injection point and each circle to a seismic event. Circles with a white face color and a different edge color are projection on the lower stereographic net and fully colored circles are projections on the upper stereographic net. The girdle pattern indicates the fitted planes inclusive pole point for different seismic clusters (colored pole point). Considering all seismic events, the girdle pattern and the pole point are black.

on a lower stereographic projection for experiment HF2 and HF8, respectively (Figure 4.8). The color of the circle indicates the frac / refrac cycles. In this representation, the location uncertainty of the seismic events impacts strongly the event orientations close to the injection point. A color saturation scheme is used to give less importance to these events: a more intense color is used for events located farther away from the injection point and linearly decreasing the color saturation towards the injection points. Events located within a radial distance of 1 m (typical location error for our seismic events) from the injection point are not represented.

In the idealized case of symmetric radial extension of the seismic cloud on a plane from the injection point, the expected pattern on the stereoplot would be a girdle pattern, i.e. all the points will line on a great circle of the stereoplot. In Figure 4.8 we present the best fit plane (for the method and results see A.5 in the Supplement) through the seismic cloud via girdle pattern for all seismic events (black pole point for HF8) and for two clusters (i.e. RF1 and RF2 for HF2, red and yellow pole point). The two HF experiments presented in Figure 4.8 do not follow this idealized pattern. In our case, the points tend to cluster that represent a linear structure.

For HF2 during RF1 (red), the points tend to distribute on an E-W sub-vertical plane and cluster on a linear structure dipping about 70° to the East. During RF2, the seismicity cloud migrates (yellow) towards a well-defined linear structure with a dip of 25° to the ESE. The mean from the first and second refrac cycle are very consistent dipping 40° to 50° to the East. The seismicity cloud of HF8 is clustered on a linear structure dipping 60° to 70° to the West. Most of the seismic events take place during refrac cycle RF1 and RF2 with more intense color saturation as they are located further away from the injection point. The mean of refrac cycle RF1 to RF3 are very consistent for experiment HF8.

4.4.7 Hydromechanical observations

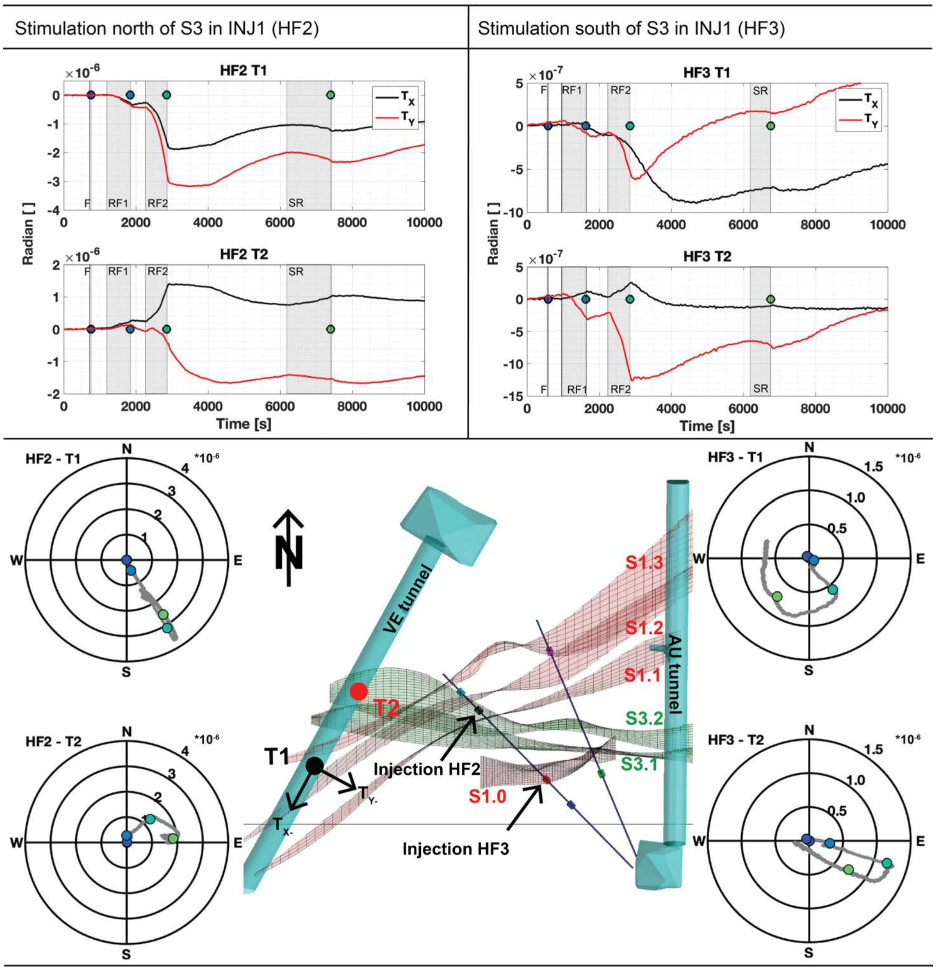

Fig. 4.9 The time series of tilt meter T1 and T2 are presented for experiment HF2 and HF3. The fluid injection is named and indicated by the grey boxes. The colored points at the end of fluid injection in the time series are presented in a polar plot. The magnitude of the circles of the polar plot are given in radians. The sketch shows the injection points, the orientation of the shear zones and the tilt device location with negative tilt magnitude tunnel parallel T_{X-} respective perpendicular to the tunnel T_{Y-}.

Two experiments, one executed north of S3 (HF2) and the other one south (HF3) are presented and compared here in terms of deformation and hydraulic pressure distribution in the rock mass. Similar information on the other experiments can be found in the supplement A.3. For the two experiments presented here, the injection fluid was water and the injection intervals were devoid of fractures prior to stimulation.

The tiltmeter data (Fig. 4.9 and Supplement Figure A.3) measure the deviation of the VE-tunnel floor from horizontal. The fluid injection is presented by grey shading in the time series of the tilt data. In general, the largest tilt is related to higher injection rates and increasing fluid volume. The magnitude of the tilt axis globally ranges between -4 to 3 microradians. The magnitude of the tilt signals decreases with respect to the injection location and shear zone as follows. Injection executed south of S3 show in general smaller magnitudes in tilt than the one executed next to S1, as they are farther away from the tilt meter locations. Also, the response of the tilt signals reacts either instantaneously or delayed depending on the location of injection (distance-controlled response). The experiments next to the shear zone S1 in borehole INJ1 (HF1 and HF2) show an instantaneous response in the tiltmeter T1 and a delayed response in the y-component of tiltmeter T2. We interpret that the tunnel floor tilts away from the injection volume, which accumulates in the intersection zone of S1 and S3.

Tiltmeter T1 of the experiments south of S3 (HF3 and HF8) tilts away from the S1.2 shear zone and T2 tilts along the strike of the S3 shear zone. Experiments executed south of S3, are expected to connect to the fracture system of the shear zone S3, which acts as a preferential flow path towards the AU-tunnel.

Figure 4.10 presents selected time series from the FBG strain sensors and the FBG strain data along the FBS boreholes at the end of refrac cycle RF1 and RF2 and the permanent change for the two aforementioned experiments HF2 and HF3. The strain data were set to zero at the beginning of the experiment, as we are interested in the relative changes during an experiment. A positive strain is associated with compression, negative strain represents tension. The permanent strain was either measured 2 hours after the experiment, or at the starting time of the next experiment. The fluid injection is indicated by the grey boxes. The time series of HF2 of the FBG sensors at 31.8 m and 33.0 m indicate a fast-tensional increase during RF1, linking to the arrival of the fluid front (i.e. the sensor at 33.0 m with one fracture along the sensor base length). The sensor at 31.8 m was placed in intact rock and indicated only compressional signals prior to the HF2 experiment. Therefore, it was hit by the hydraulic fracture during RF1. The highest tensional signals are observed in the S1 shear zone for experiment HF1, HF2, and HF6. Above 35 m the FBG sensors in FBS2, which is oriented parallel to the S3 shear zone and crosses the S1 shear zone at 35 m, indicates compression above 35 m and tension below 35 m. This is directly related to fluid flow through fractures intersecting the base length of the FBG sensors related to the S1 shear zone.

The time series of HF3 in Figure 4.10 show two FBG sensors at 22.35 m in FBS1 and at 20.0 m in FBS2 with very high transient peak strain. The time series of the FBG sensor at 20.0 m in FBS2 from HF3 indicate the largest transient peak strain during all HF experiments. Most of the observed peak strain is reversible and 50 $\mu\varepsilon$ are irreversible (permanent) strain. We assume that this tensional reversal strain is directly linked to the fluid pressure. The sensor at 23.35 m

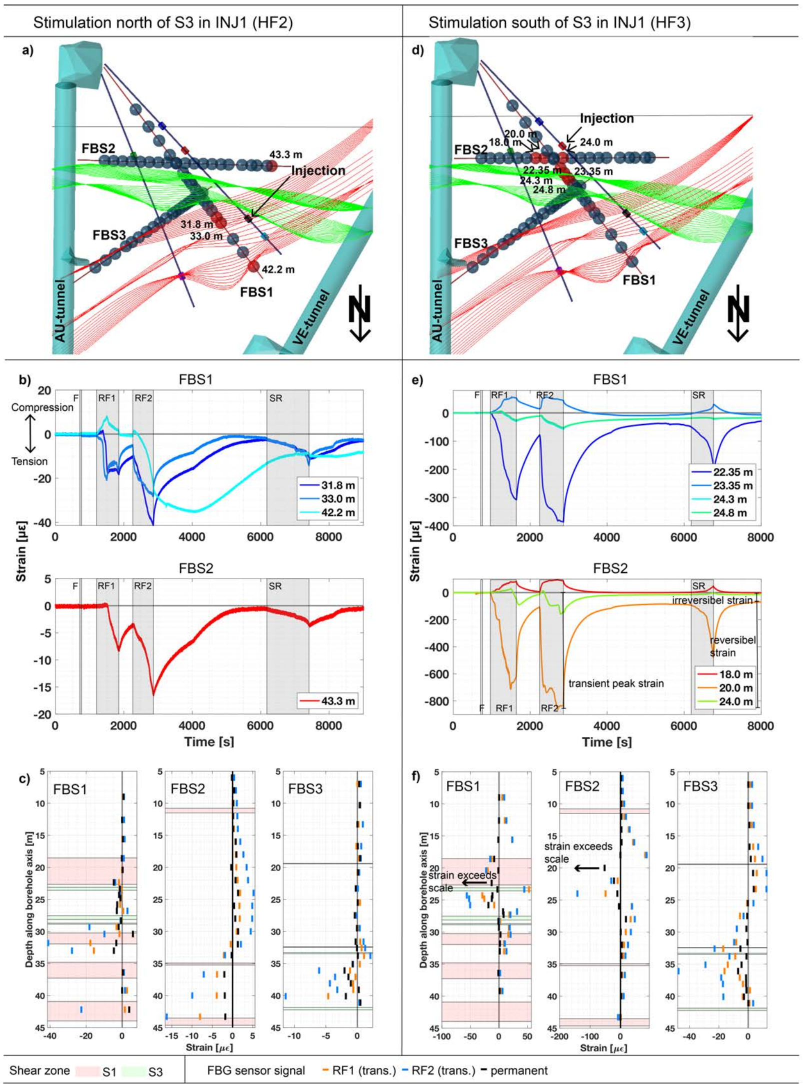

Fig. 4.10 Selected time series of FBG sensors from borehole FBS1 and FBS2 for experiment HF2 a-c) and HF3 d-f) inclusive sensor location. The fluid injection time is named and indicated by the grey boxes. The depth of the sensors measured from top is indicated in the specific legends from the time series. Positive strain indicates compression.

in FBS1 is located at the metabasic dyke. This sensor shows compression, whereas the sensors in between the two metabasic dykes indicate tension (e.g., the sensors at 24.3 and 24.8 m). The high transient strain signals (i.e. FBS1 22.35 m and FBS2 20.0 m) indicate major flow paths and are only observed for experiments executed south of S3. In FBS2 only 3 FBGs observe tensional strain, while all the other sensors are compressed, with the highest compression towards the extensional section. Along the borehole FBS3, the sensor associated with S1 shears and intact rock show compression. Note, that the most of the tensional strain signals are observed on sensors associated with the brittle-ductile shear zone S3 (i.e. FBS1 23-30 m and FBS3 > 33 m). Large permanent strain changes are not observed (changes are in a range of 20 and -30 $\mu\varepsilon$).

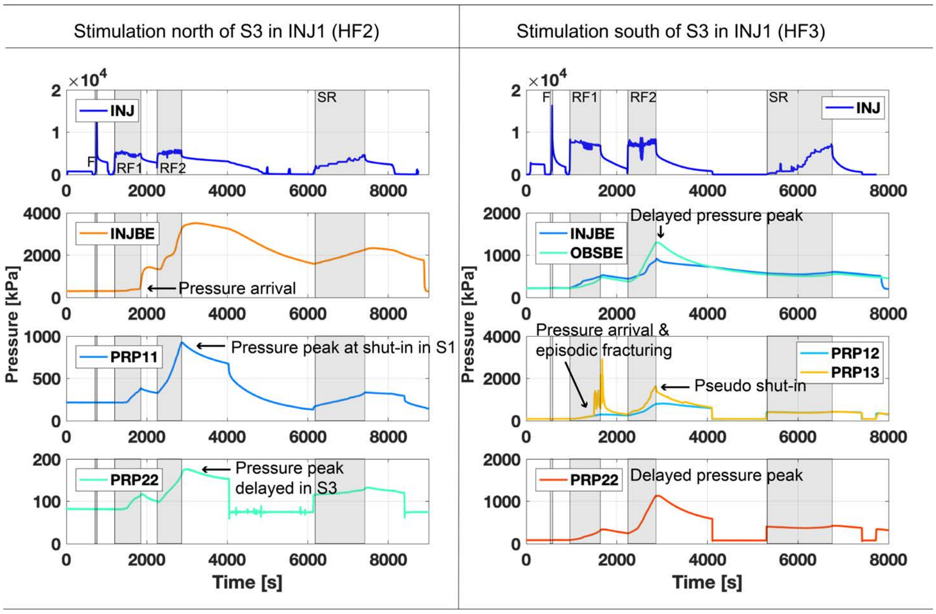

Fig. 4.11 Selected time series of pressure response are presented for experiment HF2 and HF3. The fluid injection is named and indicated by the grey boxes.

Selected time series from pressure observation intervals in the injection and observation boreholes are presented in Figure 4.11 for the hydraulic fracturing experiment HF2 and HF3 (for the other experiments see Supplement). The injection pressures (INJ) are presented on top including the grey boxes, which indicates fluid injection.

For the stimulations north of S3 (HF2) the time series from the interval below the injection (INJBE) shows a pressure arrival directly at the end of the first refrac cycle RF1. The peak of the pressure response in PRP1-1 is at the end of refrac cycle RF2. The interval PRP2-2 is located in the shear zone S3 and the injection location is next to the S1 zone. It is expected that the fractures related to the S1 zone are connected first and therefore the interval PRP2-2 located in the S3 shear zone has a delayed pressure peak. The interval INJBE is located next to the injection interval (in shear zone S1.2 and S1.3), showing pressure arrival after cycle RF1. The nearly instantaneous pressure response indicates a new complex flow path connection to the injection interval below. In addition, the largest amplitude is observed, compared to all other observation points and the maximum peak after shut-in is delayed comparing interval PRP1-1. This indicates a longer fluid path reaching interval INJBE than PRP1-1.

The HF3 injection experiment triggered a strong signal during the first refrac cycle in the observation interval PRP1-3: it indicates an abrupt pressure arrival and an episodic pressure change during and after pump shut-off. At the end of cycle RF2, pseudo shut-in is observed at the interval INJBE and PRP1-3: i.e. both pressure curves drop after pump shut-off. The pseudo shut-in in the observation interval near the injection interval is a mechanical response starting from the injection interval due to instantaneous pressure loss. The observation interval OBSBE and PRP2-2 respond with a delayed pressure peak, where the two intervals are located further away than the two intervals (INJBE and PRP1-3) showing pseudo shut-in.

4.5 Comparison between stress characterization and HF experiments

In the following section, we compare the hydraulic fracturing experiment with several small-volume (~10 l) hydraulic fractures from the stress characterization phase (hereinafter called: minifracs (MF)). The minifracs were accompanied by micro-seismic monitoring to investigate the initiation and propagation of the new induced fractures. A detailed description of the stress characterization and the minifracs has been published by Gischig et al. (2018); Jalali et al. (2018b); Krietsch et al. (2020). In the separate experimental summary cards, each minifrac experiment from SBH3 and SBH4 boreholes is presented in a similar way than the HF experiments. A summary of the injection pressure and seismic characteristics of all MF experiments (SBH1, SBH3 and SBH4) can be found in the Supplement A.4 and A.6 inclusive an overview of the injection interval locations.

4.5.1 Injection pressure observations

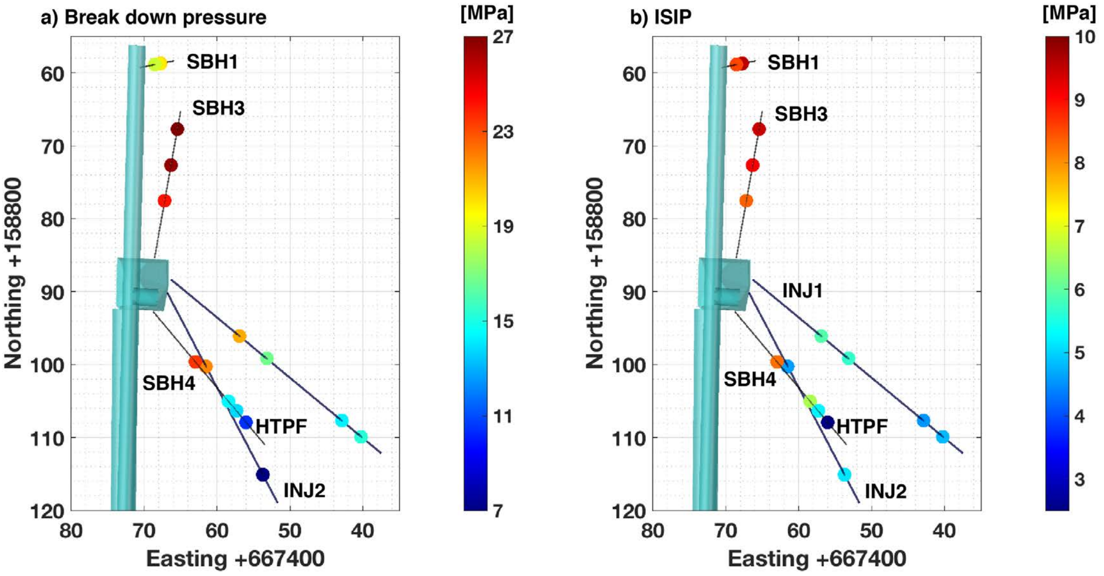

Fig. 4.12 Location of HF and MF experiments, viewed towards west with a color-coded for a) breakdown pressure and b) instantaneous shut-in pressure (ISIP).

Figure 4.12 summarizes the breakdown pressure and the ISIP from all MF and HF experiments. Breakdown pressure and ISIP decreases towards the S3 shear zone. The highest decrease is observed in borehole SBH4 approaching the S3 shear zone at the end of the borehole. The experiments executed in borehole SBH3 (MF1 – MF3) show the highest breakdown pressure between 23.4 and 26.1 MPa. The shut-in pressures range from 8.1 to 9.1 MPa. The experiments in SBH1 have smaller breakdown magnitudes ranging from 13.8 to 19.8 MPa, where the ISIP with values between 8.3 and 9.6 MPa is comparable with the minifracs executed in SBH3. The minifracs from SBH4 (MF4, MF6-MF7) start with a breakdown pressure of 22.7 MPa, which decreases towards the S3 shear zone reaching a value of only 13.5 MPa for the minifrac approaching the S3 shear zone. The ISIP shows a similar decrease from 8.0 to 5.3 MPa. The additional hydraulic test on the pre-existing fracture (HTPF) executed in the S3 shear zone indicates a joint breakdown pressure of 10.3 MPa and a jacking pressure of 2.8 MPa. The breakdown pressure of our larger-scale HF experiments does also show a decrease towards the S3 and S1 shear zones, but the change in magnitude is significantly smaller with magnitudes around 21.2 to 16.3 MPa south of S3 and 14.9 to 13.9 MPa north of S3. The ISIP was measured during cycle RF2 for the experiments using only water and during cycle RF3 for the experiments using XSW. Generally, we find that the minifracs executed in SBH1 and SBH3, i.e. away from the shear zone, have larger breakdown pressures and ISIP than the experiments performed in SBH4, INJ1, and INJ2 that are closer to the S1 and S3 shear zones. In addition, the experiments performed in the more fractured rock mass in the vicinity of the shear zone show larger variability reflecting stress heterogeneity.

4.5.2 Fracture geometry

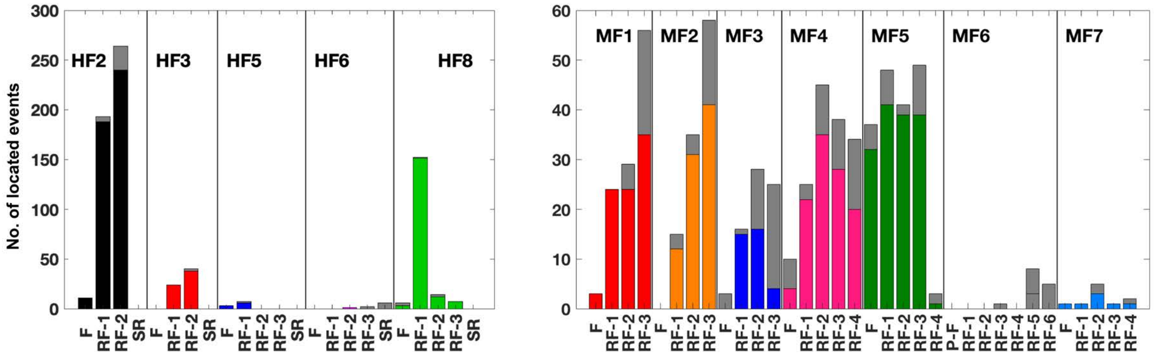

Fig. 4.13 The hydraulic fracturing (HF) and minifracs (MF) from the stress characterization phase are presented in an event versus frac / refrac histogram. The color in the histograms corresponds to the number of events during injection. The grey bar on top of the histograms indicate the seismic events after injection shut-in.

In the following, we compare the number of located seismic events between the HF and MF experiments. Then we compare the geophysical borehole logging/impression resulting in fracture traces at the wellbore with best fitting planes through the microseismic clouds giving information on the fracture orientation away from the wellbores. One should be aware that the seismic monitoring array differed between the HF and MF experiments, which results in different network sensitivities and location accuracies. The number of located microseismic events for all HF experiments and minifracs during each frac (F) / refrac (RF) cycle are presented in Figure 4.13. All located events occurring during injection are indicated by colored bars, while the grey bars on top indicate the events after fluid injection (during shut-in and bleed-off time). The following key findings from Figure 14 can be noticed:

- On average, the total number of located seismic events do not differ significantly between the MF and HF experiments, although the variability from experiment to experiment is large. This is somewhat surprising knowing that about 10 l was injected during the MF experiments and 1000 l during the HF experiments.
- The variability of the number of seismic events is particularly obvious when comparing MF6, MF7, HF5, and HF6 (all experiments exhibit less than 50 events) with for example HF2 (531 events). Note that it cannot be ruled out that the different seismic network layouts for HF and MF affect the sensitivity towards detecting lower magnitude events and thus can influence the result.
- However, looking at frequency-magnitude distributions and the corresponding magnitude of completeness analyses presented by Villiger et al. (2020) suggests that for the HF injection experiments, not all the variability in detected and located seismic events can be attributed to sensitivity variations of the seismic network. A possible explanation for the low number of located events during MF6 and MF7 is the fact that they were close to the shear-zone S3. During injection experiment HF5 a direct short-cut to a geophysical observation borehole was created. Injection experiment HF6 was executed at the wrong borehole interval, where a pre-existing fracture was stimulated, which was already stimulated before during the hydraulic shearing (HS) experiment.
- The minifracs show a tendency to have relatively more seismic events during shut-in (34.2 %) and bleed-off time compared to the hydraulic fracturing experiments (5.9 %).
- During the MF experiments, typically a small number of events occur during the formation breakdown cycle (F) compare to the refrac (RF) cycles, except for MF4 and MF5. MF5 had an insufficient sealing of the experiment section allowing the fluid to by-pass the packer. Nevertheless, the seismic response is high and the experimental summary cards (Supplement) indicate that most of the seismic events are located around the borehole up to 4 m away from the injection point, with some minor events located 7 to 10 m away from the injection interval.

- During the HF experiments, most seismicity occurs during the refrac cycles (RF) whereby the injected volume and the flowrate progressively increase. Except for experiment HF6, no seismicity was observed during the pressure-controlled step (SR) test. Prior to this experiment, we opened the valve of the injection interval to drain the fracture system. The small injection volume during the pressure-controlled step test and the small flowrates were not sufficient to re-initiate micro-seismic activity.

The poles to the fracture traces determined at the borehole wall from acoustic televiewer data (see Fig. 4.5) in the boreholes INJ1 and INJ2 for the HF experiments are presented in Figure 4.14a and the pole to the fracture traces from the minifracs using impression packer are presented in Figure 4.14b. We assume, that these traces correspond to the fractures initiated during the frac-cycle (formation breakdown). The fractures during HF experiments presented in Figure 4.14a are sub-vertical with a N to NE dipping direction. The HF traces are axial or make a small angle to the injection borehole axes. The foliation orientation (337/15°) is indicated by the magenta pole in Figure 4.14, which is also corresponding to the main brittle fracture set. The minifracs MF8-MF11 were executed in the sub-vertical borehole SBH1. The orientation of the minifracs (Fig. 4.14b) are primarily aligned with this foliation plane except for MF09 and MF10 that have a similar trace orientation to the HF experiments. The minifracs MF08 and MF11 orient towards the foliation and the brittle fracture orientation in the host rock (compare Fig. 4.2a), such that the fracture opened either along the foliation. The orientation of fracture trace MF01 and MF02 from the sub-horizontal borehole SBH3 show a radial fracture initiation, which highlights the dominating control of foliation as such orientation is not the most favorable for initiation at the borehole from a stress concentration viewpoint.

The pole points from the plane fit to the seismic clouds are presented in Figure 4.14c for the HF experiments and Figure 4.14d for the minifracs. For both HF and MF, most of the seismic best fit planes are sub-vertical, striking E-W and slightly dipping to the South. Note that some of the plane fits are poorly constraint due to the small number of located seismic events, i.e. HF3. Also, we noticed a change of orientation for HF2 with injected volume. During the first refrac cycle RF1, the seismic cloud orients itself vertically, striking ESE-WNW. Considering all seismic events including refrac cycle RF2, the seismic cloud orients itself sub-vertical, striking E-W similar to the minifracs. For experiment HF3, two different clusters are possible depending on the seismic events. The first fit indicates a sub-vertical plane striking towards S-N with a misfit of 1.2 m. The second cluster orients itself sub-vertical in E-W. The data presented in Figure 4.14 are summarized in the Supplement (A.5) with wellbore trace description and best plane fit details.

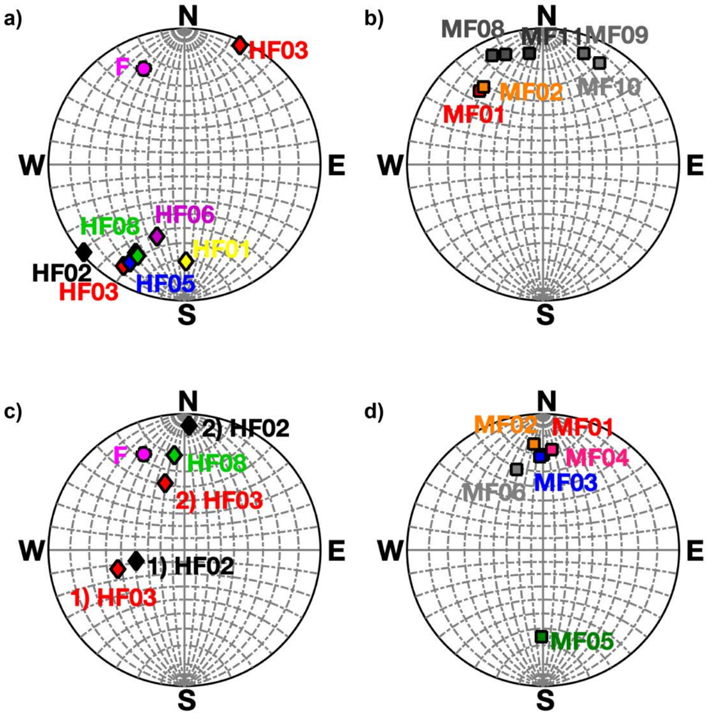

Fig. 4.14 The newly created fracture traces from geophysical borehole logging and impression packers are presented in a lower hemisphere stereonet for the HF experiment a) and the MF experiment b). The pole point of the plane fits from the seismic events are indicated in a lower hemisphere stereonet for both the HF experiment c) and the MF experiment d). The foliation is indicated by the magenta circle in panels a) and c). The color code is the same as for Figure 4.13.

4.5.3 Fracture propagation

Fracture propagation during the fluid injection can be tracked using the seismic events, which move away from the injection interval. In Fig. 4.15, all seismic events from the minifracs (MF) are presented with grey circles. The grey circles are absent after 10 l of injected volume as it is the maximum injected volume for these experiments (Figure 4.15). Further, the circle shows two localizations, one along the 10 m axis and the other increase with increasing injection volume starting at around 2 m for 0.3 l and ending at around 7 m for 10 l. The grey circles at 10 m are associated with the drained and disturbed stress field around the AU-tunnel. On the other hand, the colored circles present the HF experiments. They show a positive correlation between distance and fluid injection. The distance stops to increase after an injection of 60 l and stays around 10 m. The injection of 1 m^3 fluid into the fracture network results in observed seismic events maximally 20 m away from the injection interval, whereby the 10 l injected during the minifracs show a maximum distance between injection interval and farthest away event of 7 to 10 m.

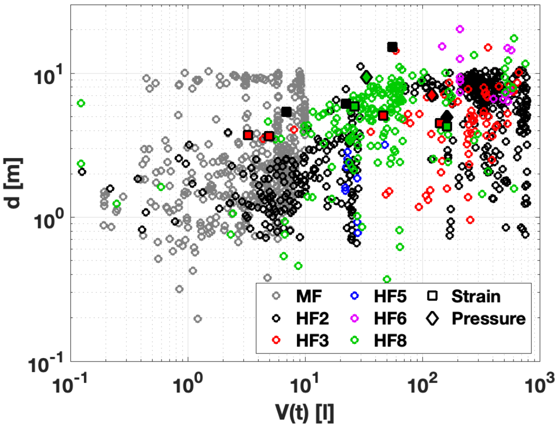

Fig. 4.15 The corrected injection volume incl. backflow correction is presented against the distance from the located seismic events to the midpoint of the injection location. The grey circles present all the located seismic events from the minifracs without subdividing them. The other circles present different HF experiments. The squares are tracked from FBG sensors or the distributed strain system (DSS) and the diamonds are taken from the transient pressure interval.

Instantaneous tensional strain and pressure response are tracked through our experiments to get the geometry of the hydraulic fractures. The midpoint of the strain or pressure sensor/interval and the injection point is known and the picked time is calculated for the corresponding corrected injection volume. The fracture distance of HF3 agrees between strain and seismic observation for small injection volume. With increasing injection volume, the seismic events propagate towards 10 m for an injection volume of 700 l. Two strain measurements indicate fracture opening 5 to 6 m away from the injection point and instantaneous pressure increases 7 m away for an injection volume of 50 to 105 l. For experiment HF8, the strain measurements at 30 l indicate a distance of 6 m from the injection point, where the farthest seismic event is 7 m away from the injection interval. The pressure data point from experiment HF8 has a distance of $\sim$9 m and respond after 20 l of injection. At the same volume, the seismic cloud indicates a distance to injection of around 8 m. Considering the strain and pressure measurements from experiment HF2, we see that the distance of the seismic events is two times smaller compared to a strain sensor. It is remarkable that the seismic events are restricted to within 10 m distance at high-pressure injection even though we know the hydraulic fracture is 15 m in length (HF2 strain sensor at 15 m). This agrees well with the observation of Warpinski et al. (2013) that the hydraulic fracture is essentially aseismic and that the stress-induced microseismicity is located at fractures with a significant dimension around the hydraulic fracture.

4.6 Discussion

4.6.1 Hydraulic and mechanical response to hydraulic fracturing

Hydraulically, two different behaviors were observed in experiments performed south of S3 (HF3 and HF8) respective north of the S3 (HF1, HF2 and HF6) shear zone. The differences consisted of lower pressure levels (fracture propagation, jacking and ISIP), larger recovered water volumes, and larger final injectivity for experiments north of S3. Our proposed explanation of this behaviour is as follows.
During the experiments performed south of S3, the new initialized HF was only able to propagate a short distance in intact rock before it connected to the densely fractured S3 shear zone, which is bounded by two metabasic dykes and therein two subnormal fracture systems are found. This high transmissive structure is able to drain the injected fluid from the HF towards the AU tunnel. None of the HF experiments performed south of S3 were able to fracture through this geological structure. This is due to two reasons 1) the structure large transmissivity drain the fluids and prevent further pressure propagation and 2) the stress variations in the structure vicinity are not favourable for further fracture propagation. This is further supported by the small fluid recovery (less than 2%) from the injection borehole for these injection tests, which suggests a strong hydraulic gradient forcing the injection fluid into the S3 shear zone and toward the AU tunnel. The HF experiments north of S3 (HF1 and HF2) were able to initialize and propagate before leak-off dominated into the natural fractures associated with the ductile shear-zone S1. This less transmissive S1 shear zone can be described by a single fracture system, where one part of the fractures are capable to transport fluid and another part only store the fluid (known as dead-end fractures). These tests are also more distant from the AU tunnel and thus in a volume isolated from its influence. Therefore, the observed fluid recovery from the injection location reaches values of 15.0-23.5% for the first two refrac cycles. The HF6 experiment is comparable with HF1 and HF2 except of pre-existing fractures influenced hydraulic fracturing initiation.

The tilt response reflect the hydraulic balance observations, i.e. the tilt magnitudes are smaller for the experiment south than north of S3. The FBG-strain sensors show both tensional and compressional signals. High tensional signals are related to fracture pressurisation and opening reflecting hydraulic connections. In response to fracture opening, some other segment of the rock mass need to compensate and this is captured by the observed compressional signals. An example of such behaviour is visible along FBS2 in Fig. 4.10f, with increasingly compressive signal from 5 to 16 m and from 40 to 26 m centered around and strongly tensional rock mass section at 20 m. The repartition of strain response is also influenced by the location of the injection south of north of S3. For the tests located south of S3, a tensional signal on the FBG sensors is predominantly observed in the S3 shear zone. The temporal evolution of strain signal also suggest modifications of flow path during the injections. Indeed, some sensors that initially react in compression shows later an abrupt reversal toward tensional strain, indicating that they are now part of the active flow system. In turn this influences previously active sections as sensor that were in tension stabilise or reverse, indicating a transfer of the flow portion towards the newly activated rock mass sections (Fig. 4.10).

For the injection locations north of S3, the geometry of our monitoring system implies that the distance between the injection points and the FBG sensors is comparatively larger. Therefore, smaller strain magnitudes are expected and observed.

4.6.2 Borehole trace and fracture tortuosity

The comparison of the fracture trace orientation at the borehole wall observed by acoustic televiewer logging with the orientation of the seismic cloud associated with a given fracture allow assessing fracture rotation, also referred to as tortuosity, in the near field of the borehole (Bunger and Lecampion, 2017). An angular difference of about 30° is typical for most of our experiments. The inflating packers isolate the injection zone, therefore the HF initiate in the region controlled by near-wellbore stress concentration. This depends on the created fracture morphology and the orientation of the borehole with respect to the in-situ stress state. This problem entirely relates to bigger uncertainty in determining the stress orientation from direct wellbore information using hydraulic fracturing. The minifracs indicate a bigger variability for the trace orientations than for the seismic cloud data (Fig. 4.14). These experiments were primarily performed in intact rock in two horizontal and one sub-vertical borehole and affected a small volume of intact rock around the borehole. For the HF experiment larger amount of fluid was injected in a moderate fractured rock mass and the flow rate was around 5 l/min during the frac cycle. The variability tend to be smaller for the HF traces using a higher flow rate promoting dominant fluid pathways compared to low flow rate (MF), which tend to have different fracture geometries in the near-wellbore. The big flow rates and the test volume interacting with the hydraulic fracture will inevitably reach some significant features that affect the geometry of the seismic cloud, which has been confirmed by our experiments (more in the following section). The fracture traces observed at the borehole wall mostly extended below the packers. It is unclear if they initiated at the packer location or grew beyond them later during the successive propagation phase of the experiments.

4.6.3 Seismic response and fracture geometry

A key element to track fracture geometries beyond the borehole wall traces is microseismic event clouds. The spatial resolution of our seismic data do not permit to map near well effect, but allow assessing the fracture geometry at a scale >1 m. Strain response and pressure observations also permit to some extent to track the geometry of hydraulic fractures. These data allow us to show that the geometry of the fractures departs strongly from the idealized radially growing penny-shaped or 2D plain strain fractures. Instead, we observe fracture extension initially vertically downward developing later along an E-W oriented plane. The flow geometry is rather one-dimensional and pipe-like, likely formed by natural fracture intersections (Evans et al., 2005). In addition, during experiment HF2, multiple fractures at the early time of the injection were observed. Evidence for these early fractures not far apart from each other are given by two tensional signals in strain monitoring borehole FBS1 at a depth of 31.8 and 33.0 m (Fig. 4.10b).

Generally, this confirms the strong influence of pre-existing fractures and fracture intersections on the structure of the hydraulic fracture propagation. It is furthermore noteworthy that the approximation of a penny-shaped fracture may not be appropriate in our case as the seismic clouds indicate a unidirectional instead of radial fracture growth (compare Figure 4.8). Therefore, multiple fractures should be considered to advect the fluid rather than a single fracture. Considering the fracture geometry with two different orientations (HF2, HF3) a leak off point may be estimated, where the fluid starts to follow the pre-existing fracture network striking in E-W direction. This leak off point seems to be at a distance of 10 m from the injection point (Fig. 4.15). Further away from the injection point no seismic activity was observed. With ongoing hydraulic fracturing, more and more pre-existing fractures will be connected, which results in an increase of swept volume and a decrease fracture fluid pressure. This decreases the efficiency to create new fractures and therefore seismicity decreases until enough overpressure is created to shear along pre-existing fractures or continue to grow tensile fractures. The interpretation agrees with the conceptual model for the HF experiment described as primary fracturing with shear stimulation leak off by McClure and Horne (2014).

The maximal number of located seismic events from the HF experiment is 730 and the one from the minifracs is 646. However, seismic activity seems to be larger for the MF given the comparably smaller injection volume of 10 l compared to >1000 l for the HFs. Only experiments HF2 and HF8 reach a number above 100 located seismic events (Fig. 4.13). A possible reason may be stress relaxation from the HS experiments (Krietsch et al., 2020) executed 5 months before the HF experiments. This would mean that shear relieved in the previously stimulated rock volume prevents new seismicity to occur. However, it seems that the HF experiments have also been conducted in a stress field that is naturally different from the MF locations.

4.6.4 Permeability creation by HF

All the performed hydraulic fractures generated a transmissivity increase of about three orders of magnitude. This increase remains after the pressure is relieved and in this sense is permanent, i.e. is not related to the transient fracture opening under high-pressure injections. This indicates that the fractures never completely close back when the pressure is relieved. The final transmissivity matches one of an unstimulated fracture in our rock mass (Jalali et al., 2018a). The final transmissivity correlates positively with the final injectivity, which characterizes the newly created hydraulic fracture. Considering the injectivity value from the pressure-controlled step test has the advantage that it is directly related to the bulk mass compliance (rock mass compliance and fracture compliance) at short timescale. In addition, we can characterize the lift-off (herein: jacking pressure) of the intersecting fracture and the injectivity after jacking in the injection interval. The drawback is that the flow is only at a quasi-steady state. For transmissivity values, we used constant head injection and pulse injection tests at low pressure (< 0.6 MPa). This method is time-consuming and it does not account for mechanical effects but has the advantage to reach steady-state conditions, which allow a characterization of the bulk volume farther away than the pressure-controlled step test.

Hence, both methods are mandatory to understand the change in the flow field and the permeability. Considering an EGS system with an injection and a production interval, then a certain injection pressure and probably a back pressure on the production interval is applied. Both injection and production intervals are able to change the hydro-mechanical parameters of the nearby fractures. Then the injectivity value is able to describe this interaction, where the transmissivity describes the overall bulk volume of the connected fracture network. In our experiment, all the newly created hydraulic fractures (except HF6) were mechanically closed after the reservoir was depressurized. Low-pressure constant head injection was insufficient to open the closed hydro-fracture. Thus, the new created transmissivity is only linked to the new hydraulic fracture intersecting the wellbore. In term of scaling we estimate transmissivity only on single wellbore and no cross-hole tests were performed to estimate the new fracture network transmissivity. Therefore, the presented values of the final transmissivity are rather small.

4.6.5 Stress heterogeneity

For experiments executed south or north of S3 the ISIP stabilize around 5 MPa and only deviates slightly. The jacking pressure is similar in magnitude compared to the ISIP for the experiments south of S3 (see Fig. 4.5). The situation differs for the experiments north of S3 as the magnitude of the jacking pressure is declined. It reaches a value between 60-80% of ISIP. The similarity of jacking pressure and ISIP is a strong indication that they reflect the minimum principal stress magnitude, but further analysis is necessary to rely on that, which is not part of this publication.

Approaching the shear zones S1 and S3 changes the stress observations significantly. For the HF experiments, it is best described by the perturbed stress field for small volumes of injection, i.e. frac and first refrac cycle. Fig. 4.16a shows the perturbed stress state as Mohr circles for the newly created hydraulic fractures from the ATV log (triangles) and the best fit plane from seismicity (squares). Assuming, higher perturbation during the breakdown cycle creating the new hydraulic fracture intersecting the borehole agrees well with the higher overpressure. Propagating the hydraulic fracture further away results in a decrease in the overpressure in the perturbed stress field (Fig. 4.16b) but an increase in the unperturbed one (Fig. 4.16c). Therefore, the unperturbed stress state cannot describe the behavior of the hydraulic fracture at the early time. The orientation of the seismic cloud is sub horizontal towards South considering all located seismic events (i.e. RF2). This reorientation of the fracture is controlled by the leak off into the pre-existing fracture network striking in E-W direction. Note, that the density of pre-existing fractures is increased approaching the S1 and S3 shear zones. At this point, the best estimate of the stress state can be described by the unperturbed stress field assuming smaller stress magnitudes. Fig. 4.16d shows the situation in terms of minor and major principal stress axis being reoriented approaching the shear zones. The perturbed stress field is a consequence of the pre-existing fractures related to S1 and S3 and scatter the perturbed one. We assume this re-orientation of the fracture depends directly on the connectivity of the pre-existing fracture network.

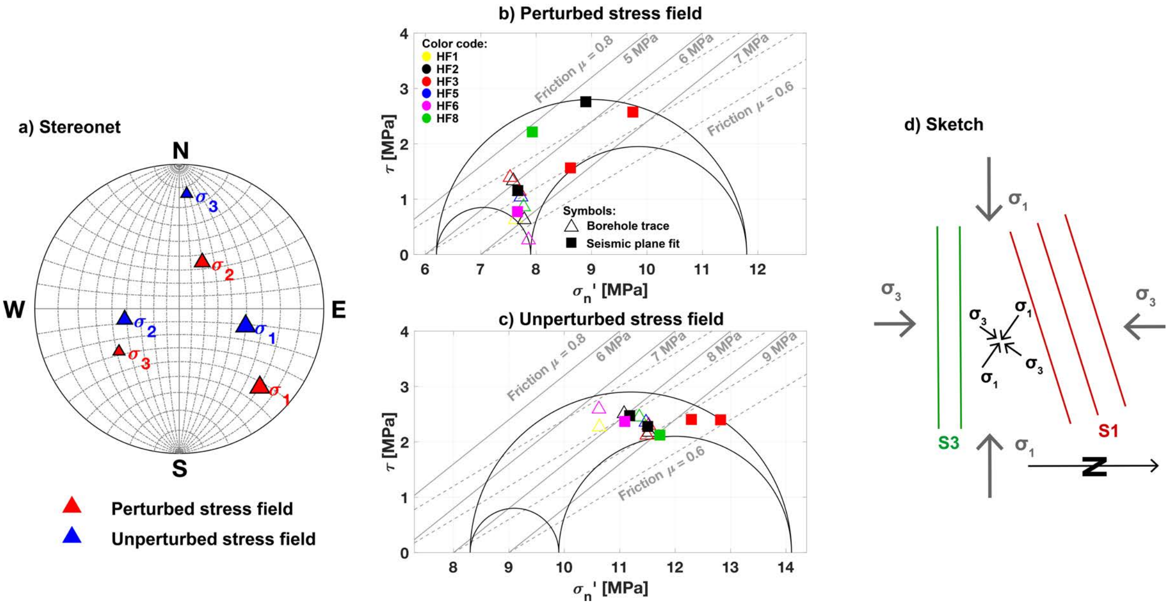

Fig. 4.16 a) Stereonet with perturbed and unperturbed stress field and Mohr-Coulomb diagram representing the perturbed b) and unperturbed c) stress field (including hydrostatic pressure of 0.3 MPa) as Mohr circles. The failure limits assuming a friction coefficient of 0.6-0.8. Overpressure of 5 to 9 MPa are shown. The new created hydraulic fractures from the ATV log (triangle) and the best fit plane from seismic (squares) are presented with computed normal stress and shear stress. The color and symbol key in figure b) is as well applicable for figure c). d) The sketch indicates the change from unperturbed (grey arrows on the outside) to the perturbed stress field (black arrows inside) approaching the two different shear zones S1 and S3.

4.7 Conclusions

In this paper, the spatial and temporal evolution of rock deformation, transient fracture fluid pressure, and seismicity during six intermediate scale hydraulic fracturing experiments are presented. One of the key findings of this work is that the fracturing processes are strongly influenced by site specific characteristics, natural fractures and local heterogeneities. This is to be expected in any rock masses since heterogeneities are always present in natural media. If the details of the observations presented in this paper are site specific, the overall processes and behaviour are likely reproducible at any site and we attempt to formulate these general behaviours in the following conclusions:

1. The heterogeneities lead to distinct behaviour in terms of pressure responses and flow: tests performed North or South of the brittle-ductile shear zone S3 respond differently. We associate these differences principally with two effects. Firstly, the shear zones have impacted the stress state locally and thus in turn this affect the fracture propagation. Secondly, the shear zones and the associated fracturing influence the flow in the experimental volume. When the hydraulic fracture grows, it connects and leaks into the pre-existing fracture network and thus at some point the energy required to create new fracture surfaces isn't sufficient and tensile fracture stops. The flow is then largely dominated by the natural fracturing. In that regard, the brittle-ductile shear-zone S3 acts as main drain and constant pressure boundary while connection to the S1 shear-zone and associated fracturing provides larger storage possibilities.
2. The deformation field associated with fracture growth is complex showing local extension on the fracture path that is compensated by compression in the surrounding rock mass. Such deformation pattern is strongly coupled to the pressure field variations associated with the injections.
3. The creation of new fractures at the borehole is clearly visible on borehole wall acoustic images. The orientation of the fracture traces are however variable and do not provide a good estimation of the independently measured far field stress orientation. The variability of the fracture trace could be explained by rock strength anisotropy (Dutler et al., 2018a). It could also be influenced by packer stresses or local stress heterogeneities induced by natural fractures as we observed that the new fracture trace extend below the packer and often abut against natural fractures. Our data set doesn't allow us to determine if the fractures initiate below the packers or in the injection interval, although since the packer pressure is always maintained above the interval pressure to insure sealing, the former is not unlikely.
4. The growth of the hydraulic fractures is strongly influenced by natural fractures. This leads in the details to complex geometry departing from theoretical mode I fracture geometries.

Our data highlights the simultaneous growth of parallel fracture strands. It also suggest channelized growth (pipe-like geometry) instead of planar growth.

5. The number of seismic events associated with each fracture treatment varies a lot. It is not related to the injected volume, but seems to be influenced by heterogeneities in stress and flow with our experimental volume.
6. A significant increase in transmissivity of 2-4 order of magnitudes from well test before and after HF was observed. The final transmissivity correlates positively with the final injectivity obtained from the pressure-controlled step tests. Such permanent permeability increase is not consistent with pure mode I fractures in a homogenous media that would close back after depressurization. The heterogeneities and associated complexity of the hydraulic fractures probably favors the permanent transmissivity gain. The final transmissivities are comparable with the unstimulated natural fractures in our rock mass (Jalali et al., 2018b) which support the conclusion that the connectivity to the natural fracture system controls the final transmissivities.
7. Despite the complexity of the local fracturing processes, the spatial distribution of microseismic events associated with the fracture growth seems to be predominantly controlled by the stress state. In that regard, we observe rotations related to stress perturbations that have been highlighted within our experimental volume (Krietsch et al., 2019). A comparison of deformation and pressure monitoring within the rock mass and the location of microseismic events suggest that the activation of seismic events lags slightly behind the propagation of the pressure front. This suggest that treatment size estimated by microseismic mapping could underestimate the actual rock volume affected by hydraulic fracturing processes.

Data availability

The Grimsel ISC Experiment Description is available at https://doi.org/10.3929/ethz-b-000310581 (Doetsch et al., 2018a) and the hydromechanical data set from the Grimsel ISC hydraulic fracturing experiment is available at https://doi.org/10.3929/ethz-b-000328270 (this publication). The data from the minifrac experiments are available at https://doi.org/10.3929/ethz-b-000217536 (Gischig et al., 2018) .

Acknowledgements

The ISC is a project of the Deep Underground Laboratory at ETH Zurich, established by the Swiss Competence Center for Energy Research - Supply of Electricity (SCCER-SoE) with the support of Innosuisse. Funding for the ISC project was provided by the ETH Foundation with grants from Shell and EWZ and by the Swiss Federal Office of Energy through a P&D grant. Hannes Krietsch is supported by SNF grant 200021_169178. Linus Villiger is supported by grant ETH-35 16-1 and Nathan Dutler is supported by SNF grant 200021_165677. We thank Gerd Klee and his staff from MeSy Solexperts, Bochum (Germany) for their good collaboration and helpful discussions. The Grimsel Test Site is operated by Nagra, the National Cooperative for the Disposal of Radioactive Waste. We are indebted to Nagra for hosting the ISC experiment in their GTS facility and to the Nagra technical staff for onsite support.

Chapter 5

Hydromechanical insight of fracture closure during in-situ hydraulic fracturing in crystalline rock

The injection protocol and operation planning were designed by N.D. and B.V. All the authors were part of the data acquisition team during the HF experiments of the ISC project, where F.A. was the project administrator. The formal analysis, data curation, data visualization inclusive writing the original draft preparation was done by N.D. The writing—review and editing was done by V.G., H.K., M.J., B.B., C.R. and F.A. The supervision and funding acquisition for this work was done by B.V.

Please cite this chapter as: Dutler, N., Valley, B., Gischig, V., Jalali, M., Brixel, B., Krietsch, H., Roques, C., and Amann, F.: Hydromechanical insight of fracture opening and closure during in-situ hydraulic fracturing in crystalline rock, IJRMMS, in review

Abstract

Six hydraulic fracturing (HF) experiments were conducted in situ at the Grimsel Test Site (GTS), Switzerland, using two boreholes drilled in sparsely fractured crystalline rock. High spatial and temporal resolution monitoring of fracture fluid pressure and strain improve our understanding of fracturing dynamics during and directly following high-pressure fluid injection. In three out of the six experiments, a shear-thinning fluid with an initial static viscosity approximately 30 times higher than water was used for three of the six experiments to understand the importance of fracture leak-off better. Diagnostic analyses of the shut-in phases were used to determine the minimum principal stress magnitude for the fracture closure cycles, yielding an estimate of the effective instantaneous shut-in pressure (effective ISIP) 4.49±0.22 MPa. The jacking

pressure of the hydraulic fracture was measured during the pressure-controlled step-test. A new method was developed using the uniaxial Fibre-Bragg Grating strain signals to estimate the jacking pressure, which agrees with the traditional flow versus pressure method. The technique has the advantage of observing the behavior of natural fractures next to the injection interval. The experiments can be divided into two groups depending on the injection location (i.e., South or North to a brittle-ductile S3 shear zone). The experiments executed South of this zone have a jacking pressure above the effective ISIP. The proximity to the S3 shear zone and the complex geological structure led to near-wellbore tortuosity and heterogeneous stress effects masking the jacking pressure. In comparison, the experiments North of the S3 shear zone has a jacking pressure below the effective ISIP. This is an effect related to shear dislocation and fracture opening. Both processes can occur almost synchronously and provide new insights into the complicated mixed-mode deformation processes triggered by high-pressure injection.

Nomenclature

C	Diffusion coefficient [m^2/s]
c_L	Carter leak-off coefficient [m/s$^{0.5}$]
C_t	Total system storage coefficient [m^3/MPa]
G	G-function [dimensionless]
g	g-function [dimensionless]
K	Consistency parameter of fluid [Pa*s, cPs]
n	Flow behaviour parameter [dimensionless]
p, p_{inj}, p_{exp}	Fluid pressure [MPa]
$p_{formation}$	Formation pressure [MPa]
q, q_{inj}	Volumetric flow rate [l/min]
q_{ave}	Averaged volumetric flow rate [l/min]
t	Time [s]
$t_{shut-in}$	Time of shut-in [s]
t_{end}	Time of the test end [s]
t_a, Δt	The actual shut-in time [s]
V	Fluid volume [m^3]
v_L	Carter leak-off velocity [m/s]
Δp	Pressure recovery [MPa]
$\Delta p'$	Bourdet derivative of pressure recovery [MPa]
δ_{exp}	FBG reading [μm]
σ_i	for i=1,2,3, principal stress magnitudes [MPa]
σ_n	Normal stress [MPa]
τ	Shear stress [MPa]
Abbreviations	
ATV	Acoustic borehole televiewer
DFIT	Diagnostic fracture injection tests
FBG	Fibre-bragg grating
HF	Hydraulic fracturing
HS	Hydraulic shearing
ISC	In-situ stimulation and circulation
ISIP	Instantaneous shut-in pressure
JP	Jacking pressure
OPTV	Optical borehole televiewer
TPA	Transient pressure analysis
F	Frac cycle
RF	Refrac cycle
SR	Pressure-controlled step-test
XSW	Xanthan-salt-water

5.1 Introduction

The dynamic injection pressure response monitored during hydraulic fracturing treatments in fractured reservoirs contains information on reservoir hydraulic and geomechanical properties which are, in turn, critical to describe and predict hydromechanical processes. However, the interpretation of pressure data is generally not trivial as it is affected by structures at different scales ranging from a single fracture to complex interactions within a three-dimensional fracture network. Historically, the transient pressure analyses (TPA) that are used as a diagnostic tool relied entirely on analytical models of fluid flow, without hydromechanical coupling. The first and most straightforward solution to constant fluid injection/withdrawal, which governs radial flow in a porous medium, was introduced by Theis (1935) for groundwater flow. Original work for TPA was mainly driven by the oil gas industry, considering both Newtonian and non-Newtonian fluids (e.g., Matthews and Russell (1967)). Subsequently, the TPA was also extended to geothermal wells, including the two-phase flow of water and steam, adsorption of steam and pressurized reservoirs (more in Zarrouk and McLean (2019)). The 'dual-porosity' model of Warren and Root (1963) was the earliest attempt to represent fractured reservoirs. Later, Barker (1988) introduced the generalized radial flow model for fractured reservoirs, which was extended to fractal fracture networks (Acuna and Yortsos, 1995; Chang and Yortsos, 1990).

5.1.1 Background on transient pressure analysis (TPA)

Various diagnostic pressure representations, such as log-log plots, semi-log plots, and various time manipulation techniques, have been developed to interpret the evolution of fluid pressure with time during high-pressure fluid injection (Economides and Nolte (2000), for a review). Many methods have the aim to identify diagnostic pressure levels and derive stress estimates (see Schmitt and Haimson (2017), for a review). In tight formations, diagnostic fracture injection tests (DFIT) are used to estimate key parameters, such as the minimum principal stress, fluid leak-off (fluid loss from the hydraulic fracture towards the rock matrix or other natural fractures), permeability, and pore pressure. Once injection stops, i.e. the injection interval is shut-in, the pressure rapidly drops at first, followed by a regime with a slower pressure decay at late times. The point of transition between the two regimes measured immediately after shut-in is referred to as the instantaneous shut-in pressure (ISIP) and is often considered to be a reasonable approximation of the minimum in-situ principal stress magnitude for fracture fluids with low viscosity in moderately fractured crystalline rock mass. Authors working in the oil gas industry argue that the fracture closure pressure may be a better estimate for tight rock formations. Problems generally arise due to the indifferent use of ISIP and fractures closure pressure in the literature (Schmitt and Haimson, 2017).

The analysis of DFIT based on G-function and its derivative introduced by Nolte (1979) also allows to quantify the minimum principal stress magnitude, under the assumptions that (1) leak-off is not pressure-dependent and (2) fracture compliance is assumed to be constant during fracture closure. Barree et al. (2007) introduced a method of analysis using the G-function and its derivative drawing a line from the origin to the tangent of the G*dp/dG. The method is referred to as the 'Barre tangent method' following the terminology after Jung et al. (2016).

It was challenged by McClure and Horne (2014) and McClure et al. (2016), who pointed out that this method has no theoretical justification. McClure and Horne (2014, 2016) and Jung et al. (2016) proposed the 'compliance method' to estimate the fracture closure, but it tends to reflect only the onset of fracture closure. Wang and Sharma (2019) pointed out that the upward curved G*dp/dG is caused by the fracture-pressure dependent leak-off with compliance variation during fracture closure. Therefore, they proposed to pick the closure, in between the compliance and Barre tangent method, which is known as the 'variable compliance method' and should give a better estimate of the minimum principal stress component. McClure et al. (2019) defined 'contact pressure', which is equivalent to the definition of 'closure pressure' (McClure et al., 2016). It is defined as the pressure, where the contact of the fracture walls causes a measurable change in the system stiffness caused by the contact of fracture walls. The method uses the G-function and the minimum of dp/dG needs to be identified prior to contact pressure. If the hydraulic fracture intersects highly conductive natural, pre-existing fractures, the dp/dG curve decrease monotonically and challenges this method.

5.1.2 Hydromechanics

Laboratory experiments conducted on single fractures have brought detailed insights on the hydromechanical properties of single fractures and their behavior during fluid injection (Rutqvist and Stephansson, 1996). Such behavior can be described by an empirical closure law including hyperbolic (Bandis et al., 1983; Goodman et al., 1968), semi-logarithmic (Evans et al., 1992; Zhao and Brown, 1992) or statistical distribution (Preisig et al., 2012) combining normal stress and normal closure using laboratory experiments (e.g., step-pressure tests or purely mechanical tests). A hysteresis effect is typically observed in the uniaxial strain component measured across the fracture when comparing the aperture state before and after the opening and closing cycle. This effect, however, cannot be detected from a diagram of injection flow-rate versus injection pressure (Cornet and Valette, 1984).

Fracture roughness induces a high spatial variability in local mechanical apertures. Zones, where the two fracture surfaces are in contact (contact area), may be strongly dependent on the scaling of the fracture roughness and the normal stress acting on the fracture plane. Changes in contact area lead to non-linear empirical closure relationships (assuming constant mechanical parameters) and spatial distribution of local mechanical apertures may create strong flow channelization and tortuosity, which in turn impacts fracture transmissivity (Méheust and Schmittbuhl, 2003). Laboratory experiments on single fractures are typically performed at the centimeter or meter-scale (0.01 - 1 m). It is well known that mechanical and hydraulic apertures are generally not equivalent (Pyrak-Nolte and Nolte, 2016; Raven and Gale, 1985; Renshaw, 1995). In-situ field experiments investigate processes that involve fracture networks. Mechanical apertures are therefore challenging to determine in situ. Based on hydraulic tests, one can only assess fracture transmissivity as a proxy for hydraulic aperture, which encompasses the effects of fracture roughness on the resistance to flow.

5.1.3 Research objectives

This study extends the analysis of presented results from in-situ hydraulic fracturing experiments performed at the Grimsel Test Site (GTS) in Switzerland (Dutler et al., 2019), which were executed in the framework of the In-situ Stimulation and Circulation (ISC) project (Amann et al., 2018). The unique and high level of experimental control allows us to extend the knowledge of the stress state. DFIT methods paired with fracture opening pressure are used to constrain the minimum principal stress magnitude. In addition, the hydraulic fracture intersecting the open wellbore section from geophysical logging and seismic cloud observation constrain the orientation of the minimum principal stress and allow to derive a stress tensor for the HF experiments.

5.2 Rock mass characterization and experimental setup

5.2.1 Rock mass characterization

The rock volume investigated is located in the southern part of the GTS and is accessed by an array of boreholes monitoring deformation (i.e., referred to FBS1, -2, -3), fluid pressure (not used in this study, PRP1, -2, -3) and seismicity (GEO-1 to -4, not shown) (Fig. 1a). Additionally, two 146-mm diameter boreholes (INJ1, -2) were drilled to high-pressure fluid injection. During the HF experiments, one of the boreholes was used for the injection while the other borehole was used as an additional pressure monitoring borehole.
The host rock consists of the Grimsel Granodiorite. It has a magmatic fabric characterized by a strong textural overprinting that occurred during Alpine orogeny resulting in a pervasive foliation oriented 157/75°. The following properties were measured in the laboratory under drained conditions: Youngs-modulus, 20 - 40 GPa (Nejati et al., 2019b), Poisson's ration, 0.1 - 0.2 (Nejati et al., 2019b), critical fracture toughness, 0.7 - 1.7 MPam (Dutler et al., 2018a) and tensile strength, 5.6 - 14.7 MPa (Dutler et al., 2018a).

The moderately fractured host rock is crosscut by two sets of shear zones that differ in terms of deformation history and orientation (Fig. 5.1a+b). The shear zones of the first set (referred to as S1.0, S1.1, S1.2, and S1.3) experienced retrograde brittle deformation. They have an ENE-WSW strike and dip towards SSE. The shear zones of the second set (referred to as S3.1

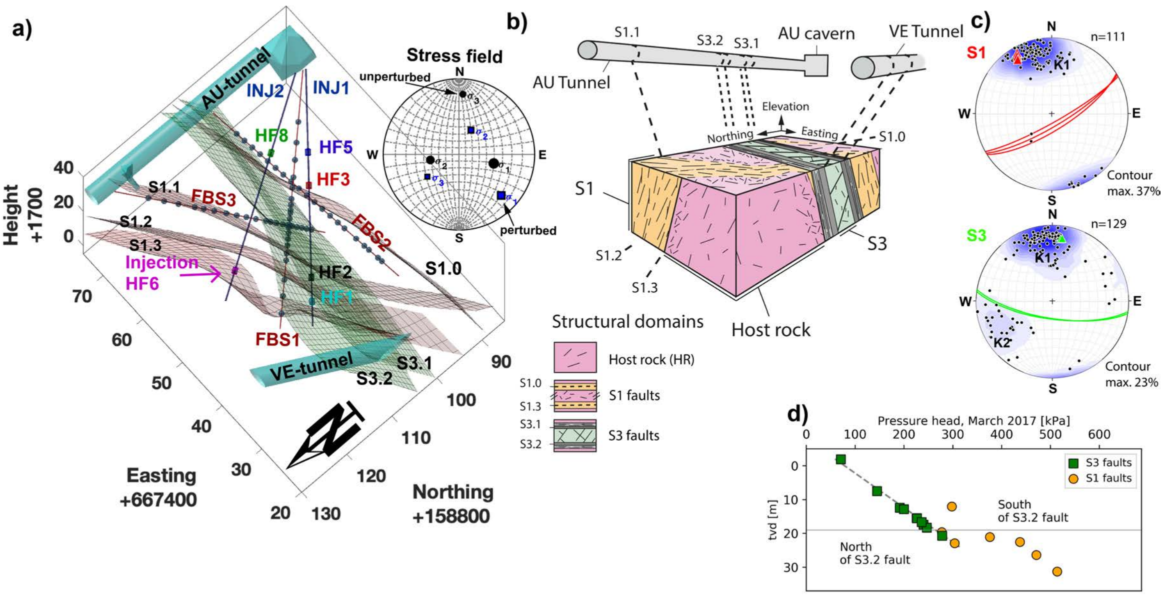

Fig. 5.1 a) Overview of the setup: the injection location in the injection boreholes (INJ1 and INJ2), the Fiber-Bragg Grating (FBG) sensors in the FBS boreholes, tunnels, and shear-zones (Krietsch et al. (2018) inclusive additional new S1.0 interpolation). The lower stereonet indicates the stress field (Krietsch et al., 2019). b) The geological model is presented in three different structural domains (Brixel et al., 2020a), and c) the two lower stereonets presenting the fractures associates with the S1 (red) and S3 (green) faults (Dutler et al., 2019). d) The pressure head (pore pressure) is given for the true vertical depth (tvd) and is differentiated into two major structures before the HF experiment.

and S3.2) are associated with the reactivation of two pre-Alpine, E-W-striking metabasic dikes. A densely fractured zone (up to 20 fractures per meter, depending on location) was identified in the eastern part of the test volume in between the two S3 shear zones. An increase in fracture density was also observed around the S1 shear zone. Two fracture sets are associated with the S3 zone, where set K1 is oriented similar to the S3 zone, and set K2 strikes NNE-SSW and dips towards ESE (Fig. 5.1c) (Brixel et al., 2020a; Doetsch et al., 2020; Krietsch et al., 2018). A fracture is considered here as a visually-detectable structure whose trace could be observed on an optical (OPTV) or acoustic (ATV) borehole log. We do not account for grain-scale micro-cracks in this study.

The ambient in-situ pore pressure based on the cross-hole hydraulic testing setup deployed prior to the HF experiments in March 2017 (field setup not shown here) is presented as a function of true vertical depth (tvd) in Fig. 5.1d. With increasing depth, the pore pressure increases, whereas the tunnel level is a natural drainage level. The pore pressure is around 250 kPa and 500 kPa for experiments on S3 and S1 structures (Fig. 5.1d). Note that on the time scales investigated in this study, pressure diffusion (hence flow) is primarily controlled by fractures. This is a consequence of the very low hydraulic transmissivity of the host rock (10^{-14} - 10^{-13} m^2/s, Jalali et al. (2018b)).

The stress field was measured on the southern side of the AU cavern in unfractured rock at distances greater than 20 m from brittle-ductile shear zones (referred as unperturbed stress tensor by Krietsch et al. (2020). Additionally, the stress state was characterized up to a few meters towards the S3.1 shear zone. With decreasing distance to the shear zones, the stress field appears to rotate and a decrease in magnitudes (i.e., especially the minimum principal stress). The stress state close to the shear zones is referred to as the perturbed stress state (Krietsch et al., 2020) (Fig. 5.1a and Tab. 5.1).

Table 5.1 Magnitudes of the unperturbed and perturbed stress state from Krietsch et al. (2020).

Stress state	σ_1 **[MPa]**	σ_2 **[MPa]**	σ_3 **[MPa]**
Unperturbed	14.4	10.2	8.6
Perturbed	13.1	8.2	6.5

5.2.2 Experimental setup

In an earlier study (Dutler et al., 2019), we showed that the location of the performed experiments significantly influences the measured hydraulic and rock mass deformation response (see Fig. 5.1a for injection location). We can divide the experimental responses depending on the main geological structures, which will influence the response e.g., S1 (HF1, HF2, and HF6) and S3 (H3, HF5, and HF8) domain. The injection interval measured 1.0 m and was equipped with a pressure transducer and flow lines. A data acquisition system recorded the pressure in the injection interval of the INJ boreholes, the flow rate, and the packer pressure in the injection intervals with a sampling rate of 20 Hz. The injection pressure and flow were measured up-hole at the water injection lines next to the injection pump. All acquisition systems were time-synchronized.

The rock mass deformation monitoring system consists of 60 Fibre-Bragg Grating (FBG) sensors in the three FBS boreholes (Fig. 5.1). 20 FBG sensors were installed along each FBS borehole to characterize the strain field in both intact and fractured rock. The FBG sensors have a base length of 1 m, and the sensors were pre-strained to enable monitoring of extension and compression. The cross-hole distances between deformation monitoring intervals and the injection interval ranged between 3 m and 35 m. In this study, we consider positive strain as compression. The strain data were recorded with a 1 kHz sampling rate. An extensive description of the ISC project, including the complete monitoring setup, characterization steps, and stimulation steps, can be found in Doetsch et al. (2018a).

5.2.3 Injection protocol

The flow rate q_{inj} and the injection pressure p_{inj} from test HF2 and HF8 are presented in Fig. 5.2a and b, respectively. HF2 is representative for tests close to S1 shear zones and HF8 is characteristic for tests south of the zone S3 (Fig. 5.1a). Both protocols start with a packer integrity test (pulse injection test), to check the packer sealing followed by the frac (F) cycle, which had the goal to initiate a new hydraulic fracture. The subsequent refrac cycles (RF1 and RF2) use flow-controlled injection with increasing flow rates. The rationale behind this is that the propagating fracture loses power at the fracture tip, which should be compensated for at the increasing flow rate. The pressure-controlled step test was added to the protocol to estimate jacking pressure and injectivity from the hydraulic fracture intersecting the open wellbore section. The injection fluid was tap water from the Grimsel Test Site, except for three out of six HF experiments (HF5, HF6 and HF8). The XSW mixture was injected during the fracture propagation cycles RF1 and RF2. The fluid consisted of 0.025% Xanthan and 0.1% salt mixed in tap water from the Grimsel Test Site. Mixing was achieved and maintained by pumping the fluid through a close loop circulation. For simplicity, we consider the Ostwald de Waele (Saramito, 2016). Literature values were used to estimate consistency parameter K =0.03 Pa*s and flow behavior parameter n = 0.6 (Amundarain et al., 2009; Mrokowska and Krztoń-Maziopa, 2019; Zhong et al., 2013). In addition, we measured the dynamic viscosity of XSW mixture at an effective shear rate of 1 Hz using an analogue dial reading viscometer PCE-RVI 1 and got an effective viscosity of $\sim$ 30 cPs (0.03 Pa*s) for the XSW mixture, which is 30 times bigger than the one for water. Fig. 5.2b includes a third refrac cycle RF3, which was added if the injection fluid in RF1 and RF2 was a Xanthan-salt-water (XSW) mixture. The goal was to dilute and flush XSW fluid out of the system. Additional complexity arises if non-Newtonian fluids are present. For enhanced-oil-recovery applications, the coexistence of Newtonian (water, oil) and non-Newtonian (polymers) fluids complexify transient pressure analysis. The injection of shear-thinning fluids (i.e., fluid viscosity decreases when shear-rates increases) were studied using pressure transient time series (Kamal et al., 2019; Tongpenyai and Raghavan, 1981). Laoroongroj et al. (2012) determined the apparent fluid viscosity of the shear-thinning fluid and the fluid front radius by TPA techniques.

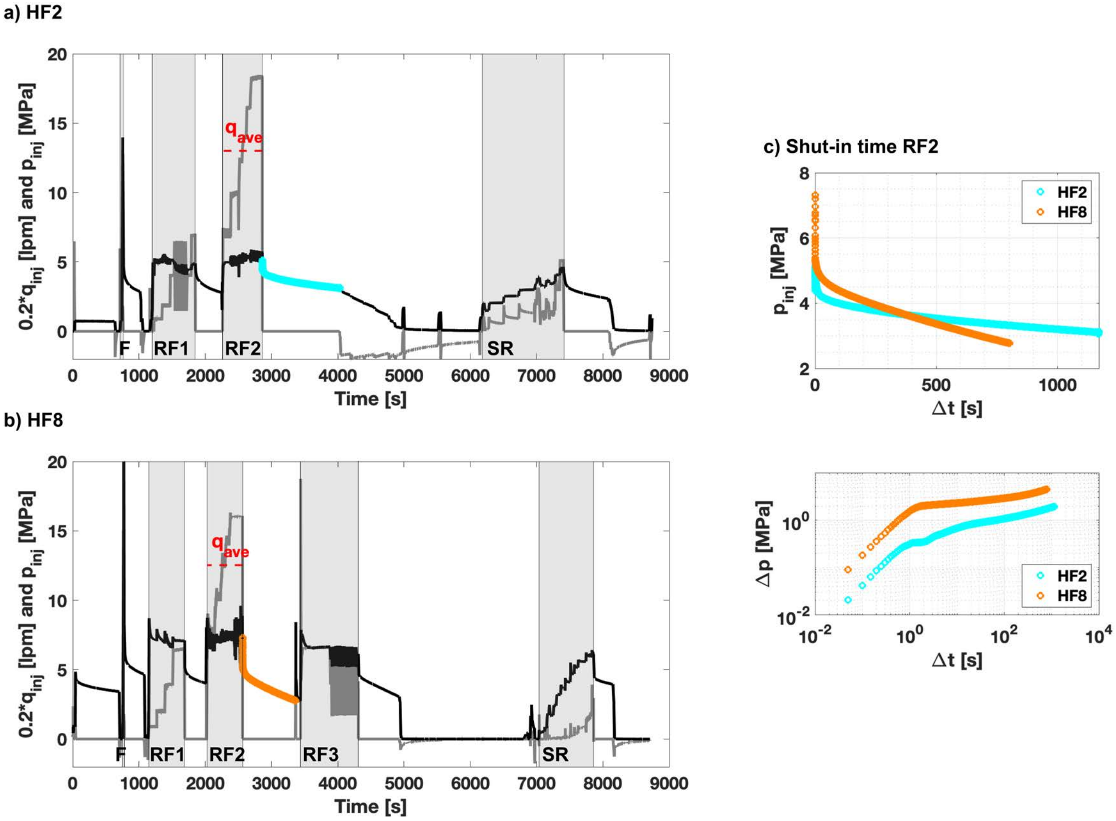

Fig. 5.2 Injection protocol showing the flow rate and injection pressure-time evolution during test HF2 a) and HF8 b). Note that the flow rate is multiplied by a factor of 0.2 to plot everything on a single axis. The first cycle (F) has the goal of creating the formation breakdown followed by refrac (RF) cycles to propagate the hydraulic fracture farther into the rock mass. The shut-in phase of cycle RF2 from test HF2 and HF8 are compared in c) in a linear scale injection pressure and a log-log scale plot recovery during the shut-in time. The last cycle (SR) is a pressure-controlled step test to evaluate fracture characteristics from the new HF.

5.3 Methods

Our approach follows two steps, which are DFIT and pressure-controlled step analyses. First, we briefly describe the basics of DFIT log-log analyses followed by a summary of the interpretation procedures for pressure-controlled steps.

5.3.1 DFIT

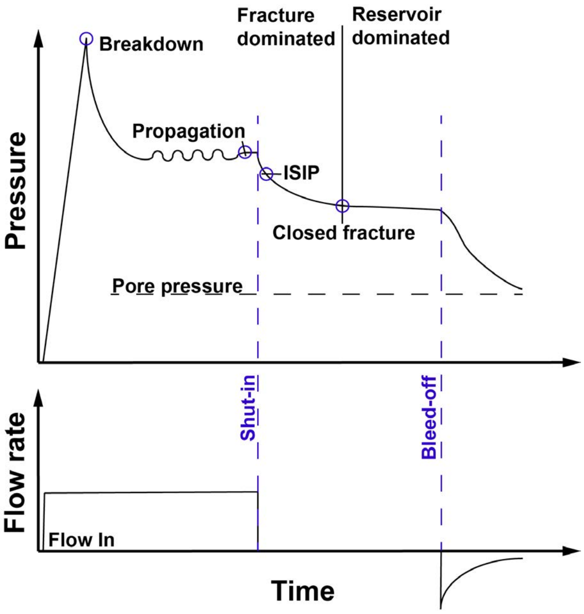

Fig. 5.3 Illustration of idealized pressure response during an hydraulic fracturing (adapted after Schmitt and Haimson (2017)).

Fig. 5.3 presents an idealized pressure and flow rate time series of a typical DFIT. Here, the flow rate is controlled, and variations in injection pressure are monitored uphole. The maximum pressure reached early during the test is referred to as the breakdown pressure and is interpreted as the moment when a new hydraulic fracture is created. Following the breakdown, the pressure drops due to the fracture propagation and associated with fracture volume increase. During fracture propagation, the fluid in the fracture reaches a pressure equilibrium referred to as the propagation pressure. This equilibrium can be influenced by fracture connection to natural fractures and leak-off. When the pump is stopped and the injection interval is shut-in, the pressure drops first abruptly, followed by a regime with a slower pressure decay. The fracture dominated regime is replaced by a reservoir dominated regime if most of the fractures are in contact. In non-ideal cases, the fracture closes rapidly and the contact pressure aligns with the ISIP. This phenomenon is driven by spatial pressure gradients due to intersection of the hydraulic fractures with pre-existing, natural fractures.

The following interpretation procedure was applied:

1. We inspect a plot with pressure, flow rate versus time to pick the start of injection, shut-in time, and the bleed-off time (Fig. 5.2).

2. We construct log-log plots of the shut-in data and derivative using the actual shut-in time (see Appendix 5.A.1 for more details) for all tests during refrac cycle RF2 to investigate the influence of test location and fluid rheology (Fig. 5.4).
3. ‘Barree tangent method’, ‘compliance method’, and ‘variable compliance method’ are presented in Fig. 5.5b), where only the ‘compliance method’ was systematically evaluated.
4. We construct the plots of the actual shut-in time with dp/dG versus G and G*dp/dG versus G (see Appendix 5.A.2). The effective ISIP is extrapolated back to G-time equal to zero if a point of minimum dp/dG prior to contact pressure can be identified (Fig. 5.5b).
5. The ISIP from the pressure-decay-rate method (Lee and Haimson, 1989) is picked from the intersection of two linear fits to the p vs dp/dt curve (Fig. 5.5b). The first line corresponds for most of the tests to a horizontal zero line, and the other line approximates the strong increase of dp/dt, where it does not deviate too far from a straight line.

5.3.2 Pressure-controlled step tests

The pressure-controlled step tests allow estimating the pressure whereby the fracture in the intersecting of the borehole opens (Doe and Korbin, 1987). The objective of these step tests is the characterization of the primary fracture in terms of jacking pressure, injectivity, and fracture stress-aperture relation. The approach adopted here is to combine the injection pressure and uniaxial FBG records.

1. An uniaxial FBG sensor was chosen for further analysis if 1) the Euclidian distance was short (i.e. < 5.4 m), and 2) the direction aligned with the fracture propagation direction using borehole trace and seismic cloud observations (Dutler et al., 2019; Villiger et al., 2020).
2. We constructed a plot of the FGB-record (δ_{exp}) and the pressure (p_{exp}) during the step test. The records were down sampled to 1 Hz, synchronized, and each pressure step was color-coded. The mean value was calculated from the time interval of the colored section and plotted with flow rate versus pressure as well as strain record versus pressure (Figs. 5.6 and 5.7).

5.4 Results and Interpretations

5.4.1 DFIT

Test comparison

Fig. 5.2c, the transient pressure record of refrac cycle RF2 is presented for the two experiments HF2 and HF8. The propagation pressure at the end of the injection is around 5.2 MPa for test HF2 and 7.7 MPa for test HF8. After shut-in, test HF2 shows a smaller pressure drop compared to test HF8. Then, the transient pressure decays slower for experiment HF2 compared to experiment HF8. In Fig. 5.4, the transient pressure records are presented for the second fracture propagation cycle RF2 of all the HF tests. The curves (normalized pressure as well as pressure derivative) are grouped according to their location, i.e. (a) south or (b) north of the S3 zone (refer to Fig. 5.1a) and according to the rheology of the injection fluid, i.e. (c) water or (d) XSW. We observed similar pressure recovery and derivative among the tests grouped by location with respect to the S3 shear zone. However, strong differences can be seen among the tests with similar fluid rheology. This indicates that fluid rheology may have played a second-order role in the observed fluid pressure propagation.

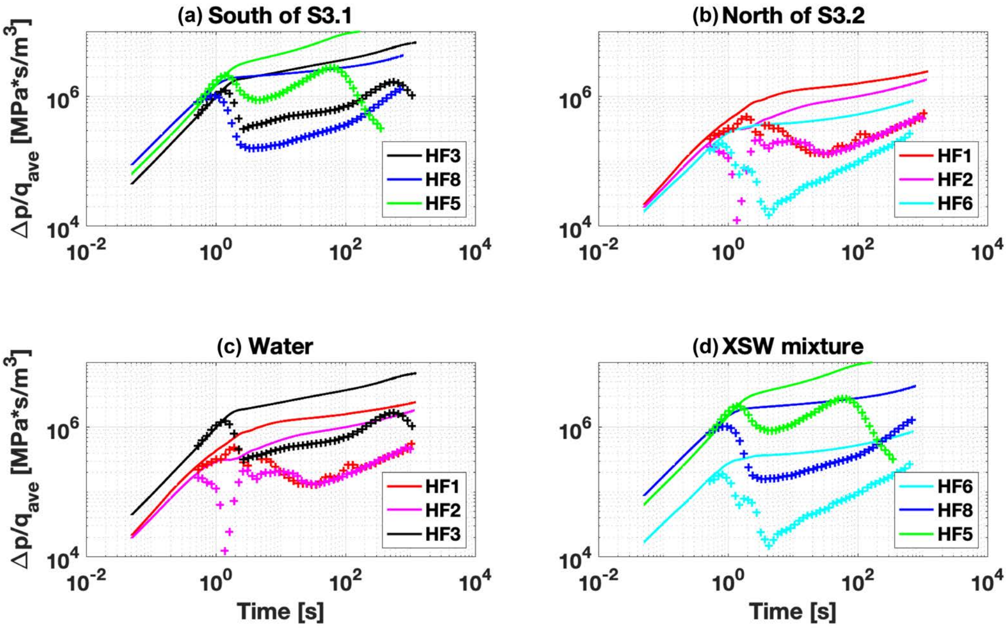

Fig. 5.4 Pressure response from fracture propagation cycle RF2 for all six experiments normalized by the averaged fluid injection rate from cycle RF2, where the pressure and the derivative are indicated by a solid line and crosses, respectively.

Fig. 5.5 presents the evolution of pressure records and their derivatives during actual shut-in time for the HF3 experiment. The sketches (Fig. 5.5a-d) indicate the connectivity of the hydraulic fracture with the natural, pre-existing fractures. The hydraulic fracture was initiated during the frac cycle (Fig. 5.5a) with a maximum injection volume of 1.7 litres (l). A rapid pressure decay is observed and the derivative reaches a maximum at 70 seconds (s). Both have a concave shape. During refrac cycle RF1 a total of 214.4 l was injected. The pressure record (Fig. 5.5b-1) show a strong slope change at 1 s. The pressure record and derivative before one second have the same slope, due to wellbore storage. After one second, the pressure record and their derivative deviate and fracture network response dominates. The global maximum in the derivative is observed at the end of the shut-in time at 500 s. A similar pressure response is observed during refrac cycle RF2 (Fig. 5.5c-1), where a cumulative volume of 835.5 l was injected. The global maximum in the derivative is also observed at 500 s. A bleed-off phase was placed in between refrac cycle RF2 and the pressure step test. Therefore, the cumulative injected volume for the step test is only 71.4 l and the pressure does not reach the magnitudes of previous cycles. The derivative reaches the global maximum at 200 s. The bleed-off lead to a depressurization of the rock mass and a new pressurization takes place during the step test. The smaller injection volume leads to a smaller pressurization front in the rock volume with a dominant leak-off towards the natural fractures. This the reason why the curve of the step test looks squeezed compared to the previous cycle RF2 (Fig. 5.5d-1).

Contact pressure from the G*dp/dG versus G method

Fig. 5.5b-2) shows the pressure versus G time and the G*dp/dG versus G time with different picking methods. The compliance method is the only method systematically applied during all frac, refrac, and step test cycles. The ‘variable compliance method’ and the ‘Barree tangent method’ are presented for illustrative purposes. The ‘compliance method’ gives a contact pressure of 4.7 MPa for the refrac cycle RF1 (Fig. 5.5b-2). The ‘variable compliance method’ and the ‘Barree tangent method’ give values of 3.2 MPa and 2.2 MPa. These two methods always give values below the one estimated from the compliance method. Both methods were generally not suitable due to the short time series as the pick point of both methods come up after the time series. For refrac cycle RF2, the value is 4.9 MPa for the ‘compliance method’ and agrees well with the previous cycle. The value of 6.5 MPa from the frac cycle is bigger than from the refrac cycles and the value from the step-test is smaller with 3.9 MPa.

ISIP from the Pressure-decay-rate method

The ISIP from the Pressure-decay-rate method is 5.9 MPa for the frac cycle (Fig. 5.5a). It is smaller than the value from the ‘compliance method’ for the frac cycle, which is different for the following refrac cycles. The ISIP is 5.5 MPa and 5.6 MPa for the refrac cycles RF1 and RF2, respectively. It indicates the biggest magnitude for the refrac cycles compared to the other methods for this experiment. The ISIP is 4.7 MPa and smallest for the step test compared to the previous steps.

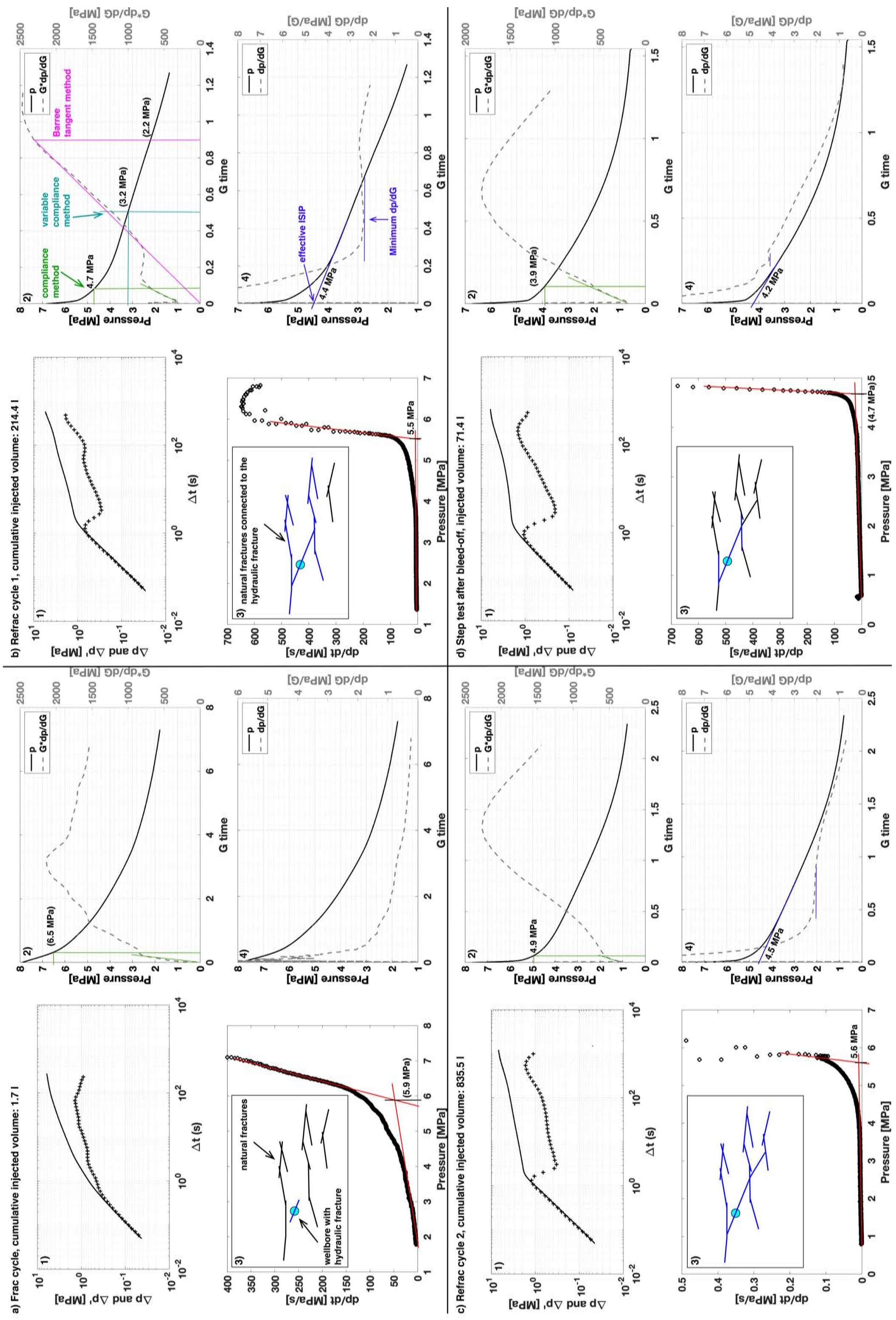

Fig. 5.5 Evolution of shut-in data on Δp and Δp' versus Δt plot (1), dp/dt-pressure (3), G*dp/dG (2) and dp/dG (4) versus G time for a) frac cycle, b) refrac cycle RF1, c) refrac cycle RF2, and d) pressure-controlled step test (SR). All the different methods presented are used to estimate the ISIP, effective ISIP or contact pressure. The numbers in bracket are not used for the summary Fig. 5.8. The 'Barree tangent method', the 'variable compliance method' and the 'compliance method' are presented in b), where only the compliance method was systematically applied to all data.

Effective ISIP from the dp/dG versus G method

Fig. 5.5b-4) shows a plot with dp/dG and G-time. For convenience, the dp/dG is always plotted positive. The effective ISIP is estimated by the weak minimum of the dp/dG curve. The G time of this minimum is used and a tangent is set to the point on the pressure curve to extrapolate the pressure versus G-time back to zero. Its value is 4.4 MPa for refrac cycle RF1. The fracture contact is reflected by an increasing slope of dp/dG, but the deviation from Carter leak-off and spatial pressure gradients mask this effect with a decreasing dp/dG slope. The evolution of actual shut-in data of dp/dG versus G-time for the frac cycle (Fig. 5.5a-4) is monotonically decreasing. For refrac cycle 2 and the step test, we picked the effective ISIP at 4.5 respective 4.2 MPa at the point, where the dp/dG flattens. The interpretation of our experiments is labeled as 'lower confidence' because the 'increase' in dp/dG with contact is very weak.

5.4.2 Pressure-controlled step tests

Two examples are presented, one based on a test carried out next to the S1 structure (Fig. 5.6, HF2) and another one south of the S3 shear zone (Fig. 5.7, HF8). For both experiments, the field setup including boreholes, injection interval and FBG sensors, main geological domain, fractures, and main flow paths (in blue) are presented. Seismic events are indicated by colored circles with a color scheme depending on the respective refrac cycle inherently depending on the cumulative volume. The pressure-controlled step test was executed after a bleed-off phase, and the time series of flow, pressure, and two FBG records are presented in Fig. 5.6b) and Fig. 5.7b).

The flow rate and pressure record for HF2 (Fig. 5.6b) and HF8 (Fig. 5.7b) is color-coded to account for the different steps with greenish colors if the fracture is closed, reddish colors if the fracture is open and greyish colors if it is unclear if the fracture is open or not. The flow rate versus pressure plot of HF2 (Fig. 6c) shows a bilinear behavior with a jacking pressure of 3.6 MPa using the intersection point after Hartmaier et al. (1998). The grey points indicate that flow drops in between periods of stable increased flow rate, which indicates that the pressure is approaching the jacking pressure. The area of contact of two fracture surfaces decreases during fracture opening until a critical fracture aperture is reached and the flow rate strongly increases. This starts to happen at about 3.2 MPa. The FBG sensor at 33.0 m is intersected by two natural fractures, where one of the fractures is more or less oriented normal to the borehole (Fig. 5.6a). The FBG sensor at 31.8 m is intersected by a quartz vein. The FBG sensor at 33.0 m indicates a three-time stronger opening component than the one at 31.8 m during the SR test (Fig. 5.6b). The FBG sensor at 31.8 and 33.0 m has a permanent value of +2.5 respective +2.2 after the SR test. The jacking pressures estimated from Fig. 5.6d and e) are 3.6 and 3.5 MPa, respectively, using the intersection point between the two linear fits. The two stain records versus pressure (Fig. 5.6d and e) present the same characteristics. The solid black bar in Fig. 5.6c, d, and e)

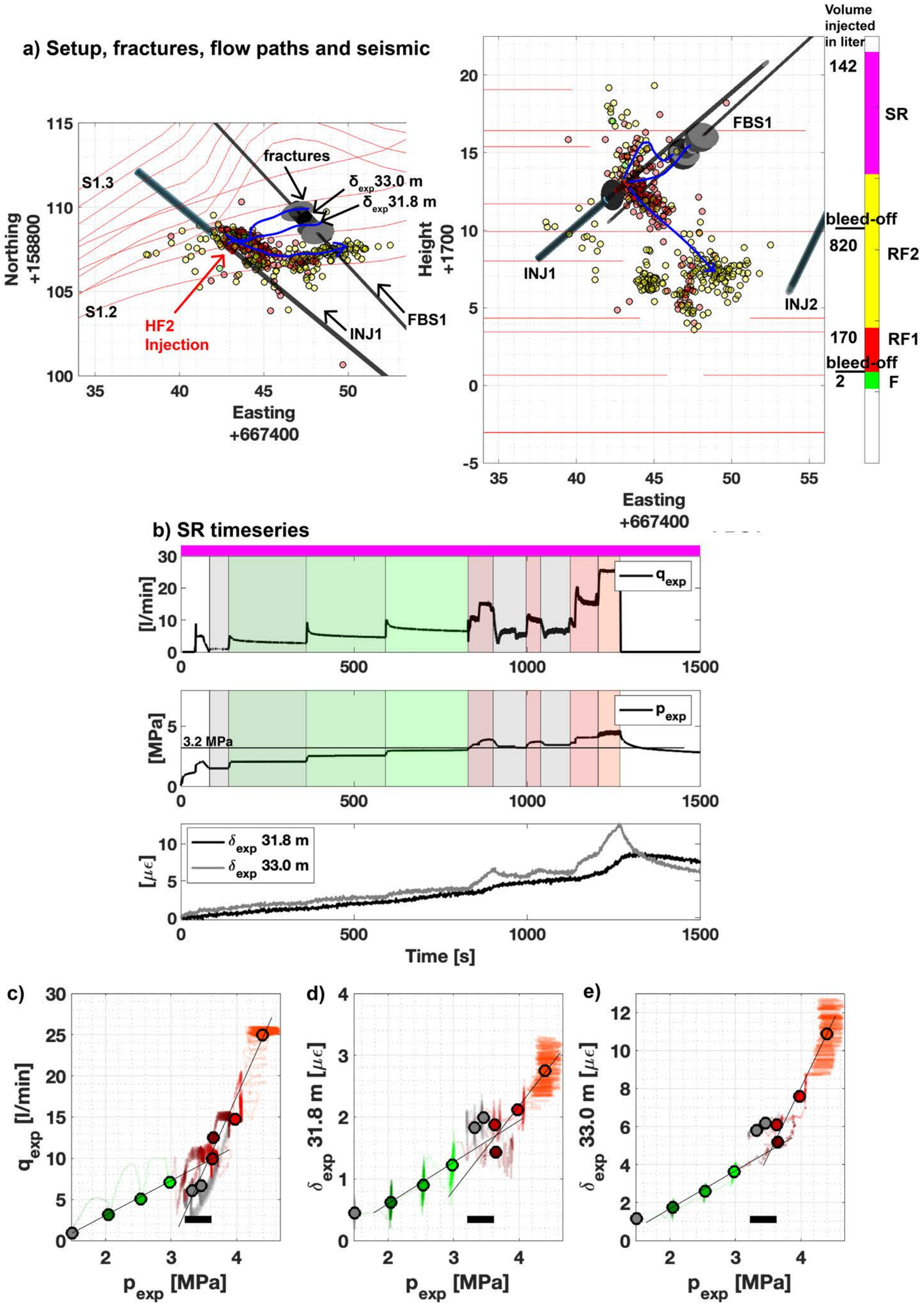

Fig. 5.6 a) The setup of experiment HF2 in plane and map view shows the open injection interval (red cylinder), the fractures (grey discs) with the FBG sensors, the seismic cloud depending on time/volume of injection fluid and the flow paths. b) The timeseries of the step test is presented for the flow rate, the pressure and two FBG strain records in the surrounding of the injection interval and each valid step is colored with red or green. The cross plot is presented to estimate jacking pressure using c) flow rate, d) δ_{exp}=31.8 m and e) δ_{exp}=33.0 m versus pressure. The circles indicate the mean of the corresponding colored sections.

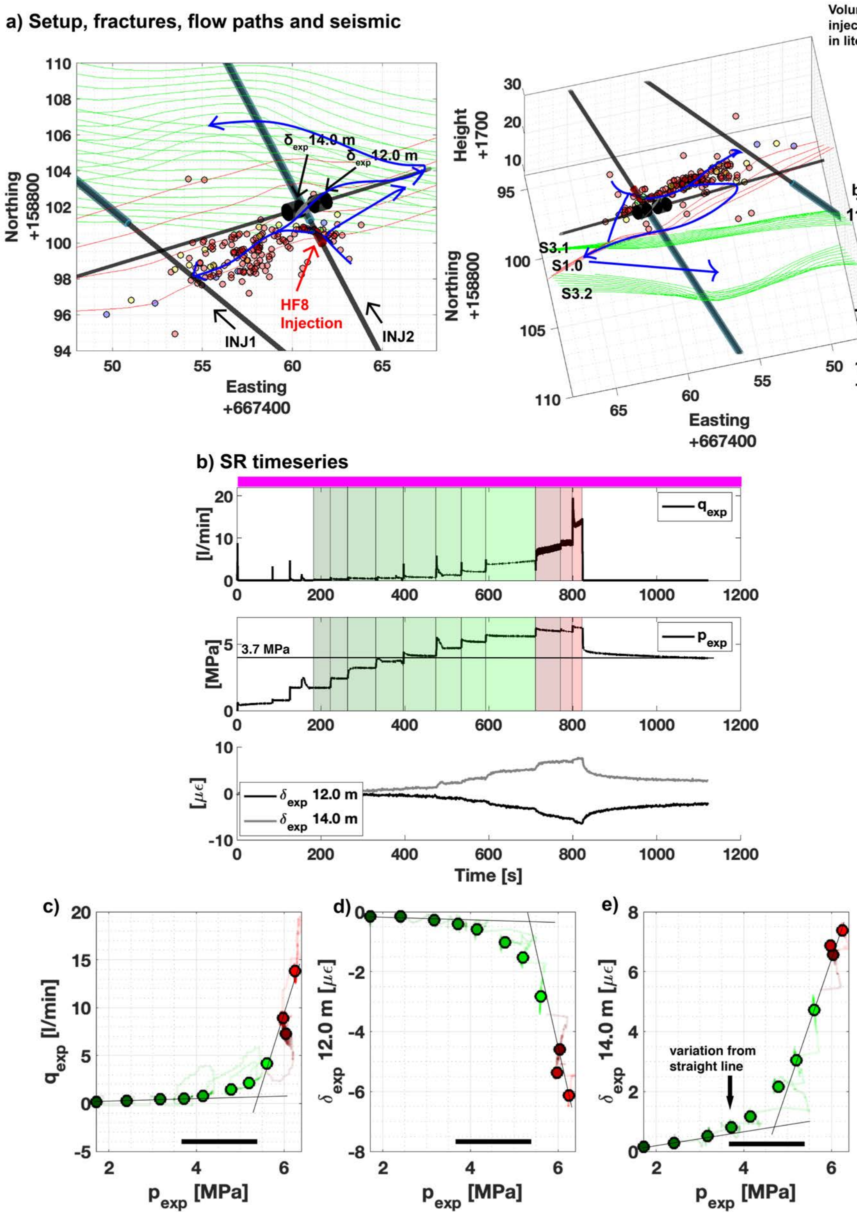

Fig. 5.7 a) The setup of experiment HF2 in plane and map view shows the open injection interval (red cylinder), the fractures (grey discs) with the FBG sensors, the seismic cloud depending on time/volume of injection fluid and the flow paths. b) The timeseries of the step test is presented for the flow rate, the pressure and two FBG strain records in the surrounding of the injection interval and each valid step is colored with red or green. The cross plot is presented to estimate jacking pressure using c) flow rate, d) δ_{exp}=12.0 m and e) δ_{exp}=14.0 m versus pressure. The circles indicate the mean of the corresponding colored sections.

indicates the reliable jacking pressure interval with values ranging between 3.2 and 3.6 MPa.

The flow rate versus pressure plot of HF8 (Fig. 5.7c) shows a bilinear behavior with a jacking pressure of 5.3 MPa using the intersection point, assuming that the primary fracture is jacked open for the last three steps. The situation looks different considering (Fig. 5.7e) the strain record at 14.0 m versus pressure. The intersection of the two linear fits is around 4.7 MPa. The variation from a straight-line during opening indicates an increase in fracture aperture, meaning a loss of contact between the two rough fracture surfaces. The pressure threshold of losing contact is at 3.7 MPa. The FBG sensor at 14.0 m is in intact rock prior to the stimulation of HF8. The tensional increase indicates a new hydraulic connection from the injection interval towards this strain sensor. The strain sensor at 14.0 m is intersected by one natural fracture. The curve of Fig. 5.7e) does not follow a bilinear behavior. It shares similarities in a hyperbolic function. Fig. 5.7d) shows consistently a similar curve but in a compressional manner. The FBG sensor at 12.0 and 14.0 m has a permanent value of -4.7 respective +2.3 after the SR test. The solid black bar in Fig. 5.7c, d, and e) indicates the reliable jacking pressure interval all applied methods.

5.4.3 Comparison of methods

As ISIP is generally picked using the tangent to the pressure curve method, it is picked earlier and reflects the upper boundary of the minimum principal stress magnitude (Fig. 5.8a). The ISIP (from Dutler et al. (2019)), the p - dp/dt ISIP (Fig. 5.8b), and G-function (Fig. 5.8c) ‘compliance method’ agree well for a specific refrac cycle. The different refrac cycle shows different trends due to different injection volumes, bleed-off, and injection metrics. For HF1 and HF5, multiple cycles are performed during RF1. For the refrac cycle RF2 for all experiments, we notice that the ISIP is between 4.2 and 6.3 MPa. The cumulative injection volume is biggest for the refrac cycle RF2 and the pressurized zone has the largest extension, therefore this cycle is most important to characterize the minimum stress magnitude. The compliance method ranges between 4.3 and 7.0 MPa for the refrac cycle RF2 and is similar to the ISIP. In contrast, the ‘variable compliance method’ ranges between 3.5 and 4.4 MPa and gives the smallest magnitudes of all methods.

The effective ISIP (Fig. 5.8d) using the dp/dG curve shows smaller magnitudes than the other ISIP methods. There is a tendency of bigger variation for the effective ISIP. For the effective ISIP, we see a clear magnitude change for experiment HF6 between frac, refrac, and step test correlated by different injection volumes. The injection of HF6 took place at a pre-existing fracture and during frac cycle, no new fracture was initiated. All the other tests indicate bigger magnitudes during the frac cycle with decreasing effective ISIP for the refrac cycles. The effective ISIP ranges between 4.1 and 5.5 MPa for refrac cycle RF2. If we do not account for

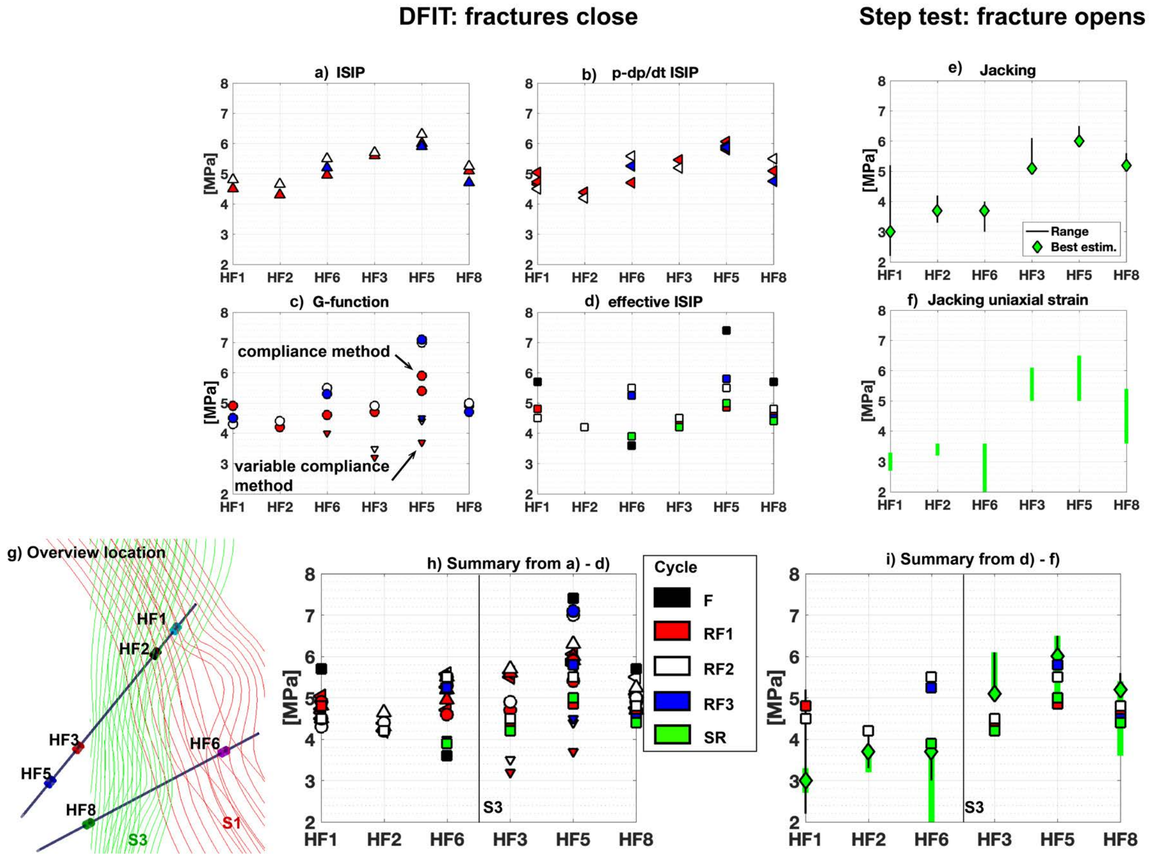

Fig. 5.8 Summarizes a) ISIP (Dutler et al., 2019), b) p - dp/dt ISIP, c) G-function with compliance and variable compliance method, d) effective ISIP, e) jacking pressure (Dutler et al., 2019) and f) jacking from uniaxial strain with color codes for the different injection cycles (see legend). The x-axis indicates the different HF tests with a pseudo-depth starting from the wellbore toe executed test HF1 going up hole to the borehole rim. The overview of each test is indicated in g). A summary of all different picks from the DFIT is presented in h). A summary of the jacking and the effective ISIP is presented in i).

experiment HF6, pre-existing fracture in the interval, and HF5, short-cut during the frac cycle to an existing borehole, the effective ISIP ranges only between 4.1 and 4.9 MPa.

The jacking pressure (Fig. 5.8e) and the jacking from the uniaxial strain record versus pressure (Fig. 5.8f) is presented together in Fig. 8i. Both methods indicate a very similar jacking magnitude for the primary fracture: the pressure ranges between 1.9 to 5.2 MPa with a mean around 3.5 MPa for the tests executed next to the S1 structure (HF1, HF2, and HF6). The effective ISIP (Fig. 8i) indicate bigger magnitudes compared to the jacking pressure.

For the tests executed south of the S3 domain (HF3, HF5, and HF8), the jacking pressure is between 3.6 and 6.5 MPa (with a mean around 5.0 MPa). The magnitudes of the jacking pressure are similar to slightly above the effective ISIP for these tests.

5.5 Discussion

5.5.1 Transient pressure effects: geology and fluid rheology

The tests analyzed in this study (Fig. 5.4) are comparable in terms of pressure response and pressure derivative when grouped by spatial location. The test volume consisting of crystalline rock contains natural, pre-existing fractured zones. These zones are responsible for the majority of present-day fluid flow. Depending on the number and orientation of fracture sets in the test volume, the pressure response can significantly vary. The hydraulic fracture initialized during the experiments located south of the S3 zone (refer to Fig. 5.1c (S3) and 5.4a) connect towards the highly fractured S3 zone during the refrac cycles, which dominates the flow field due to the two different oriented fracture sets (the one developed along shear zones and the one linking the two sub-parallel shear zones). In addition, the true vertical depth from the injection location towards the tunnel is only 15 m. Pressure diffuses along the pre-existing fractures towards the atmospheric tunnel boundaries and may lead to faster fracture surface contact than experiments performed north of the S3 zone. These experiments (refer to Fig. 5.4b) indicate a connection from the hydraulic fracture towards the fracture set associated with the S1 zone, which is further disconnected to the tunnel (Fig. 5.1c). This single fracture set and the increase in true vertical depth of 30 m from the tunnels to the injection location are captured by the pressure and derivative response.

In contrast, the similarities disappear if the tests are grouped by injection-fluid rheology (Fig. 5.4c and d). The pressure time series from RF1 and RF2 is potentially affected by the rheology with a maximal pressure increase of 0.5 MPa (Dutler et al., 2019). The effect on the ISIP is potentially smaller depending on the applied pick method and is more likely dominated by the injection volume and leak-off. The change in fluid rheology does not appear to dominate the pressure response, but the change from XSW to water during the additional flushing cycle can nevertheless influence the response. First, the water will push the XSW farther into the fracture system. Then, given the initially-low viscosity contrast, the two fluids are partly miscible and the XSW is likely held back in the irregularities of the rough fractures. Nevertheless, the viscosity contrast of approximately 30 in our case is most likely insufficient to strongly influence the pressure response. However, it is still unclear, how such contrasts affect the leak-off from the hydraulic fracture towards the natural, pre-existing fractures. Our data do therefore not allow to quantify the influence on fracture leak-off.

5.5.2 Best estimate of the minimum principal stress magnitude

Higher stress magnitudes are observed for the effective ISIP (e.g., Fig. 5.8d) during the frac cycle compared to the following refrac cycles. No data points are given, if the dp/dG curve

Table 5.2 Summary of magnitudes from the different minimum principal stress estimates from the refrac cycles and step tests (see Fig. 5.9a).

Test	σ_{JP}^{SR} **[MPa]**	σ_{ISIP}^{RF} **[MPa]**	$\sigma_{eff.ISIP}^{RF}$ **[MPa]**
HF1	3.28 ± 1.15	4.62 ± 0.22	4.65 ± 0.21
HF2	3.60 ± 0.39	4.39 ± 0.17	4.20 ± 0.00
HF6	3.22 ± 0.87	5.25 ± 0.30	5.38 ± 0.18
HF3	5.48 ± 0.57	5.25 ± 0.59	4.45 ± 0.07
HF5	6.00 ± 0.61	6.07 ± 0.73	5.38 ± 0.49
HF8	5.00 ± 0.80	4.98 ± 0.29	4.67 ± 0.15

monotonically decreases. The ISIP and effective ISIP from the refrac cycles do not show a correlation with the injection volume (Fig. 5.8b-d). The following bleed-off phase leads to strong pressure release in the rock mass. This changes the system behavior and allows to characterize the initialized hydraulic fracture intersecting the open injection interval with the shortcoming that the assumption of uniform pressure in the fracture is not valid. For these reasons, only the refrac cycles were used to calculate the ISIP (σ_{ISIP}^{RF}) and effective ISIP ($\sigma_{eff.ISIP}^{RF}$). The mean and standard deviation of all refrac cycles together for each experiment are presented in Table 5.2 and Fig. 5.9a. Besides the mean and standard deviation of the jacking pressure (σ_{JP}^{SR}) is calculated from the flow rate versus pressure (Fig. 5.8e) and two uniaxial strain versus pressure (Fig. 5.8f) results for each experiment.

The ISIP is 4.81±0.38 MPa (Fig. 5.9b). It indicates the pressure that is measured in the wellbore. The effective ISIP is 4.49±0.22 MPa (Fig. 5.9b). The effective ISIP is smaller than the ISIP measured in the wellbore, as it is picked later and should be a better estimate for the minimum principal stress at the fracture tip. The difference of the two values are rather small for our crystalline rock with natural, pre-existing fractures. McClure et al. (2019) analyzed over 30 field DFIT from shale and indicated that the minimum principal stress is slightly below the contact pressure, which was identified from a plot of dp/dG or relative system stiffness. Our observations from the plot of dp/dG (e.g., Fig. 5.5) is often monotonically decreasing, which was identified to be related by the hydraulic fracture intersecting highly permeable natural, pre-existing fractures. The fracture closes quickly and the reversible mechanical strain released due to shut-in might develop spatial pressure gradients. The relative stiffness plot (McClure et al., 2019) assumes a uniform pressure everywhere in the fracture, therefore we did not use them in our analysis.

Experiments HF1, HF2, and HF6 executed next to the S1 structure (Fig. 5.9c) indicate similar jacking pressure with a magnitude of 3.37±0.20 MPa (Fig. 5.9b), proving an estimate of the primary fracture opening. This pressure is around 1.1 MPa smaller than the effective ISIP. The mean and standard deviation of the jacking pressure is 5.49±0.50 MPa (Fig. 5.9b) for the

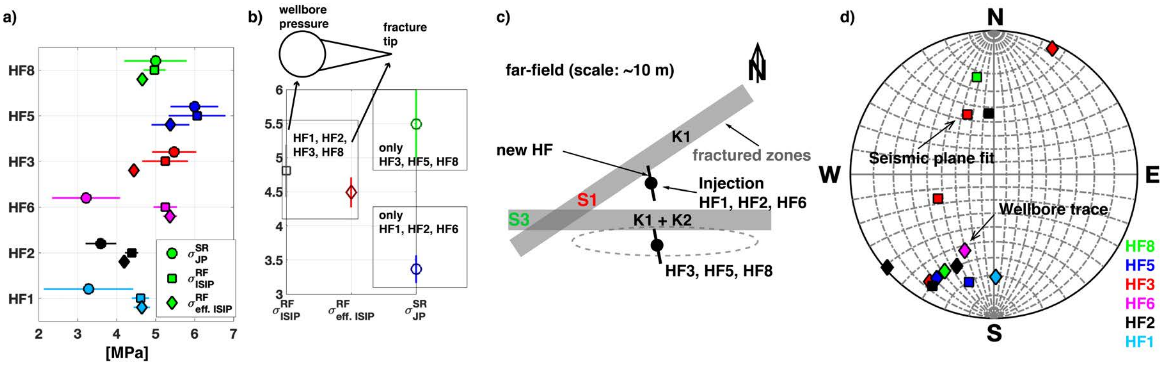

Fig. 5.9 a) Summarizes the results from Fig. 5.8 for the mean and standard deviation of the jacking pressure (σ^{SR}_{JP}), the ISIP (σ^{RF}_{ISIP}) and effective ISIP ($\sigma^{RF}_{eff.ISIP}$) for each experiment and b) the mean and standard deviation over all experiments without experiment HF6 (due to the pre-existing fracture in the interval). c) Sketch from the location of the experiments relative to the fractured zones. d) The lower stereonet presents the pole points of the wellbore trace (diamonds) from Dutler et al. (2019) and seismic plane fit (squares) from Villiger et al. (2020) and Dutler et al. (2019).

Table 5.3 Summary of magnitudes, dip direction, and dip from the three stress components used in this study.

Stress component	Magnitude [MPa]	Dip direction [°]	Dip [°]
σ_1	13.1	104	39
σ_2	6.7	313	46
σ_3	4.5	206	19

experiments HF3, HF5, and HF8 executed south of the S3 structure (Fig. 5.9c). The jacking pressure for the experiments executed south of the S3 structure is around 1.0 MPa bigger than the one from the effective ISIP. It is likely that the magnitudes of the jacking pressure from the pressure-controlled step tests overestimate the minimum principal stress magnitude for fracture tortuosity near the wellbore. It is unlikely, that the jacking pressure is below this value, which might be an indication for shear reactivation. Therefore, we conclude that effective ISIP gives the best estimate for the minimum principal stress magnitude due to small differences between different experiments (Table 5.3).

5.5.3 Implication for the stress field

The pole points of the hydraulic fractures intersecting the open wellbore interval (here: wellbore traces) and the seismic plane fits from Dutler et al. (2019) and Villiger et al. (2020) are presented in a lower-hemisphere stereonet (Fig. 5.9d). All pole points of the wellbore traces (diamonds) indicate a consistent orientation. In addition, the seismic plane fit for HF5 and one cluster of HF2 (during the early time of fracturing) is oriented in a similar manner. The dip and dip direction for the minimum principal stress was assumed to correspond to the wellbore traces. All observed wellbore traces were used to calculate (Allmendinger et al., 2011; Cardozo and Allmendinger, 2013) the Fischer distribution giving the dip direction and dip for σ_3 in Table 5.3. The major principal stress magnitude, dip direction, and dip is used by Krietsch et al. (2019). Major and minor principal stress was successfully checked for orthogonality. The limiting pressure is 5.4 MPa and 6.8 MPa (see Fig. 5.4a in Dutler et al. (2019)) for the experiments north (e.g., HF2) and south of S3 (e.g., HF8). We assume that, this overpressure is able to reactivate the corresponding fractures leading to the overall seismic plane fit in Fig. 5.10b. This allowed us to derive the magnitude of σ_2 with 6.7 MPa. As mentioned in the above, Krietsch et al. (2019 presented, therefore, two different stress states, one which was assumed to be perturbed near the S3 structure, where the fracture density increases. This perturbation leads to a switched position between σ_2 and σ_3, where the magnitude has to be in a similar range.

The stress tensor (Table 5.3) is presented in the lower-hemisphere stereonet with the normal stress component presented in Fig. 5.10a). The wellbore traces (diamonds) and seismic plane fits (squares) are located in the part indicating small normal stress magnitudes. The Kirsch solution was used to derive the minimum normal stress on all possible oriented fractures for the injection borehole orientation (BH: 310/56°). Fig. 5.10 shows only one injection borehole trace, the other borehole is oriented similar and has been omitted for the sake of simplicity. Fig. 5.10b) consists of the minimum normal stress on the borehole wall and the anisotropic tensile strength. The tensile strength varies between 5.6 and 14.0 MPa, which is aligned with the foliation plane (schistosity: 330/15°). The orientation of the wellbore traces indicate that 1) the breakdown pressure includes a tensile strength of around 13.0 to 14.0 MPa and 2) the combined minimum normal stress and tensile strength for a wellbore pressure of 14.0 MPa are minimal. Together with the minimum normal stress from the Kirsch solution, this agrees well with the observed formation breakdown pressure ranging between 14 and 21 MPa (Dutler et al., 2019).

Hydraulic fracturing theory dictates that the plane of a hydraulic fracture is oriented perpendicular to the minimum principal stress. Most likely, this was achieved at the early stage of fracturing (frac cycle and refrac RF1). A small slip tendency is indicated for the wellbore trace of HF3, HF5, and HF8 and the seismic cloud of HF2 next to σ_3 (Fig. 5.10d + e). With additional injection volume and flow rate, the hydraulic fracture grows and interconnects to natural, pre-existing fractures and leaks more and more fluid towards them. Consequently, the seismic cloud starts to change the orientation resulting in a seismic plane fit of HF8, HF3, and HF2 oriented towards N-aligning with the pre-existing, natural fracture set K1 (red and green triangles). A second red square (HF3) is located next to the other fracture set K2 associated with the S3 structure, indicating a low slip tendency. The most substantial slip tendency is

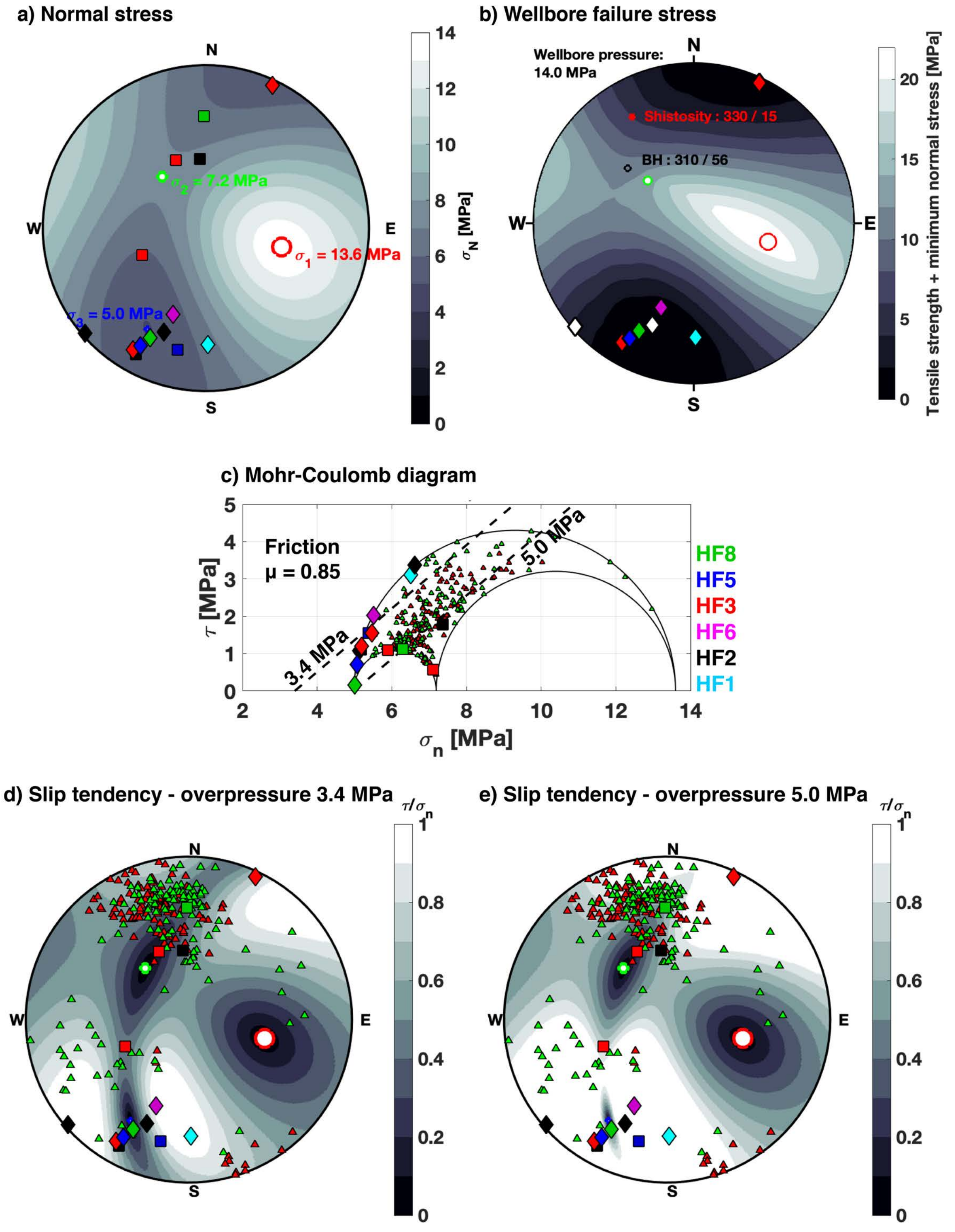

Fig. 5.10 a) The normal stress under the given stress state and b) wellbore failure stress consisting of the Kirsch solution for the given borehole direction (BH) and the anisotropic tensile strength from the shistosity at a given wellbore pressure of 14.0 MPa. c) The Mohr-Coulomb diagram is calculated from stress field given by Table 5.3. The Mohr circles include the hydro-static pressure of 0.5 MPa. The failure limits assuming a friction of 0.85, no cohesion and overpressure of 3.4, and 5.0 MPa. The diamonds and the squares are the pole points of the wellbore trace and seismic plane fit (Fig. 5.9). The red and green triangles are the natural fractures related to the S1 and S3 structure (Fig. 5.1). The slip tendency is presented for an overpressure of d) 3.4 MPa and e) 5.0 MPa.

associated with the wellbore traces from experiment HF1, HF2, and HF6. The shear-stress ranges between 2.0 and 3.4 MPa (Fig. 5.10b). It is evident from an inspection of Fig. 5.10 that slip occurs between 3.0 and 4.0 MPa overpressure (evidence in Fig. 5.6c). Therefore, the jacking pressure (Fig. 5.9a) of these experiments indicate shear dilation and not fracture opening. In comparison, the effective ISIP and ISIP (Fig. 5.9a) was similar for all experiments with two exceptions (HF5 and HF6).

The experiment HF3, HF5, and HF8 (Fig. 5.9c) indicate a small slip tendency. The maximum shear stress is around 1.5 MPa. The overpressure needed to open or reactivate the fractures in shear is between 3.5 and 5.5 MPa. The jacking pressure of these experiments indicates fracture opening, with a tendency to overestimate σ_3 due to near-wellbore tortuosity. Experiment HF5 shows tendential bigger magnitudes for σ_3. This is probably related to hydraulic short-cut towards an unpacked geophysical borehole during the frac cycle and/or local stress effects. Most of the fractures related to the S1 (red triangles) and S3 (green triangles) structures can be reactivated with an overpressure of 5.0 MPa.

5.6 Conclusions

The DFIT methods: ISIP, p-dp/dt ISIP, and G-function allow to pick pressure consistently in the crystalline rock mass. The ‘compliance method’ for the G-function reproduced similar values as the ISIP from other methods. The overall ISIP is 4.81 ± 0.38 MPa and indicates the pressure in the open wellbore interval. These selected ISIPs do yield slightly larger pressure magnitudes than the picked effective ISIP from the dp/dG curve. It is assumed that the effective ISIP to be a better estimate of the minimum principal stress magnitude referred to the fracture tip. The overall effective ISIP is 4.49 ± 0.22 MPa. The jacking pressure for the experiments executed South of the S3 structure is 5.49 ± 0.50 MPa from the pressure-controlled step test. The proximity to the S3 structure and the complex geological structure led to near-wellbore tortuosity and heterogeneous stress effects masking the jacking pressure. In comparison, the tests executed North of the S3 structure show smaller jacking pressure than effective ISIP.

A new method was introduced to estimate the jacking pressure from uniaxial strain records versus pressure plot. The values agree with the observations from the jacking pressure from the flow versus pressure plot. The permanent changes in strain are indicative of shear dislocation as well as fracture opening during the pressure-controlled step tests. One experiment presented had a jacking pressure below the effective ISIP, and another experiment vice versa. The slip-tendency analysis showed that the jacking pressure below the effective ISIP is related to shear dislocation and not indicative of the fracture opening.

The orientation of σ_3 was estimated from the hydraulic fracture intersecting the wellbore with the assumption that the maximum principal stress axis is stable in orientation. The minimum principal stress magnitude of 4.49±0.22 MPa was estimated from the DFIT methods using effective ISIP. The orientation of σ_2 is aligned next to the fracture system K1. The difference in magnitude of σ_2 and σ_3 is small, such that they can switch place. Besides, the hydraulic fracture connects to the pre-existing, natural fracture set K1 and forces the fluid to follow this fracture set, indicating possible shear slip. The newly derived stress tensor for the HF experiments is σ_1=13.1 MPa (104/39°), σ_2=6.7 MPa (313/46°), and σ_3=4.5 MPa (206/19°).

5.A.1 Change in pressure and derivative

The change in pressure is defined by

$$\Delta p(t) = p(t = t_{shut-in}) - p(t),\, t \in (t_{shut-in}, t_{end}] \tag{5.1}$$

All derivatives used for the diagnostic plots in this paper correspond to first-order, logarithmic time derivatives (Bourdet et al., 1989). The involved signal was resampled with a spline interpolation at a fixed number of time intervals regularly spaced in a logarithmic scale (Renard et al., 2009). The derivatives were taken with respect to actual shut-in time, t_a.

$$\Delta p'(t) = \frac{d\Delta p}{d \ln \sqrt{t_a}} = \sqrt{t_a}\frac{d\Delta p}{d\sqrt{t_a}} \tag{5.2}$$

5.A.2 G-function

The G-time (or G-function) is a dimensionless function relating to shut-in time with the duration of the injection. It allows estimating the minimum principal stress, pore pressure, and permeability (Nolte, 1979) with the assumption that the cumulative leak-off after shut-in is linearly proportional to G-time. The G-function is given by:

$$G(t_a, \alpha) = \frac{4}{\pi}[g(t_a, \alpha) - g(0, \alpha)] \tag{5.3}$$

with

$$g(t_a, \alpha = 1) = \frac{4}{3}[(1 + t_a)^{1.5} - t_a^{1.5}] \tag{5.4}$$

$$g(t_a, \alpha = 0.5) = (1 + t_a)\sin^{-1}(1 + t_a)^{-0.5} + t_a^{0.5} \tag{5.5}$$

where $t_a = \Delta t / t_p$, Δt is the time since shut-in, t_p is the duration of injection taking place prior shut-in and α is the power law exponent for fracture growth. The G-function depends weakly on α and the reasonable bounds of are between 0.5 and 1.0 (Nolte, 1979). The higher bound is for low leak-off with high efficiency fracturing, where the fracture area depends linearly on time. We choose α=1 for our tests in low permeability rock. The choice of α does not affect the method of picking contact pressure.

The G-function is derived based on the assumption of Carter leak-off. The analytical solution of the 1D fluid flow leak-off from a fracture into an infinite homogeneous and isotropic porous medium is described by a 1D seepage model (Wang, 2000):

$$\frac{\partial p}{\partial t} = C\frac{\partial^2 p}{\partial x^2} \tag{5.6}$$

with $x > 0$, $t > 0$. It corresponds to a simple 1D diffusion model with a conductivity C. The initial and boundary conditions are $p(0,t) = p_{inj}$ for $t > 0$, $p(\infty,t) = p_{formation}$ for $t > 0$ and $p(x,0) = p_{formation}$ for $x \geq 0$. Carter's leak-off equation links the fluid velocity v_L in the hydraulic fracture with Carter's leak-off coefficient c_L:

$$v_L = \frac{c_L}{\sqrt{t - t_{shut-in}}} \tag{5.7}$$

where the spatial derivation of the solution to the 1D seepage model leads to the leak-off velocity. The solution to the 1D seepage model is given by:

$$p(x,t) = (p_{inj} - p_{formation})\text{erfc}(\frac{x}{2\sqrt{Ct}}) + p_{formation} \tag{5.8}$$

Relying on the assumption that the cumulative leak-off after shut-in is proportional to G-time, the derivative of the cumulative leak-off with respect to G-time is equal to a constant. The pressure versus G-time plot should form a straight line. It also means that the fracture stiffness before contact is constant, as well as the total system storage, which is truly an ideal theoretical case.

$$\frac{\partial p}{\partial G} = \frac{1}{C_t}\frac{dV}{dG} = \text{constant} \tag{5.9}$$

Chapter 6

The poroelastic far-field response from in-situ hydraulic stimulations

The injection protocol and operation planning were designed by N.D. and B.V. All the authors were part of the data acquisition team during the HF experiments of the ISC project, where F.A. was the project administrator. The formal analysis, data curation, data visualization inclusive writing the original draft preparation was done by N.D. The writing—review and editing was done by B.V., F.A., M.J., V.G., J.D., H.K., and L.V. The supervision and funding acquisition for this work was done by B.V.

Please cite this chapter as: Dutler, N.O., Valley, B., Amann, F., Jalali, M., Krietsch, H., Villiger, L., Gischig V., Doetsch, J.: The poroelastic far field response from in-situ hydraulic stimulations, in prep. for Science

Abstract

High-pressure injections can cause transient pore pressure changes over large distances and may cause induced seismicity. The zone of influence for such an injection was studied at high spatial resolution in six decameter-scaled in-situ fluid injection experiments hosted in crystalline rock. The pore pressure data differentiate two distinct responses based on lag time and magnitudes. We can distinguish a near and far-field reply. The near field response is due to pressure diffusion. The far-field response shows a fast time response and the magnitude decay in the order of suggesting a link to the effective stress changes in a deviatoric stress field. Independent of the injection location, the far-field pore pressure response is consistent for all experiments, indicating the dominant failure mechanism induced by the stimulation process. Our findings show that the far-field pore pressure response is dependent on the injection

volumes. However, the far-field response is not dominated by active fluid transport and can serve as a complementary method to seismic monitoring during hydraulic stimulations.

6.1 Introduction

Hydraulic stimulation operations for enhanced geothermal systems (EGS), petroleum applications, and wastewater disposal wells are potentially sources of seismic hazard. The high-pressure and/or massive volume injections led to an increase in earthquake rates and magnitudes (Bao and Eaton, 2016; Ellsworth, 2013; Frohlich, 2012). Predictions of seismic hazard from injections remains difficult. Explaining the causality of earthquake located at large distance (> 10 km) from the injection points is particularly arduous (Goebel et al., 2017; Keranen et al., 2014) and the possible underpinning mechanisms are debated.

Injection-induced seismicity is frequently explained by pore pressure increase within the rock mass connected with the injection well. This zone can be referred as the ’pressurized zone’ and be illuminated by active seismic measurements during high-pressure fluid injections (Calò et al., 2011; Doetsch et al., 2018b; Schopper et al., 2020), as the relative change in p-wave velocity is directly linked to pore-pressure changes. This pore pressure changes can lead to fault rupture and, if the energy at the fracture tip overcomes the tensile strength of the rock, new fractures can be created.

Within the pressurized zone, in the near-field of the injection, the pore pressure distribution is dominated by fluid diffusion. However, the time scale for diffusion induced pore pressure changes is too slow to explain far-field pressure changes and remotely induced seismic events. A hypothesis explaining remote seismicity might be associated with aseismic slip processes. Aseismic slip has been observed in-situ in response to fluid injection (Guglielmi et al., 2015) and can potentially extend beyond the ’pressurized zone’ (Bhattacharya and Viesca, 2019). An alternate hypothesis is that of poroelastic processes, i.e. pressure changes explained by rock deformation and associated pore space variations reaching beyond the pressurized zone. This hypothesis is invoked for explaining earthquakes induced more than 30 km away from the injection point (Goebel and Brodsky, 2018). Mechanical and hydraulic effects act on different timescales in response to non-local deformation induced by pressure perturbation. Therefore, linear poroelastic theory (Biot, 1941) should predict the mechanical driven pore pressure changes. We propose in this paper a first direct in-situ observation of these injection induced poroelastic effects.

In situ observation of poroelastic effects water level variations in wells have been related to earthquake are also explained by poroelastic effects. The offer insights to hydromechanical coupled processes in the crust. The pressure response in wells can range from short oscillation periods in water levels (Cooper et al., 1965) to recompilation of streamflow leading to permanent changes in the reservoir properties and the wellhead response (King et al., 1999; Montgomery and Manga, 2003).

Regional-scale effects of earthquakes, as inferred from wellbore water level fluctuations, have also been found by Roeloffs et al. (2003). They found that the size of gradual water-level changes generally increases with earthquake magnitude and decrease with hypocentral distance. Based on coseismic water-level fluctuations and strain changes in the Long Valley Caldera, they were able to distinguish between local and regional earthquakes. In geothermal wells in south Iceland, co- and post-seismic well level changes were observed and correlated with ground motion observations from synthetic aperture radar interferograms (Jónsson et al., 2003). Jónsson et al. (2003) found that a poroelastic rebound was dominant following the earthquakes with rapid recovery of the water-level. The dependency of pore pressure on the deviatoric stress component may explain far-field water level fluctuations observed during an earthquake near Parkfield California (Wang, 1997).

In contrast to these in-situ poroelastic observation related to deformation induced by large earthquakes, our study presents poroelastic deformation and pressure changes induced by fluid injection. Our study is part of the In-situ Stimulation and Circulation (ISC) project (Amann et al., 2018), which was carried out at the Grimsel Test Site (GTS), Switzerland, between 2015 and 2018. The laboratory is located 480 m below surface in the crystalline rock mass of the Aar Massive. The decameter-scale test volume consists of granitic rocks and a series of brittle to ductile fault zones (Krietsch et al., 2018). The ISC rock mass is accessible through three tunnels from different sides at a different elevation.

6.2 Method

We present here the data collected during 6 hydraulic fracturing experiments (Dutler et al., 2019). The injection protocol of each experiment consisted of several cycles including: (1) break down of the formation, (2) 2-3 refracturing cycles, and (3) a pressure-controlled step-test. The pressure in the injection interval reached a maximum magnitude of 21.2 MPa during the breakdown cycle (injected fluid volume < 2 liters). During the subsequent fracture propagation phase, the pressure at the injection point reaches magnitudes between 5.5 - 9.0 MPa for flow rates up to 90 l/min. In total, volumes of approximately 1000 l /test were injected.

Sixty-three packer-isolated intervals in boreholes drilled from these tunnels (Fig. 6.1A) allowed us to capture the 3D pore fluid pressure response related to six stimulation experiments (Dutler et al., 2019). The Euclidian distance from the injection point to the pressure monitoring interval ranges from a few meters up to 100 m. Most of the pore pressure intervals in the far-field are above the injection location, with an elevation difference of 10 – 40 m.

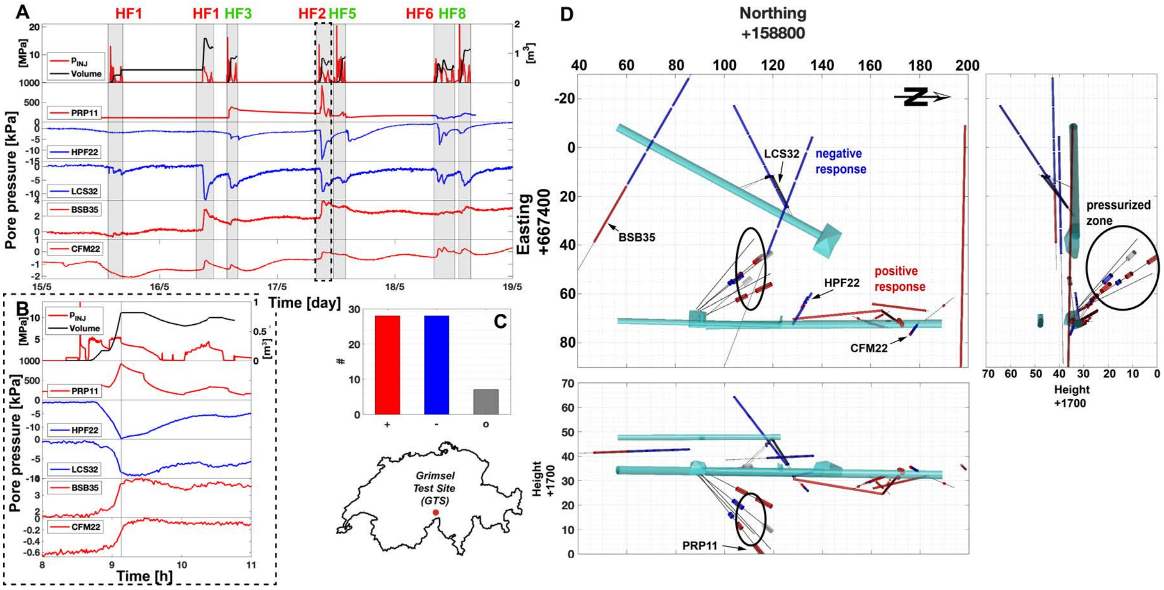

Fig. 6.1 The timeseries of the pore pressure observations can be classified by positive or negative response. (A) Timeseries of the injection pressure and volume, PRP11 open interval pressure in the pressurized zone and 4 open intervals indicating the far field response. (B) Zoom on the timeseries for experiment HF2 presented in (A). (C) Proportion of positive, negative and mixed responses. The interval locations are indicated and labeled in (D) the plane and profile view showing the positive (red), negative (blue) and mixed (white) magnitude response in the open intervals inclusive the approximative pressurized zone and the access tunnels. Coordinates on panel (D) is referenced to the Swiss metric coordinate system (CH1903).

Dataset

The presented analysis is based on the hydraulic fracturing (Dutler et al., 2019) and hydraulic shearing (Krietsch et al., 2020) public datasets:

- Dutler, N., Gischig, V., Doetsch, J., Jalali, M., Krietsch, H., and Amann, F.: Hydro mechanical data set from the six Grimsel ISC hydraulic fracturing experiments, https://doi.org/10.3929/ethz-b-000328270, 2019.
- Krietsch, H., Gischig, V., Doetsch, J., Jalali, M. and Amann, F.: Hydro mechanical data set from the six Grimsel ISC hydraulic shearing experiments, https://doi.org/10.3929/ethz-b-000328266, 2019.

For this analysis we used pressure and strain observations. The ISC monitoring setup and the description is published (Doetsch et al., 2018a).

The geological model incl. borehole logs and visualization is available (Krietsch et al., 2018) as public dataset:

- Krietsch, H., Doetsch, J., Dutler, N., Jalali, M., Gischig, V., Loew, S. and Amann, F.: Comprehensive geological dataset for a fractured crystalline rock volume at the Grimsel Test Site, https://doi.org/10.3929/ethz-b-000243199, 2018.

During the hydraulic fracturing (HF) experiments, the pore pressure observation records from the far-field were added to the repository. The far-field pore pressure was sampled all 60 s during the HF experiments. The Data includes the location of the borehole and the borehole intervals. For this the geological model visualization was updated with the additional boreholes and intervals and can be inquired by the corresponding author.

Filtering and picking

The timeseries were filtered with a lowpass second order Butterworth filter for picking. The timeseries were cut into the refrac cycles (RF1, RF2 and RF3 in Fig. 6.2). The highlighted section in the picking plots indicates fluid injection. The shut-in time ts is defined as the time, when fluid injection is stopped followed by an observation phase, which ends either with a new injection cycle or the depressurization of the system, opening the ISC injection and pore pressure observation intervals. The characteristic time t_c is the difference between the picking time t_{pick} and shut-in time t_s. For the pore pressure and strain observations, the time was picked due to reaching a minimum, maximum or a notable change in magnitude during the observation phase (Fig. 6.2). For the pore pressure timeseries we used in general the latter pick with bigger absolute magnitude, which is hydraulically driven. For the uniaxial strain timeseries, the earliest pick was used as it is an indication of mechanical driven one. All results can be found in repository.

For each HF experiment the absolute maximum magnitudes were picked from the pore pressure timeseries during the two refrac cycles RF1 and RF2. These two cycles correspond to the biggest fluid volume without depressurization and highest flow rates. The corresponding injected volume was calculated for the time corresponding to the absolute maximum magnitude. Both results can be found in the repository and both are visualized (see Fig. 6.5B, 6.6A and 6.7B).

Volumetric strain in comparison with uniaxial strain observations

Outside of the pressurized zone, we assume that the change in pore pressure is linked with the mean stress change $\sigma_m = 1/3 \cdot (\Delta\sigma_{11} + \Delta\sigma_{22} + \Delta\sigma_{33})$ and the Biot-Willis coefficient α. Volumetric strain is then calculated from the mean stress change and the known Young's modulus K for the rock mass. Then,

$$\Delta p = \alpha \sigma_m$$

$$\sigma_m = K \varepsilon_{vol}$$

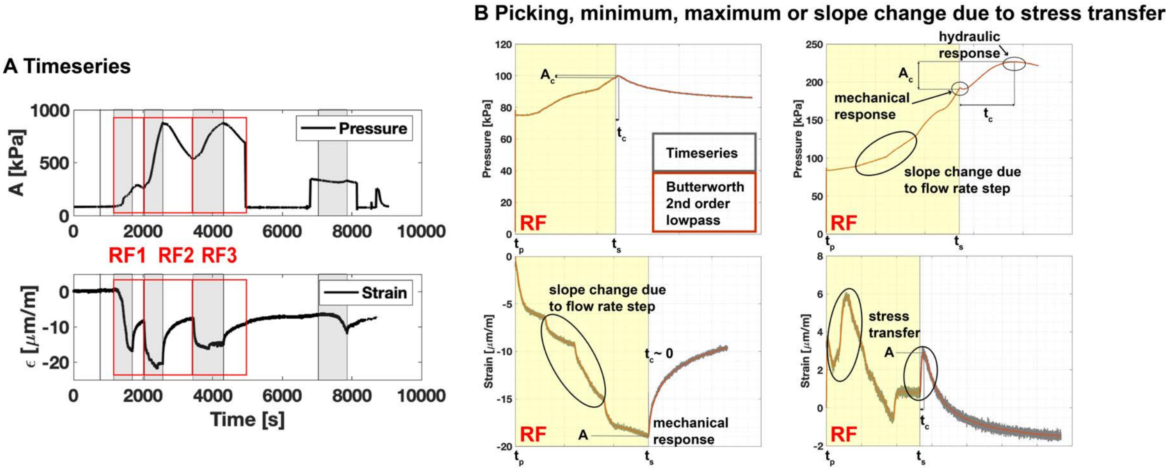

Fig. 6.2 (A) The timeseries for one pore pressure and one FBG strain sensor are presented with grey shaded sections corresponding to fluid injection into the interval. (B) The timeseries (grey solid) and the lowpass filtered timeseries (red solid) are presented for a specific time interval. The yellow shaded section corresponds to the fluid injection. Hence, characteristic time and amplitude is picked after shut-in for pore pressure and strain timeseries. The pore pressure indicates different superimposed effects like mechanical response due to shut-in and erratic slope changes due to flow rate steps. The hydraulic response needs to be picked and often corresponds to the absolute maximal observed pressure. For intervals far away from the injection this hydraulic response does not exist anymore, therefore we pick the only response which was observed. If no response was observed or the response was too small, we decided not tom pick. For the uniaxial strain timeseries only mechanical responses are relevant. Therefore, the picked characteristic time is due to the minimum, maximum or characteristic slope change. The timeseries are also superimposed by slope changes due to flow rate steps, stress transfers between fractures, or poroelastic effects.

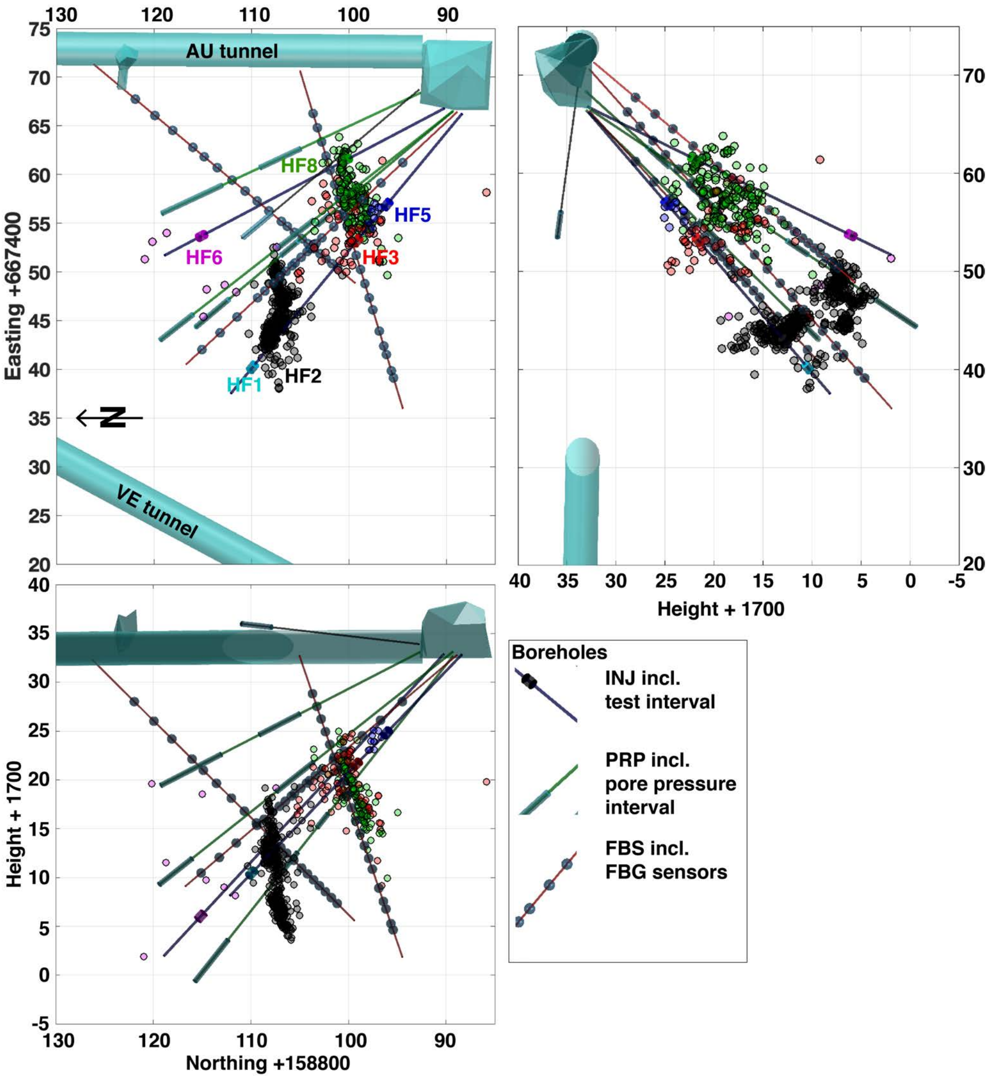

Fig. 6.3 The monitoring setup of the ISC project incl. tunnels and INJ, PRP and FBS boreholes in plane and profile view inclusive injection intervals (HF#), pore pressure observation intervals (light blue cylinder) and FBG sensors (blue spheres). The seismicity points of each experiment have the same color then the 3-D cylinders, and labels (HF#).

where α is between 0.64 and 0.71 and $K = 19$ GPa (Selvadurai et al., 2019).

Poroelastic pore pressure response for a cylinder in a non-hydrostatic stress field

Extract from Detournay and Cheng (1988) presenting the pore-pressure solution induced by the pressurization of a vertical cylinder. The three fundamental modes to solve the problem are (i) the far-field isotropic stress, (ii) the in-situ pore pressure and (iii) the far-field stress deviator.

Mode 1

The mode 1 corresponds to the classical Lamé solution and does not include a pore pressure term.

Mode 2

The pore pressure field is solved for an uncoupled homogeneous diffusion equation taking the Laplace transform. For the boundary conditions in the far-field the in-situ pore pressure, p_0, is reached and the stress component vanish. The solution reads (Eq. 23 from Detournay and Cheng (1988)):

$$\frac{s\tilde{p}^{(2)}}{p_0} = -\frac{K_0(\xi)}{K_0(\beta)} \tag{6.1}$$

where K_0 is the modified Bessel function of second kind of order zero, $\xi = r\sqrt{(s/D)}$and $\beta = a\sqrt{(s/D)}$. The parameters r, a, s and D are radius, cylinder radius, inversion parameter and the diffusion coefficient.

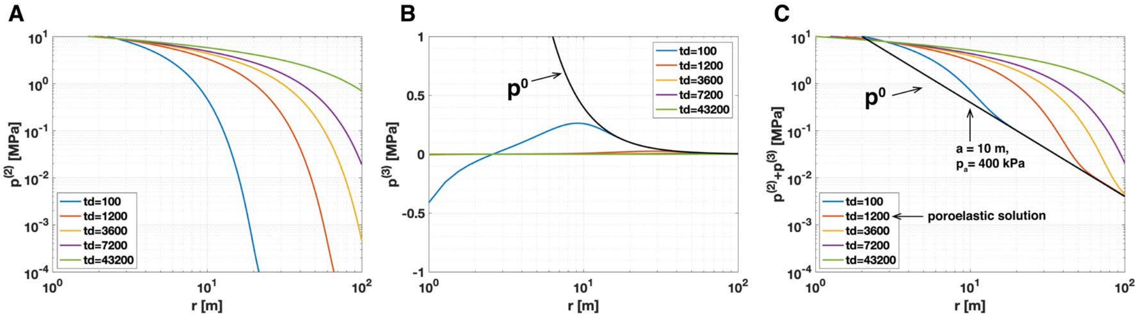

Fig. 6.4 (A) Solution for the pore pressure mode 2, (B) mode 3 and (C) the superposition of both modes presented in Text 6.2. The pressure profile is drawn against the radial distance for different injeciton times td. The unit of time td is seconds. The red solid line corresponds to the best match and is presented in Fig. 6.5, 6.6, and 6.7, as the 'poroelastic solution' with the parameters given in Table 6.1.

Mode 3

For a deviatoric stress field the pore pressure solution is also given in the Laplace transform domain. The solution reads:

$$\frac{s\tilde{p}^{(3)}}{S_0 \cos 2\theta} = \tfrac{B^2(1-\nu)(1+\nu_u)^2}{9(1-\nu_u)(\nu_u-\nu)} C_1 K_2(\xi) + \tfrac{B(1+\nu_u)}{3(1-\nu_u)} C_2 \tfrac{a^2}{r^2} \tag{6.2}$$

$$C_1 = -\tfrac{12\beta(1-\nu_u)(\nu_u-\nu)}{B(1+\nu_u)(D_2-D_1)} \tag{6.3}$$

$$C_2 = \tfrac{4(1-\nu_u)D_2}{D_2-D_1} \tag{6.4}$$

$$D_1 = 2(\nu_u - \nu)K_1(\beta) \tag{6.5}$$

$$D_2 = \beta(1-\nu)K_2(\beta) \tag{6.6}$$

where K_n is the modified Bessel function of second kind of order n. The parameters, S_0, B, ν_u, ν are stress deviator, Skempton coefficient, undrained and drained Poisson's ratio. The $\cos(2\theta)$ on the lhs indicate that the problem is not axisymmetric. The first term on the rhs depends only on the modified Bessel function of order 2 all the other parameters are constant. The second term on the rhs depends on r^{-2} and is the mechanical component, which drives the magnitude decay in the far-field. The instantaneous drilling of the cylinder generates the following approximation for the undrained pore pressure distribution given by Eq. 50 from Detournay and Cheng (1988):

$$p^0 = \tfrac{4}{3} S_0 B (1+\nu_u) \tfrac{a_c^2}{r^2} \cos 2\theta \tag{6.7}$$

In the following we describe the fitting process, to achieve the 'poroelastic solution' presented in Fig. 6.5B, 6.6A and 6.7B. Two fitting parameters are introduced with a corresponding cylinder radius, a_c and a corresponding injection time, td. The parameters for the pore pressure solution can be found in Table 6.1. The late time approximation $p(r,\theta)$ and p^0 are equated, where the values p_a and a for the envelope $p(r,\theta)$ are given. The two terms equated and solved for a_c to achieve the new corresponding cylinder radius. The mean stress p_0 is estimated from the six injection experiments during the refracturing cycles and the deviatoric component S_0 is the difference of the minimum and maximum principal stress magnitude divided by 2. The diffusion coefficient is estimated from the pressurized near-field zone presented in Fig. 6.5A. The other values are from the literature or calculated from the values given in Table 6.1. The first fitting parameter gives a value a_c equal to 2.80 m allow us to match the elastic approximation with the far-field observations decaying with a rate r^{-2}. Nevertheless, we use a value of 2.60 m for pore pressure solution obtained by the numerical Laplace inversion model, due to inaccuracies due to the transformation. The numerical results in the time domain are obtained using a numerical Laplace inversion model of Stehfest (Stehfest, 1970). Fig. 6.4A and 6.4B present the solutions for Mode 2 and Mode 3 for various times td, which corresponds to possible injection times. The pore pressure solution is then presented by the superposition of $p^{(2)} + p^{(3)}$ in Fig. 6.4C.

Table 6.1 Parameters of the poroelastic model used for the poroelastic solution.

Quantity	Value	Unit
p_0	7812	[kPa]
S_0	4000	[kPa] (Dutler et al., view)
ν	0.2	[] (Dambly et al., 2019)
ν_u	0.33	[] (Wang, 2000)
α	0.68	[] (Selvadurai et al., 2019)
D	0.1	[m^2/s]
B	0.719	[]
K	19	[GPa] (Dambly et al., 2019)
G	10	[GPa] (Dambly et al., 2019)

The injection time in our case is around 1200 s. Indeed, the solution for td equal to 1200 s is able the build an envelope to the observations, which is a good match between the model and our observations.

The Skempton coefficient is given by (Wang, 2000):

$$B = \frac{3(\nu_u - \nu)}{\alpha(1-2\nu)(1+\nu_u)} \tag{6.8}$$

6.3 Results and Discussion

Examples of pressure data are presented in Fig. 6.1B and C. All pressure records were classified based on their pressure response being positive, negative or mixed meaning sometimes positive and sometimes negative. In addition, for each monitoring point the following parameter were extracted. The perturbation magnitude is defined as the extremum (negative or positive) pressure perturbation magnitude observed during each experiment. The distances to the injection location, r, is calculated by the Euclidian distance from the midpoint of the injection interval to the midpoint of the observation interval. The characteristic time is estimate by the elapsed time between the maximum pressure in the injection interval (shut-in time) and pressure perturbation extremum in the observation intervals (Fig. 6.2).

In total, we observed 28 positive, 28 negatives, and 7 mixed responses (Fig. 6.1C). Far field monitoring interval tend to always present the same response, while mixed responses are more common in the near field.

In the near-field (up to 30 m), the pressure response is dominantly positive (Fig. 6.1D) although mixed and negative response are also present. An example of mixed response is given by PRP11 interval presented on Fig. 6.1A which typically showed a positive response (HF1-HF5, red) except during HF6 where a negative response is observed (blue in Fig. 6.1A). These exceptions are induced by local heterogeneities in structure and flow and can be explained only when the small-scale heterogeneities and their configuration with respect to the injection point are considered (Dutler et al., 2020). Negative pore pressure responses are associated with normal fracture opening, dilation accompanying shearing, or volume expansion. Positive responses are primarily associated with hydraulic connection to the injection point, they can also be related to fracture closure and volumetric compression. The near field zone dominated by positive and mixed response is referred to as the 'pressurized zone'.

The pore pressure intervals in the far-field are consistently negative or positive for all experiment (no mixed responses), but for the experiment HF5. This can be explained by the peculiar flow situation during this test because a short-cut was created to an open borehole during the first refracturing cycle and far field pressure perturbation during this test was below our detection threshold. The spatial repartition of positive and negative response is not aleatory, but entire zones seems to consistently present positive or negative response.

The analyses of characteristic time allow differentiating two zones (Fig. 6.5A), a near-field zone dominated by pore pressure diffusion, and a far-field zone dominated by a mechanical response.

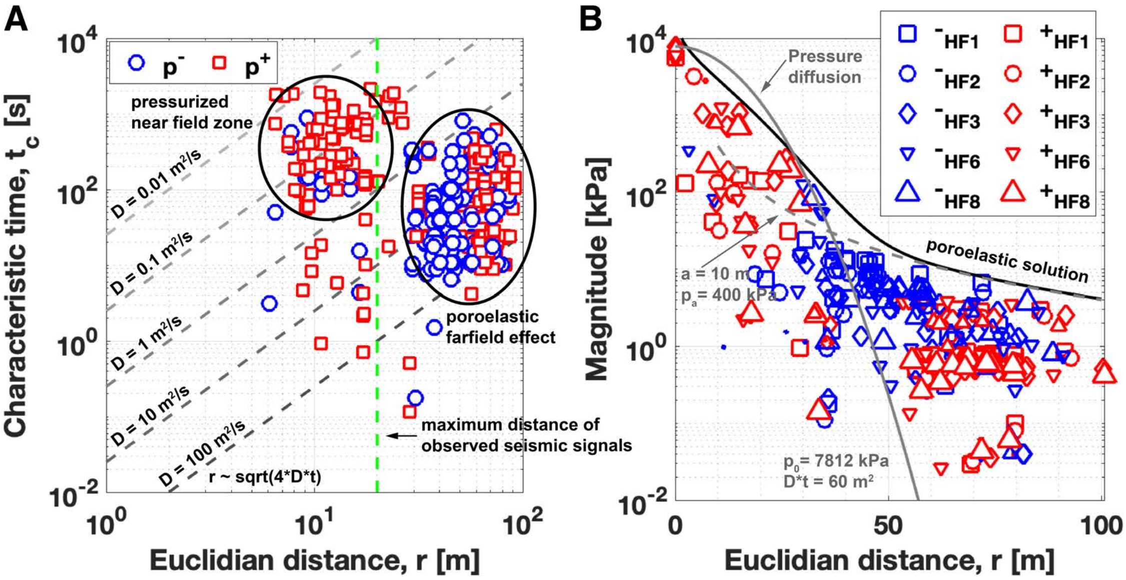

Fig. 6.5 The spatial time increase and the spatial maximum absolute magnitude are classified by positive (red) and negative (blue). (A) The loglog plot presents the characteristic time t_c against the Euclidian distance r inclusive grey dashed lines indicating different diffusivity coefficients for the 1D diffusion equation. Two different patches are observed for the pressure observations one corresponding to the pressurized near-field zone and the poroelastic far field response. The green dashed line indicates the maximum distance of observed seismic signals. (B) The maximum magnitude is presented including a volume dependent size of the symbols against the Euclidian distance r for specific tests in semi log scale (see Fig. 6.6A for loglog scale). The poroelastic solution (black solid line), the radial pressure diffusion (grey solid line) and the far-field pore pressure solution are drawn (grey dashed line).

The pressurized near field zone has a dominant positive response with a diffusion coefficient equivalent to 0.01 and 1 m^2/s estimated assuming normal radial diffusion in 2D as indicated by the grey dashed lines in Fig. 6.5A. The broad range of coefficient indicates that pressure propagation is not dominated by simple linear diffusion. Pressure propagation occurs in an interconnected fracture network with a hierarchical organization of flow from main channels initiating at the injection point branching to subsidiary channels further away from the injection point. This geometry expands during continuous stimulation operations (Dutler et al., view). In the main channels directly connected to the injection point super diffusion and dominant non-laminar transport is probable. This leads to a very heterogeneous flow field with large contrast of flow velocity leading to the broad range of equivalent diffusion coefficient observed.

Based on our characteristic time analyses, this near-field zone extends up to about 30 m for our experiments (Fig. 2A). This size is comparable with the extend of the ’pressurized zone’ estimated by Schopper et al. (2020) based on seismic tomography. However, the zone, where we observed seismic signals is significantly smaller as it extended up to 20 m as indicated by the dashed green line of Fig. 6.5A (Dutler et al., 2019; Villiger et al., 2020).

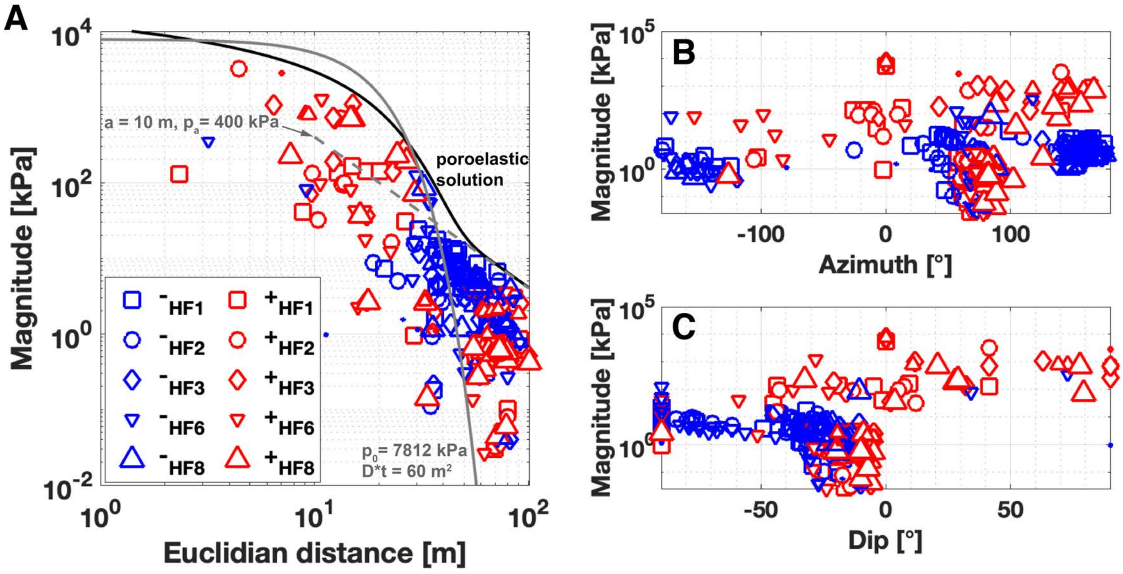

Fig. 6.6 (A)The maximum magnitude is presented including a volume dependent size of the symbols against the Euclidian distance *r* for specific tests in a loglog plot. The poroelastic solution (black solid line), the radial pressure diffusion (grey solid line) and the far-field approximation are presented (grey dashed lines). (B) The magnitudes are presented against the deviation from North and (C) the deviation from a horizontal plane, where positive values indicate dip.

In addition, 60 uniaxial strain gages captured the strain response in this zone, indicating complex hydromechanical interactions. We observed generally on the strain signal very rapid responses that can explained either by poroelastic effects or by focused flow channeling. Both processes are likely active simultaneously as supported by the observation of some rapid pressure perturbation in the near field that are evidences of focused flow in deformed fractures (Fig. 6.7).

Far field data forms a distinct group with higher equivalent diffusion coefficient with values ranging from 1 – 100 m^2/s (Fig. 6.5A). The 1/60 Hz sampling rate used to capture the far-field pore pressure responses give limitations for estimating the maximal diffusivity coefficient. As already observed, the far field responses can be both positive and negative. The near-instantaneous pore pressure response in the far-field zone suggests a strong mechanical coupling.

The analyses of the pressure perturbation magnitude (Fig. 6.5B) further indicates the presence of two different processes. The pressure perturbation in largest at the injection point and in its vicinity. In the far-field, our stimulations were visible up to 100 m away from the injection location, although the pore pressure change was 4 kPa only. So, the ratio between the size of the 'pressured zone' (radius of about 30 m) and the farthest perturbation reach is in the order of 3 to 5. The maximum or minimum pore pressures were generally observed during injection phases with the highest flow-rates (Fig. 6.1B). After each experiment, a depressurization phase was carried out by venting the packer intervals within the 'pressurized zone'. Up to 12 hours were required to recover initial pore-pressure levels.

The largest observed pressure perturbations in the near field up to a distance of 30 m are not exceeding the pressure predicted by a radial pressure diffusion model with a diffusivity of 0.1 m^2/s, a test time of 600 s, and the actual imposed pressure at the injection point (Fig. 6.5B). Beyond 30 m however such model predicts pressure perturbation magnitude that are an order of magnitude or more below the largest observed perturbation. In addition, between 40 and 60 m, we mainly observed negative pressure responses, which cannot be explained by pressure diffusion.

Detournay and Cheng (1988) presented a solution for the pore-pressure, displacement and stress induced by the pressurization of a vertical borehole with in-situ principal stress parallel to the borehole axis. Three fundamental modes describe the problem: (i) the far-field isotropic stress, (ii) the in-situ pore pressure and (iii) the far-field stress deviator. Each mode has to be solved and the superposition of all three modes lead to the solution (Text 6.2). The far-field approximation of the pore pressure is asymmetric and depends on a magnitude decay in the order of r^{-2}. A simplified approximation is presented for the volumetric pore pressure changes:

$$p(r,\theta) = \quad p_a \tfrac{a^2}{r^2} \cos 2\theta \tag{6.9}$$

where a given uniform radial stress p_a= 400 kPa and cylinder radius a = 10 m with θ = 0 corresponds to the upper envelope for the far-field distance in Fig. 6.5B. The solution shares similarity with the Lamé solution with an asymmetric deviator and is used to estimate the

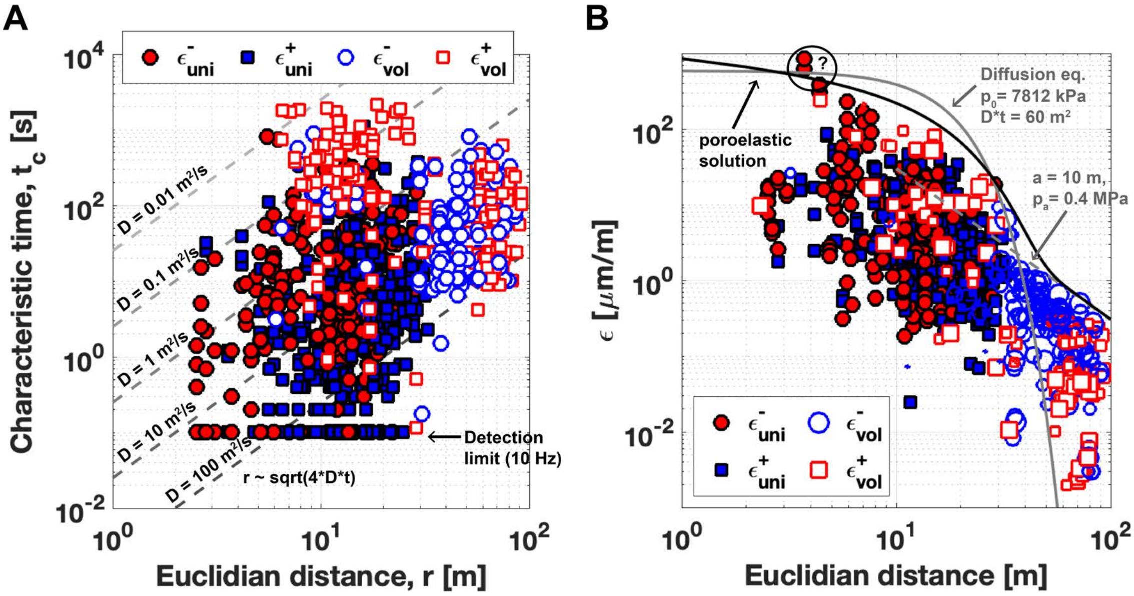

Fig. 6.7 (A) The loglog plot presents the characteristic time t_c against the Euclidian distance r for the picked uniaxial strain and the calculated volumetric strain from the pore pressure picks inclusive grey dashed lines indicating different diffusivity coefficients for a simple 1D diffusion equation. The detection limit for the uniaxial strain is at 10 Hz. Negative uniaxial response corresponds with fracture opening or shearing and has positive pore pressure. Hence, the red color indicates the similarity between negative uniaxial and positive volumetric strain and vice versa. (B) The pore pressure was recalculated to volumetric strain (Text 6.2) and compared with the observations from the uniaxial strain results. The poroelastic solution, the diffusion solution and the far-field pore pressure approximation are drawn (similar to Fig. 6.6), where also recalculated with the same formulas (Text 6.2). The uniaxial strain plots mostly below the given diffusion line. There are two exceptions (marked by a questions mark), which indicate larger strain extension, whereby these observations are uniaxial and the fracture topography is not well known, such that channelized flow or slip cannot be excluded.

poroelastic solution (Text 6.2). The zone between 30 and 50 m represents a transition zone between the pressurized zone dominated by pressure diffusion in the near-field and volumetric pore deformation in the far-field.

A similar approach was used for fluid disposal wells in Oklahoma, where the fluid disposal wells were about 40 km away from the earthquake epicenter (Goebel et al., 2017). The decoupling of elasticity and diffusion has its limitation since positive and negative pore pressure response remains unexplained. To explain the observed spectrum of pressure responses, a solution with a deviatoric stress boundary is required. The poroelastic solution for a cylinder given by Detournay and Cheng (1988) inherently contains this effects and explain changes of criticality on faults in the far-field of a stimulation. The applied poroelastic solution was fitted by to independent values, the corresponding cylinder radius and the injection time (Text 6.2). This actually allowed us to achieve a good match for the observations and the poroelastic solution presented in Fig. 6.5B (and Fig. 6.6A and 6.7B). Fluid flow during the experiments is limited to interconnected fractures. In the far-field zone, pressure changes are assumed independent of active fluid transport from the pressurized zone, which agrees well with the presented poroelastic solution.

The pore pressure solution is presented by a diffusion and deviatoric component (Fig. 6.8). The diffusion component of the pore pressure solution dominates up to 42 m from the injection location. The radial pressurization is a strong simplification. Two fault zone sets S1 and S3 striking through the targeted volume. The S3 structures are brittle-ductile fault zone (Fig. 6.8C) containing two-fracture systems. One strikes parallel to the S3 fault zone and the other abutting at high angles to the fault zone. The second set of ductile fault zones (S1, Fig. 6.8D) is associated with a single fracture system striking parallel to the fault zones. It is more likely that the injections create an ellipsoidal shaped pressurized zone along S3 faults due to the (1) stress field, (2) the fracture connectivity (3) and fracture orientation. These interconnected, permeable fractures allow for transporting fluids over larger distances but are not necessarily the most critical structures to fail depending on the stress regime. The ellipsoidal shape causes compression normal to the S3/S1 fault zones and negative pore pressure response at the ellipsoidal tip (Fig. 6.8C and 6.8D).

Pore-pressure responses in the far-field are biggest in magnitude for tests (HF1, HF2, and HF6) located next to the S1 structure (Fig. 6.1A) and reach only part of the magnitude for tests next to the S3 structure. The deviatoric pore pressure component (Fig. 6.8B) is not radial-symmetric due to the deviatoric stress field component (Fig. 6.8E) given in the lower stereographic projection for the presented solution on a vertical cylinder. In the rock volume of interest, Krietsch et al. (2019) derived the stress state South of the S3 structure. The six hydraulic fracturing experiments allowed us (Dutler et al., view) to re-define the stress state towards North of the S3 structure, which is presented in the lower stereographic projection. The orientation of the minimum and maximum principal stress component was used (S_1 and S_3) for the rotation of the deviatoric component. It leads to a far-field pore deformation with characteristic positive/negative response, which is dominant outside of the cylinder (Fig. 3E). The observations agree often with the presented solution outside of the cylinder. A few exceptions exist around the tunnels, which are most probable secondary effects due to (1) the stress field and (2) the drained rock mass.

Our observations prove the first time experimentally, that pore pressure perturbations around the injection point are not limited to the near-field, which is affected by diffusion processes. Our data show that pressure in the far-field is associated with pore volume changes. The observation indicates that already small volumes of injected fluid can cause a far-field poroelastic pressure response. The spatial distribution of negative and positive responses allows gaining information about the dominant failure mechanism before any hazardous seismicity occurs. This can serve as a complementary method to seismic monitoring during hydraulic stimulations. The technique can be used for mitigation strategy avoiding induced seismic hazard if pre-existing drilled boreholes are equipped with a pressure gage and packers. The method is powerful cost-effective monitoring tool.

Acknoledgment

This study is part of the In-situ Stimulation and Circulation (ISC) project established by the Swiss Competence Center for Energy Research-Supply of Electricity (SCCER-SoE) with the support of the Innosuisse. Funding for the ISC project was provided by the ETH Foundation with grants from Shell and EWZ and by the Swiss Federal Office of Energy through a P&D grant. Nathan Dutler is supported by SNF Grant No. 200021_165677. The Grimsel Test Site is operated by Nagra, the National Cooperative for the Disposal of Radioactive Waste. We are indebted to Nagra for hosting the ISC experiment in their GTS facility and to the Nagra technical staff for on-site support and allowing us to publish the dataset of the far-field pressure response. We thank, Bill Lanyon for data compilation of the far-field pressure response.

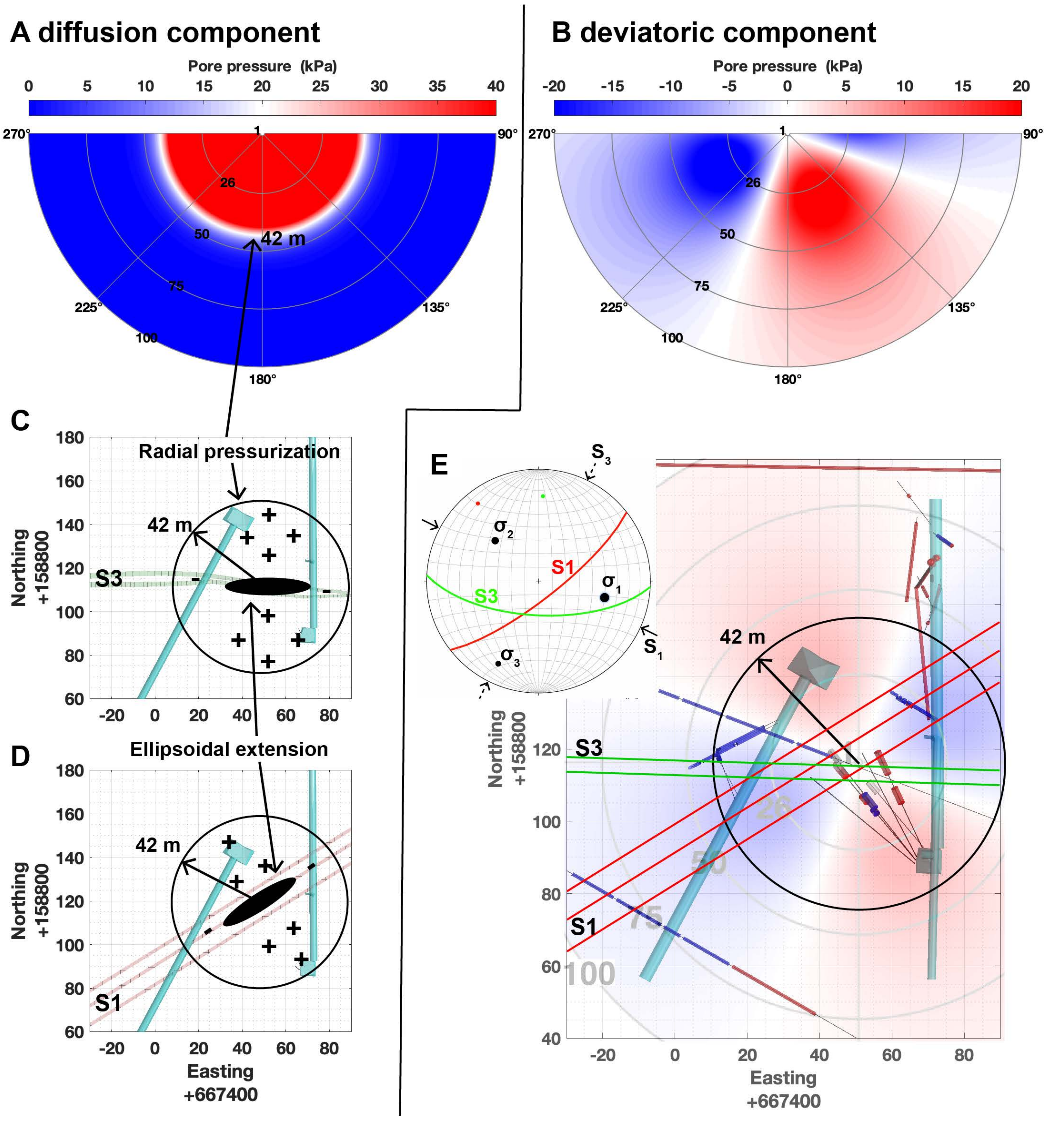

Fig. 6.8 The pore pressure response is interpreted by a diffusion and deviatoric component. (A) The pressurized radial-symmetric solution for a cylinder dominates up to 42 m with a magnitude of 20 kPa. (B) The deviatoric component starts to dominate after 42 m (solid circle). Depending on the injection location (C) next to the structure S3 or (D) S1, the near field is more likely along the natural, pre-existing fractures and form an ellipsoidal extension. (E) The pore pressure observations outside of the cylinder agrees often with the deviatoric component. Even in the cylinder negative pore pressure is observed due to deviatoric stress field and undrained dominant fault response, which acts in concert.

Chapter 7

High pressure periodic injection tests

The analysis and data curation inclusive writing the first draft was done by N.D.

7.1 Introduction

Periodic pumping tests can be applied during production or injection and allow a continuation of the fracturing or extraction operation (oil/gas or intelligent management of water resources) (Crosnier et al., 1985; Hollaender et al., 2002; Kuo, 1972). Main target is often the characterisation of the heterogeneous reservoir (Cheng and Renner, 2018; Fischer et al., 2018; Renner and Messar, 2006). Another recent application assumes that periodic high-pressure stimulation (so called soft stimulation or fatigue technique) limit the seismic risk due to enhanced fracture branching on the fracture tip (Hofmann et al., 2019; Zang et al., 2013; Zimmermann et al., 2019). Another study (Vinci et al., 2015) investigates the effect of hybrid-dimensional hydro-mechanical coupled and uncoupled diffusion for pressure transient observations in fractures.

In the following study, I characterize the harmonic responses of pressure transient records from the injection location and pore pressure monitoring observations during harmonic pumping operation. The harmonic signal has a sinusoidal shape with a given period and amplitude. The attenuation and phase shift are compared between the injection pressure and the observations. The goal is to characterize the fractured reservoir and if possible major single flow paths during the hydraulic fracturing operation using pressure observations in term of phase changes and signal attenuation. The high-quality records of strain and pore pressure data allow me to investigate hydro-mechanical coupling during periodic injection and possibly allow me to investigate the fracture tip behaviour and the interaction between new created fractures and the natural fractures. In addition, the flow rate is compared with injection pressure record leading to injectivity values.

7.2 Experimental details

7.2.1 Injection and monitoring record

Six hydraulic fracturing (HF) experiments (Dutler et al., 2019) were executed in May 2017 at the Grimsel Test Site (GTS) during the In-situ stimulation and circulation (ISC) project (Amann et al., 2018). During five of six experiments, cyclic pumping tests were performed. This injection either took place during the first refrac cycle RF1 or during the third one (RF3), which was performed as a flushing cycle. This cycle was executed in case the injection fluid for refrac cycle RF1 and RF2 was a high viscous shear-thinning fluid (Xanthan-salt-water mixture), which was the case for HF6 and HF8. The injection rate and pressure are presented (Fig. 7.1) for two experiments, HF3 and HF8. During the HF3 experiment, only one cyclic pumping test was executed with twelve cycles having a period of 15.7 s during the first refrac cycle. Four cyclic pumping tests with periods between 3.9 and 31.3 s were executed during the flushing cycle of experiment HF8. The geological model (Krietsch et al., 2018) and the monitoring setup of the ISC experiment are summarized in Fig. 7.1 (c) highlighting the tunnels, the brittle-ductile shear zones and the injection (INJ) and pore pressure monitoring (PRP) boreholes. Detailed description can be found in chapter 4 and in the Grimsel ISC Report (Doetsch et al., 2018a).

7.2.2 Pumping procedure

We performed cyclic pumping tests with periods between 3.9 and 31.3 s. The individual tests have 3 to 28 full cyclic periods (Table 7.1). In total 14 cyclic pumping tests were performed. To create sinusoidal signals, we controlled the frequency converter (brand: HITACHI) of the injection pump (brand: SPECK) with a variable current signal. This was controlled and executed through a python script installed on the field computer. The injection flow rate, injection pressure, packer of the injection pressure interval, observation pressure and packer of the observation pressure interval are sampled at 20 Hz and measured uphole. The flow rate of the injection line was measured uphole by different flow meters depending on the flow rate to achieve high resolution measurements. The pressure monitoring system was designed to observe transient pressure changes at specific locations (see Fig.7.1). Costumized grout packer systems were installed in the PRP and SBH4 boreholes. The open interval sections were equipped with pressure sensors and separated with hydromechanical packers and resin. The pressure sensors (PAA33-X Keller) of the monitoring setup (intervals of the PRP and SBH borholes) were connected to the Solexpert data acquisition system with a sampling rate of 20 Hz and a resolution of < 1 kPa. The maximum possible pressure range of the pressure sensors was up to 10 MPa.

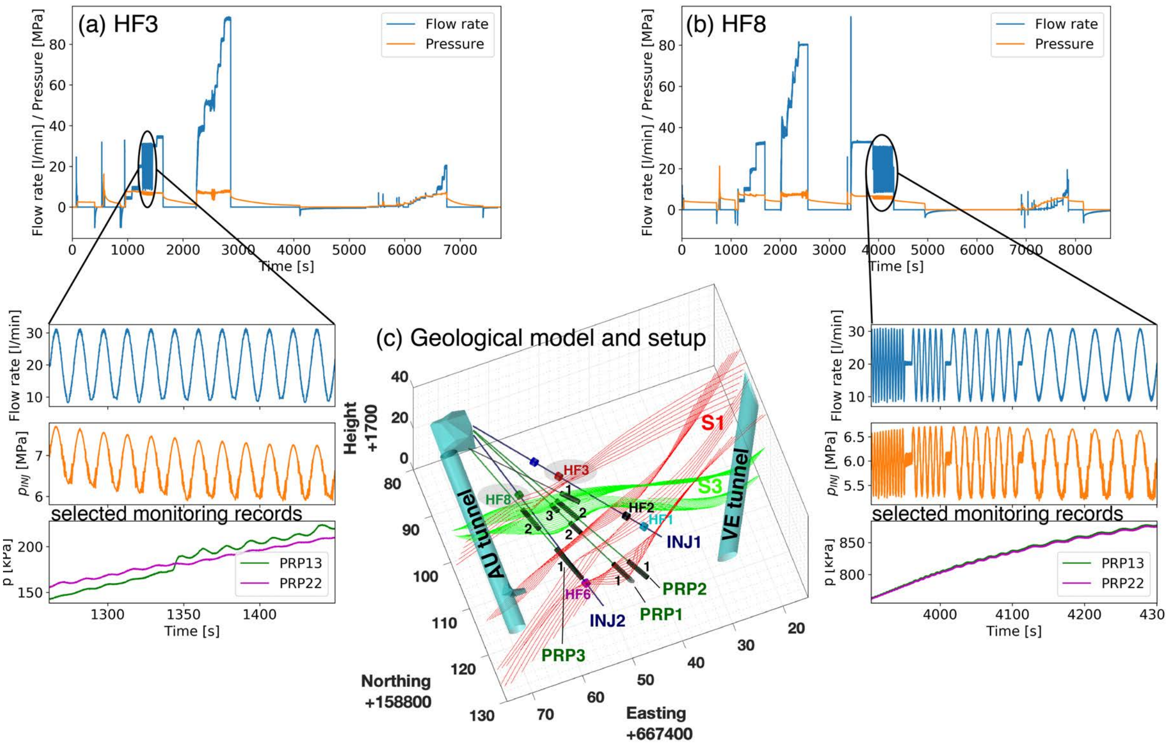

Fig. 7.1 Injection pressure and injection flow rate of experiment (a) HF3 and (b) HF8 inclusive the zoomed section during periodic pumping with selected monitoring pressure records. (c) The geological model includes the brittle-ductile shear zones S1 and S3, the AU and VE tunnel and the injection (INJ) and pressure monitoring (PRP) boreholes inclusive experimental injection intervals (HF#) and pore pressure intervals (PRP##, black cylinders).

7.2.3 Processing

Characteristics of pressure and flow records were determined by fast Fourier transformation (FFT) analysis and Digital Lock-in amplifier analysis. Both methods allow to extract amplitude and phase of periodic components in the time series. The finite time series contains 3 to 28 oscillation. The records were cut containing the full length of the same imposed pumping period. Different pressure records with different time stamps were used. The sampling rate of the acquisition system was 0.05 s. For data comparison the time vector of the data set were resampled. This was done using a mean interpolation on an equal spaced time vector with 10 Hz. The linear trend was removed subtracting a linear least-squares fit to the data.

The time step of the records is very small compared to the length of the test sequence. Hence, the Nyquist frequency is small and the values of the phase shift are exact. If the harmonic signal is contained in one of the monitoring records, the spectra decay strongly towards high frequencies (Fig. 7.2). The FFT analysis is able to determines phase shift and amplitude

Table 7.1 Summary of periodic pumping tests during hydraulic fracture treatment. The injection fluid was water except for two tests (indicated by (x)) injecting a high viscous shear-thinning fluid.

Experiment	Test cycle	Period T (s)	No. of oscillations	Mean flow rates (l/min)	Imposed amplitude (l/min)
HF1	RF1b	7.83	28	20	7.5
HF2	RF1	15.67	6	20	12.5
HF2	RF1	31.33	3	20	12.5
HF3	RF1	15.67	12	20	11
HF6	RF1 (x)	15.67	7	21	11
HF6	RF1 (x)	31.33	3	24	11
HF6	RF3	3.92	10	21	11
HF6	RF3	7.83	12 (6 and 6)	21	11
HF6	RF3	15.67	6	21	11
HF6	RF3	31.33	6	21	11
HF8	RF3	3.92	12	20	11
HF8	RF3	7.83	6	20	11
HF8	RF3	15.67	6	20	11
HF8	RF3	31.33	6	20	11

between two signals within one cycle. It is important to know how the signals are delayed for the right interpretation of the phase shift. This can be done by eye or by more sophisticated methods like correlation analysis.

Both methods, sliding FFT and digital lock-in amplifier, allow to investigate the temporal evolution and variability of amplitude ratios and phase shift. The variability over time is used as a measure of uncertainty between two signals. The window used in the FFT analysis had a length of two periods and was shifted along the record by steps of a sixth of a period. The values of amplitude and phase shift are only reported if a local maximum was observed in the amplitude spectrum during the pumping frequency. The lock-in amplifies the pressure record. It is multiplied by the lock-in reference signal and allow the extraction of the amplitude and phase-shift at sampling frequency with respect to the reference signal (more in 7.6). To compare two different signals (e.g. the injection pressure record and a monitoring record), the digital lock-in amplifier is applied for each signal. The resulting amplitude can be divided and the phase shift subtracted from each other to get attenuation and phase shift between the two pressure records.

7.3 Preliminary results

The amplitude with a local maximum at the pumping frequency in the amplitude spectra (Fig. 7.2) are marked with a red circle. All the marked records are analysed by the digital lock-in amplifier and sliding FFT to calculate attenuation and phase shift between two signals. In the following section, the comparison between flow rate q and injection pressure p record is called injectivity test and the comparison of different pressure records is called interference test.

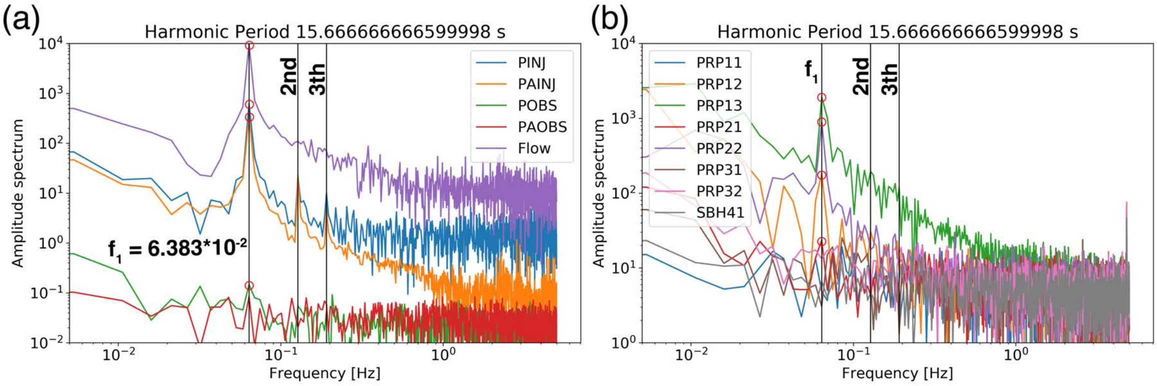

Fig. 7.2 (a) The amplitude spectra of pressure records in injection interval (PINJ) and the observation interval (POBS) and the packers (PAINJ and PAOBS) given in MPa. The pumping rate (flow) is given in l/min with a period of 15.67 s. (b) Additional pressure records from the fixed installed observation intervals are presented in kPa. The amplitudes at the pumping frequency are indicated (f_1) with the second and third overtone for a perfect sinusoidal signal. The pumping frequency corresponds to the global maximum in each spectrum, if the monitoring - injection distance is not too far.

7.3.1 Lock-in amplifier vs. sliding FFT

The results in amplitude attenuation and phase shift from digital lock-in amplifier and the sliding FFT method are comparable. To minimise boundary effects, the first and last periods of the signals are cut in both methods. The digital lock-in amplifier method indicate smoother results over time then the sliding method (Fig. 7.3), but overall the results for the interference tests are very similar (see Fig. 7.4) using the mean of attenuation and phase shift. The relation between injection pressure and flow rate (Fig. 7.3 a and c) indicate a phase shift of a full cycle. This is due to the negative phase shift observed comparing the flow rate response with the injection pressure record. A modulo function is used to map the offset changes of two signals between zero and one periodic cycle. The interference test between the injection pressure PINJ and the monitoring interval PRP13 (Fig. 7.3 b and d) indicate a sudden deviation during periodic injection in the PRP13. For this kind of drastic signal change it can make sense to split the signal into two parts excluding the part with sudden deviation. For the following analysis using only the mean and standard deviation of the attenuation and phase shift, I have decided not to investigate the impact of this kind of signal change.

7.3.2 Observations from experiment HF8

The presented raw data in Fig. 7.1 for experiment HF8 with the pressure records from interval PRP13 and PRP22 are presented in Fig. 7.5. The injection pressure has an impulse amplitude of around 1 MPa. Four different cyclic stimulations were executed with ascending periods, T,

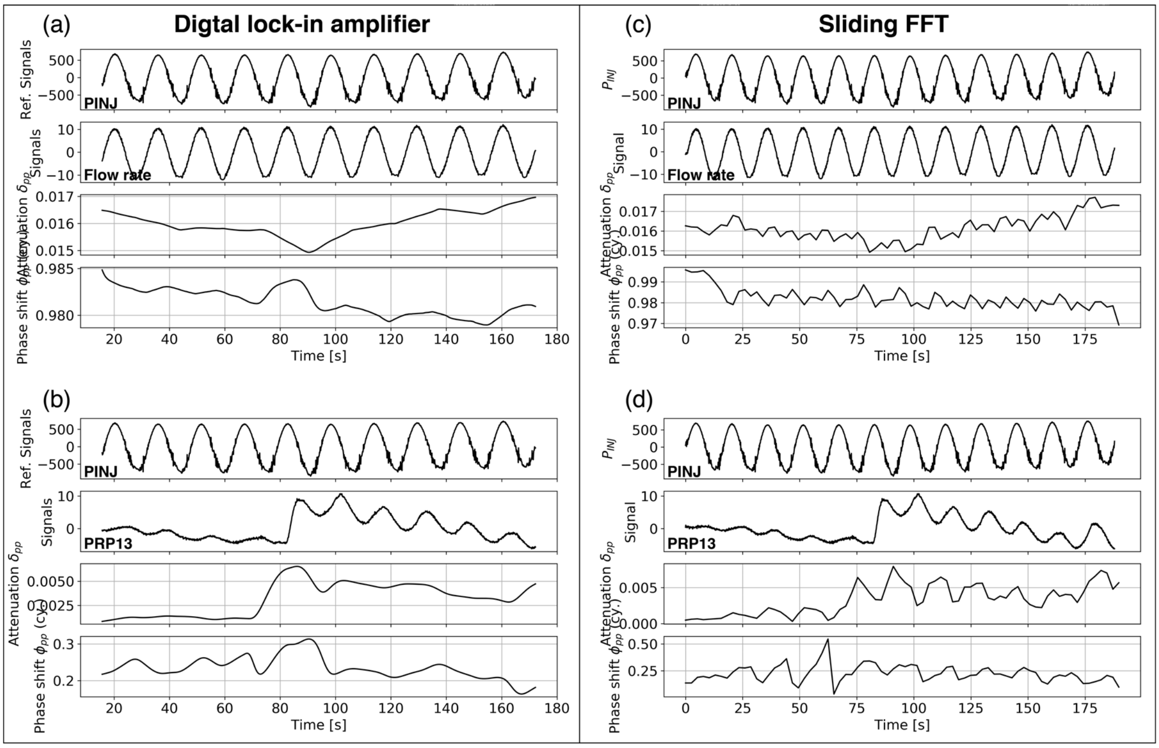

Fig. 7.3 (a) and (b) the digital lock-in amplifier was used with the reference signal on top, the compared signal on second position and the resulting attenuation and phase shift over time are presented on row three and four. (c) and (d) use the sliding FFT method. The same signals are presented in (a)/(c) and (b)/(d) to compare the two methods.

from 4 to 31 s. Figure 7.5a) indicates that a smaller period lead to larger amplitude reduction and larger phase shifts including increasing uncertainty. The records from both intervals are similar for longer periods and show differences at smaller injection periods. The pressure records of PRP22 show a stronger attenuation and phase shift compared to the record of PRP13. Where the PRP13 interval is located 9.1 m away from the injection location and PRP22 is only 7.0 m away and still, the amplitude reduction is larger in the sensor located closer to the injection. The Euclidean distance is the shortest way between two points. Therefore, the distance is too short and does not account for actual flow path. Accordingly, in the present case we would assume that the pressure wave in the flow channels first hit the interval farther away and then the other interval. Because of the aformentioned argument, Figure 7.5b) needs to be interpreted with care. The used solution for amplitude reduction is given by a simple radial pressure decay $\delta_{pp}(r) \sim \exp \frac{-r^2}{4DT}$ with given radius r, diffusivity D and periods T. The decay rates for diffusivity has to be somewhere in between of D=0.1 m^2/s and D=1 m^2/s. This is still work in progress and better analytical description can improve the understanding.

Prior to the cyclic injection, the formation break down cycle and two refrac cycles took place. For an idealized case, the maximum fracture length is estimated to be around 30 m after

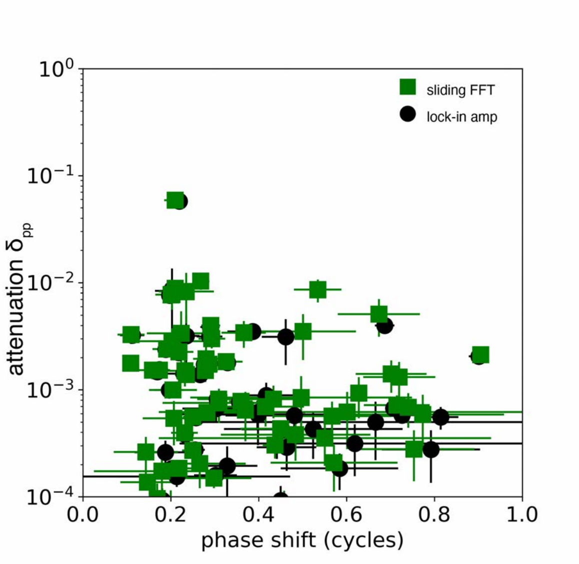

Fig. 7.4 The results of the sliding FFT and digital lock-in amplifier.

the second refrac cycle for a penny-shaped fracture assumption. Our results show a strong amplitude reduction several meters from the injection location. Regarding that the fracture tip is again several meters away from the observation point, the amplitude of the cyclic injection is completely attenuated and not seen in the fracture tip. In this light, the process of fracture branching is questionable. The necessary fluctuating pressure at the fracture tip is not reaching it at cyclic injection periods given in our project or for smaller periods.

7.3.3 Interference analysis

The observed attenuation and phase shift values between the pressure signals range from 0.00002 and 0.06 and from 0.1 to 0.9 cycles (Fig. 7.6 a). The smaller the amplitude the bigger the uncertainty in attenuation and phase shift. Pure water injection took place for experiment HF1, HF2 and HF3, where cyclic injection were performed during refrac cycle RF1. During experiment HF6 and HF8, a shear thinning fluid was injected during RF1, which was 35 times more viscous than water. For the flushing cycle RF3, water was used. Hence, we can not exclude effects related to the previous high viscous fluid injection. Generally, the amplitude of the observations decrease with distance away from the injection interval (Fig. 7.8 a).

The shorter the period, the less the amplitude and the bigger the uncertainties (Fig. 7.8 b). There is a trend of smaller amplitudes during RF1 compared to RF3, where the injection volume prior to periodic pumping is around 70 l and for RF3 it is around ∼700 l. The signal response in the observation intervals are different for various locations of the injection interval. There is a

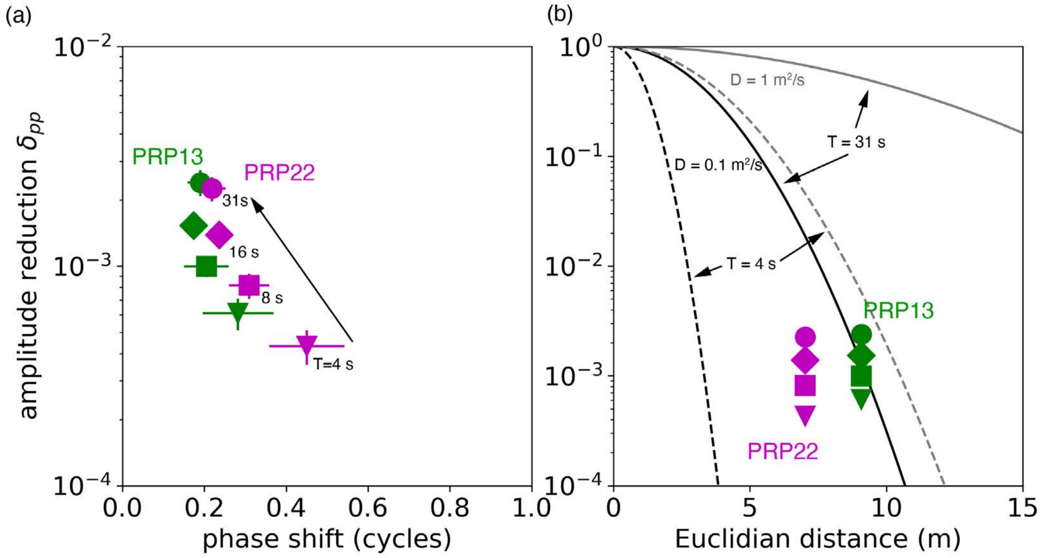

Fig. 7.5 (a) Results of eight interference tests for two intervals PRP22 and PRP13 presented in Fig. 7.1 with four different stimulation periods T. (b) The same results for amplitude reduction are presented against the Euclidian distance from the injection location. The solid and dashed lines indicate possible decay rates for two different diffusivities (colors) and for two different stimulation periods (line style).

tendency of larger amplitudes for tests executed next to zone S1 (see Fig. 7.1 c and 7.8 b, e.g. experiment HF1, HF2 and HF6).

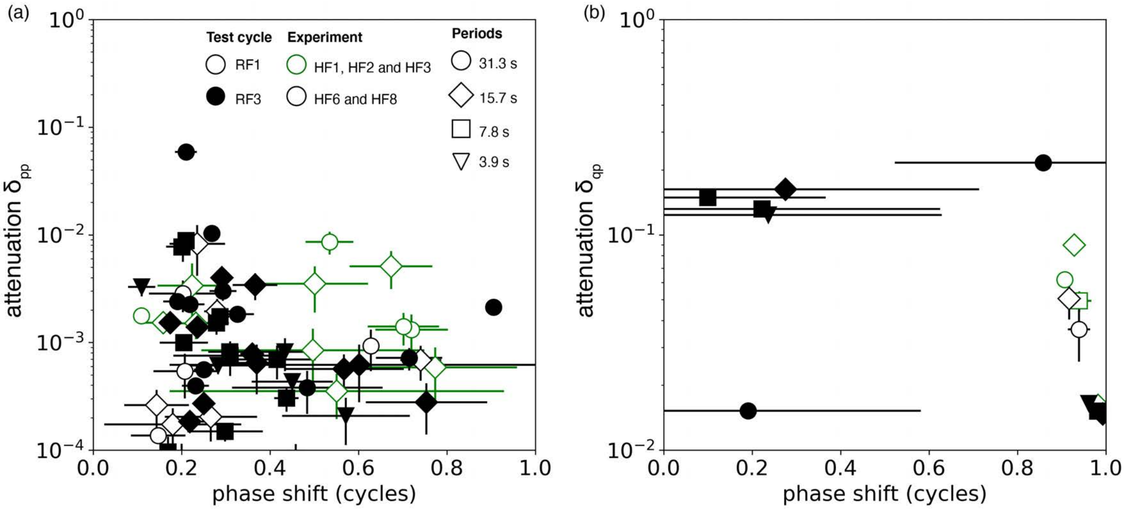

Fig. 7.6 (a) Results of pressure interference tests between injection and monitoring pressure (b) and between injection pressure and flow rate. The results are indicated by experiment (color), test cycle (marker face color) and periods (symbols). Both visualisations share the same legend in (a).

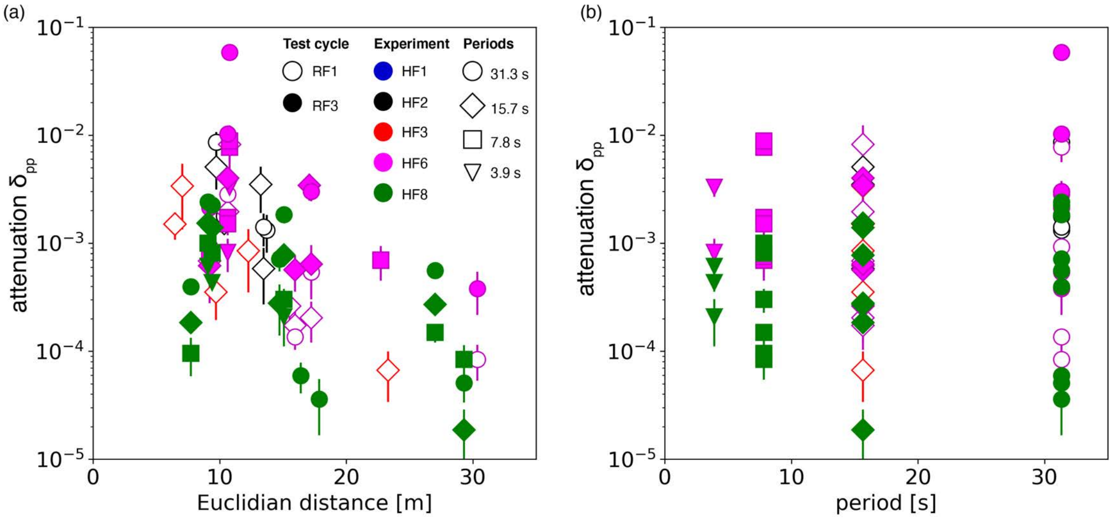

Fig. 7.7 (a) The Euclidian distance between injection and observation interval and (b) the pumping periods are presented against the amplitude attenuation. Both visualisations share the same legend in (a).

7.3.4 Injectivity analysis

The injection pressure exhibit a characteristic delay with respect to the flow rate. Where this delay during RF3 can be influenced by viscous effects in the supply pipes and the reservoir due to switching from high viscous fluid to water. The injectivity values range from 0.015 and 0.22 l/min/kPa. The injectivity analysis indicate a strong linkage to the location, where a test was executed. Generally, the injectivity observed for experiment HF3 and HF8 are very small. These experiments are located south of S3 (Fig. 7.1 c). The injectivity for experiment HF8 is constant independent of the period. For cycle RF1 the injectivity decrease with longer periods, taking into account that the shorter period is executed prior to the longer one. The injectivity values of HF6 build the upper limit and the injectivity values increase with longer periods. Experiment HF6 is located north of S3, in between two fracture zone related with the brittle-ductile structure S1.

7.4 Preliminary conclusions

- Our experimental setup allowed us to generate very clean sinusoidal flow singal. These clear signals have the advantage of easy interpretation and less problems in term off noise or edge effects for the sliding FFT.

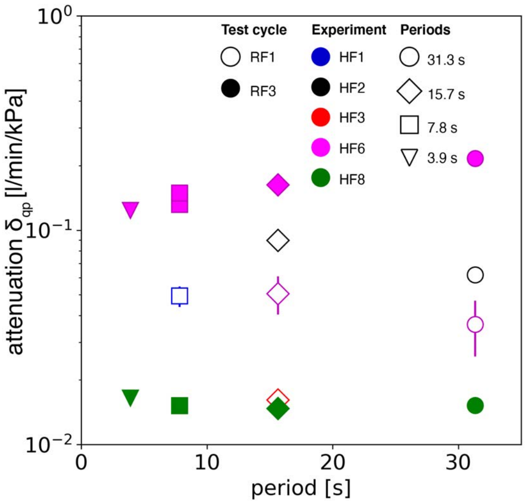

Fig. 7.8 The pumping periods are presented against the injectivity.

- Both methods, Lock-in amplifier and sliding FFT deliver comprehensive and comparable values for attenuation and phase shift. For this perfect sinusoidal signals, the Lock-in amplifier allows to study real time changes during periodic stimulation, which gain insights of possibly hidden changes due to flow break through, flow path changes or/and stress transfer between fractures.
- The strong amplitude attenuation in the monitoring intervals during experiment HF8 indicate that the amplitude is completely attenuated at the fracture tip. Our experiments used maximum injection periods of 31 s and the amplitude observed in the monitoring interval was already two orders of magnitude smaller. We conclude, that fracture branching at the fracture tip can not be achieved and even in the existing fracture (or flow paths) this process is critical and depends on many parameters (e.g. distance to injection, fracture connectivity, fracture roughness, fracture aperture, fracture orientation and fracture stiffness).

7.5 Outlook

The following analyses and interpretations are planned for the completion of the study. For the interference tests, I will calculate diffusivity from the phase shift and attenuation. For this, I implement different flow models (i.e. linear, bilinear, radial and general radial flow model). This interpretation can be challenging as actually hydromechanical models should be used to account for fracture aperture change during injection. However, as this is beyond the scope of this draft, further collaboration will be seek for a proper interpretation using hydromechanical coupled analysis.

I will extend the injectivity analysis, including values from periodic pumping and static injection values. This comparison should allow a better description of the geological structures in term of fluid absorption during hydraulic stimulation from single interval analysis. These in turn can be confirmed or clarified by the interference observations.

The rock mechanical monitoring consists of 60 uniaxial strain gages, which will be analysed during periodic pumping and compared with the observations from the interference tests. Including this information could possibly allow me to reconstruct some of the main flow paths during cyclic injection and it allows me to describe rock mass changes during periodic pumping.

7.6 Digital lock-in amplifier

The sinusoidal pressure record can be defined $p(t) = p_0 \sin(\omega_r t + \theta_{sig})$. The angular frequency is defined as $\omega_r = \frac{2\pi}{T}$, with T the oscillation period of the signal. Two reference signals are constructed, with a given frequency $p_R(t) = A_R \sin(\omega_R t + \theta_{ref})$ and $p_L(t) = A_R \cos(\omega_R t + \theta_{ref})$. The angular frequency of the reference signal $\omega_R = \frac{2\pi}{T_f}$ was calculated using the pumping period. For simplicity we set $\theta_{ref} = 0$ and $A_R = 1$. As a consequence, the two reference signals are orthonormal. Then, the reference signals are multiplied by the pressure record

$$X = p_0 \cos(\theta_{sig})$$

$$Y = p_0 \sin(\theta_{sig})$$

The amplitude and phase shift are calculated by $p_0 = \sqrt{X^2 + Y^2}$ and $\theta_{sig} = \tan^{-1}(\frac{Y}{X})$.

Chapter 8

Synthesis, conclusions and recommendations

8.1 Conclusions

The topics and results presented in this thesis are a subset of the results obtained in the framework of the decameter-scaled In-situ Stimulation and Circulation (ISC) project, which took place between 2015 and 2018 at the Grimsel Test Site, Switzerland. The work contributes to the understanding of the evolution of fracture propagation and hydro-mechanical coupled processes during high-pressure fluid injections into a fractured crystalline rock mass in an heterogeneous stress field. It involves hydromechanical evolution during fracture opening and closure under steady and periodic injection conditions in the pressure controlled zone and the poroelastic response in the far-field zone. In addition, this involves the investigation of the fracture process zone under tensional loading on lab-scale. The main outcomes of the thesis are summarized in the following section.

Fracture process zone mode I at lab-scale

- Laboratory experiments of Grimsel Gneiss on notched semi-circular bend tests show anisotropy ratios of 2.27 and 2.61 for fracture toughness and Brazilian tensile strength, respectively. This indicates that the resistance against material failure is significantly higher when driving mode I fractures across the foliation plane than along it. In addition, the post-mortem analysis indicates bigger roughness and smaller fracture process zone (FPZ) in the direction across the foliation compared to the direction along the foliation. The experiments were conducted under dry conditions.
- The experiment showed that the boundary of the FPZ is formed before reaching peak load. The digital image correlation (DIC) results confirm the development of a semi-

elliptical process zone with an average length to width ratio of about two for the principal directions. The experimental results give supporting evidence, that a nonlinear cohesion stress distribution provide the best match between experimental results and cohesive model.

Fracture propagation on in-situ scale

- New hydraulic fractures (HF) were observed from borehole wall acoustic images after the breakdown cycle of the in-situ hydraulic fracturing experiment. The orientations observed are similar with minor variability for the six experiments and give a good estimate of the independently measured far field stress orientation.
- The small variability of fracture trace seems to be related to rock strength anisotropy and local stress heterogeneity induced by natural fractures and packer stresses. Overall, the stress field dominates the orientation of the fractures intersecting the well bore (Fig. 8.1).
- It was often observed that the fracture trace extended below the packer and often abut against a natural fracture. We can still not decipher between fracture initiation in the open injection interval or below the packer, although the packer pressure is always above the open interval pressure to insure sealing, the former is not unlikely.
- The spatial distribution of microseismic events associated with the fracture growth seems to be predominantly controlled by the pre-existing, natural fractures. The cloud rotations shows the interplay from a fracture propagation under the in-situ stress state with small or no leak-off towards a leak-off dominated situation, where the fluid flow follows the pre-existing, natural fractures. Hence, hydraulic fracturing under mode I stops and shear along existing fractures dominate (Fig. 8.1).
- Our data highlight the simultaneous growth of parallel fracture strands and it also suggest channelized growth instead of planar growth. This complex fracture geometries indicate the difference from theoretical mode I fracture geometries.

Hydraulics

- The well tests executed before and after the in-situ hydraulic fracturing experiment indicate an increase of transmissivity of 2-4 orders of magnitude. The final injectivity from the pressure-controlled step test characterizing the new created hydraulic fracture in the near-field of the open injection interval correlate positive with the transmissivity values estimated from constant head test. The gain in transmissivity goes to a level comparable with the one observed on unstimulated natural fractures in our rock mass. Hence, the final transmissivities seems to be controlled by the connectivity towards the pre-existing, natural fractures, where we observe an increase in density towards the core of the shear-zones.

- When the hydraulic fracture grows, it connects and leaks into the pre-existing fracture network and thus at some point the energy required to create new fracture surfaces isn't sufficient and tensile fracture stops. The flow is then largely dominated by the pre-existing, natural fractures. In that regard, the brittle-ductile shear-zone S3 acts as main drain and constant pressure boundary (atmospheric pressure at the tunnel level) while connection to the S1 shear-zone and associated fracturing provides larger storage possibilities.

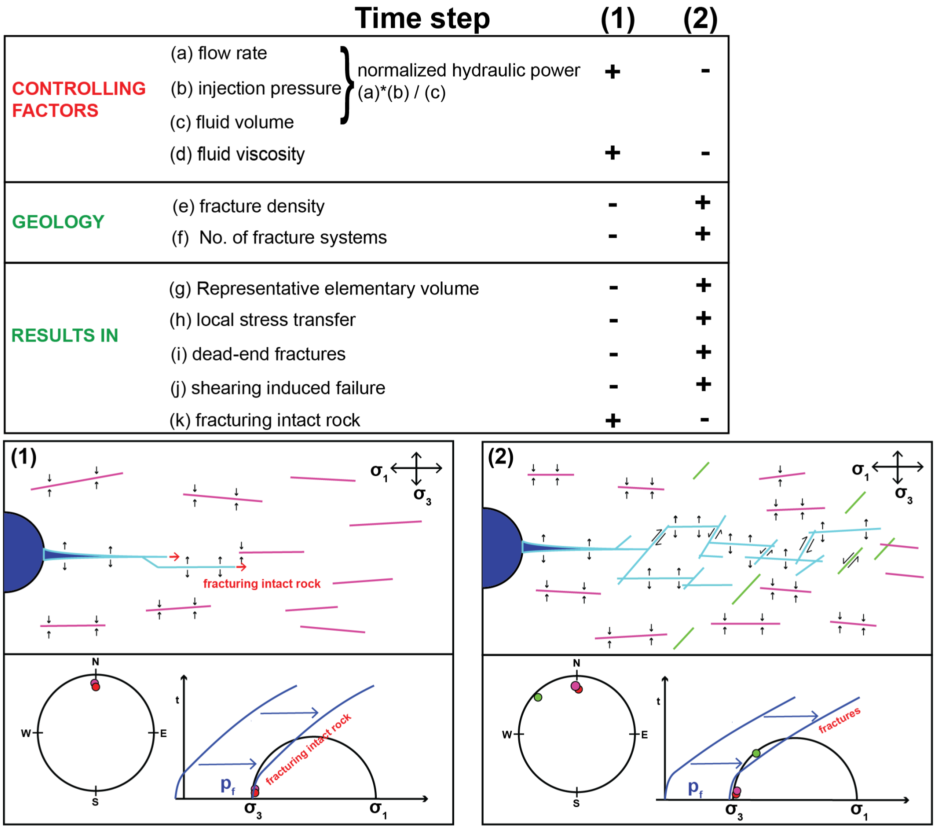

		Time step	(1)	(2)
CONTROLLING FACTORS	(a) flow rate (b) injection pressure (c) fluid volume	normalized hydraulic power (a)*(b) / (c)	+	-
	(d) fluid viscosity		+	-
GEOLOGY	(e) fracture density		-	+
	(f) No. of fracture systems		-	+
RESULTS IN	(g) Representative elementary volume		-	+
	(h) local stress transfer		-	+
	(i) dead-end fractures		-	+
	(j) shearing induced failure		-	+
	(k) fracturing intact rock		+	-

Fig. 8.1 Two schematic interpretations of hydraulic fracturing at (1) early (low fracture density and number of fracture sets) and (2) late time.

Stress field

- Different diagnostic fracture injection techniques were applied. The overall ISIP is 4.81±0.38 MPa and indicates the pressure in the open wellbore interval. The selected ISIPs do yield slightly larger pressure magnitudes than the picked effective ISIP from the dp/dG curve. It is assumed that the effective ISIP to be a better estimate of the minimum principal stress magnitude referred to the fracture tip. The overall effective ISIP is 4.49±0.22 MPa and corresponding to the minimum principal stress magnitude.

- The jacking pressure was measured with a new method using uniaxial strain records versus pressure plot. The values agree with the observations from the jacking pressure from the flow versus pressure plot. The permanent changes in strain are indicative of shear dislocation as well as fracture opening during the pressure-controlled step tests.
- The orientation of σ_3 was estimated from the hydraulic fracture intersecting the wellbore with the assumption that the maximum principal stress axis is stable in orientation.
- The slip-tendency analysis showed that the jacking pressure below the effective ISIP is related to shear dislocation and fracture opening. Both processes can occur almost synchronously and provide new insights into the complicated mixed-mode deformation processes triggered by high-pressure injection.

Hydromechanical response during high pressure injection

- The structural heterogeneities found in our rock mass lead to distinct behaviour in terms of pressure, strain and flow response. The tests performed North or South of the brittle-ductile shear zone S3 respond differently. This differences are principally affected by two effects. Firstly, the shear zone have impacted the stress state locally and thus in turn this affect the fracture propagation and the hydromechanical effects related to stress transfer, fracture extension, fracture dilation and pressure diffusion. Secondly, the shear zones and the associated fracturing influence the flow in the experimental volume.
- Depending on the elapsed time between shut-in and pressure response in the pore-pressure observation intervals, the time lag can be used to divide between a dominant pore pressure diffusion response in the near field of the injection and a poroelastic driven response in the far-field. Both effects can be described using a poroelastic solution for a radial cylinder with the superposition of different boundary conditions. The in-situ hydraulic fracturing experiments showed for all six injection locations the same far-field response. The maximum observed magnitude in the pore-pressure monitoring intervals indicate that the strain field in the far-field decays in the order of r^{-2}. During the experiments, we observed changes in the pressure monitoring intervals as far as 100 m. The spatial distribution of negative and positive responses allow us to gain information about the deviatoric stress field and can potentially link towards the dominant failure mechanism before any hazardous seismicity occurs.

- The periodic pumping tests applied during the hydraulic fracturing experiment with cyclic periods between 4 and 31s show an amplitude reduction of two orders of magnitude in two monitoring intervals compared to the injection interval for one of the experiments. In addition, the phase shift increases with smaller periods. We conclude that the big amplitude reduction in the monitoring interval does not achieve fracture branching at the fracture tip. Nevertheless, harmonic injection has the advantage to allow characterisation of hydrogeological and hydromechanical properties and is able to illuminate flow paths and hidden hydromechanical interactions during high pressure injection.

Implication for reservoir mechanics in fractured crystalline rocks

Reservoir development for deep geothermal systems is a very critical task, where a priori knowledge often decides on success or failure. The hidden unknowns are the biggest risk for this kind of projects. This is mostly due to the scarce data acquisition due to the enormous drilling costs. The small number of drillings for a project limits the a-priori knowledge. Borehole data is providing as 1D information for three-dimensional geological structures, which makes the extrapolation of geological structures very uncertain. Therefore, this uncertainty should be accounted for in the stimulation procedure to avoid unintentional reactivation of large fracture zones. The following points should be considered during high-pressure stimulation:

- The in-situ hydraulic fracturing experiments demonstrated that the enhancement of transmissivity is ceiled to a common transmissivity upper bound. In addition, the initial intact intervals with low transmissivity were stimulated and the new created hydraulic fracture was propagated into the natural fracture system. The transmissivity enhancement in the stimulated interval achieves transmissivity values of the order of the natural fractures. I argue, that fracture connectivity enhancement on the cross-hole scale is far more important than overall transmissivity increase. The transmissivity of the low transmissive intervals will be enhanced by the connection towards the pre-existing, natural fractures and reconnecting them. Thus, the early tensile fracture initiated can be propagated until a critical distance where it starts to include not only tensile as well as shear failure. In fractured crystalline rocks, this is potentially driven by the leak-off from the hyraulic fracture towards the pre-existing, natural fractures. The distance of the driven hydraulic fracture is directly related to the hydraulic power available at the fracture tip and decreases with distance and therefore with the number of natural fractures hit.
- The beformentioned issues can potential be overcome or the distance of a mode I driven hydraulic fracture can be enhanced with the usage of modified viscosity of

the injection fluid. The potential of modified fluid in crystalline rock is still under elaboration and needs more research.

- The choice of the injection interval and the injection protocol can only be used to control the fracture at the beginning of injection. At later time and increasing injected volume, the overall fracture mechanism is dominated by the natural fractures and the acting normal- and shear stress control this mechanism.
- Based on the above conclusions, I recommend limiting the open interval sections for injection and either avoiding very high transmissivity zones or limiting the injection volumes into these zones. The hydraulic experiments showed that stimulations near these zones always connected rapidly the initiated fracture to this zone. In addition, the back flow of injection fluid is minor and therefore, the control on fluid diffusion is limited. The pressure increase propagates along this structure and controls the fracture behaviour over distances that can not be predicted if no knowledge exists about them from existing exploration data (e.g. geophysics, exploration or drilling).

8.2 Perspectives and recommendations for future research

This dissertation gives insights into the hydromechanical coupled processes within the crystalline rock mass during hydraulic fracturing treatments. The generated high quality, high-resolution data set did not allow me to study everything in detail. In addition, during analysis and interpretation of the data set new questions arose. In the following, a list of open points on which further research can be done.

What is the effect of different injection protocols on the outcome of reservoir mechanics?

During the ISC, we made the decision to stay with one injection protocol for each of the two main experiments. The focus was to characterize rock mass, pore fluid and seismic response due to the geological structures for a given protocol. Due to space limitation, only six experiments could take place during each main experiment. The results from the different responses show a strong impact due to injection location and the activated geological structures. The impact of different injection protocols was not tested during the ISC experiments. I suggest, to investigate a broader spectrum of injection protocols at the new Bedretto Underground Laboratory for Geoenergies (BULG).

How does a realistic hydromechanical coupling describe the interplay of injection pressure, fracture aperture and normal stress?

This questions is actually related with an ongoing modelling project with Patrick Schmidt from the University of Stuttgart characterizing the observations presented in chapter 5. The HF2 step test observations with fluid injection, injection pressure and aperture at a given position along the fracture is characterized by a numerical approach. The hydro-mechanical processes in a biphasic poroelastic medium with interacting boundary conditions between the poroelastic and fracture domain allow to include an in-situ hydro-mechanical fracture stiffness formulation. The study focus on the description of the early fracture behaviour (fracture is partly open) in term of aperture evolution for different fracture configurations (single fracture or two parallel fractures).

In extension, further modelling work can include a similar approach characterizing the fracture propagation for a single fracture and or multi-fracture branches. In addition, the fracture propagation under heterogeneous stress field could be compared with the observations. Hence, the numerical models need to include fracturing in Mode I and Mode II/III.

How does the transmissivity enhancement perform over time?

There was no study proposed to investigate the performance of the crosshole transmissivity enhancement after the hydraulic fracturing experiments. I suggest, that going back to the site and develop the same kind of well tests performed before and after the hydraulic shearing experiments bring valuable insights of the transmissivity and fracture connectivity performance several months after injection treatment was performed.

How do fluid properties change the performance of fracture propagation?

Two injection fluids, water (1 cP) and xanthan-salt-water (30 cPs) with different viscosity and rheology were used for the hydraulic fracturing experiments. Unfortunately, this topic was given far too little attention in this thesis. For a proper interpretation and to be able to characterize the performance of the fracture propagation, I propose to perform a laboratory study injecting both kind of fluids into the Grimsel Granodiorit cylinders under in-situ stress conditions. The new LabQuake machine installed in the Rock Physics and Mechanics Laboratory at ETHZ could allow to study not only (1) the change of modified rheology during break down and fracture propagation, (2) it allows to test the two in-situ stress conditions observed at the ISC scale and (3) the 4D seismic tomography can be applied to track changes directly during injection. In addition, the temperature could be increased to investigate the changes at more realistic temperature observed at depths ($\sim$5 km) associated with EGS. Further, the results can be compared with existing analytical solutions for fracture propagation with given fracture shape.

Is proppant able to keep the fracture open around the injection interval?

The hydraulic fracturing experiments showed that the new created fracture intersecting the borehole have often smaller apertures compared to natural fractures. The question arise, if this fracture can be kept open using proppant. And if so, if the proppant is able to keep the fractures open under in-situ reservoir stress and temperature conditions.

Is stick-split fracturing a realistic fracture scenario?

The World Geothermal Congress contribution presents an observation, which I was interpreting as a stick-split fracturing. The stick-split fracturing was proposed by Van der Baan et al. (van Der Baan et al., 2016). The proposed episodic growth periods last for milliseconds. My observations show a period of seconds to minutes. I assumed that the involved volumes and the connection of pre-existing sealed fractures allow to upscale this proposed episodic fracturing. It is still not clear, what are the necessairy conditions to achieve this kind of behaviour. Therefore, insights from numerical models can help to better interpret the observations.

Can poroelastic far-field observations be used to predict Earthquakes on critically stressed geological structures?

A poroelastic solution was compared with the observations in chapter 6. This forward model approach was able to reproduce the data. Therefore, a real time inversion should be implemented and tested. The new Bedretto Underground Laboratory for Geoenergies (BULG) with different hydraulic stimulation projects could allow to implement and test this approach. The best case would allow to invert the pore-pressure observations together with the seismic observations in real time, which would generate a benefit in natural hazard assessment during high-pressure fluid injection.

References

ABAQUS/CAE (2014). *Abaqus 6.14 Online Documentation*. Dassault Systemes Simulia Corp., Providence, RI, USA.

Abé, H., Keer, L. M., and Mura, T. (1976). Growth rate of a penny-shaped crack in hydraulic fracturing of rocks, 2. *Journal of Geophysical Research*, 81(35):6292–6298.

Achtziger-Zupančič, P., Loew, S., and Mariéthoz, G. (2017). A new global database to improve predictions of permeability distribution in crystalline rocks at site scale. *Journal of Geophysical Research: Solid Earth*, 122(5):3513–3539.

Acuna, J. A. and Yortsos, Y. C. (1995). Application of Fractal Geometry to the Study of Networks of Fractures and Their Pressure Transient. *Water Resources Research*, 31(3):527–540.

Adachi, J., Siebrits, E., Peirce, A., and Desroches, J. (2007). Computer simulation of hydraulic fractures. *International Journal of Rock Mechanics and Mining Sciences*, 44(5):739–757.

Akbardoost, J. and Ayatollahi, M. R. (2014). Experimental analysis of mixed mode crack propagation in brittle rocks: The effect of non-singular terms. *Engineering Fracture Mechanics*, 129:77–89.

Alam, S. Y., Loukili, A., Grondin, F., and Rozière, E. (2015). Use of the digital image correlation and acoustic emission technique to study the effect of structural size on cracking of reinforced concrete. *Engineering Fracture Mechanics*, 143:17–31.

Alam, S. Y., Saliba, J., and Loukili, A. (2014). Fracture examination in concrete through combined digital image correlation and acoustic emission techniques. *Construction and Building Materials*, 69:232–242.

Albright, J. and Pearson, C. (1982). Acoustic emissions as a tool for hydraulic fracture location: Experience at the Fenton Hill Hot Dry Rock site. *Old SPE Journal*, 22(August):523–530.

Aliha, M. R., Ayatollah, M. R., Smith, D. J., and Pavier, M. J. (2010). Geometry and size effects on fracture trajectory in a limestone rock under mixed mode loading. *Engineering Fracture Mechanics*, 77(11):2200–2212.

Aliha, M. R., Sistaninia, M., Smith, D. J., Pavier, M. J., and Ayatollahi, M. R. (2012). Geometry effects and statistical analysis of mode I fracture in guiting limestone. *International Journal of Rock Mechanics and Mining Sciences*, 51:128–135.

Allmendinger, R. W., Cardozo, N., and Fisher, D. M. (2011). *Structural geology algorithms: Vectors and tensors*, volume 9781107012.

Amadei, B. and Stephansson, O. (1997). *Rock Stress and Its Measurement*, volume 49.

Amann, F., Gischig, V., Evans, K., Doetsch, J., Jalali, R., Valley, B., Krietsch, H., Dutler, N., Villiger, L., Brixel, B., Klepikova, M., Kittilä, A., Madonna, C., Wiemer, S., Saar, M. O., Loew, S., Driesner, T., Maurer, H., and Giardini, D. (2018). The seismo-hydromechanical behavior during deep geothermal reservoir stimulations: open questions tackled in a decameter-scale in situ stimulation experiment. *Solid Earth*, 9(1):115–137.

Amundarain, J. L., Castro, L. J., Rojas, M. R., Siquier, S., Ramírez, N., Müller, A. J., and Sáez, A. E. (2009). Solutions of xanthan gum/guar gum mixtures: Shear rheology, porous media flow, and solids transport in annular flow. *Rheologica Acta*, 48(5):491–498.

Anders, M. H., Laubach, S. E., and Scholz, C. H. (2014). Microfractures : A review. *Journal of Structural Geology*, 69:377–394.

Asanuma, H., Soma, N., Kaieda, H., Kumano, Y., Izumi, T., and Tezuka, K. (2005). Microseismic Monitoring of Hydraulic Stimulation at the Australian HDR Project in Cooper. *Proceedings World Geothermal Congress*, (April):1–5.

ASTM (2008). Standard Test Method for Direct Tensile Strength of Intact Rock Core Specimens. *ASTM International*, D 3967-08.

Athavale, A. and Miskimins, J. (2008). Laboratory Hydraulic Fracturing Tests on Small Homogeneous and Laminated Blocks. In *The 42nd US Rock Mechanics Symposium and 2nd US-Canada Rock Mechanics Symposium, 29 June - 2 July*, San Francisco.

Ayatollahi, M. R. and Akbardoost, J. (2012). Size effects on fracture toughness of quasi-brittle materials - A new approach. *Engineering Fracture Mechanics*, 92:89–100.

Ayatollahi, M. R. and Aliha, M. R. (2007). Wide range data for crack tip parameters in two disc-type specimens under mixed mode loading. *Computational Materials Science*, 38(4):660–670.

Ayatollahi, M. R. and Aliha, M. R. (2008). On the use of Brazilian disc specimen for calculating mixed mode I-II fracture toughness of rock materials. *Engineering Fracture Mechanics*, 75(16):4631–4641.

Backers, T. (2004). *Fracture toughness determination and micromechanics of rock under mode I and mode II loading*. PhD thesis, Geoforschungszentrum, Germany.

Backers, T., Stanchits, S., and Dresen, G. (2005). Tensile fracture propagation and acoustic emission activity in sandstone: The effect of loading rate. *International Journal of Rock Mechanics and Mining Sciences*, 42(7-8 SPEC. ISS.):1094–1101.

Bahat, D. and Engelder, T. (1984). Surface morphology on cross-fold joints of the Appalachian Plateau, New york and Pennsylvania. *Tectonophysics*.

Baisch, S. and Harjes, H.-P. (2003). A model for fluid-injection induced seismicity at the KTB, Germany. *Geophys. J. Int.*, 152:160–170.

Bakar, H. A. and Zarrouk, S. J. (2018). Transient pressure analysis of geothermal wells fractured during well testing. *Geothermics*, 76(June 2017):26–37.

Bandis, S. C., Lumsden, A. C., and Barton, N. R. (1983). Fundamentals of rock joint deformation. *International Journal of Rock Mechanics and Mining Sciences and.*

Banks-sills, L., Hershkovitz, I., Wawrzynek, P. A., Eliasi, R., and Ingraffe, A. R. (2005). Methods for calculating stress intensity factors in anisotropic materials : Part I — z = 0 is a symmetric plane. *Engineering Fracture Mechanics*, 72:2328–2358.

Banks-sills, L., Wawrzynek, P. A., Carter, B., Ingraffea, A. R., and Hershkovitz, I. (2007). Methods for calculating stress intensity factors in anisotropic materials : Part II — Arbitrary geometry. *Engineering Fracture Mechanics*, 74:1293–1307.

Bao, X. and Eaton, D. W. (2016). Fault activation by hydraulic fracturing in western Canada. *Science*, 354(6318):1406–1409.

Barenblatt, G. I. (1959). The formation of equilibrium cracks during brittle fracture. General ideas and hypotheses. Axially-symmetric cracks. *Journal of Applied Mathematics and Mechanics*, 23(3):622–636.

Barker, J. A. (1988). A generalized radial flow model for hydraulic tests in fractured rock. *Water Resources Research*, 24(10):1796–1804.

Barla, G. and Innaurato, N. (1973). Indirect tensile testing of anisotropic rocks. *Rock Mechanics*, 5(4):215–230.

Barree, R. D., Barree, V. L., Llc, A., and Craig, D. P. (2007). Holistic Fracture Diagnostics. *SPE Rocky oil & gas technology symposium.*

Barton, C. A., Zoback, M. D., and Moos, D. (1995). Fluid flow along potentially active faults in crystalline rock. *Geology*, 23(8):683–686.

Bauer, C., Burgherr, P., Hirschberg, S., Miotti, M., Oshikawa, H., Schenler, W., Spada, M., Treyer, K., Zhang, X., Evans, K., Giardini, D., Kant, M., Kissling, E., Kraft, T., Landtwing, D., Moser, C., Muggli, N., Obermann, A., von Rohr, P. R., Rothenfluh, T., Schechinger, B., Schuler, M., Stathopoulos, P., Stauffacher, M., Valley, B., Wiemer, S., Benighaus, C., Benighaus, L., Jovanovic, A., Renn, O., Abegg, A., and Wiederkehr, R. (2015). *Energy from the Earth: Deep Geothermal as a Resource for the Future?* vdf Hochschulverlag AG, Zurich.

Baujard, C., Genter, A., Dalmais, E., Maurer, V., Hehn, R., Rosillette, R., Vidal, J., and Schmittbuhl, J. (2017). Hydrothermal characterization of wells GRT-1 and GRT-2 in Rittershoffen, France: Implications on the understanding of natural flow systems in the rhine graben. *Geothermics*, 65:255–268.

Bearman, R. (1999). The use of the point load test for the rapid estimation of Mode I fracture toughness. *International Journal of Rock Mechanics and Mining Sciences*, 36(2):257–263.

Bennour, Z., Ishida, T., Nagaya, Y., Chen, Y., Nara, Y., Chen, Q., Sekine, K., and Nagano, Y. (2015). Crack Extension in Hydraulic Fracturing of Shale Cores Using Viscous Oil, Water, and Liquid Carbon Dioxide. *Rock Mechanics and Rock Engineering*, 48(4):1463–1473.

Bhattacharya, P. and Viesca, R. C. (2019). Fluid-induced aseismic fault slip outpaces pore-fluid migration. 468(May):464–468.

Bieniawski, Z. and Bernede, M. (1979). Suggested methods for determining the uniaxial compressive strength and deformability of rock materials. *International Journal of Rock Mechanics and Mining Sciences & Geomechanics Abstracts*, 16(2):137–140.

Biot, M. A. (1941). General theory of three-dimensional consolidation. *Journal of Applied Physics*.

Boroumand, N. and W. Eaton, D. (2012). Comparing Energy Calculations - Hydraulic Fracturing and Microseismic Monitoring. In *74th EAGA, Conference and Exhibition incorporating EUROPEC, 4 - 7 June*, page 4, Copenhagen.

Bourdet, D., Ayoub, J., and Pirard, Y. (1989). Use of Pressure Derivative in Well Test Interpretation. *SPE Formation Evaluation*, 4(02):293–302.

Bredehoeft, J. D., Wolf, R. G., Keys, W. S., and Shutter, E. (1976). Hydraulic fracturing to determine regional in situ stress filed, in the Piceance Basin, Colorado. *Geol. Soc. Amer. Bull.*, 87(60211):250–258.

Breede, K., Dzebisashvili, K., Liu, X., and Falcone, G. (2013). A systematic review of enhanced (or engineered) geothermal systems: past, present and future. *Geothermal Energy*, 1(1):4.

Brixel, B., Klepikova, M., Jalali, M., Roques, C., Lei, Q., Krietsch, H., and Loew, S. (2020a). Tracking fluid flow in shallow crustal fault zones: 1. New in situ permeability measurements. *Journal of Geophysical Research: Solid Earth*, 125:e2019JB018200.

Brixel, B., Klepikova, M., Lei, Q., Roques, C., Jalali, M. R., Krietsch, H., and Loew, S. (2020b). Tracking fluid flow in shallow crustal fault zones : 2. Insights from cross-hole forced flow experiments in damage zones. *Journal of Geophysical Research: Solid Earth*, 125:e2019JB019108.

Brooks, Z. (2013). Fracture Process Zone : Microstructure and Nanomechanics in Quasi-Brittle Materials. *PhD Thesis*, page 355.

Brooks, Z., Ulm, F.-J., and Einstein, H. H. (2012). Role of Microstructure Size in Fracture Process Zone Development of Marble. *American Rock Mechanics Association*.

Brooks, Z., Ulm, F. J., and Einstein, H. H. (2013). Environmental scanning electron microscopy (ESEM) and nanoindentation investigation of the crack tip process zone in marble. *Acta Geotechnica*, 8(3):223–245.

Brown, D. W. (2009). Hot dry rock geothermal energy: important lessons from Fenton Hill. *Thirty-Fourth Workshop on Geothermal Reservoir Engineering*, pages 3–6.

Brown, D. W., Duchane, D. V., Heiken, G., Hriscu, V. T., and Kron, A. (2012). *Mining the earth's heat: Hot dry rock geothermal energy*. Springer.

Bunger, A. and Lecampion, B. (2017). Four Critical Issues for Successful Hydraulic Fracturing Applications. *Rock Mechanics and Engineering*, (Chapter 16).

Bunger, A. P. and Detournay, E. (2007). Early-time solution for a radial hydraulic fracture. *Journal of Engineering Mechanics-Asce*, 133(5):534–540.

Calò, M., Dorbath, C., Cornet, F. H., and Cuenot, N. (2011). Large-scale aseismic motion identified through 4-D P-wave tomography. *Geophysical Journal International*, 186(3):1295–1314.

Cardozo, N. and Allmendinger, R. W. (2013). Spherical projections with OSXStereonet. *Computers and Geosciences*, 51:193–205.

Casas, L., Miskimins, J., Black, A., and Green, S. (2006). Laboratory hydraulic fracturing test on a rock with artificial discontinuities. *SPE Annual Technical Conference and Exhibition*, SPE 103617:1–9.

Challandes, N., Marquer, D., and Villa, I. M. (2008). P-t-t modelling, fluid circulation, and 39ar-40ar and rb-sr mica ages in the aar massif shear zones (swiss alps). *Swiss Journal of Geosciences*, 101(2):269–288.

Chandler, M. R., Meredith, P. G., Brantut, N., and Crawford, B. R. (2016). Fracture toughness anisotropy in shale. *Journal of Geophysical Research: Solid Earth*, 121:1706–1729.

Chandler, M. R., Meredith, P. G., Brantut, N., and Crawford, B. R. (2017). Effect of temperature on the fracture toughness of anisotropic shale and other rocks. *Geological Society, London, Special Publications*, page SP454.6.

Chang, J. and Yortsos, Y. C. (1990). Pressure-Transient Analysis of Fractal Reservoirs. *SPE Formation Evaluation*, 5(March):31–38.

Chen, C.-s., Pan, E., and Amadei, B. (1998). Determination of deformability and tensile strength of anisotropic rock using Brazilian Tests. *International journal of rock mechanics and mining sciences & geomechanics abstracts*, 35(1):43–61.

Chen, Y., Nagaya, Y., and Ishida, T. (2015). Observations of Fractures Induced by Hydraulic Fracturing in Anisotropic Granite. *Rock Mechanics and Rock Engineering*, 48(4):1455–1461.

Cheng, Y. and Renner, J. (2018). Exploratory use of periodic pumping tests for hydraulic characterization of faults. *Geophysical Journal International*, 212(1):543–565.

Chengyong, W., Peidet, L., and Rongshengt, H. (1990). Study of the Fracture Process Zone in Rock by Laser Speckle Interferometry. *International Journal of Rock Mechanics & Mining Sciences & Geomechanics abstracts*, 27(1):65–69.

Cipolla, C. L., Mack, M. G., Maxwell, S. C., and Downie, R. C. (2011). A Practical Guide to Interpreting Microseismic Measurements. (June):14–16.

Cladouhos, T. T., Petty, S., Swyer, M. W., Uddenberg, M. E., Grasso, K., and Nordin, Y. (2015). Results from Newberry Volcano EGS Demonstration, 2010–2014. *Geothermics*, 63:44–61.

Claesson, J. and Bohloli, B. (2002). Brazilian test: Stress field and tensile strength of anisotropic rocks using an analytical solution. *International Journal of Rock Mechanics and Mining Sciences*, 39(8):991–1004.

Cooper, H., Bredehoeft, J., Papadopulos, I., and Bennett, R. (1965). The Response of Well-Aquifer Systems to Seismic Waves. *Journal of Geophysical Research*, 70(16):3915–3926.

Cornet, F. H. and Valette, B. (1984). In Situ Stress Determination From Hydraulic Injection Test Data. *Journal of Geophysical Research*, 89:11527–11537.

Corr, D., Accardi, M., Graham-Brady, L., and Shah, S. (2007). Digital image correlation analysis of interfacial debonding properties and fracture behavior in concrete. *Engineering Fracture Mechanics*, 74(1-2):109–121.

Correlated Solutions, Inc. (2016). Vic-3D Digital Imager Correlation Version 7.2.6. *Irmo, Columbia, USA*.

Crosnier, B., Fras, G., and Jouanna, P. (1985). Reconnaissance of fractured media with several systems of fractures by means of harmonic techniques. *Rock Mechanics and Rock Engineering*, 18(2):77–105.

Crouch, S. L., Starfield, A. M., and Rizzo, F. J. (1983). Boundary Element Methods in Solid Mechanics. *Journal of Applied Mechanics*, 50(3):704–705.

Cummings, R. and Morris, G. (1979). *Mining earth's heat-Hot dry rock geothermal energy*. Springer, 2012 edition.

Dai, F., Xia, K., and Nasseri, M. H. B. (2013). Micromechanical model for the rate dependence of the fracture toughness anisotropy of Barre granite. *International Journal of Rock Mechanics and Mining Sciences*, 63:113–121.

Dambly, L., Nejati, M., Vogler, D., and Saar, M. O. (2018). On the direct measurement of the shear moduli in transversely isotropic rocks using the uniaxial compression test. *International Journal of Rock Mechanics and Mining Sciences*, page Under Review.

Dambly, M. L. T., Nejati, M., Vogler, D., and Saar, M. O. (2019). On the direct measurement of shear moduli in transversely isotropic rocks using the uniaxial compression test. *International Journal of Rock Mechanics and Mining Sciences*, 113(December 2018):220–240.

Das, I. and Zoback, M. (2011). Long-period, long-duration seismic events during hydraulic fracture stimulation of a shale gas reservoir. *The Leading Edge*, 30(7):778–786.

Davies, J. H. and Davies, D. R. (2010). Earth's surface heat flux. *Solid Earth*, 1(1):5–24.

Detournay, E. (2016). Mechanics of Hydraulic Fractures. *Annual Review of Fluid Mechanics*, 48(1):311–339.

Detournay, E. and Cheng, A.-D. (1988). Poroelastic response of a borehole in a non-hydrostatic stress field. *International Journal of Rock Mechanics and Mining Sciences & Geomechanics Abstracts*, 25(3):171–182.

Diehl, T., Kraft, T., Kissling, E., and Wiemer, S. (2017). The induced earthquake sequence related to the St. Gallen deep geothermal project (Switzerland): Fault reactivation and fluid interactions imaged by microseismicity. *Journal of Geophysical Research: Solid Earth*, 122(9):7272–7290.

Doe, T. W. and Korbin, G. E. (1987). A Comparison Of Hydraulic Fracturing And Hydraulic Jacking Stress Measurements. *The 28th U.S. Symposium on Rock Mechanics (USRMS)*, pages 283–290.

Doetsch, J., Gischig, V., Krietsch, H., Villiger, L., Amann, F., Dutler, N., Jalali, R., Brixel, B., Giertzuch, P., Maurer, H., Wiemer, S., Loew, S., Saar, M., and Giardini, D. (2018a). Grimsel ISC Experiment Description. Technical Report December, SCCER-SoE, ETH Zurich, Zurich.

Doetsch, J., Gischig, V. S., Villiger, L., Krietsch, H., Nejati, M., Amann, F., Jalali, M., Madonna, C., Maurer, H., Wiemer, S., Driesner, T., and Giardini, D. (2018b). Subsurface Fluid Pressure and Rock Deformation Monitoring Using Seismic Velocity Observations. *Geophysical Research Letters*, 45(19):10,389–10,397.

Doetsch, J., Krietsch, H., Lajaunie, M., Schmelzbach, C., Maurer, H., and Amann, F. (2017). GPR imaging of shear zones in crystalline rock. In *Conference: 2017 9th International Workshop on Advanced Ground Penetrating Radar (IWAGPR)*.

Doetsch, J., Zurich, E., Jalali, M., Krietsch, H., Schmelzbach, C., Gischig, V., Villiger, L., Amann, F., and Maurer, H. (2020). Characterizing a decametre-scale granitic reservoir using GPR and seismic methods-A case study for preparing hydraulic stimulations Anisotropic characteristics of transversal isotropic quasi-brittle material View project Characterizing a decametre-scale g. *Solid Earth Discussions*, (March):1–28.

Dong, W., Wu, Z., Zhou, X., Dong, L., and Kastiukas, G. (2017a). FPZ evolution of mixed mode fracture in concrete: Experimental and numerical. *Engineering Failure Analysis*, 75:54–70.

Dong, W., Wu, Z., Zhou, X., Wang, N., and Kastiukas, G. (2017b). An experimental study on crack propagation at rock-concrete interface using digital image correlation technique. *Engineering Fracture Mechanics*, 171:50–63.

Dontsov, E. V. (2016). An approximate solution for a penny-shaped hydraulic fracture that accounts for fracture toughness, fluid viscosity and leak-off. *Royal Society Open Science*, 3(12):160737.

Dresen, G., Renner, J., Bohnhoff, M., Konietzky, H., Kwiatek, G., Plenkers, K., Klee, G., and Backers, T. (2019). STIMTEC – a mine-back experiment in the Reiche Zeche underground. In *EGU Geophysical Research Abstracts*, volume 21, page 9357, Vienna. EGU.

Dugdale, D. (1960). Yielding of steel sheets containing slits. *Journal of the Mechanics and Physics of Solids*, 8(2):100–104.

Dutler, N., Nejati, M., Valley, B., Amann, F., and Molinari, G. (2018a). On the link between fracture toughness, tensile strength, and fracture process zone in anisotropic rocks. *Engineering Fracture Mechanics*, 201:56–79.

Dutler, N., Valley, B., Gischig, V., Villiger, L., Krietsch, H., Doetsch, J., Brixel, B., Jalali, M., and Amann, F. (2019). Hydraulic fracture propagation in a heterogeneous stress field in a crystalline rock mass. *Solid Earth*, 10(6):1877 – 1904.

Dutler, N. O., Valley, B., Gischig, V. S., Jalali, M., Brixel, B., Krietsch, H., Roques, C., and Amann, F. ((in review)). Hydromechanical insight of fracture opening and closure during in-situ hydraulic fracturing in crystalline rock. *Int. J. Rock Mech. Min. Sci.*

Dutler, N. O., Valley, B., Gischig, V. S., Jalali, M., Doetsch, J., Krietsch, H., Villiger, L., and Amann, F. (2018b). Observations of fracture propagation during decameter-scale hydraulic fracturing experiments. In *52nd US Rock Mechanics / Geomechanics Symposium, 17–20 June*, pages ARMA2018–0256, Seattle. American Rock Mechanics Association.

Dutler, N. O., Valley, B., Villiger, L., Gischig, V., and Amann, F. (2020). Observation of a repeated step-wise fracture growth during hydraulic fracturing experiment at the Grimsel Test Site. In *World Geothermal Conference, 27.4-1.5.2019*, pages 1–10, Reykjavik.

Dwivedi, R., Soni, A., Goel, R., and Dube, A. (2000). Fracture toughness of rocks under sub-zero temperature conditions. *International Journal of Rock Mechanics and Mining Sciences*, 37(8):1267–1275.

Eaton, D. W. and Igonin, N. (2018). What controls the maximum magnitude of injection-induced earthquakes? *The Leading Edge*, 37(2):135–140.

Eaton, D. W., van der Baan, M., Birkelo, B., and Tary, J. B. (2014). Scaling relations and spectral characteristics of tensile microseisms: Evidence for opening/closing cracks during hydraulic fracturing. *Geophysical Journal International*, 196(3):1844–1857.

Economides, M. and Nolte, K. (2000). *Reservoir Stimulation*. Number May. Wiley, Chichester.

Ellsworth, W. L. (2013). Injection-Induced Earthquakes. *Science*, 341(6142):142+.

Emmermann, R. and Lauterjung, J. (1997). The German Continental Deep Drilling Program KTB: Overview and major results. *Journal of Geophysical Research-Solid Earth*, 102(B8):18179–18201.

Enfedaque, A., Gálvez, J. C., and Suárez, F. (2015). Analysis of fracture tests of glass fibre reinforced cement (GRC) using digital image correlation. *Construction and Building Materials*, 75:472–487.

Evans, K. and Meier, P. (1995). Hydrojacking and hydrofracturing tests in a fissile schist in south-west Switzerland: In-situ stress characterisation in difficult rock. *Mechanics of Jointed and Faulted Rock*, (April):415–421.

Evans, K. F., Kohl, T., Rybach, L., and Hopkirk, R. J. (1992). The effects of fracture normal compliance on the long term circulation behavior of a hot dry rock reservoir: a parameter study using the new fully-coupled code FRACTure . *Geothermal Resources Council Transactions*, 16(October):449–456.

Evans, K. F., Moriya, H., Niitsuma, H., Jones, R. H., Phillips, W. S., Genter, A., Sausse, J., Jung, R., and Baria, R. (2005). Microseismicity and permeability enhancement of hydrogeologic structures during massive fluid injections into granite at 3 km depth at the Soultz HDR site. *Geophysical Journal International*, 160(1):388–412.

Evans, K. F., Wieland, U., Wiemer, S., and Giardini, D. (2014). Deep Geothermal Energy R&D Roadmap for Switzerland, 2014. Technical report, Swiss Competence Center for Energy Research - Supply of Electricity.

Evans, K. F., Zappone, A., Kraft, T., Deichmann, N., and Moia, F. (2012). A survey of the induced seismic responses to fluid injection in geothermal and CO2 reservoirs in Europe. *Geothermics*, 41:30–54.

Exadaktylos, G. E. and Kaklis, K. N. (2001). Applications of an explicit solution for the transversely isotropic circular disc compressed diametrically. *International Journal of Rock Mechanics and Mining Sciences*, 38(2):227–243.

Fakhimi, A., Tarokh, A., and Labuz, J. F. (2017). Cohesionless crack at peak load in a quasi-brittle material. *Engineering Fracture Mechanics*, 179:272–277.

Faulkner, D. R., Mitchell, T. M., Jensen, E., and Cembrano, J. (2011). Scaling of fault damage zones with displacement and the implications for fault growth processes. *Journal of Geophysical Research: Solid Earth*, 116(5):1–11.

Fischer, P., Jardani, A., Cardiff, M., Lecoq, N., and Jourde, H. (2018). Hydraulic analysis of harmonic pumping tests in frequency and time domains for identifying the conduits networks in a karstic aquifer. *Journal of Hydrology*, 559:1039–1053.

Fokker, P. A., Salina, E., Verga, F., and Viberti, D. (2018). Harmonic pulse testing for well performance monitoring. *Journal of Petroleum Science and Engineering*, 162(August 2017):446–459.

Fowell, R. J. (1995). Suggested method for determining mode I fracture toughness using Cracked Chevron Notched Brazilian Disc (CCNBD) specimens. *International Journal of Rock Mechanics and Mining Sciences and*, 32(1):57–64.

Frohlich, C. (2012). Two-year survey comparing earthquake activity and injection-well locations in the Barnett Shale, Texas. *Proceedings of the National Academy of Sciences of the United States of America*, 109(35):13934–13938.

Funatsu, T., Takashi, T., and Kuruppu, M. (2012). Effect of Anisotropy on Fracture Toughness of Sandstone by SCB Specimen. *ISRM Regional Symposium - 7th Asian Rock Mechanics Symposium*, pages ISRM–ARMS7–2012–041.

Geertsma, J. and De Klerk, F. (1969). A Rapid Method of Predicting Width and Extent of Hydraulically Induced Fractures. *Journal of Petroleum Technology*, 21:1571–1581.

Genter, A., Evans, K., Cuenot, N., Fritsch, D., and Sanjuan, B. (2010). Contribution of the exploration of deep crystalline fractured reservoir of Soultz to the knowledge of enhanced geothermal systems (EGS). *Comptes Rendus - Geoscience*, 342(7-8):502–516.

Genter, A., Guillou-Frottier, L., Feybesse, J. L., Nicol, N., Dezayes, C., and Schwartz, S. (2003). Typology of potential Hot Fractured Rock resources in Europe. *Geothermics*, 32(4):701–710.

Gischig, V., Amann, F., Bethmann, F., Brixel, B., Doetsch, J., Doonechaly, N. G., Driesner, T., Dutler, N. O., Evans, K. F., Hertrich, M., Jalali, M., Kittilä, A., Krietsch, H., Loew, S., Ma, X., Maurer, H., Meier, P., Nejati, M., Obermann, A., Saar, M., Valley, B., Villiger, L., Wiemer, S., and Giardini, D. (2019). Hydraulic stimulation and fluid circulation experiments in underground laboratories: stepping up the scale towards engineered geothermal systems. *Journal Geomechanics for Energy and the Environment.*, (Physical behavior of Fluid-Induced earthquakes).

Gischig, V. and Preisig, G. (2015). Hydro-fracturing versus hydro-shearing: a critical assessment of two distinct reservoir stimulation mechanisms. In *13th International Congress of Rock Mechanics*, number September 2016, Montréal, Canada. ISRM.

Gischig, V. S., Doetsch, J., Maurer, H., Krietsch, H., Amann, F., Evans, K. F., Nejati, M., Jalali, M., Valley, B., Obermann, A. C., Wiemer, S., and Giardini, D. (2018). On the link between stress field and small-scale hydraulic fracture growth in anisotropic rock derived from microseismicity. *Solid Earth*, 9(1):39–61.

Goebel, T., Weingarten, M., Chen, X., Haffener, J., and Brodsky, E. (2017). The 2016 Mw5.1 Fairview, Oklahoma earthquakes: Evidence for long-range poroelastic triggering at >40 km from fluid disposal wells. *Earth and Planetary Science Letters*, 472:50–61.

Goebel, T. H. and Brodsky, E. E. (2018). The spatial footprint of injection wells in a global compilation of induced earthquake sequences. *Science*, 361(6405):899–904.

Goodman, R., Taylor, R., and Brekke, T. (1968). A model for the mechanics of jointed rock. *Soil Mechanics and Foundations Division ASCE*, 94(SM3):367–659.

Grigoli, F., Cesca, S., Rinaldi, A. P., Manconi, A., López-Comino, J. A., Clinton, J. F., Westaway, R., Cauzzi, C., Dahm, T., and Wiemer, S. (2018). The November 2017 Mw 5.5 Pohang earthquake: A possible case of induced seismicity in South Korea. *Science*, 360(6392):1003–1006.

Guglielmi, Y., Cappa, F., Lancon, H., Janowczyk, J. B., Rutqvist, J., Tsang, C. F., and Wang, J. S. Y. (2014). ISRM suggested method for step-rate injection method for fracture in-situ properties (SIMFIP): Using a 3-components borehole deformation sensor. *Rock Mechanics and Rock Engineering*, 47(1):303–311.

Guglielmi, Y., Elsworth, D., Cappa, F., Henry, P., Gout, C., Dick, P., and Durand, J. (2015). In situ observations on the coupling between hydraulic diffusivity and displacements during fault reactivation in shales. *Journal of Geophysical Research: Solid Earth*, 120(11):7729–7748.

Guo, Z. K., Kobayashi, A. S., and Hawkins, N. M. (1993). Further studies on fracture process zone for mode I concrete fracture. *Engineering Fracture Mechanics*, 46(6):1041–1049.

Haberfield, C. M. and Johnston, I. W. (1990). Determination of the fracture toughness of a saturated soft rock. *Canadian Geotechnical Journal*, 27:276–284.

Haimson, B. C. and Cornet, F. H. (2003). ISRM suggested methods for rock stress estimation part 3: Hydraulic fracturing (HF) and/or hydraulic testing of pre-existing fractures (HTPF). *International Journal of Rock Mechanics and Mining Sciences*, 40(7-8):1011–1020.

Häring, M. O., Schanz, U., Ladner, F., and Dyer, B. C. (2008). Characterisation of the Basel 1 enhanced geothermal system. *Geothermics*, 37(5):469–495.

Hartmaier, H., Doe, T., and Dixon, G. (1998). Evaluation of Hydrojacking Tests for an Unlined Pressure Tunnel. *Tunnelling and Underground Space Technology*, 13(4):393–401.

Hasanov, A. K., Dugan, B., Batzle, M. L., and Prasad, M. (2019). Hydraulic and Poroelastic Rock Properties From Oscillating Pore Pressure Experiments. *Journal of Geophysical Research: Solid Earth*, 124(5):4473–4491.

Hertrich, M. and Maurer, H. (2019). Understanding Deep Geothermal Reservoirs: A journey from laboratory-scale experiments to investigations at realistic scales.

Hills, D. A., Kelly, P. A., Dai, D. N., and Korsunsky, A. M. (1996). *Solution of Crack Problems*, volume 44 of *Solid Mechanics and Its Applications*. Springer Netherlands, Dordrecht.

Hoagland, R. G., Hahn, G. T., and Rosenfield, A. R. (1973). Influence of microstructure on fracture propagation in rock. *Rock Mechanics*, 5(2):77–106.

Hofmann, H., Zimmermann, G., Farkas, M., Huenges, E., Zang, A., Leonhardt, M., Kwiatek, G., Martinez-Garzon, P., Bohnhoff, M., Min, K. B., Fokker, P., Westaway, R., Bethmann, F., Meier, P., Yoon, K. S., Choi, J. W., Lee, T. J., and Kim, K. Y. (2019). First field application of cyclic soft stimulation at the Pohang Enhanced Geothermal System site in Korea. *Geophysical Journal International*, 217(2):926–949.

Hollaender, F., Hammond, P. S., and Gringarten, A. C. (2002). Harmonic Testing for Continuous Well and Reservoir Monitoring. *SPE Annual Technical Conference and Exhibition, San Antonio, Texas, U.S.A, 29 Sept-2 Oct*.

Hondros, G. (1959). The evaluation of Poisson's ratio and the modulus of materials of a low tensile resistance by the Brazilian (indirect tensile) test with particular reference to concrete. *Aust J Appl Sci*, 10(3):243–268.

Hubbert, M. K. and Willis, D. G. (1957). Mechanics of hydraulic fracturing. *Transactions of the american institute of mining and metallurgical engineers*, 210(6):153–163.

Iqbal, M. J. and Mohanty, B. (2007). Experimental Calibration of ISRM Suggested Fracture Toughness Measurement Techniques in Selected Brittle Rocks. *Rock Mechanics and Rock Engineering*, 40(5):453–475.

Irwin, G. (1957). Analysis of Stresses and Strains Near the End of a Crack Traversing a Plate. *Journal of Applied Mechanics*, 24(September):361–364.

Irwin, G. R. (1961). Plastic zone near a crack and fracture toughness. *Sagamore Research Conference Proceedings*, 4:63–78.

Ishida, T., Aoyagi, K., Niwa, T., Chen, Y., Murata, S., Chen, Q., and Nakayama, Y. (2012). Acoustic emission monitoring of hydraulic fracturing laboratory experiment with supercritical and liquid CO ₂. *Geophys. Res. Lett.*, 39:L16309.

Ishida, T., Chen, Q., Mizuta, Y., and Roegiers, J.-C. (2004). Influence of Fluid Viscosity on the Hydraulic Fracturing Mechanism. *Journal of Energy Resources Technology*, 126(3):190.

Ishida, T., Fujito, W., Yamashita, H., Naoi, M., Fuji, H., Suzuki, K., and Matsui, H. (2019). Crack Expansion and Fracturing Mode of Hydraulic Refracturing from Acoustic Emission Monitoring in a Small-Scale Field Experiment. *Rock Mechanics and Rock Engineering*, 52(2):543–553.

Ishida, T., Mizuta, Y., Matsunaga, I., Sasaki, S., and Chen, Q. (2000). Effect of Grain Size in Granitic Rocks on Hydraulic Fracturing Mechanism. In *4th North American Rock Mechanics Symposium, 31 July - 3 August*, pages 1105–1111, Seattle.

Jacob, C. E. and Lohman, S. W. (1952). Nonsteady flow to a well of constant drawdown in an extensive aquifer. *Transactions, American Geophysical Union*, 33(4):559.

Jaeger, J. C. (1963). Extension Failures in Rocks subject to fluid Pressure. *Journal of Geophysical Research*, 68(21):6066–6067.

Jalali, M., Gischig, V., Doetsch, J., Näf, R., Krietsch, H., Klepikova, M., Amann, F., and Giardini, D. (2018a). Transmissivity Changes and Microseismicity Induced by Small-scale Hydraulic Fracturing Tests in Crystalline Rock. *Geophysical Research Letters*, page 45.

Jalali, M., Klepikova, M., Doetsch, J., Krietsch, H., Brixel, B., Dutler, N. O., Gischig, V. S., and Amann, F. (2018b). A Multi-Scale Approach to Identify and Characterize the Preferential Flow Paths of a Fractured Crystalline Rock. In *2nd International DFNE Conference*, page 0734, Seattle.

Janssen, C., Wagner, F., Zang, A., and Dresen, G. (2001). Fracture process zone in granite: a microstructural analysis. *International Journal of Earth Sciences*, 90(1):46–59.

Jaupart, C., Labrosse, S., Lucazeau, F., and Mareschal, J. C. (2015). Temperatures, Heat, and Energy in the Mantle of the Earth. *Treatise on Geophysics: Second Edition*, 7:223–270.

Jeffrey, R., a.P. Bunger, Lecampion, B., Zhang, X., Chen, Z., van As, a., Allison, D., de Beer, W., Dudley, J., Siebrits, E., Thiercelin, M., and Mainguy, M. (2009). Measuring Hydraulic Fracture Growth in Naturally Fractured Rock. *SPE Annual Technical Conference and Exhibition*, pages 1–19.

Jeffrey, R. G. and Bunger, A. (2007). A Detailed Comparison of Experimental and Numerical Data on Hydraulic Fracture Height Growth Through Stress Contrasts. In *SPE Hydraulic Fracturing Technology Conference, 29 - 31 January*, College Station, Texas.

Jeffrey, R. G., Chen, Z., Mills, K., and Pegg, S. (2013). Monitoring and Measuring Hydraulic Fracturing Growth During Preconditioning of a Roof Rock over a Coal Longwall Panel. In *Effective and Sustainable Hydraulic Fracturing*, volume 45, pages 893–914. InTech.

Johnson, E. and Cleary, M. P. (1991). Implications of recent laboratory experimental results for hydraulic fractures. In *Rocky Mountain Regional Meeting and Low-Permeability Reservoirs Symposium, 15 - 17 April*, pages 413–428, Colorado.

Jónsson, S., Segall, P., Pedersen, R., and Björnsson, G. (2003). Post-earthquake ground movements correlated to pore-pressure transients. *Nature*, 424(6945):179–183.

Jost, M. L., Büßelberg, T., Jost, Ö., and Harjes, H. P. (1998). Source parameters of injection-induced microearthquakes at 9 km depth at the KTB deep drilling site, Germany. *Bulletin of the Seismological Society of America*, 88(3):815–832.

Jung, H., Sharma, M. M., Cramer, D. D., Oakes, S., and McClure, M. W. (2016). Re-examining interpretations of non-ideal behavior during diagnostic fracture injection tests. *Journal of Petroleum Science and Engineering*, 145:114–136.

Kamal, M. M., Tian, C., and Suleen, F. (2019). Pressure Transient Analysis of Polymer Flooding With Coexistence of Non-Newtonian and Newtonian Fluids. *SPE Reservoir Evaluation & Engineering*, 22(03):1172–1184.

Karrenbach, M., Ridge, A., Cole, S., Boone, K., Inc, O., Kahn, D., Rich, J., Silver, K., Langton, D., and Energy, D. (2017). DAS Microseismic Monitoring and Integration with Strain Measurements in Hydraulic Fracture Profiling. In *Unconventional Resources Technology Conference (URTeC), 24 - 26 July*, pages 24–26, Austin.

Kataoka, M. and Obara, Y. (2012). Estimation of fracture toughness of anisotropic rocks by SCB test and visualization of fracture by means of X-ray CT. *Test*, pages 667–670.

Kataoka, M., Obara, Y., and Kuruppu, M. (2015a). Estimation of Fracture Toughness of Anisotropic Rocks by Semi-Circular Bend (SCB) Tests Under Water Vapor Pressure. *Rock Mechanics and Rock Engineering*, 48(4):1353–1367.

Kataoka, M., Yoshioka, S., Cho, S.-H., Soucek, K., Vavro, L., and Obara, Y. (2015b). Estimation of Fracture Toughness of Sandstone by Three Testing Methods. *Vietrock2015 an ISRM specialized conference*, (March).

Ke, C. C., Chen, C. S., and Tu, C. H. (2008). Determination of fracture toughness of anisotropic rocks by boundary element method. *Rock Mechanics and Rock Engineering*, 41(4):509–538.

Keranen, K. M., Weingarten, M., Abers, G. A., Bekins, B. A., and Ge, S. (2014). Sharp increase in central Oklahoma seismicity since 2008 induced by massive wastewater injection. *Science*, 345(6195):448–451.

Keusen, H. R., Ganguin, J., Schuler, P., and Buletti, M. (1989). Geologie. Technical Report NTB87-14, Nagra, Wettingen.

Khan, K. and Al-Shayea, N. A. (2000). Effect of Specimen Geometry and Testing Method on Mixed Mode I-II Fracture Toughness of a Limestone Rock from Saudi Arabia. *Rock Mechanics and Rock Engineering*, 33(3):179–206.

Khanlari, G., Rafiei, B., and Abdilor, Y. (2015). Evaluation of strength anisotropy and failure modes of laminated sandstones. *Arabian Journal of Geosciences*, 8(5):3089–3102.

Khristianovic, S. A. and Zheltov, Y. P. (1955). Formation of Vertical Fractures by Means of Highly Viscous Liquid. *Proceeding of the 4th World Petroleum Congress*, 5:579–586.

Kim, K.-H., Ree, J.-H., Kim, Y., Kim, S., Kang, S. Y., and Seo, W. (2018). Assessing whether the 2017 M w 5.4 Pohang earthquake in South Korea was an induced event. *Science*, 360(6392):1007–1009.

King, C.-Y., Azuma, S., Igarashi, G., Ohno, M., Saito, H., and Wakita, H. (1999). Earthquake-related water-level changes at 16 closely clustered wells in Tono, central Japan. *Journal of Geophysical Research: Solid Earth*, 104(B6):13073–13082.

King, G. E. and Corporation, A. (2012). HF King George 2012 Fracturing 101 SPE-152596-MS-P. pages 1–80.

Kittilä, A., Jalali, M. R., Evans, K. F., Willmann, M., Saar, M. O., and Kong, X. (2019). Field Comparison of DNA-Labeled Nanoparticle and Solute Tracer Transport in a Fractured Crystalline Rock. *Water Resources Research*, 55(8):6577–6595.

Klee, G. (2015). Grimsel Test Site : Hydraulic-Fracturing and HTPF - Tests. Technical report.

Klepikova, M., Brixel, B., and Jalali, M. (2020). Transient hydraulic tomography approach to characterize main flowpaths and their connectivity in fractured media. *Advances in Water Resources*, 136:103500.

Kneafsey, T., Dobson, P., Ajo-Franklin, J., Valladao, C., Blankenship, D., Knox, H., Schwering, P., Morris, J., Smith, M., White, M., Johnson, T., Podgorney, R., Mattson, E., Neupane, G., Roggenthen, W., and Doe, T. (2018). The EGS Collab Project : Stimulation and Simulation. pages ARMA2018–1345, Seattle. American Rock Mechanics Association.

Kobayashi, R., Matsuki, K., and Otsuka†, N. (1986). Size effect in the fracture toughness of Ogino tuff. *International Journal of Rock Mechanics and Mining Sciences & Geomechanics Abstracts*, 23(I):13–18.

Krietsch, H., Doetsch, J., Dutler, N., Jalali, M., Gischig, V., Loew, S., and Amann, F. (2018). Comprehensive geological dataset describing a crystalline rock mass for hydraulic stimulation experiments. *Scientific Data*, 5:180269.

Krietsch, H., Gischig, V., Doetsch, J., Evans, K., Villiger, L., Jalali, M., Valley, B., Loew, S., and Amann, F. (2020). Hydromechanical processes and their influence on the stimulated volume: Observation from a decameter-scale hydraulic rock mass stimulation experiment. *Solid Earth Discussions*.

Krietsch, H., Gischig, V., Evans, K., Doetsch, J., Dutler, N. O., Valley, B., and Amann, F. (2019). Stress Measurements for an In Situ Stimulation Experiment in Crystalline Rock: Integration of Induced Seismicity, Stress Relief and Hydraulic Methods. *Rock Mechanics and Rock Engineering*, 52(2):517–542.

Krietsch, H., Gischig, V., Jalali, M., Amann, F., Evans, K., Doetsch, J., and Valley, B. (2017). Stress measurements in crystalline rock : Comparison of overcoring, hydraulic fracturing and induced seismicity results. *American Rock Mechanics Association*.

Krishnan, G., Zhao, X., Zaman, M., and Roegiers, J.-C. (1998). Fracture toughness of a soft sandstone. *International Journal of Rock Mechanics and Mining Sciences*, 35(6):695–710.

Kuo, C. (1972). Determination of Reservoir Properties from Sinusoidal and Multirate Flow Tests in One or More Wells. *Society of Petroleum Engineers Journal*, 12(06):499–507.

Kuruppu, M. D., Obara, Y., Ayatollahi, M. R., Chong, K. P., and Funatsu, T. (2014). ISRM-Suggested Method for Determining the Mode I Static Fracture Toughness Using Semi-Circular Bend Specimen. *Rock Mechanics and Rock Engineering*, 47(1):267–274.

Labuz, J., Shah, S., and Dowding, C. (1985). Experimental analysis of crack propagation in granite. *International Journal of Rock Mechanics and Mining Sciences & Geomechanics Abstracts*, 22(2):85–98.

Labuz, J. F., Shah, S. P., and Dowding, C. H. (1987). The fracture process zone in granite: evidence and effect. *International Journal of Rock Mechanics and Mining Sciences & Geomechanics Abstracts*, 24(4):235–246.

Lacazette, A. and Engelder, T. (1992). Fluid-driven Cyclic Propagation of a Joint in the Ithaca Siltstone, Appalachian Basin, New York. *International Geophysics*, 51(C):297–323.

Laoroongroj, A., Zechner, M., Clemens, T., and Gringarten, A. (2012). Determination of the in-situ polymer viscosity from fall off tests. In *SPE Europec/EAGE Annual Conference, 4-7 June*, number June, pages 4921–4933, Copenhagen, DK.

Laqueche, H., Rousseau, A., and Valentin, G. (1986). Crack propagation under mode I and II loading in slate schist. *International Journal of Rock Mechanics and Mining Sciences & Geomechanics Abstracts*, 23(5):347–354.

Lecampion, B., Jeffrey, R., and Detournay, E. (2005). Resolving the geometry of hydraulic fractures from tilt measurements. *Pure and Applied Geophysics*, 162(12):2433–2452.

Lee, H. P., Olson, J. E., Holder, J., Gale, J. F. W., and Myers, R. D. (2015). The interaction of propagating opening mode fractures with preexisting discontinuities in shale. *Journal of Geophysical Research: Solid Earth*, 120:169–181.

Lee, K.-K., Ellsworth, W. L., Giardini, D., Townend, J., Ge, S., Shimamoto, T., Yeo, I.-W., Kang, T.-S., Rhie, J., Sheen, D.-H., Chang, C., Woo, J.-U., and Langenbruch, C. (2019). Managing injection-induced seismic risks. *Science*, 364(6442):730–732.

Lee, M. Y. and Haimson, B. C. (1989). Statistical evaluation of hydraulic fracturing stress measurement parameters. In *Int. J. Rock Mech. Min. Sci. & Geomech. Abstr.*, volume 26, pages 447–456. Elsevier.

Lekhnitskiy, S. G. (1969). Anisotropic Plates. *Anisotropic Plates*, page 477.

Li, D. and Wong, L. N. Y. (2013). The brazilian disc test for rock mechanics applications: Review and new insights. *Rock Mechanics and Rock Engineering*, 46(2):269–287.

Lim, I. L., Johnston, I. W., Choi, S. K., and Boland, J. N. (1994). Fracture testing of a soft rock with semi-circular specimens under three-point bending. Part 2—mixed-mode. *International Journal of Rock Mechanics and Mining Sciences & Geomechanics Abstracts*, 31(3):185–197.

Lin, Q., Fakhimi, A., Haggerty, M., and Labuz, J. F. (2009). Initiation of tensile and mixed-mode fracture in sandstone. *International Journal of Rock Mechanics and Mining Sciences*, 46(3):489–497.

Lin, Q. and Labuz, J. F. (2013). Fracture of sandstone characterized by digital image correlation. *International Journal of Rock Mechanics and Mining Sciences*, 60:235–245.

Lin, Q., Yuan, H., Biolzi, L., and Labuz, J. F. (2014). Opening and mixed mode fracture processes in a quasi-brittle material via digital imaging. *Engineering Fracture Mechanics*, 131:176–193.

Lister, J. R. and Kerr, R. C. (1991). Fluid-mechanical models of crack propagation and their application to magma transport in dykes. *Journal of Geophysical Research*, 96(B6):10049.

López-Comino, J. A., Cesca, S., Heimann, S., Grigoli, F., Milkereit, C., Dahm, T., and Zang, A. (2017). Characterization of Hydraulic Fractures Growth During the Äspö Hard Rock Laboratory Experiment (Sweden). *Rock Mechanics and Rock Engineering*, (August):1–17.

Louis, C., Dessenne, J., and Feuga, B. (1977). Interaction between water flow phenomena and themechanical behavior of soil or rock masses. In Gudehus, G., editor, *Finite Elements in Geomechanics*, pages 479–511. John Wiley & Sons, New York.

Majer, E. L. and Doe, T. W. (1986). Studying hydrofractures by high frequency seismic monitoring. *International Journal of Rock Mechanics and Mining Sciences and*, 23(3):185–199.

Manning, C. E. and Ingebritsen, S. E. (1999). Permeability Implications of the Continental of Geothermal Data Crust and Metamorphic Systems. *Reviews of Geophysics*, 37(1):127–150.

Martínez-Garzón, P., Bohnhoff, M., Kwiatek, G., and Dresen, G. (2013). Stress tensor changes related to fluid injection at the Geysers geothermal field, California. *Geophysical Research Letters*, 40(11):2596–2601.

Matthews, C. and Russell, D. G. (1967). Pressure Buildup and Flow Tests in Wells. *Society of Petroleum Engineers of AIME*, pages 130–133.

Maxwell, S., Rutledge, J., Jones, R., and Fehler, M. (2010). Petroleum reservoir characterization using downhole microseismic monitoring. *Geophysics*, 75(5):75A129–75A137.

McClure, M., Bammidi, V., Cipolla, C., Cramer, D., Martin, L., Savitski, A., Sobernheim, D., and Voller, K. (2019). A Collaborative Study on DFIT Interpretation: Integrating Modeling, Field Data, and Analytical Techniques. In *Proceedings of the 7th Unconventional Resources Technology Conference*, pages 1–39, Tulsa, OK, USA. American Association of Petroleum Geologists.

McClure, M. W. and Horne, R. N. (2014). An investigation of stimulation mechanisms in Enhanced Geothermal Systems. *International Journal of Rock Mechanics and Mining Sciences*, 72:242–260.

McClure, M. W., Jung, H., Cramer, D. D., and Sharma, M. M. (2016). The Fracture-Compliance Method for Picking Closure Pressure From Diagnostic Fracture-Injection Tests (see associated supplementary discussion/reply). *SPE Journal*, 21(04):1321–1339.

McGarr, A. (2014). Maximum magnitude earthquakes induced by fluid injection. *J. Geophys. Res. Solid Earth*, 119:1008– 1019.

Méheust, Y. and Schmittbuhl, J. (2003). Scale effects related to flow in rough fractures. *Pure and Applied Geophysics*, 160(5-6):1023–1050.

Meier, P. M., Rodríguez, A., and Bethmann, F. (2015). Lessons Learned from Basel: New EGS Projects in Switzerland Using Multistage Stimulation and a Probabilistic Traffic Light System for the Reduction of Seismic Risk. *Proceedings World Geothermal Congress*, (April):19–25.

Moeck, I., Bloch, T., Graf, R., Heuberger, S., Kuhn, P., Naef, H., Sonderegger, M., Uhlig, S., and Wolfgramm, M. (2015). The St. Gallen project: development of fault controlled geothermal systems in urban areas. In *Proceedings World Geothermal Congress*, pages 1–5.

Molenda, M., Stöckhert, F., Brenne, S., and Alber, M. (2015). Acoustic Emission monitoring of laboratory scale hydraulic fracturing experiments. In *49th US Rock Mechanics / Geomechanics Symposium, 28 June - 1 July*, page 69, San Francisco.

Montgomery, D. R. and Manga, M. (2003). Streamflow and water well responses to earthquakes. *Science*, 300(5628):2047–2049.

Morales, R. H. and Abou-Sayed, A. S. (1989). Microcomputer analysis of hydraulic fracture behavior with a pseudo-three-dimensional simulator. *SPE production engineering*, 4(01):69–74.

Mrokowska, M. M. and Krztoń-Maziopa, A. (2019). Viscoelastic and shear-thinning effects of aqueous exopolymer solution on disk and sphere settling. *Scientific Reports*, 9(1):1–13.

Näf, R. (2017). Microseismic monitoring of hydrofractures in crystalline rock. Master's thesis, ETHZ.

Nasseri, M. H. B., Grasselli, G., and Mohanty, B. (2010). Fracture toughness and fracture roughness in anisotropic granitic rocks. *Rock Mechanics and Rock Engineering*, 43(4):403–415.

Nasseri, M. H. B. and Mohanty, B. (2008). Fracture toughness anisotropy in granitic rocks. *International Journal of Rock Mechanics and Mining Sciences*, 45(2):167–193.

Nasseri, M. H. B., Mohanty, B., and Robin, P. Y. F. (2005). Characterization of microstructures and fracture toughness in five granitic rocks. *International Journal of Rock Mechanics and Mining Sciences*, 42(3):450–460.

Nasseri, M. H. B., Mohanty, B., and Young, R. P. (2006). Fracture toughness measurements and acoustic emission activity in brittle rocks. *Pure and Applied Geophysics*, 163(5-6):917–945.

Nasseri, M. H. B., Rezanezhad, F., and Young, R. P. (2011). Analysis of fracture damage zone in anisotropic granitic rock using 3D X-ray CT scanning techniques. *International Journal of Fracture*, 168(1):1–13.

Nasseri, M. H. B., Tatone, B. S. A., Grasselli, G., and Young, R. P. (2009). Fracture toughness and fracture roughness interrelationship in thermally treated westerly granite. *Pure and Applied Geophysics*, 166(5-7):801–822.

Nejati, M., Dambly, L., and Saar, M. O. (2019a). A methodology to determine the elastic properties of anisotropic rocks from a single uniaxial compression test. *Rock Mechanics and Geotechnical Engineering*, 11(6):1166 – 1183.

Nejati, M., Dambly, M. L. T., and Saar, M. O. (2019b). A methodology to determine the elastic properties of anisotropic rocks from a single uniaxial compression test. *Journal of Rock Mechanics and Geotechnical Engineering*, 11(6):1166–1183.

Nejati, M., Paluszny, A., and Zimmerman, R. W. (2015). A disk-shaped domain integral method for the computation of stress intensity factors using tetrahedral meshes. *International Journal of Solids and Structures*, 69-70:230–251.

Niitsuma, H., Fehler, M., Jones, R., Wilson, S., Albright, J., Green, A., Baria, R., Hayashi, K., Kaieda, H., Tezuka, K., Jupe, A., Wallroth, T., Cornet, F., Asanuma, H., Moriya, H., Nagano, K., Phillips, W. S., Rutledge, J., House, L., Beauce, A., Alde, D., and Aster, R. (1999). Current status of seismic and borehole measurements for HDR/HWR development. *Geothermics*, 28(4-5):475–490.

Nolen-Hoeksema, R. C. and Ruff, L. J. (2001). Moment tensor inversion of microseisms from the B-sand propped hydrofracture, M-site, Colorado. *Tectonophysics*, 336(1-4):163–181.

Nolte, K. G. (1979). Determination of fracture parameters from fracturing pressure decline. In *SPE Annual Technical Conference and Exhibition, 23-26 September*, Las Vegas, Nevada. Society of Petroleum Engineers.

Nordgren, R. R. (1972). Propagation of a Vertical Hydraulic Fracture. *Society of Petroleum Engineers Journal*, 12(04):306–314.

Obermann, A., Kraft, T., Larose, E., and Wiemer, S. (2015). Potential of ambient seismic noise techniques to monitor the St. Gallen geothermal site (Switzerland). *Journal of Geophysical Research: Solid Earth*, 120(6):4301–4316.

Olgaard, D. L. and Brace, W. F. (1983). The microstructure of gouge from a mining-induced seismic shear zone. *International Journal of Rock Mechanics and Mining Sciences and*, 20(1):11–19.

Otsuka, K. and Date, H. (2000). Fracture Process Zone in Concrete Tension Specimen. *Engineering Fracture Mechanics*, 65(2-3):111–131.

Ouchterlony, F. (1988). Suggested methods for determining the fracture toughness of rock. *International Journal of Rock Mechanics and Mining Sciences & Geomechanics Abstracts*, 25(2):71–96.

Patel, S. M., Sondergeld, C. H., and Rai, C. S. (2017). Laboratory studies of hydraulic fracturing by cyclic injection. *International Journal of Rock Mechanics and Mining Sciences*, 95(August 2016):8–15.

Perkins, T. K. and L. R. Kern (1961). Widths of Hydraulic Fractures. *Journal of Petroleum Technology*, 13(09):937 – 949.

Perras, M. A. and Diederichs, M. S. (2014). A Review of the Tensile Strength of Rock: Concepts and Testing. *Geotechnical and Geological Engineering*, 32(2):525–546.

Pine, R. J. and Batchelor, A. S. (1984). Downward migration of shearing in jointed rock during hydraulic injections. *International Journal of Rock Mechanics and Mining Sciences and*, 21(5):249–263.

Preisig, G., Cornaton, F. J., and Perrochet, P. (2012). Regional Flow Simulation in Fractured Aquifers Using Stress-Dependent Parameters. *Groundwater*, 50(3):376–385.

Pyrak-Nolte, L. J. and Nolte, D. D. (2016). Approaching a universal scaling relationship between fracture stiffness and fluid flow. *Nature Communications*, 7(1):10663.

Randolph, J. B. and Saar, M. O. (2011). Combining geothermal energy capture with geologic carbon dioxide sequestration. *Geophysical Research Letters*, 38(10):1–7.

Raven, K. G. and Gale, J. E. (1985). Water flow in a natural rock fracture as a function of stress and sample size. *International Journal of Rock Mechanics and Mining Sciences and Geomechanics Abstracts*, 22(4):251–261.

Renard, P., Glenz, D., and Mejias, M. (2009). Understanding diagnostic plots for well-test interpretation. *Hydrogeology Journal*, 17(3):589–600.

Renner, J. and Messar, M. (2006). Periodic pumping tests. *Geophysical Journal International*, 167(1):479–493.

Renshaw, C. E. (1995). On the relationship between mechanical and hydraulic apertures in rough-walled fractures. *J of Geophysical Research*, 100(B12):629–636.

Roberts, R. (2006). User's manual for nSIGHTS.

Roeloffs, E., Sneed, M., Galloway, D. L., Sorey, M. L., Farrar, C. D., Howle, J. F., and Hughes, J. (2003). Water-level changes induced by local and distant earthquakes at Long Valley caldera, California. *Journal of Volcanology and Geothermal Research*, 127(3-4):269–303.

Rubin, A. M. (1995). Propagation of Magma-Filled Cracks. *Annual Review of Earth and Planetary Sciences*, 23(1):287–336.

Rutledge, J. T., Phillips, W., and Mayerhofer, M. (2004). Faulting Induced by Forced Fluid Injection and Fluid Flow Forced by Faulting: An Interpretation of Hydraulic-Fracture Microseismicity, Carthage Cotton Valley Gas Field, Texas. *Bulletin of the Seismological Society of America*, 94(5):1817–1830.

Rutledge, J. T. and Phillips, W. S. (2003). Hydraulic stimulation of natural fractures as revealed by induced microearthquakes, Carthage Cotton Valley gas field, east Texas. *Geophysics*, 68(2):441.

Rutqvist, J. (1995). Determination of hydraulic normal stiffness of fractures in hard rock from well testing. *International Journal of Rock Mechanics and Mining Sciences and Geomechanics Abstracts*, 32(5):513–523.

Rutqvist, J., Noorishad, J., Tsang, C.-f., and Stephansson, O. (1998). Determination of fracture storativity in hard rocks using high-pressure injection testing. *Water Resources Research*, 34(10):2551–2560.

Rutqvist, J. and Stephansson, O. (1996). A cyclic hydraulic jacking test to determine the in situ stress normal to a fracture. *International Journal of Rock Mechanics and Mining Sciences and Geomechanics*, 33(7):695–711.

Rutqvist, J. and Stephansson, O. (2003). The role of hydromechanical coupling in fractured rock engineering. *Hydrogeology Journal*, 11(1):7–40.

Saar, M. O. (2011). Review: Geothermal heat as a tracer of large-scale groundwater flow and as a means to determine permeability fields. *Hydrogeology Journal*, 19(1):31–52.

Saar, M. O. and Manga, M. (2004). Depth dependence of permeability in the Oregon Cascades inferred from hydrogeologic, thermal, seismic, and magmatic modeling constraints. *Journal of Geophysical Research: Solid Earth*, 109(B4):1–19.

Saouma, V. E., Ayari, M. L., and Leavell, D. A. (1987). Mixed mode crack propagation in homogeneous anisotropic solids. *Engineering Fracture Mechanics*, 27(2):171–184.

Saramito, P. (2016). *Complex fluids*, volume 79 of *Mathématiques et Applications*. Springer International Publishing, Cham.

Sasaki, S. (1998). Characteristics of microseismic events induced during hydraulic fracturing experiments at the Hijiori hot dry rock geothermal energy site, Yamagata, Japan. *Tectonophysics*, 289(1-3):171–188.

Savitski, A. and Detournay, E. (2002). Propagation of a penny-shaped fluid-driven fracture in an impermeable rock: asymptotic solutions. *International Journal of Solids and Structures*, 39(26):6311 – 6337.

Schaltegger, U. (1989). *Geochemische und isotopengeochemische Untersuchungen am zentralen Aaregranit und seinen assoziierten Gesteinen zwischen Aare und Reuss (Aaremassiv, Schweiz)*. PhD thesis, Diss. phil.-nat. Bern, 1989, Bern.

Schmidt, R. A. (1980). A Microcrack Model And Its Significance to Hydraulic Fracturing And Fracture Toughness Testing. *The 21st U.S. Symposium on Rock mechanics (USRMS)*, pages ARMA–80–0581.

Schmidt, R. A. and Lutz, T. J. (1979). KIc and JIc of Westerly Granite-Effects of Thickness and In-Plane Dimensions. *ASTM International*, pages 166–182.

Schmitt, D. R. and Haimson, B. (2017). Hydraulic fracturing stress measurements in deep holes. In *Rock Mechanics and Engineering Volume 1*, chapter 6, page 43. Feng, Xia-Ting.

Schneeberger, R., de La Varga, M., Egli, D., Berger, A., Kober, F., Wellmann, F., and Herwegh, M. (2017). Methods and uncertainty estimations of 3-d structural modelling in crystalline rocks: a case study. *Solid Earth*, 8(5):987–1002.

Scholz, C. H., Dawers, N. H., Yu, J.-Z., Anders, M. H., and Cowie, P. A. (1993). Fault growth and fault scaling laws: Preliminary results. *Journal of Geophysical Research: Solid Earth*, 98(B12):21951–21961.

Schopper, F., Doetsch, J., Villiger, L., Krietsch, H., Gischig, V. S., Jalali, M., Amann, F., Dutler, N., and Maurer, H. (2020). On the Variability of Pressure Propagation during Hydraulic Stimulation based on Seismic Velocity Observations. *Journal of Geophysical Research: Solid Earth*, page 2019JB018801.

Selvadurai, P., Selvadurai, P. A., and Nejati, M. (2019). A multi-phasic approach for estimating the Biot coefficient for Grimsel granite. *Solid Earth*, 10(6):2001–2014.

Settari, A. and Cleary, M. P. (1984). Three-Dimensional Simulation of Hydraulic Fracturing. *Journal of Petroleum Technology*, (July):1177–1190.

Shih, C. F. and Asaro, R. J. (1988). Elastic-plastic analysis of cracks on bimaterial interfaces: Part I—Small scale yielding. *Journal of Applied Mechanics*, 55:299–316.

Sih, G. C., Paris, P. C., and Irwin, G. R. (1965). On cracks in rectilinearly anisotropic bodies. *International Journal of Fracture Mechanics*, 1(3):189–203.

Singh, R. N. and Sun, G. (1990). A numerical and experimental investigation for determining fracture toughness of Welsh limestone. *Mining Science and Technology*, 10:61–70.

Skaråyåski, Å., Syroka, E., and Tejchman, J. (2011). Measurements and calculations of the width of the fracture process zones on the surface of notched concrete beams. *Strain*, 47:319–332.

Skarzyński, Kozicki, J., and Tejchman, J. (2013). Application of DIC Technique to Concrete-Study on Objectivity of Measured Surface Displacements. *Experimental Mechanics*, 53(9):1545–1559.

Skarzyński, L. and Tejchman, J. (2013). Experimental investigations of fracture process using DIC in plain and reinforced concrete beams under bending. *Strain*, 49(6):521–543.

Smith, D. J., Ayatollahi, M. R., and Pavier, M. J. (2001). The role of T-stress in brittle fracture for linear elastic materials under mixed-mode loading. *Fatigue and Fracture of Engineering Materials and Structures*, 24(2):137–150.

Sneddon, I. N. and Elliott, H. A. (1946). The opening of a griffith crack under internal pressure. *Quarterly of Applied Mathematics*, 4(3):262–267.

Spence, D. A. and Sharp, P. (1985). Self-similar solutions for elastodynamic cavity flow. *Proc. R. Soc. Lond.*, A 400:289–313.

Stehfest, H. (1970). Algorithm 368: Numerical inversion of Laplace transforms [D5]. *Communications of the ACM*, 13(1):47–49.

Stephansson, O., Semikova, H., Zimmermann, G., and Zang, A. (2019). Laboratory Pulse Test of Hydraulic Fracturing on Granitic Sample Cores from Äspö HRL, Sweden. *Rock Mechanics and Rock Engineering*, 52(2):629–633.

Sutton, R. P., Cox, S. A., and Barree, R. D. (2010). Shale gas plays: A performance perspective. *Society of Petroleum Engineers - SPE Tight Gas Completions Conference 2010*, 2009(November):416–427.

Swanson, P. L. and Spetzler, H. (1984). Ultrasonic probing of the fracture process zone in rock using surface waves. *The 25th US Symposium on Rock Mechanics (USRMS).*

Tarokh, A., Makhnenko, R. Y., Fakhimi, A., and Labuz, J. F. (2017). Scaling of the fracture process zone in rock. *International Journal of Fracture*, 204(2):191–204.

Tavallali, A. and Vervoort, A. (2010). Behaviour of layered sandstone under Brazilian test conditions: Layer orientation and shape effects. *International Journal of Rock Mechanics & Mining Sciences*, 47:313–322.

Tester, J. W., Anderson, B. J., Batchelor, A. S., Blackwell, D. D., DiPippo, R., Drake, E. M., Garnish, J., Livesay, B., Moore, M. C., Nichols, K., Petty, S., Toksoz, M. N., Veatch, R. W., Baria, R., Augustine, C., Murphy, E., Negraru, P., and Richards, M. (2007). Impact of enhanced geothermal systems on US energy supply in the twenty-first century. *Philosophical transactions. Series A, Mathematical, physical, and engineering sciences*, 365(1853):1057–94.

The MathWorks Inc. (2017). Matlab version 9.3.0 (R2017b). *Natick, Massachusetts, USA*.

Theis, C. V. (1935). The relation between the lowering of the Piezometric surface and the rate and duration of discharge of a well using groundwater storage. *Eos, Transactions American Geophysical Union*, 16(2):519–524.

Tongpenyai, Y. and Raghavan, R. (1981). Effect of Wellbore Storage and Skin on Interference Test Data. *JPT, Journal of Petroleum Technology*, 33(1):151–160.

Turcotte, D. and Schubert, G. (2014). *Geodynamics*. Cambridge University Press, 3 edition.

van As, A. and Jeffrey, R. G. (2000). Caving Induced by Hydraulic Fracturing at Northparkes Mines. *Pacific Rocks 2000*, pages 353–360.

van der Baan, M., Eaton, D., and Dusseault, M. (2013). Microseismic Monitoring Developments in Hydraulic Fracture Stimulation. In Bunger, A., McLennan, J., and Jefrey, R., editors, *Effective and Sustainable Hydraulic Fracturing*, pages 439–466. InTech.

van Der Baan, M., Eaton, D. W., and Preisig, G. (2016). Stick-split mechanism for anthropogenic fluid-induced tensile rock failure. *Geology*, 44(7):503–506.

Vermilye, J. M. and Scholz, C. H. (1998). The process zone: A microstructural view of fault growth. *Journal of Geophysical Research*, 103:12223–12237.

Vervoort, A., Min, K.-b., Konietzky, H., Cho, J.-w., Debecker, B., Dinh, Q.-d., Frühwirt, T., and Tavallali, A. (2014). Failure of transversely isotropic rock under Brazilian test conditions. *International Journal of Rock Mechanics and Mining Sciences*, 70:343–352.

Villiger, L., Gischig, V. S., Doetsch, J., Krietsch, H., Dutler, N. O., Jalali, M., Valley, B., Selvadurai, A. P. abd Mignan, A., Plenkers, K., Giardini, D., Amann, F., and Wiemer, S. (2020). Influence of reservoir geology on seismic response during decameter scale hydraulic stimulations in crystalline rock. *Solid Earth*, 11(2):627–655.

Vinci, C., Steeb, H., and Renner, J. (2015). The imprint of hydro-mechanics of fractures in periodic pumping tests. *Geophysical Journal International*, 202(3):1613–1626.

Walter, W. R. and Brune, J. N. (1993). Spectra of seismic radiation from a tensile crack. *Journal of Geophysical Research*, 98(B3):4449–4459.

Wang, H. (2000). *Theory of linear poroelasticity with applications to geomechanics and hydrogeology*. Princeton University Press.

Wang, H. F. (1997). Effects of deviatoric stress on undrained pore pressure response to fault slip. *Journal of Geophysical Research*, 102(97):17943—–17950.

Wang, H. Y. and Sharma, M. M. (2019). Determine In-Situ Stress and Characterize Complex Fractures in Naturally Fractured Reservoirs from Diagnostic Fracture Injection Tests. *Rock Mechanics and Rock Engineering*, 52(12):5025–5045.

Wang, S. S., Yau, J. F., and Corten, H. T. (1980). A mixed-mode crack analysis of rectilinear anisotropic solids using conservation laws of elasticity. *International Journal of Fracture*, 16(3):247–259.

Warpinski, N. (2009). Microseismic Monitoring: Inside and Out. *Journal of Petroleum Technology*, 61(11):80–85.

Warpinski, N., Branagan, P., Engler, B., Wilmer, R., and Wolhart, S. (1997). Evaluation of a downhole tiltmeter array for monitoring hydraulic fractures. *International Journal of Rock Mechanics and Mining Sciences*, 34(3-4):329.e1–329.e13.

Warpinski, N. R. (1985). Measurement of width and pressure in a propagating hydraulic fracture. *Society of Petroleum Engineers Journal*, 25(01):46–54.

Warpinski, N. R. and Branagan, P. T. (1989). Altered-Stress Fracturing. *Journal of Petroleum Technology, SPE-17533-PA*, 41(09):990 – 997.

Warpinski, N. R., Mayerhofer, M. J., and Agarwal, K. (2013). Hydraulic Fracture Geomechanics and Microseismic Source Mechanisms. *SPE Journal*, 18(4):766–780.

Warren, J. and Root, P. (1963). The Behavior of Naturally Fractured Reservoirs. *Society of Petroleum Engineers Journal*, 3(03):245–255.

Warren, W. E. and Smith, C. W. (1985). In situ stress estimates from hydraulic fracturing and direct observation of crack orientation. *Journal of Geophysical Research*, 90(B8):6829.

Wenning, Q. C., Madonna, C., Haller, A. D., and Burg, J.-p. (2018). Permeability and seismic velocity anisotropy across a ductile-brittle fault zone in crystalline rock. *Solid Earth*, 9(March):683–698.

Whittaker, B. N., Singh, R. N., and Sun, G. (1992). Rock fracture mechanics: principles, design and applications. *Rock fracture mechanics: principles, design and applications*.

Wild, K. M., Wymann, L. P., Zimmer, S., Thoeny, R., and Amann, F. (2015). Water Retention Characteristics and State-Dependent Mechanical and Petro-Physical Properties of a Clay Shale. *Rock Mechanics and Rock Engineering*, 48(2):427–439.

Wright, C. A., Davis, E. J., Golich, G. M., Ward, J. F., Demetrius, S. L., Minner, W. A., and Weijers, L. (1998). Downhole tiltmeter fracture mapping: finally measuring hydraulic fracture dimensions. *SPE Western Regional Conference*, pages 1–11.

Wu, Z., Rong, H., Zheng, J., Xu, F., and Dong, W. (2011). An experimental investigation on the FPZ properties in concrete using digital image correlation technique. *Engineering Fracture Mechanics*, 78(17):2978–2990.

Wyborn, D., De Graaf, L., Davidson, S., and Hann, S. (2005). Development of Australia ' s First Hot Fractured Rock (HFR) Underground Heat Exchanger , Cooper Basin , South Australia. *Workshop Geothermal Congress 2005*, (April):24–29.

Yushi, Z., Xinfang, M., Tong, Z., Ning, L., Ming, C., Sihai, L., Yinuo, Z., and Han, L. (2017). Hydraulic Fracture Growth in a Layered Formation based on Fracturing Experiments and Discrete Element Modeling. *Rock Mechanics and Rock Engineering*, 50(9):2381–2395.

Zang, A., Stephansson, O., Stenberg, L., Plenkers, K., Specht, S., Milkereit, C., Schill, E., Kwiatek, G., Dresen, G., Zimmermann, G., Dahm, T., and Weber, M. (2017). Hydraulic fracture monitoring in hard rock at 410 m depth with an advanced fluid-injection protocol and extensive sensor array. *Geophysical Journal International*, 208(2):790–813.

Zang, A. and Wagner, F. (2000). Fracture process zone in granite. *Journal of Geophysical Research*, 105(B10):23651–23661.

Zang, A., Yoon, J. S., Stephansson, O., and Heidbach, O. (2013). Fatigue hydraulic fracturing by cyclic reservoir treatment enhances permeability and reduces induced seismicity. *Geophysical Journal International*, 195(2):1282–1287.

Zang, A., Zimmermann, G., Hofmann, H., Stephansson, O., Min, K.-B., and Kim, K. Y. (2019). How to Reduce Fluid-Injection-Induced Seismicity. *Rock Mechanics and Rock Engineering*, 52(2):475–493.

Zangerl, C., Evans, K. F., Eberhardt, E., and Loew, S. (2008). Normal stiffness of fractures in granitic rock: A compilation of laboratory and in-situ experiments. *International Journal of Rock Mechanics and Mining Sciences*, 45(8):1500–1507.

Zarrouk, S. J. and McLean, K. (2019). *Geothermal Well Test Analysis*. Katie Hammon, London.

Zhao, J. and Brown, E. T. (1992). Hydro-thermo-mechanical properties of joints in the Carnmenellis granite. *Quarterly Journal of Engineering Geology and Hydrogeology*, 25(4):279–290.

Zhong, L., Oostrom, M., Truex, M. J., Vermeul, V. R., and Szecsody, J. E. (2013). Rheological behavior of xanthan gum solution related to shear thinning fluid delivery for subsurface remediation. *Journal of Hazardous Materials*, 244-245:160–170.

Zietlow, W. K. and Labuz, J. F. (1998). Measurement of the Intrinsic Process Zone in Rock Using Acoustic Emission. *Int. J. Rock Mech. Min. Sci.*, 35(3):291–299.

Zimmermann, G., Zang, A., Stephansson, O., Klee, G., and Semiková, H. (2019). Permeability Enhancement and Fracture Development of Hydraulic In Situ Experiments in the Äspö Hard Rock Laboratory, Sweden. *Rock Mechanics and Rock Engineering*, 52(2):495–515.

Zoback, M. D. (2007). *Reservoir Geomechanics.*

Zoback, M. D. and Harjes, H.-P. (1997). Injection-induced earthquakes and crustal stress at 9 km depth at the KTB deep drilling site, Germany. *Journal of Geophysical Research*, 102(B8):18477.

Zoback, M. D., Kohli, A., Das, I., and Mcclure, M. W. (2012). The Importance of Slow Slip on Faults During Hydraulic Fracturing Stimulation of Shale Gas Reservoirs. *SPE Americas Unconventional Resources Conference*, (2011).

Zoback, M. D., Rummel, F., Jung, R., and Raleigh, C. B. (1977). Laboratory hydraulic fracturing experiments in intact and pre-fractured rock. *International Journal of Rock Mechanics and Mining Sciences and*, 14(2):49–58.

Appendix A

Supplement: Hydraulic fracture propagation in a heterogeneous stress field in a crystalline rock mass

The formal analysis, data curation and data visualization inclusive writing the original draft preparation and review was done by N.D with help of B.V.

Please cite this chapter as: Dutler, N., Valley, B., Gischig, V., Villiger, L., Krietsch, H., Doetsch, J., Brixel, B., Jalali, M., and Amann, F.: Supplement: Hydraulic fracture propagation in a heterogeneous stress field in a crystalline rock mass, https://doi.org/10.5194/se-2019-111-supplement, 2019.

A.1 Pressure vs. Flow-rate analysis

We use pressure vs flow rate analysis to extract diagnostic injection parameters including the jacking pressure (JP). Since the best way of determining such pressure is debated in the literature, we describe here our approach. We first use the injection HF3 to exemplify our approach (Fig. A.1). We apply then the approach systematically to all our tests (Fig. A.2).

The first step of our analyses is to determine conditions close to steady state. We did this on flow-controlled injection (RF1 and RF2 cycles) and pressure-controlled injection (SR). In both cases we extracted the pressure p_{inj} and the flow q_{inj} at the point just prior the next step of flow or pressure is initiated (Fig. A.1 a, zoomed frame). In our tests, we typically waited long enough to have an almost stabilized pressure and flow prior initiating the next step and we assume then the conditions are in quasi-steady state.

We report the data in a q_{inj} vs. p_{inj} diagram including only data from the SR cycle (Fig. A.1b) or data from both SR and RF cycles (Fig. A.1c). Typically, these data form a bilinear pattern. At low pressures, the determination of a linear trend is straight forward (orange dashed line on Fig. A.1b and c). The inverse of the slope of this linear relationship corresponds to what will be referred to as the injectivity index before jacking (II_b) given in l/min/MPa and it is equal for HF3 at 0.88 l/min/MPa.

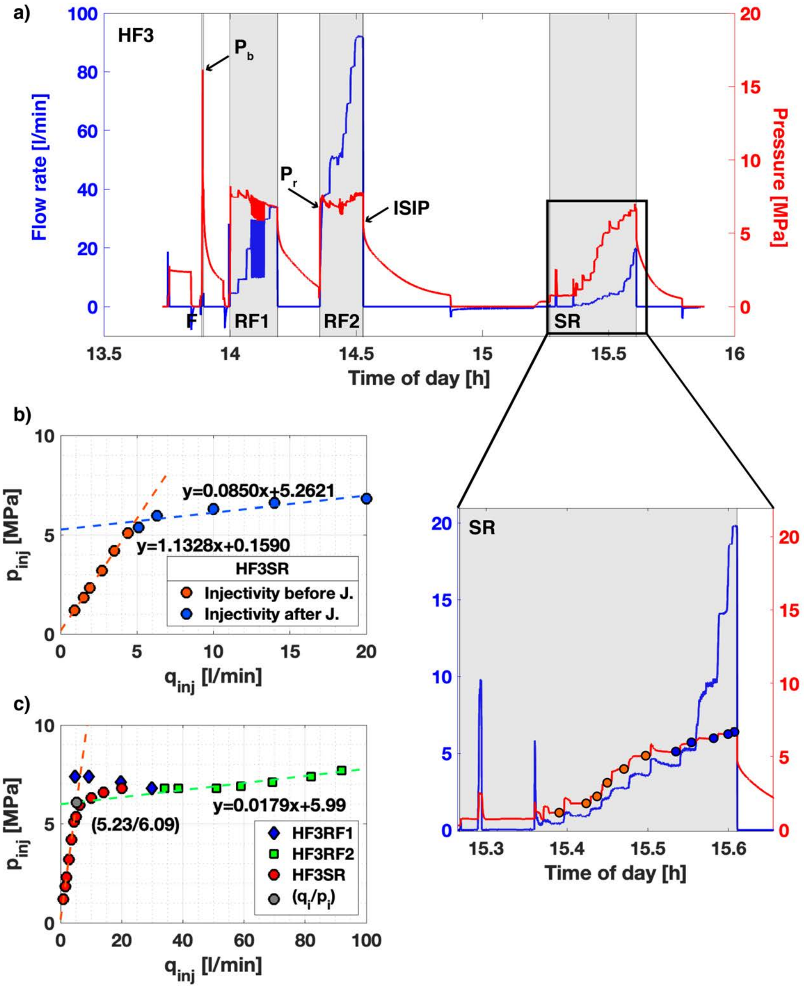

Fig. A.1 a) Testing procedure for HF3 experiment, with breakdown pressure, P_b, fracture reopening pressure, P_r, and instantaneous shut-in pressure, $ISIP$, inclusive pressure-controlled step tests with evaluated flowrate (q_{inj}) vs. injection pressure (p_{inj}) points. b) The q_{inj} vs. p_{inj} plot shows the final matrix injectivity (reverse of the slope of the orange dashed line) and the jacking pressure from the SR cycle (intersection of the blue dashed line with y-axis). c) The q_{inj} vs. p_{inj} point at pseudo steady-state from the second refrac cycle RF2 are included to estimate the fracture injectivity (reverse of the slope of the green dashed line) and the jacking pressure from two different methods.

At high pressure the injectivity increases because the fracture opens (Doe and Korbin, 1987). The linearity of the high-pressure data point is less evident as it depends on what data are included. We took the approach to determine the linear trend including the SR data only (Fig. A.1b) and both the SR and RF data (Fig. A.1c). The linear trend is typically

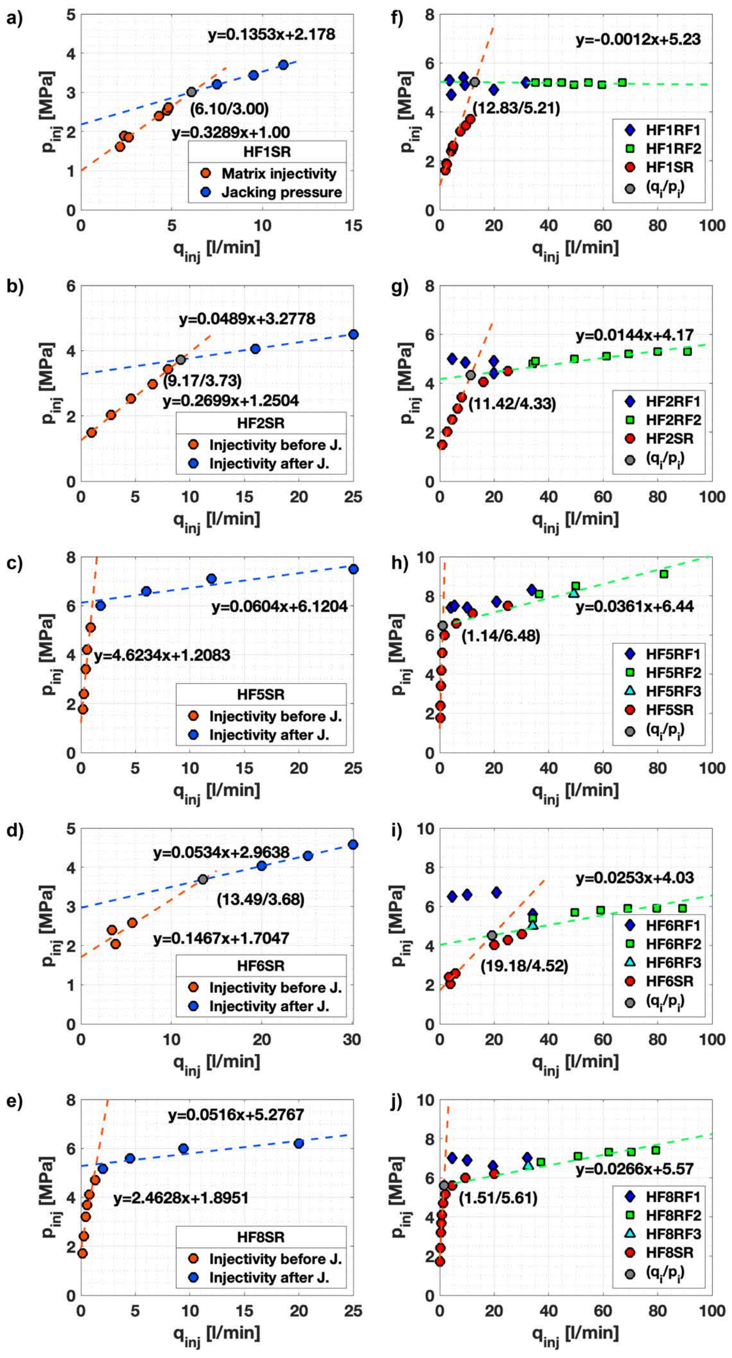

Fig. A.2 a-e) The q_{inj} vs. p_{inj} plots show the final injectivity (inverse of the slope of the orange dashed line) and the jacking pressure from the SR cycle for the HF tests. g-j) The q_{inj} vs. p_{inj} point at pseudo steady state from the second refrac cycle RF2 are included to estimate the fracture injectivity (inverse of the slope of the green dashed line) and the jacking pressure from two different methods.

flatter when all data are included. The inverse of the slope of these linear relationships is

Table A.1 The jacking pressure and injection index are estimated as described in the text. Values in red are the best estimate of jacking pressure for a specific test. “not considering the points from the cycle SR, would increase this value; *takes only the points into account from SR

Test	JP_{min} **[MPa]**	JP_{max} **[MPa]**	II_b **[l/min/MPa]**	II_a^{min} **[l/min/MPa]**	II_a^{max} **[l/min/MPa]**	q_i **[l/min]**	p_i **[MPa]**
HF1	2.18	5.23	3.040	7.39	28.74"	6.10*	3.00*
HF2	3.28	4.17	3.693	20.45	69.44	9.17*	3.73*
HF3	5.26	5.99	0.882	9.81	55.87	5.23	6.09
HF5	6.12	6.44	0.206	14.63	27.70	1.14	6.48
HF6	2.96	4.03	2.774	18.69	39.53	13.49*	3.68*
HF8	5.28	5.57	0.347	15.69	37.59	1.51	5.61

the injectivity after jacking (II_a), where we define a low value (II_a^{min}) using only SR data and a high value (II_a^{max}) using all data.

We define the jacking pressure (JP) following the approach of Rutqvist and Stephansson (1996) by the intersection of the high-pressure trend line with the zero-flow ordinate. Since depending on what data, we included (only SR or all data), we defined two different high-pressure trend line, we also have to intersection with the zero-flow ordinate: JP_{min} using only SR data and JP_{max} using all data.

As an alternate diagnostic parameter, we report also — following Hartmaier et al. (1998) — the intersection point q_i /p_i between the low- and high-pressure trend lines using all data.

The p_{inj} vs q_{inj} data for all other injection tests are presented in Fig. A.2 and the diagnostic parameters are summarized in Table A.1. For tests HF1, HF2 and HF6, the gradual change in slope of p_{inj} vs q_{inj} data would give an overestimate of the pi including all data points. Therefore, we used only the SR data to determine the point q_i /p_i and the advantage is that pi is in the range of JP_{min} and JP_{max}. JP_{max} are in the same range than p_i for the other three tests. Therefore, no data were excluded.

The best estimate of jacking pressure depends actually on the p_{inj} vs q_{inj} curve. HF3, HF5 and HF8 show a strong bi-linear trend, where the change in the number of data points does not show a strong variation in a possible jacking pressure. Nevertheless, the smallest possible jacking was used to account for earliest variation in the hydraulic fracture aperture. We decided not to do so for test HF1, HF2 and HF8, as the bi-linear trend is less pronounced. The range between JP_{min} and JP_{max} is much bigger and a reliable midway between this two was found using the intersection method.

Table A.2 Transmissivity estimated from PI tests before and from CHI tests and injectivity after the HF experiments.

Borehole	**Experiment**	**Depth [m]**	**before HF**	**after HF**	
			T$_{PI}$ [m^2/s]	**T$_{CHI}$ [m^2/s]**	**T$_{inj}$ [m^2/s]**
INJ1	HF1	40.5	3.1 10^{-13}	1.9 10^{-9}	1.3 10^{-7}
	HF2	36.3	3.0 10^{-13}	2.5 10^{-9}	1.6 10^{-7}
	HF3	20.3	4.0 10^{-13}	2.1 10^{-10}	3.9 10^{-8}
	HF5	14.5	2.3 10^{-13}	2.0 10^{-10}	9.1 10^{-9}
INJ2	HF6	38.9	-	4.8 10^{-7}	1.2 10^{-7}
	HF8	15.7	5.7 10^{-13}	3.6 10^{-11}	1.5 10^{-8}

A.2 Transmissivity values

The transmissivity of each tested interval was determined prior hydraulic fracturing by analyzing a Pulse injection (PI) and after the injection by converting the injectivity determined during the SR cycle to transmissivity assuming steady-state radial flow regime (De Marsily, p 150) and by performing 3 month later Constant Head Injection (CHI) tests. All estimates are summarized in Tab. A.2. The transmissivity estimated from injectivity are typically 2 to 3 orders of magnitude higher than the one estimated by CHI tests. We attribute these differences to:

∗ The CHI depends only on one constant pressure. Injectivity is measured at different pressures.

∗ The increase in pressure during injectivity measurement can influence the fracture compliance and fracture aperture. The assumption of radial flow is than violated.

∗ The step tests for injectivity uses many steps where the pressure was progressively increased. If the time for a single step is too short, the results can include values with non-pseudo steady state flow. For these reasons, we assume that the transmissivity obtained from both methods are relevant. Depending on the injection pressure, the transmissivity increases due to an increase in the hydraulic aperture.

A.3 Detailed observation of tilt, strain and pressure

Tilt:

∗ HF2 and HF1 are located next to the intersection of the S1 and S3 zone. Both experiments show similar tilt signals. HF6 is farther away towards the AU tunnel and the water is injected in the S1 fracture network. The tiltmeters indicate a tensional and/or shearing signal related to the S1 zone.

∗ HF3 and HF8 are executed more or less at the same position in INJ1 and the other in INJ2 borehole. Therefore, the two signals are very similar and show small magnitudes.

The flow shortcut toward an existing borehole during HF5 did not allow to store fluid in the fracture, such that the tilt signals are very small.

- We do not recognize changes in the tilt signal due to different fluid metrics. The location of the injection and the associated geological structures dominate the tilt signal.

Strain:

- HF2 and HF1 are next to the intersecting S1 and S3 zone and have very similar strain signals. Especially in FBS2 and FBS3 borehole the FBG's behave similar and show comparable magnitudes at the end of refrac cycle RF2. The last two FBG sensors in the FBS1 borehole indicate a tensional signal during HF1, where only the last sensor reacts tensional during HF2.
- The time series presented from test HF6 in FBS1 show the deepest three FBG sensors, where two of them show a tensional signal and the sensor at 42.2 m indicates compressional signal during RF2. At the end of the test, the sensor shows a relaxation drift. The FBG sensor at 23.3 m located along the S1 zone show a tensional signal and the signal from FBG sensor at 36.1 m shows a strong compressional signal. For test HF6, the sensor at 31.6 m depth presents more or less the change from tensional to compressional signal in the borehole FBS3 and vice versa for the tests HF1/HF2.
- The sensors from test HF8 at 22.35 m depth in FBS1 and at 20 m depth in FBS2 have the strongest tensional signal similar to the test HF3. The strain response during the first refrac cycle RF1 is delayed for test HF8 compared to test HF3. Note that the tensional signals are very localized comparing the sensors along the borehole (FBS1 and FBS2). The viscous fluid used during this test is amenable to form a single dominant hydraulic fracture.
- The time series presented from HF5 show a direct tensional signal in FBS1 (15.6 m) at the beginning of RF1, where the connection towards the geophysical borehole was established. Therefore, magnitudes reached for transient peak strain are much smaller compared to the tests HF3 and HF8. At the end of the test, when the injection packer was released, all the presented time series responded with a tensional or compressional change.
- Note, we decided to focus our data presentation on time series from tensional signals, as they can be indicators for fluid paths.

Fracture fluid pressure observations:

- Test HF1 does not show strong responses in the observation intervals. Comparing PRP2-2 with test HF2 shows a similar response during and after RF2. It is reaching the peak pressure with a delay. The response in PRP1-1 (S1) during the test HF1 was smaller than for PRP1-2 and PRP1-3, both located in the S3 zone. All the presented PRP intervals show a very similar fracture fluid pressure response except PRP2-1.

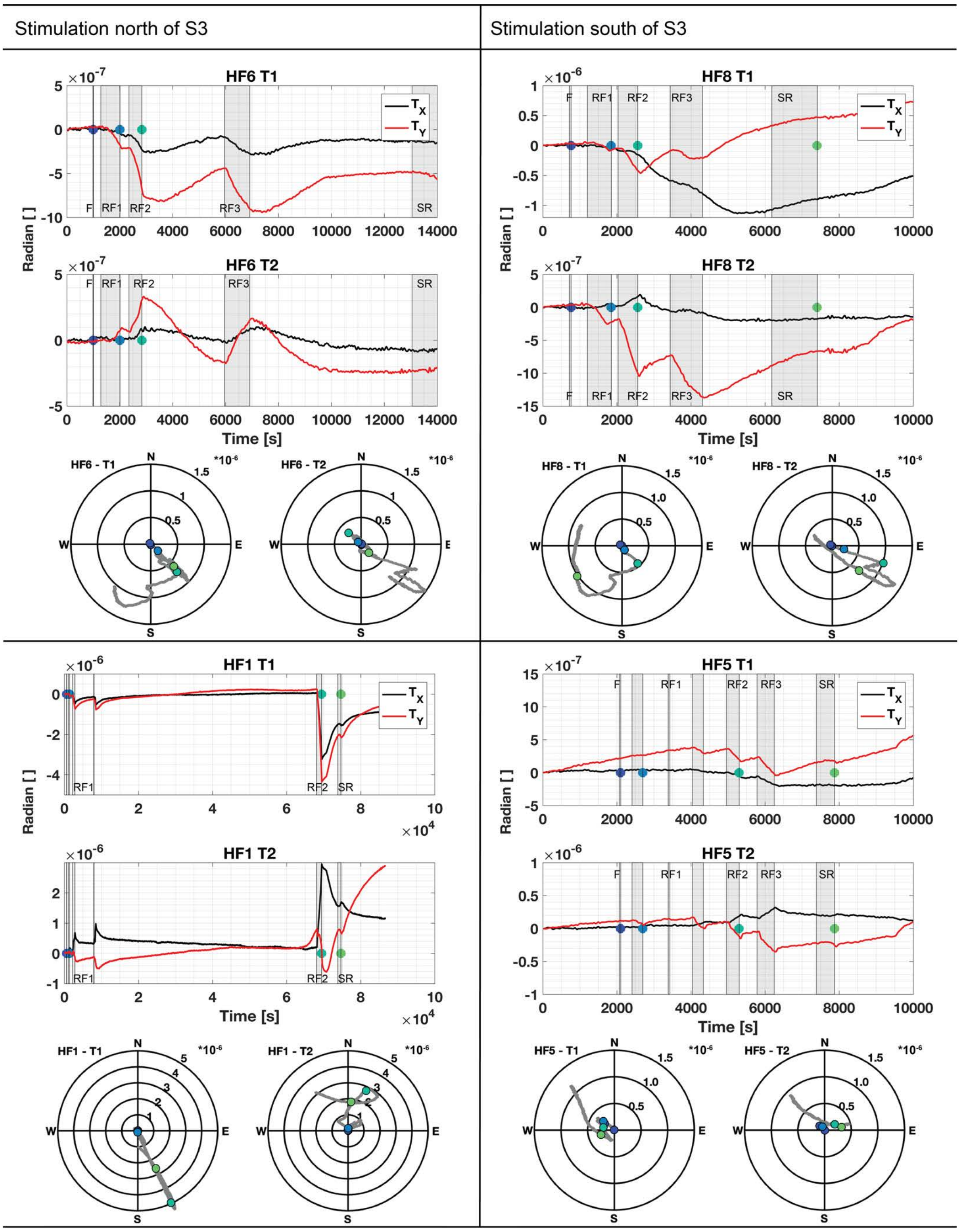

Fig. A.3 The time series of tilt meter T1 and T2 are presented for the experiment HF6/HF1 and HF8/HF5. The fluid injection time are named and indicated by the grey boxes. The color points at the end of fluid injection in the time series are presented in a polar plot. The circles correspond to the magnitude given in microradian.

The interval below injection show very large pressure response during HF2 but none was observed during test HF1. The small fracture fluid pressure response towards East indicates a less connected fracture network.

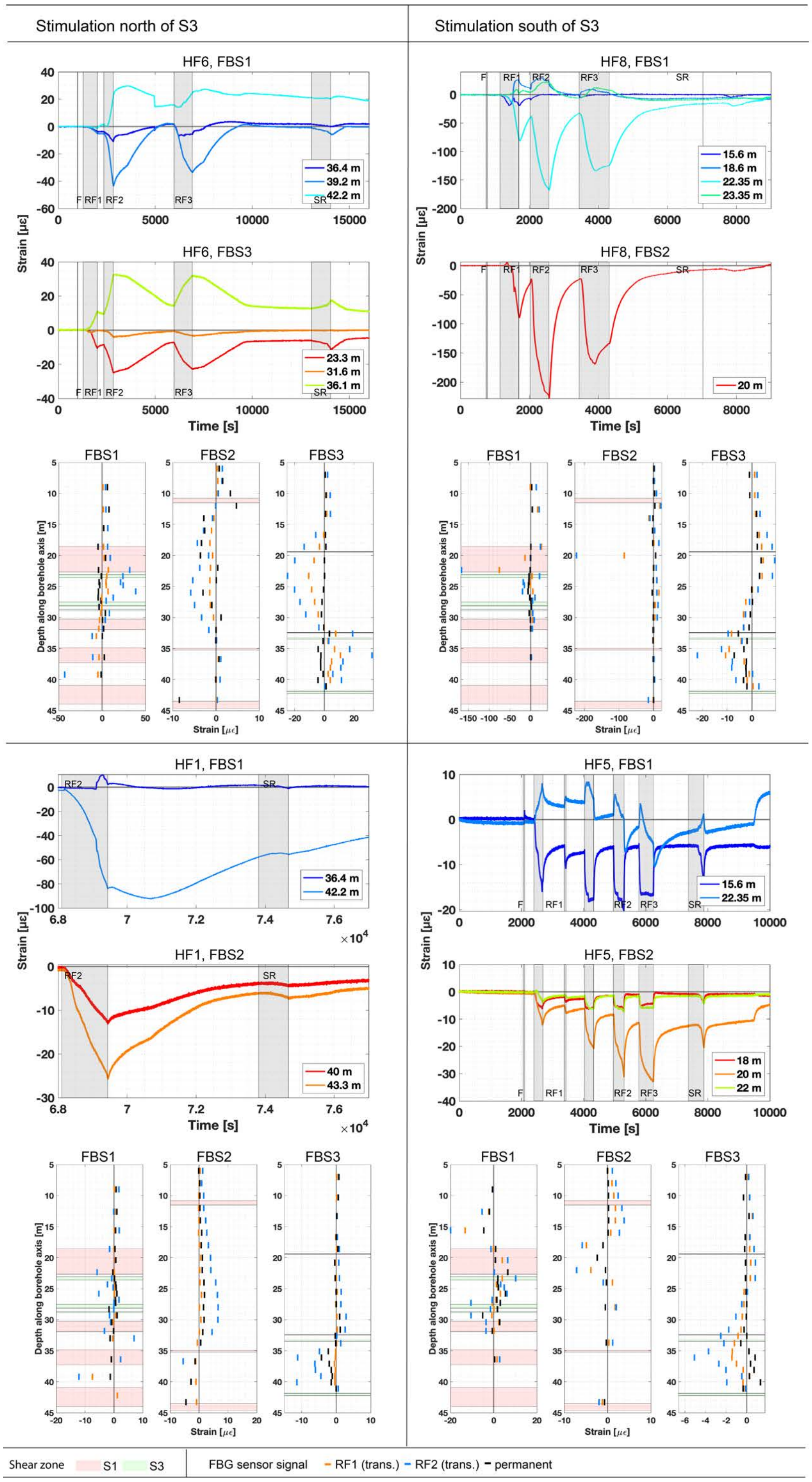

Fig. A.4 Selected time series and overview of the FBG strain signals for experiment HF6/HF1 and HF8/HF5. The fluid injection time is named and indicated by the grey boxes.

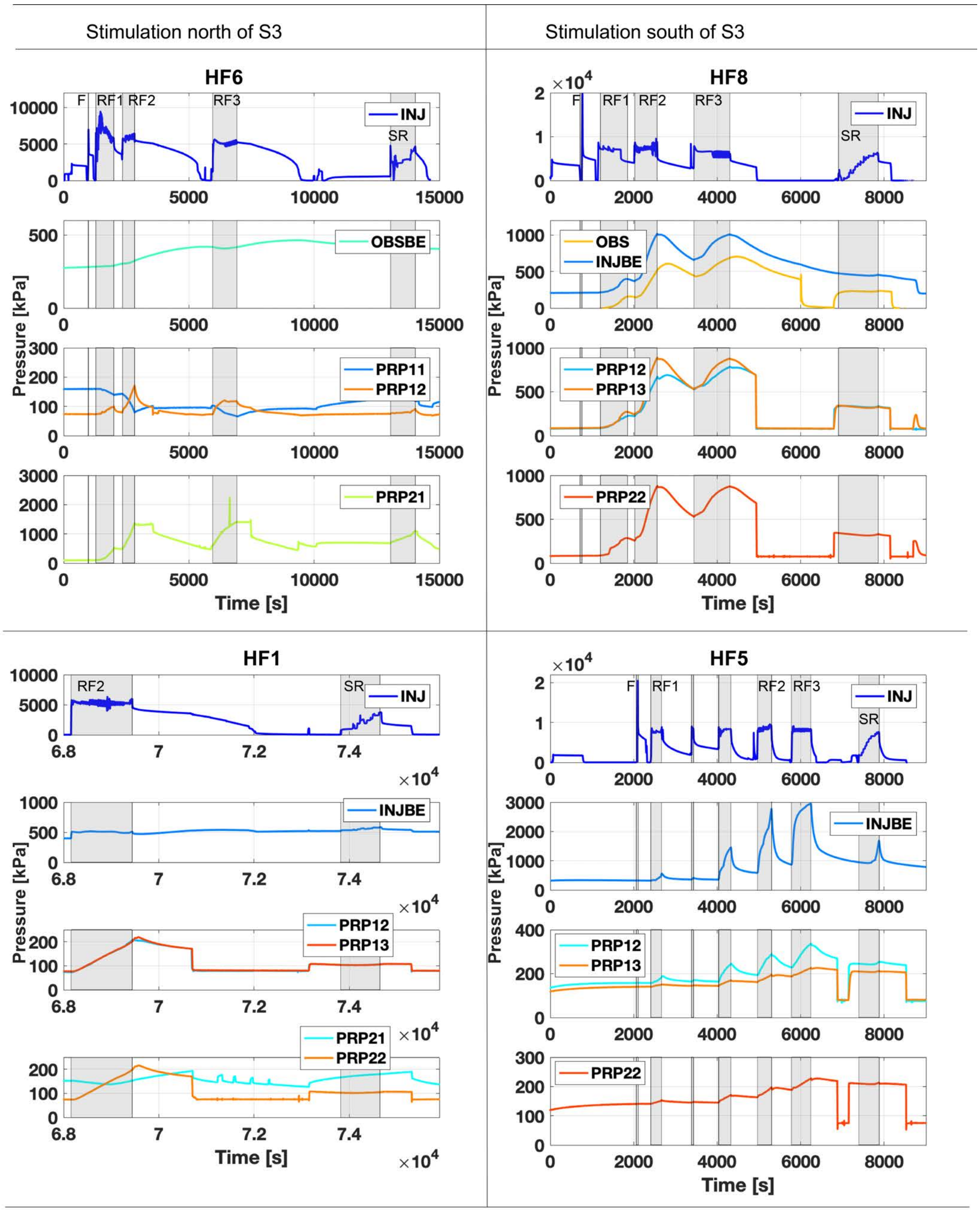

Fig. A.5 Selected time series of pressure response are presented for experiment HF6/HF1 and HF8/HF5. The fluid injection time is named and indicated.

∗ During test HF6, strong responses are recognized for interval PRP2-1. This interval shows an increase during injection with a delay reaching the peak and stabilizing until bleed-off. The signal observed in borehole interval PRP1-1, is very interesting. It shows a pressure release during injection and PRP1-2 an increase in the same range of magnitude. In addition, only a fracture fluid pressure signal is observed in the OBSBE. This actually tells us, that the related fracture from HF1/HF2 and HF6 injections are different and not related with each other and that the fractures connected to injection interval HF6 are as well connected to the densely fractured zone S3, but in a different way than for HF1/HF2.

- We observe smaller magnitudes during the HF8 experiment than for HF3. All the presented time series for the observation interval are very similar. It does not matter if the signal was observed in the PRP borehole or below the injection. For all PRP observation intervals and the INJBE we see a pseudo shut-in at the end of refrac cycle RF2. Only the observation interval (OBS) shows no pseudo shut-in and the longest delay time reaching the pressure peak. We noted that the signals for all observation points are very similar indicating an existing fluid path between all intervals. Therefore, we increase the connectivity and this leads to larger swept volume, which is a key factor for successful fracturing.
- The test HF5 shows small increase in pressure for the PRP observation intervals during injection. The INJBE interval has magnitudes up to 3 MPa, which seems to indicate a short-cut towards this interval. A packer sealing issue is unlikely as no seismicity is observed. The pressure increase observed in the interval INJBE, drives the fluid/pressure into the most conductive features in S3 and raise the pressure in the PRP intervals.

A.4 Summary of the MF injection pressure and seismic characteristics

The event catalogue and the data from the injection location (e.g. flow rate and injection pressure) used in here, is published by Gischig et al. (2018) (direct link to the dataset: https://doi.org/10.3929/ethz-b-000217536). The in-situ test procedure and the test analysis followed the ISRM guideline (Haimson and Cornet, 2003). The breakdown pressure was measured during the frac-cycle. The instantaneous shut-in pressure (ISIP) was obtained during each cycle using the tangent method. The re-opening pressure (P_r) was measured for the refrac cycle RF (Table A.3) using the tangent method. For the MF experiment the injected water was outside of the borehole measured with a flowmeter. The accumulation of the injected water corresponds to the injection volume V_i. The backflow was measured at the injection interval during venting. Thus, the fluid recovery V_r is the total recovery for the MF experiments. The earthquake catalogue has a calculated error ellipsoid with principle component direction for each event. An event was approved for the minifrac MF1, MF2 and MF3, when the maximum ellipsoid axis was equal or smaller than 2 m. For the minifrac MF4 to MF7, this threshold value was set to 3 m.

Table A.3 Overview of injection pressure, fluid injection and seismic characteristics of the seven hydraulic fracturing experiments during stress characterization phase. All seven hydraulic fractures were propagated in multiple refracturing phases. Comparison of fracture breakdown pressure (P_c), fracture reopening pressure (P_r) and additional hydraulic test parameters (V_i, injected volume; V_r, recovered volume) and localized AE event numbers. *MF5 indicate an insufficient sealing of the test section.

Stage No.	Experiment	P_c & P_r [MPa]	ISIP [MPa]	V_i [l]	V_r [l]	Number of localized AE
1	MF1-F	23.4	8.5	1.1	0.15	3
2	MF1-RF1	7.6	8.4	1.8	0.2	24
3	MF1-RF2	7.6	8.1	3.3	0.2	29
4	MF1-RF3	-	8.0	4.2	0.2	56
				10.4	7 %	112
5	MF2-F	25.7	-	1.0	0.6	0
6	MF2-RF1	9.6	9.0	1.5	1.0	15
7	MF2-RF2	10.1	8.6	3.3	2.4	35
8	MF2-RF3	10.3	8.8	4.2	3.2	58
				10.0	72 %	108
9	MF3-F	26.1	-	0.5	0.35	3
10	MF3-RF1	11.55	9.2	1.6	1.0	16
11	MF3-RF2	12.5	8.9	2.5	1.8	28
12	MF3-RF3	12.5	9.1	3.3	2.5	25
				7.9	72 %	72
13	MF4-F	22.7	-	0.5	0.4	13
14	MF4-RF1	8.45	-	1.1	0.6	25
15	MF4-RF2	8.2	8.2	2.2	1.2	45
16	MF4-RF3	8.4	8.0	3.3	1.5	38
17	MF4-RF4	8.4	7.9	3.8	0.7	34
				10.9	41 %	155
18	*MF5-F	19.1	-	0.8	0.2	37
19	*MF5-RF1	13.6	12.6	0.8	0.2	48
20	*MF5-RF2	14.4	11.7	2.6	0.15	41
21	*MF5-RF3	17.7 (20.5)	14.7	4.6	0.2	49
22	*MF5-RF4	15.6	14.1	0.9	0.2	3
				9.7	10 %	178
23	MF6-F	13.5-14.7	9.6	0.3	0.15	0
24	MF6-RF1	11.6	7.8	0.6	0.15	0
25	MF6-RF2	12.1	6.7	2.3	0.15	0
26	MF6-RF3	9.4	6.5	1.8	0.15	1
27	MF6-RF4	-	6.1	0.7	0.1	0
28	MF6-RF5	-	6.3	2.3	0.15	8
29	MF6-RF6	10.2	6.7	1.1	0.15	5
				9.1	11 %	14
30	MF7-F	13.5	5.9	1.0	0.5	1
31	MF7-RF1	5.8	5.7	1.2	0.5	1
32	MF7-RF2	6.0	5.45	2.2	1.5	5
33	MF7-RF3	6.3	5.3	3.1	2.5	1
34	MF7-RF4	6.4	5.2	4.0	2.5	2
				11.5	65 %	10

Table A.4 Summary of injection pressure and fluid injection of the four hydraulic fracturing tests from borehole SBH1 during stress characterization phase. All hydraulic fractures were propagated in multiple refracturing cycles.

Experiment	P_c [MPa]	P_r [MPa]	ISIP [MPa]	V_i [l]	V_r [l]
MF8	17.9	8.9	8.3	6.4	2.7
MF9	19.7	9.8	9.2	13.8	1.4
MF10	13.7	11	9.6	9.5	0.8
MF11	19.1	9.65	9.2	8.8	5.2

A.5 Fracture orientation determination from borehole logging and seismic plane analyses

Table A.5 summarize the trace description from the acoustic televiewer for the HF experiments inclusive sinusoidal trace fit with the software wellcad (advance logic technology) resulting in true dip direction and dip (xxx/xx°) at the specific depth. The optical televiewer borehole logging was done for the fracture traces in SBH3 and impression packer were used for the tests executed in SBH1. For each HF experiment, we tried to fit a plane through the seismic cluster using an orthogonal distance regression criterion. The same approach was used for the minifracs by Gischig et al. (2018) (Gischig et al., 2018). The planes considering all located seismic events for test HF8 show a comparable orientation with the MF planes. The misfit of the plane for the test HF8 is 0.52 m. Test HF2 show two clusters with different oriented planes. The first cluster is located next to the injection borehole and occurs mainly through injection cycle RF1 and the second one is located further towards E during cycle RF2. One plane is oriented towards NNE with a dip of 83° and the misfit is 0.26 m and the other plane is oriented towards S with a dip of 76° (misfit: 0.34 m). Two clusters are observed for HF3 with one cluster aligned towards E with a dip of 42° and a second one towards S with a dip of 62°. The misfit is 1.17 respective 1.47 m. The cluster with the smaller misfit includes all seismic events occurring between frac cycle and to the end of the refrac cycle RF2 (inclusive bleed-off). The seismic events occurring between the end of RF2 and the end of the experiment show a big misfit, with many events occurring during the shut-in phase. The dip and dip direction of HF3 become more comparable with test HF2 and HF8. This was done due to the fact that two different fracture systems associated with the zone S3 show the same orientation than the two plane fits from test HF3. Both fracture systems together are able to effectively drain the fracture fluid towards the AU tunnel. The few seismic events occurring during HF5, show similar orientation for the ATV trace and the seismic cluster with a small misfit of 0.18 m.

Table A.5 Trace description form geophysical borehole logging incl. trace fit and plane fit through located micro-seismic events. HF1-HF8 trace fit from ATV geophysical borehole logging; MF1-MF3 and MF8-MF11 trace fit from optical teleview logging and impression packer (Klee, 2015) and seismic plane fit (Gischig et al., 2018; Näf, 2017). ^{a,b} two clusters were observed

Experiment	**Borehole**	**Trace description**	**Trace fit** xxx/xx°	**Plane fit** xxx/xx°
HF1	INJ1	axial trace hits pre-existing fracture; 39.5 - 41.0 m	359/71° @ 40.55 m	NA
HF2	INJ1	steeply inclined incomplete axial trace; 35.8 - 37.1 m	049/89° @ 35.44 m 022/69° @ 36.21 m	029/83°^{a} 175/46°^{a}
HF3	INJ1	steeply inclined axial trace; 20.1 - 21.1 m	205/88° @ 20.72 m 031/82° @ 21.08 m	067/46°^{b} 156/49°^{b}
HF5	INJ1	axial singel trace; 13.8 - 15.6 m	029/79° @ 14.8 m	013/75°
HF6	INJ2	2 pre-existing axial traces between two fractures; 39.2 - 39.9 m	(021/59° @ 39.71 m)	-
HF8	INJ2	steeply inclined axial trace; 15.8 - 16.4 m	027/74° @ 16.01 m	179/69°
MF1	SBH3	steeply inclined fracter	139/71°	180/72°
MF2	SBH3	inclined fracture	143/71°	175/76°
MF3	SBH3	no fracture detected	-	178/69°
MF4	SBH4	-	-	185/73°
MF5	SBH4	-	-	001/65°
MF6	SBH4	-	-	162/64°
MF7	SBH4	-	-	185/73°
MF8	SBH1	steeply inclined sub-horizontal fracture	155/83° 161/81°	-
MF9	SBH1	axial single trace	200/82°	-
MF10	SBH1	axial single trace	209/81°	-
MF11	SBH1	steeply inclined fracture	173/79°	-

A.6 Experimental summary cards

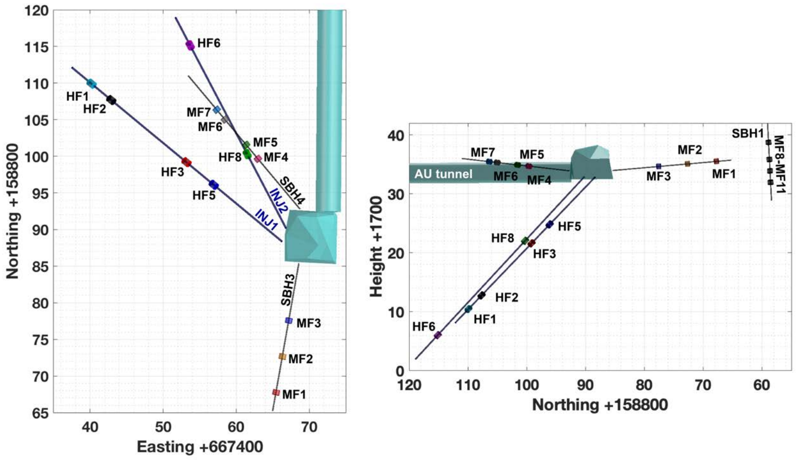

Fig. A.6 Overview of the injection interval locations for the experimental summary cards presented hereinafter.

Figure A.6 presents an overview of the injection interval locations for the HF tests and the minifracs (MF) from the stress characterization phase. The following figures present each test and summarize in short, the injection protocol inclusive flow rate and injection pressure, the seismic location in map and profile view over different frac /refrac cycles. In addition, the radial distance from the injection point (inclusive amplitude magnitude for the minifracs) and fluid injection and fluid backflow volume are presented.

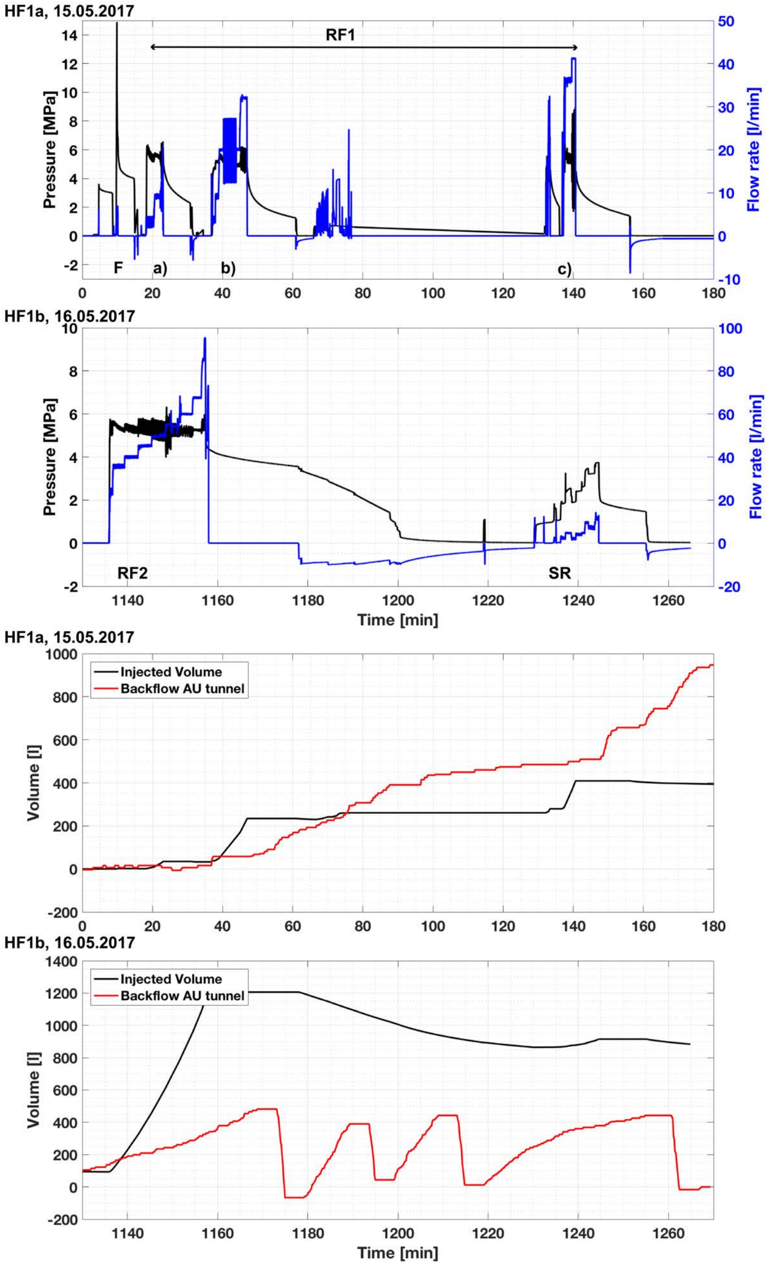

Fig. A.7 a) Injection pressure [MPa] and flow rate [l/min] for HF1a executed at the 15.05.2017 and HF1b at the 16.05.2017. The test HF1a was stopped due to water supply problems. The new supply pump arrived the day later and was able to give flow rates of up to 90 l/min. The injected volume corresponds to the trapezoidal integration of the flow rate incl. negative flow. The backflow from the AU tunnel is indirect measured by pressure sensor and should not be used for this test as additional water was added to the AU tunnel testing the pump and installing Gas-Equilibrium Membrane Inlet Mass Spectrometry on the seepage zone of the S3 shear zone in the AU tunnel.

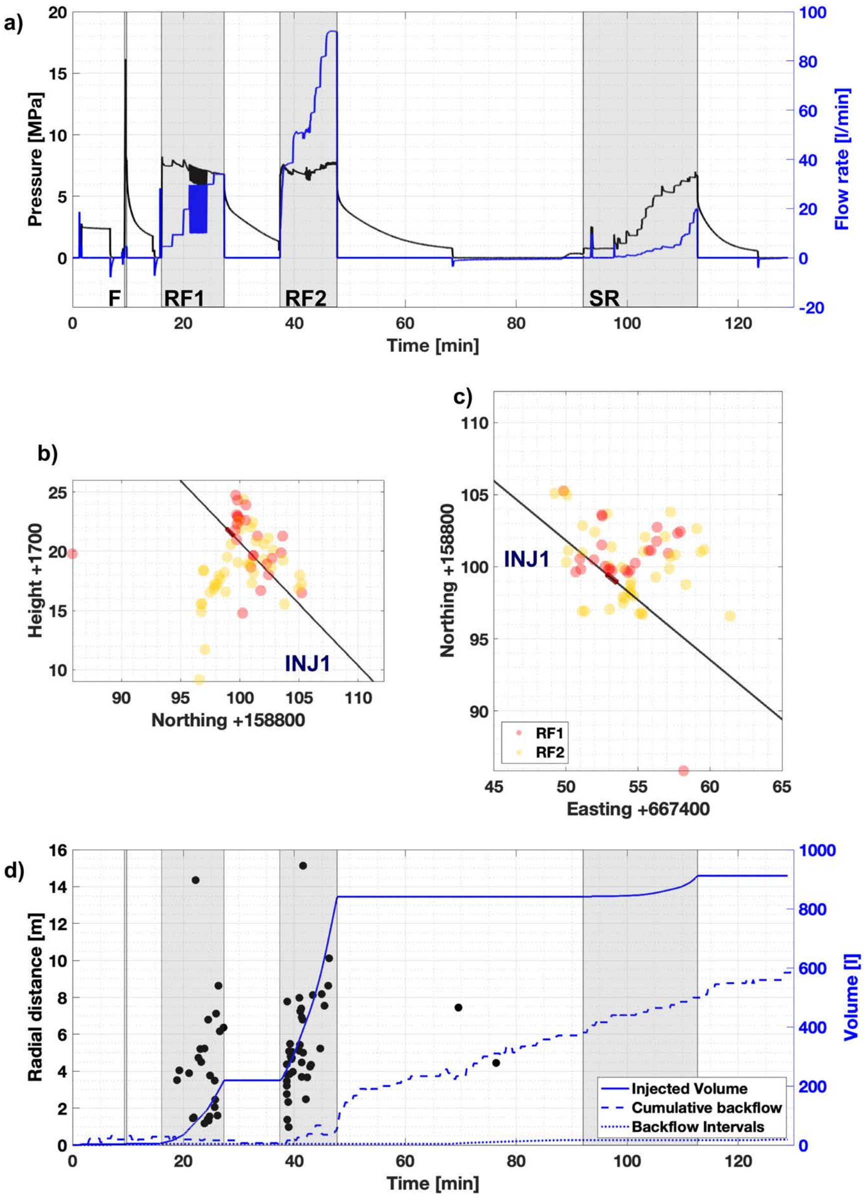

Fig. A.8 a) Injection pressure [MPa] and flow rate [l/min] are indicated for HF3 with gray shaded boxes during fluid injection. The overview of the located seismic events is presented in plane (b) and profile view (c). The red cylinder corresponds to the injection interval and the located seismic events are differently colored depending on the injection stage. d) The radial distance from the injection interval to the seismic event is presented and the magnitude is indicated by color code. The cumulative injection volume and the cumulative backflow are presented by blue solid respective dashed line. All seismic events taking place during fluid injection.

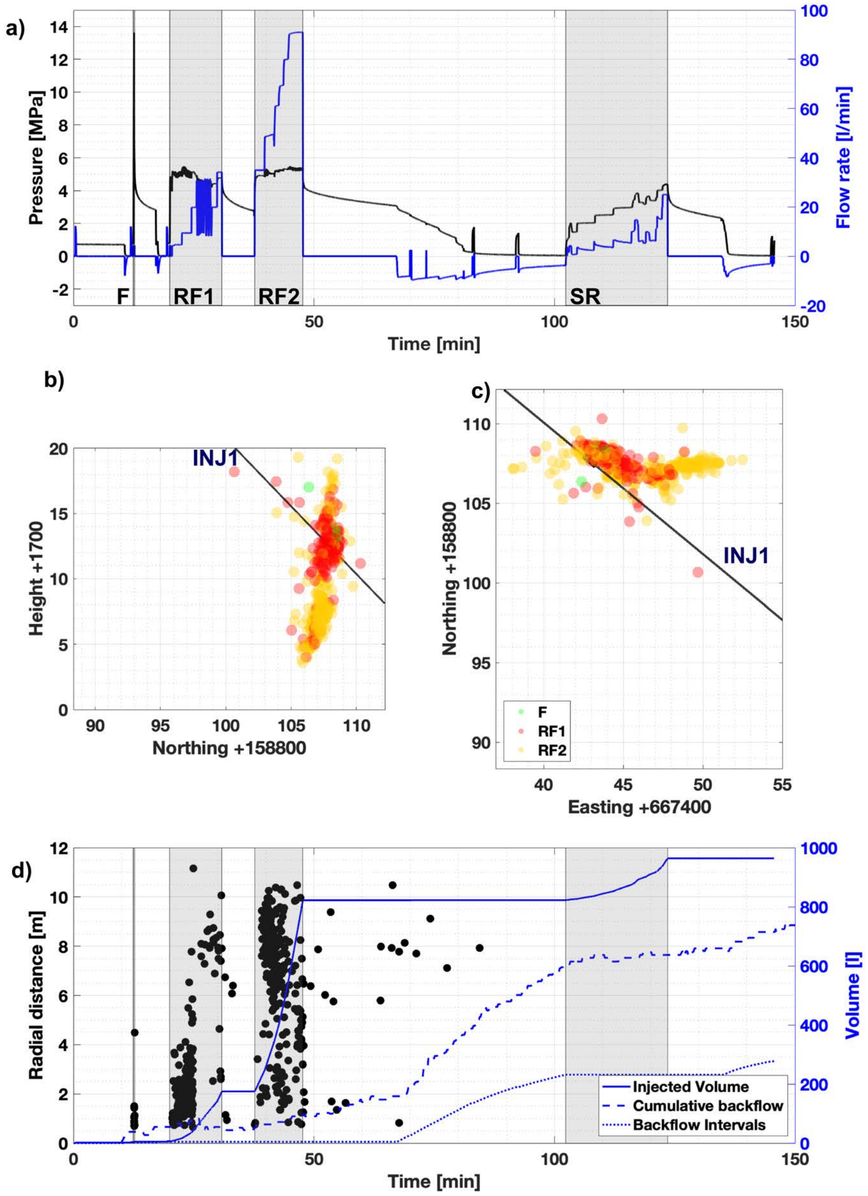

Fig. A.9 a) Injection pressure [MPa] and flow rate [l/min] are indicated for HF2 with gray shaded boxes during fluid injection. The overview of the located seismic events is presented in plane (b) and profile view (c). The black cylinder corresponds to the injection interval and the located seismic events are differently colored depending on the injection stage. d) The radial distance from the injection interval to the seismic event is presented and the magnitude is indicated by color code. The cumulative injection volume and the cumulative backflow are presented by blue solid respective dashed line. Most seismic events taking place during fluid injection.

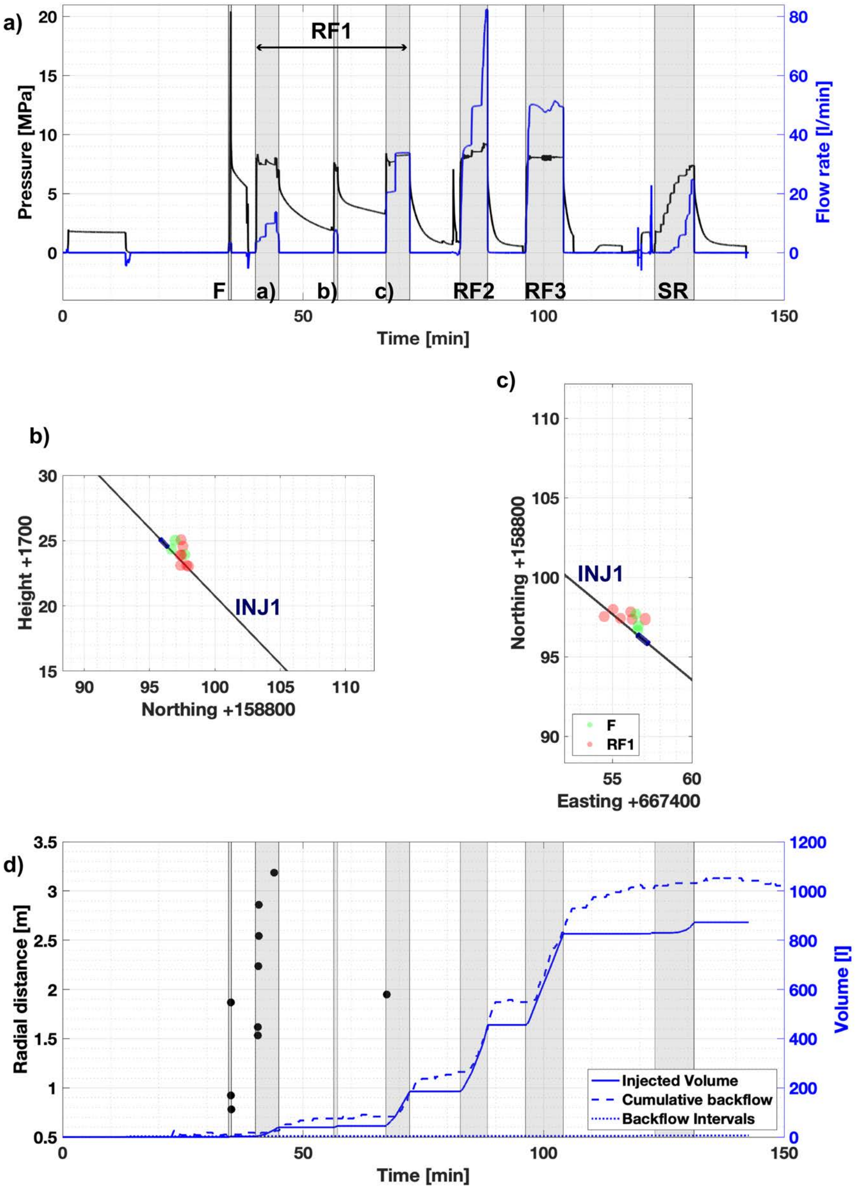

Fig. A.10 a) Injection pressure [MPa] and flow rate [l/min] are indicated for HF5 with gray shaded boxes during fluid injection. The protocol differs due to a short-cut to one of the geophysical boreholes. The overview of the located seismic events is presented in plane (b) and 3D view (c). The blue cylinder corresponds to the injection interval and the located seismic events are differently colored depending on the injection stage. d) The radial distance from the injection interval to the seismic event is presented and the magnitude is indicated by color code. The cumulative injection volume and the cumulative backflow are presented by blue solid respective dashed line. Only a few seismic events were located during this experiment. As one of the geophysical boreholes was hit during the first propagation cycle, the outflow through the borehole increased the noise at the seismic sensors placed in the borehole.

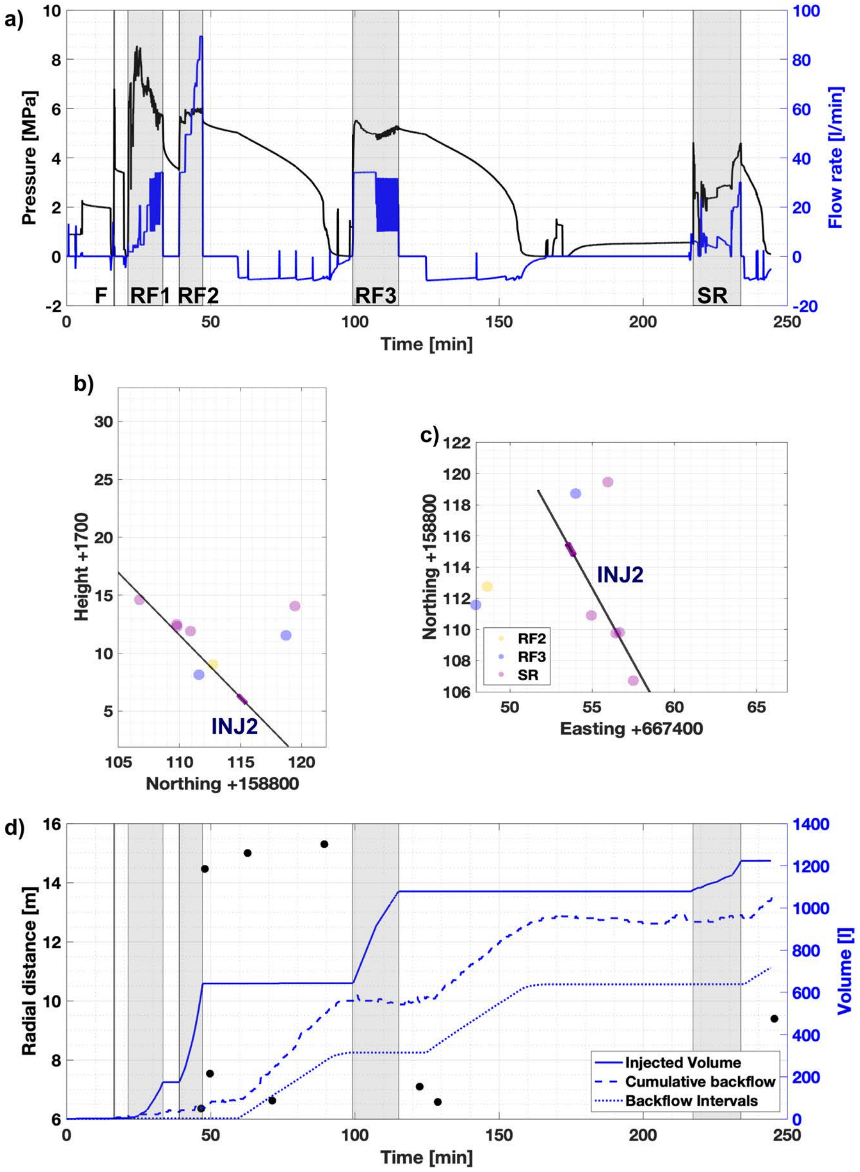

Fig. A.11 a) Injection pressure [MPa] and flow rate [l/min] are indicated for HF6 with gray shaded boxes during fluid injection. This experiment was mistakenly stimulated at the wrong position with a pre-existing fracture, which directly is correlated with a small break down pressure. The overview of the located seismic events is presented in plane (b) and profile view (c). The violet cylinder corresponds to the injection interval and the located seismic events are differently colored depending on the injection stage. Most of the seismic takes place along the PRP2 borehole. d) The radial distance from the injection interval to the seismic event is presented and the magnitude is indicated by color code. The cumulative injection volume and the cumulative backflow are presented by blue solid respective dashed line. Only a few seismic events were located during this experiment. During this experiment larger magnitudes are observed. In addition, most of seismic took place during shut-in and bleed-off.

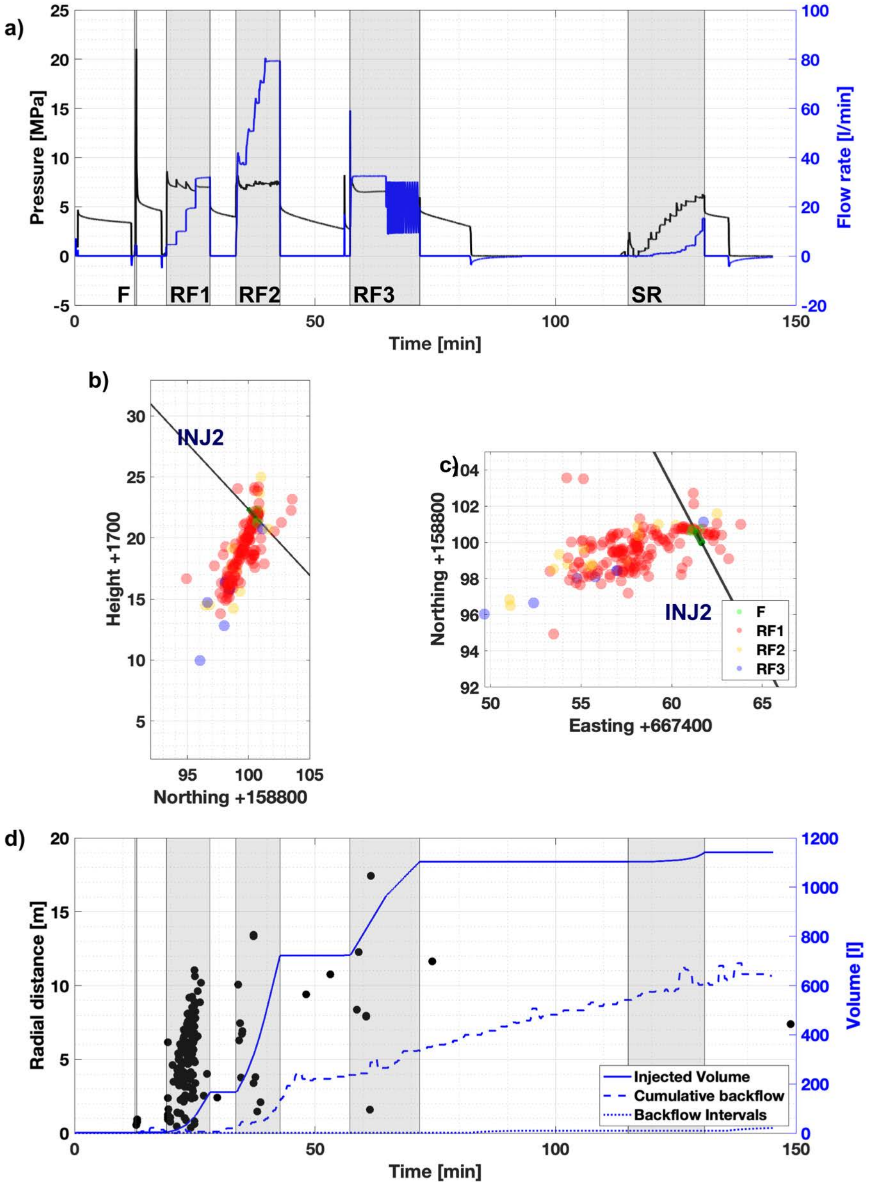

Fig. A.12 a) Injection pressure [MPa] and flow rate [l/min] are indicated for HF8 with gray shaded boxes during fluid injection. The overview of the located seismic events is presented in plane (b) and profile view (c). The green cylinder corresponds to the injection interval and the located seismic events are differently colored depending on the injection stage. d) The radial distance from the injection interval to the seismic event is presented and the magnitude is indicated by color code. The cumulative injection volume and the cumulative backflow are presented by blue solid respective dashed line. Most of the seismic took place during the first fracture propagation cycle.

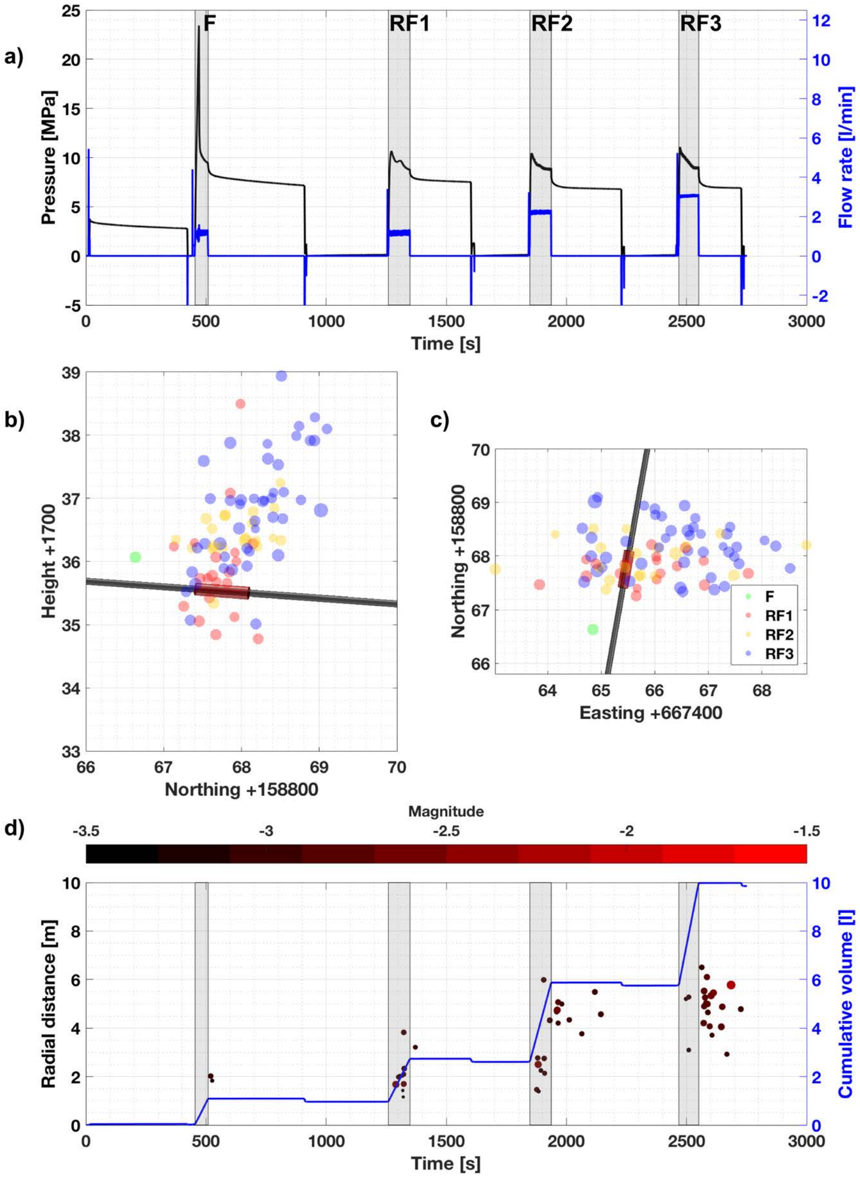

Fig. A.13 a) Injection pressure [MPa] and flow rate [l/min] are indicated for MF1 with gray shaded boxes during fluid injection. The overview of the located seismic events is presented in plane (b) and profile view (c). d) The radial distance from the injection interval to the seismic event is presented and the magnitude is indicated by color code. The cumulative injection volume is presented by blue solid line.

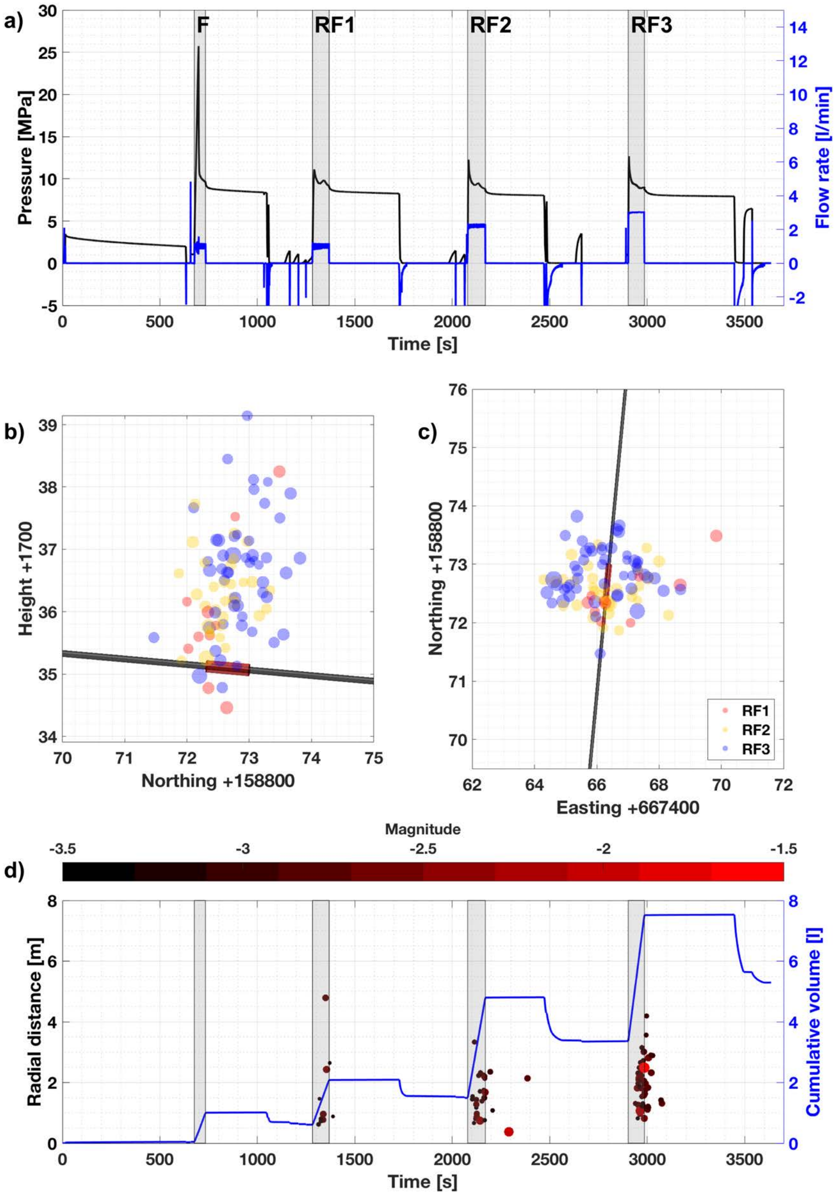

Fig. A.14 a) Injection pressure [MPa] and flow rate [l/min] are indicated for MF2 with gray shaded boxes during fluid injection. The overview of the located seismic events is presented in plane (b) and profile view (c). d) The radial distance from the injection interval to the seismic event is presented and the magnitude is indicated by color code. The cumulative injection volume is presented by blue solid line.

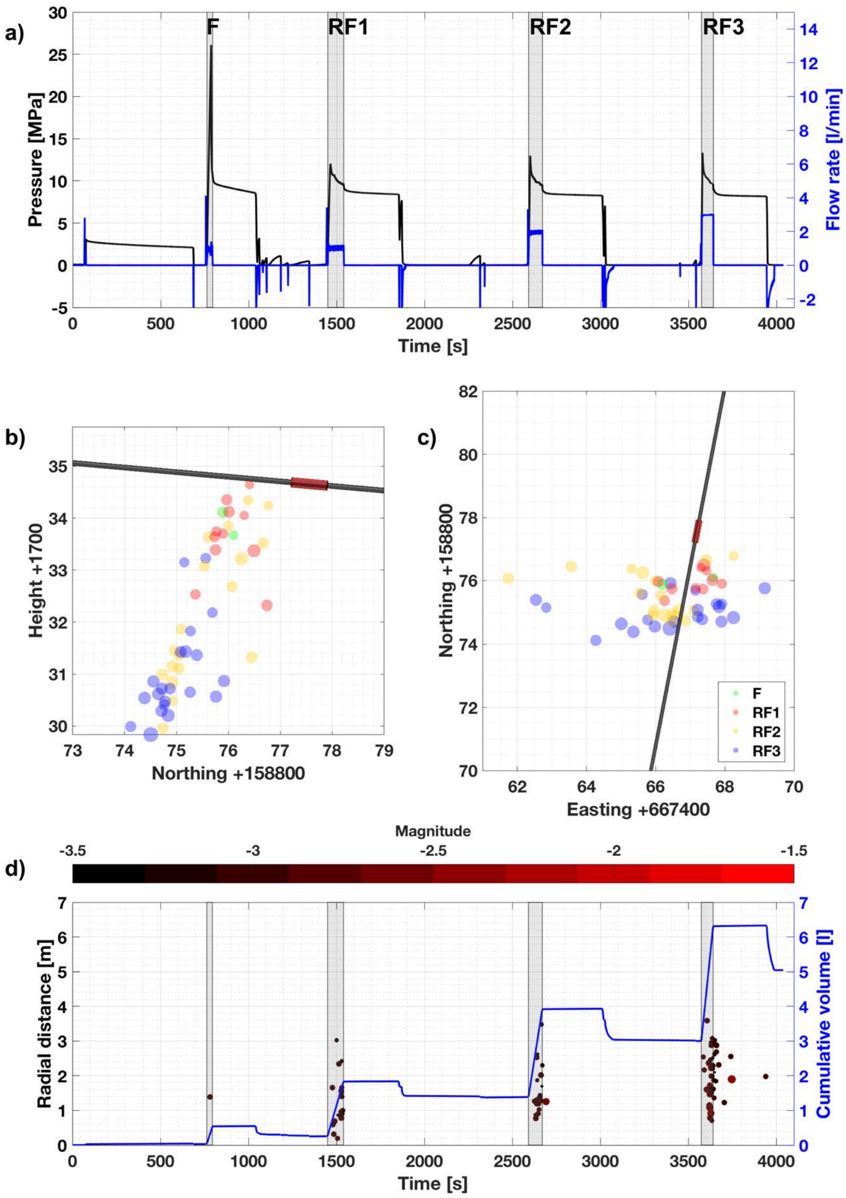

Fig. A.15 a) Injection pressure [MPa] and flow rate [l/min] are indicated for MF3 with gray shaded boxes during fluid injection. The overview of the located seismic events is presented in plane (b) and profile view (c). d) The radial distance from the injection interval to the seismic event is presented and the magnitude is indicated by color code. The cumulative injection volume is presented by blue solid line.

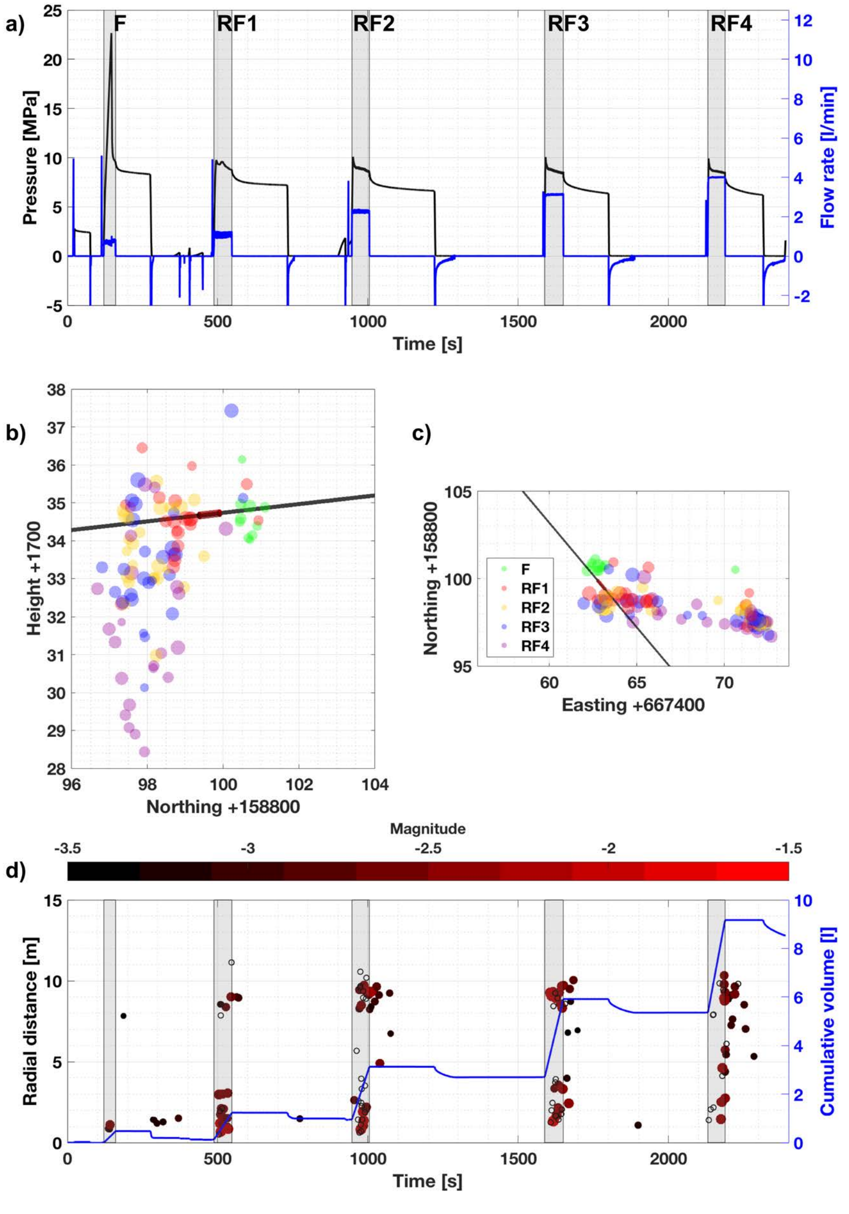

Fig. A.16 a) Injection pressure [MPa] and flow rate [l/min] are indicated for MF4 with gray shaded boxes during fluid injection. The overview of the located seismic events is presented in plane (b) and profile view (c). d) The radial distance from the injection interval to the seismic event is presented and the magnitude is indicated by color code. The cumulative injection volume is presented by blue solid line.

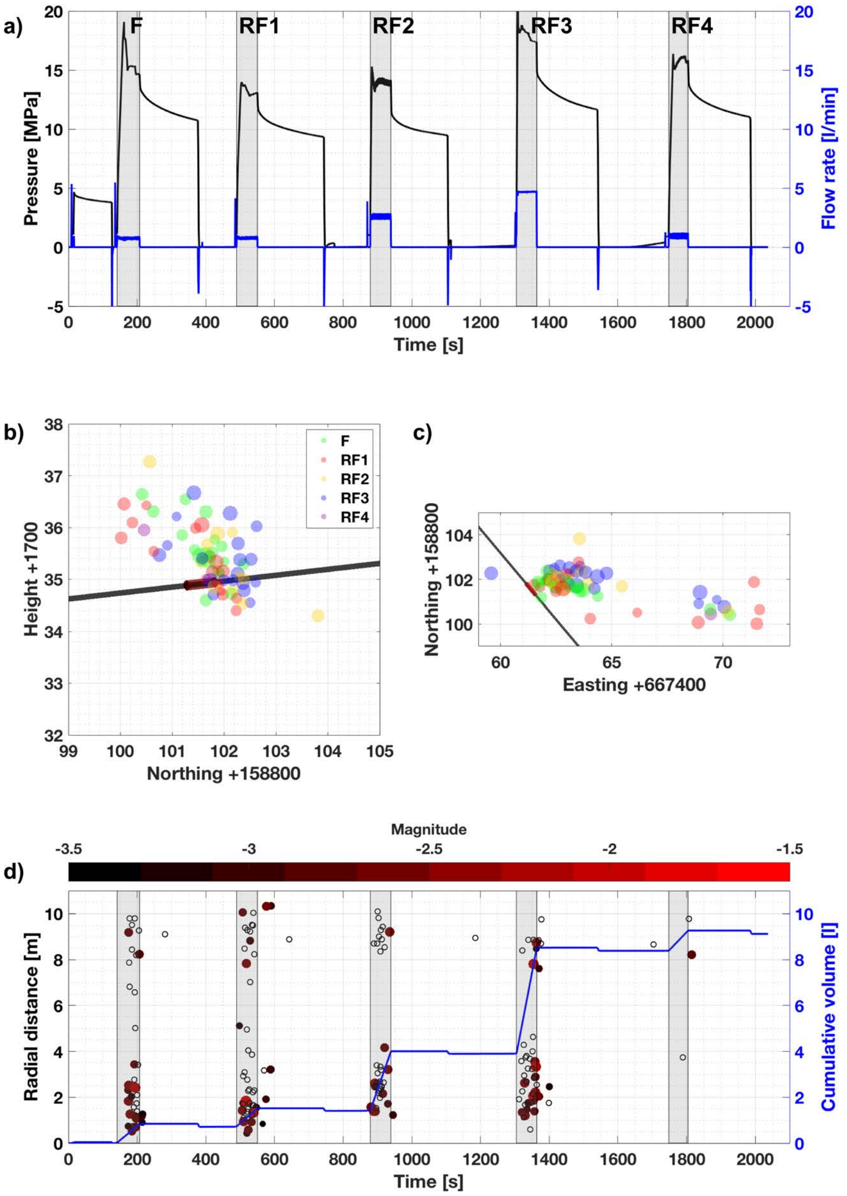

Fig. A.17 a) Injection pressure [MPa] and flow rate [l/min] are indicated for MF5 with gray shaded boxes during fluid injection. The overview of the located seismic events is presented in plane (b) and profile view (c). d) The radial distance from the injection interval to the seismic event is presented and the magnitude is indicated by color code. The cumulative injection volume is presented by blue solid line.

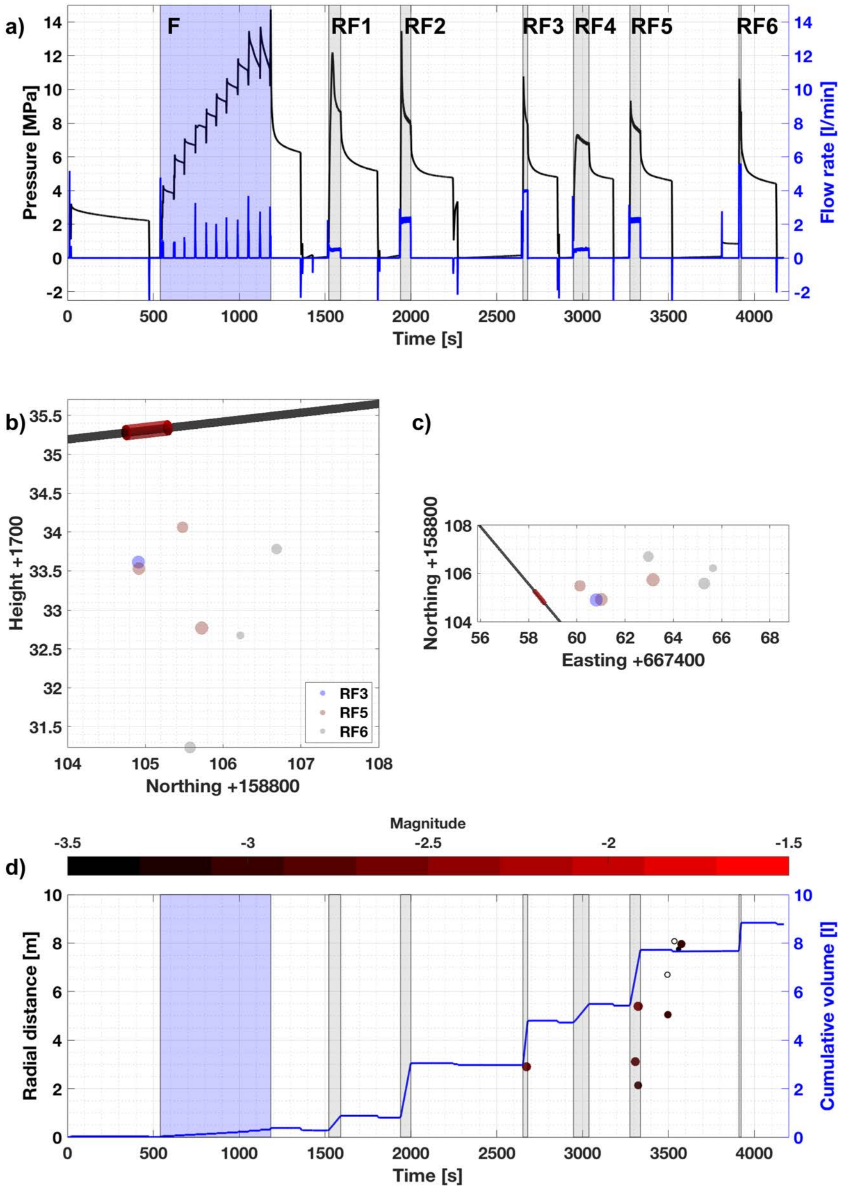

Fig. A.18 a) Injection pressure [MPa] and flow rate [l/min] are indicated for MF6 with blue shaded box during fluid pulse injection and gray shaded boxes for constant fluid injection. The overview of the located seismic events is presented in plane (b) and profile view (c). d) The radial distance from the injection interval to the seismic event is presented and the magnitude is indicated by color code. The cumulative injection volume is presented by blue solid line.

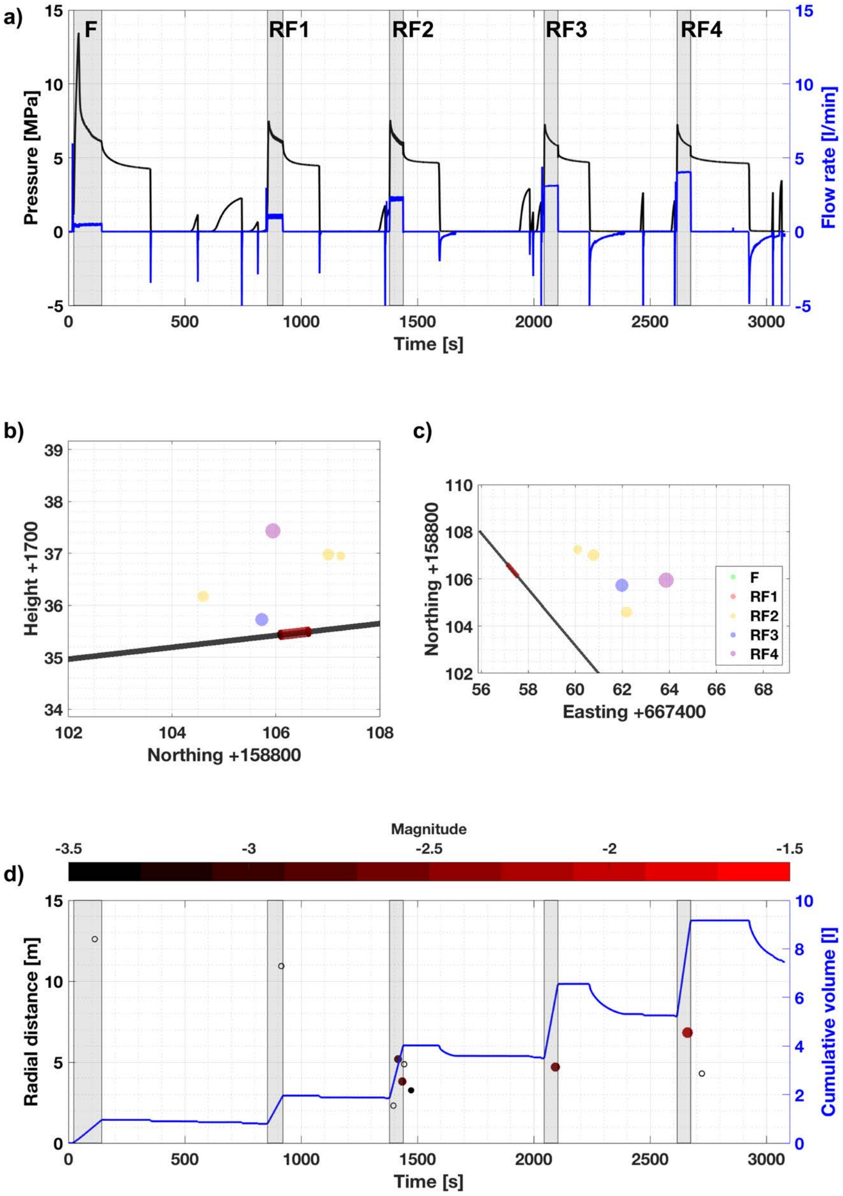

Fig. A.19 a) Injection pressure [MPa] and flow rate [l/min] are indicated for MF7 with gray shaded boxes during fluid injection. The overview of the located seismic events is presented in plane (b) and profile view (c). d) The radial distance from the injection interval to the seismic event is presented and the magnitude is indicated by color code. The cumulative injection volume is presented by blue solid line.

Appendix B

Observations of fracture propagation during decameter-scale hydraulic fracturing experiments

Please cite this section as: Dutler, N. O., Valley, B., Gischig, V., Jalali, MR., Doetsch, J., Krietsch, H., Villiger, L., Amann, F., Observations of fracture propagation during decameter-scale hydraulic fracturing experiments, American rock mechanics association (2018), 18-0256, Seattle.

Abstract

Various in-situ hydraulic fracturing experiments were carried out in the naturally fractured, crystalline rock mass of the Grimsel Test Site (GTS) in Switzerland. The purpose was to study the geometry of the newly created fractures and their interaction with the pre-existing fracture network using transient pressure and rock mass deformation observations. Under controlled conditions, six hydraulic fractures with similar injection protocols were executed in two sub-vertical injection boreholes. The rock mass is intersected by two E-W striking shear zones (S3), and two biotite-rich meta-basic dykes with a densely fractured zone in between. The S3 shear-zone intersecting the rock volume of interest acts as a high-permeability connection to the tunnel for the experiments executed south of it. Strong variation in injectivity enhancement, jacking pressure, break down pressure, instantaneous shut-in pressure and fluid flow recovery among the different injection intervals indicate different stress conditions north and south of S3.

B.1 Introduction

The main requirement for extracting energy from the subsurface is sufficient fluid flow through permeable pathways to transport heat or oil/gas from the underground to a production well. The crustal permeability decreases with depth (Manning and Ingebritsen, 1999; Rutqvist and Stephansson, 2003), which influences the productivity in a negative manner. Thus, the permeability in deep target reservoirs has to be enhanced through hydraulic stimulation. Only by enhancing the permeability of the underground, sufficient conductivity and connectivity are achieved. Geothermal projects utilizing permeability enhancement techniques are referred as enhanced geothermal systems (EGS) (Cummings and Morris, 1979). Two main processes are typically invoked during permeability enhancement: 1) hydraulic fracturing and 2) hydraulic shearing. Hydraulic fracturing is the initiation and propagation of tensile (mode I) fractures. It occurs when tensile stress exceeds tensile strength and the energy, which is required to create new surfaces in the rock exceeds fracture toughness (Detournay, 2016). When the stimulation operation is completed, the newly formed hydraulic fractures keep a residual aperture resulting in permeability enhancement (Jalali et al., 2018a). Hydraulic shearing is associated with the shear reactivation along a pre-existing discontinuity in direction of maximum in-situ shear stress on the fracture plane (Gischig and Preisig, 2015; Pine and Batchelor, 1984). Associated with fracture slip, shear dilation increases the permeability of natural fractures. This process is referred as the self-propping mechanism and is assumed to be permanent (McClure and Horne, 2014). Although these concepts are conceptually and theoretically well understood, their interactions and relative importance during hydraulic stimulation are debated. Our limitations in quantifying their respective effects prevent our ability to anticipate rock mass response to hydraulic stimulation and thus to propose a rational for hydraulic stimulation design. In addition, the quantitative relationships between these stimulation mechanisms and induced seismicity are currently poorly understood, posing a risk management issue for hydraulic stimulation operations (Eaton and Igonin, 2018). Data sets obtained from full-scale field stimulation operations (Evans et al., 2012; McClure and Horne, 2014) provide valuable information, but limited access to the reservoir volume prevents conclusive assessments of the detailed rock mass response. This motivates the execution of well-controlled in-situ hydraulic fracturing experiments with extensive access to the experimental volume. Only a few of such experiments were performed so far and they provided invaluable insights into the details of rock mass response to hydraulic injections. The mine back experiment at the Nevada test site showed complex fractures shapes due to pressure and fluid distribution (Warpinski, 1985). At Northpark mine, fracture growth in naturally fractured rock was studied. The fracture geometries were studied from microseismcity and tilt data and were mapped after backmining (Jeffrey et al., 2009). The results obtained in these studies illustrated the dominant control of 1) the stress state on the overall geometry of stimulated volume and 2) the pre-existing fracture network on the development of flow path. An experiment was carried out in 2015 at the Aspö hard rock laboratory (López-Comino et al., 2017; Zang et al., 2017) to test alternative water injection schemes (continuous, progressively increasing and cyclic pressurization) in crystalline rock with various monitoring systems. These experiments showed that site specific conditions (e.g., rock type, natural fracturing, stress state, etc.) have a major influence on the rock mass response. This motivated us to perform the In-Situ Stimulation and Circulation experiment (ISC-experiment). This decameter-scale experiment aimed to investigate in great detail rock mass responses (i.e., during both hydroshearing and hydrofracturing), as well as fluid circulation in moderately fractured granitic rocks. We performed this experiment at the Grimsel Test Site (GTS), Switzerland. The granitic rock mass in the GTS is a suitable analogue of the crystalline basement in the Alpine foreland basin and can act as a proxy for potential future EGS sites (Amann et al., 2018). A detailed rock mass characterization, including geological, hydrological and geophysical prospecting of the experimental rock volume took place prior to stimulation. The main experiment consisted of six hydraulic shearing and six hydraulic fracturing experiments. Six hydraulic fracturing (HF) experiments were conducted to study 1) the geometry of new created fractures, 2) their interaction with the natural fracture system, 3) the response of the rock mass at different injection locations and 4) the influence of different injection metrics (e.g. fluid viscosity). HF can propagate in different propagation regimes (i.e. toughness or viscosity dominated) (Savitski and Detournay, 2002), whereby the goal was to achieve similar behavior than for high rate stimulation in EGS projects. During the tests we used water and a rheology modifier to achieve viscosity dominated propagation regime. The latter one consists of xanthan-salt-water (XSW) and has a 35 times higher viscosity than water. Several monitoring systems were installed to study transient pressure propagation, deformation within the rock mass and along shear zones at high spatial and temporal resolution and seismic activities. We present in this paper some preliminary results of our hydro-mechanical data. We focus on the comparison of some characteristic parameters (i.e. injectivity enhancement ratio, jacking pressure and fluid recovery) of each hydraulic fracture and we show distinct fracture propagation behaviors within our experimental volume.

B.2 Geological site description

The GTS is located in the Central Swiss Alps, around 480 m below ground level. The ISC test volume is located in the southern part of the test site (Fig. B.1A). The ISC experimental volume is situated slightly south of the boundary between Central Aare Granite (towards north) and Grimsel Granodiorite (towards south). The moderately fractured rock mass is

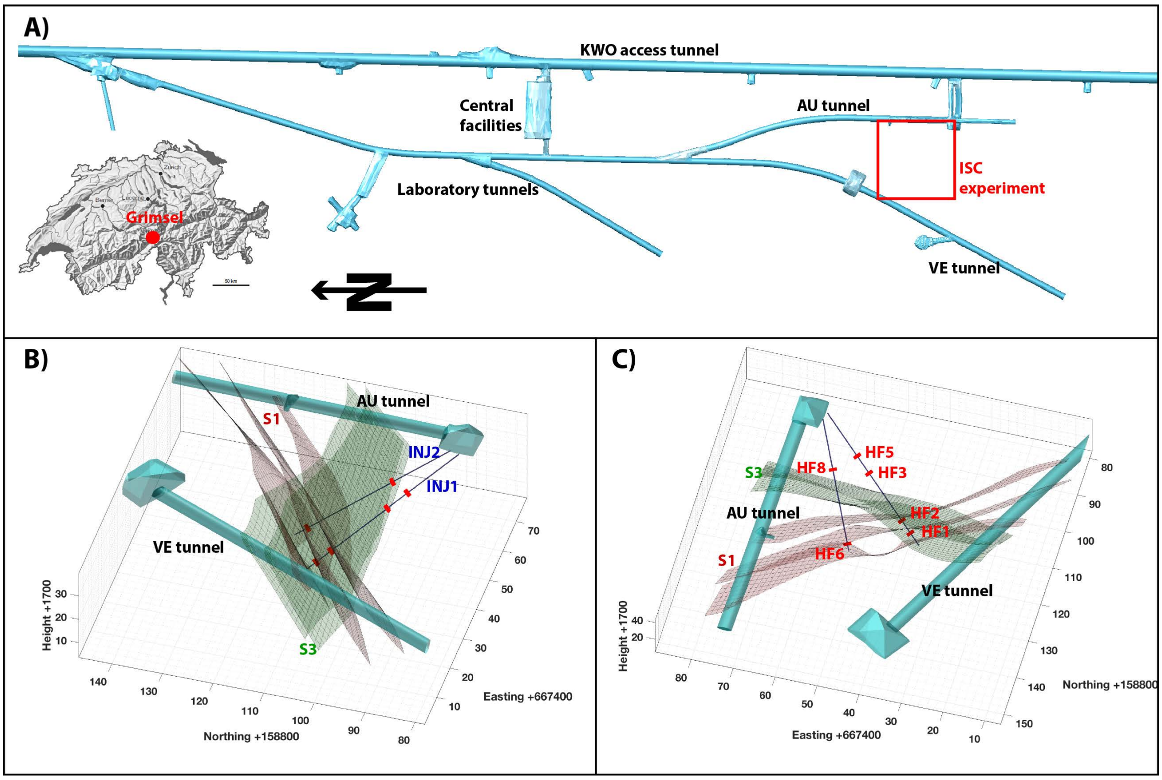

Fig. B.1 A) Map view of the GTS facilities with the ISC experiment located at the southern part of the GTS between AU and VE tunnels. B) The ISC experiment is intersected by two sets of major features S1 and S3 shear-zone. The two injection boreholes INJ1 and INJ2 are shown, too. C) View showing the position of the six hydraulic fracturing tests performed. Coordinates on figure B) and C) are given in Swiss metric coordinate system (CH1903).

crosscut by five subvertical ductile and brittle-ductile shear-zones. The first set (referred to as: S1.1, S1.2 and S1.3) included three ductile shear zones that were characterized by a strong increase in the degree of foliation and mylonitization. All three shear zones had an ENE-WSW strike and dip towards SE. The second set (referred to as S3.1 and S3.2) contained two brittle-ductile shear zones. The S3 brittle-ductile shear-zones consists of a densely fractured zone (>20 fractures per meter) in between two biotite-rich meta-basic dykes. The fracture frequency in the INJ boreholes is 0-3 fractures per meter, with higher frequency towards the shear zones. Optical televiewer logging in INJ1 and INJ2 indicated a preferred fracture orientation striking E-W along the main structural features (S1: red triangles; S3: green diamonds) (Krietsch et al., 2018) (Fig. B.2).

During the pre-stimulation phase, the in-situ local stress field was measured by overcoring methods (i.e. USBM and CSIRO-HI probes) and hydraulic fracturing. Impression packers and microseismic monitoring were used to map hydraulic fracture orientation which revealed consistent E-W, subvertical fracture extension. The unperturbed stress field has a

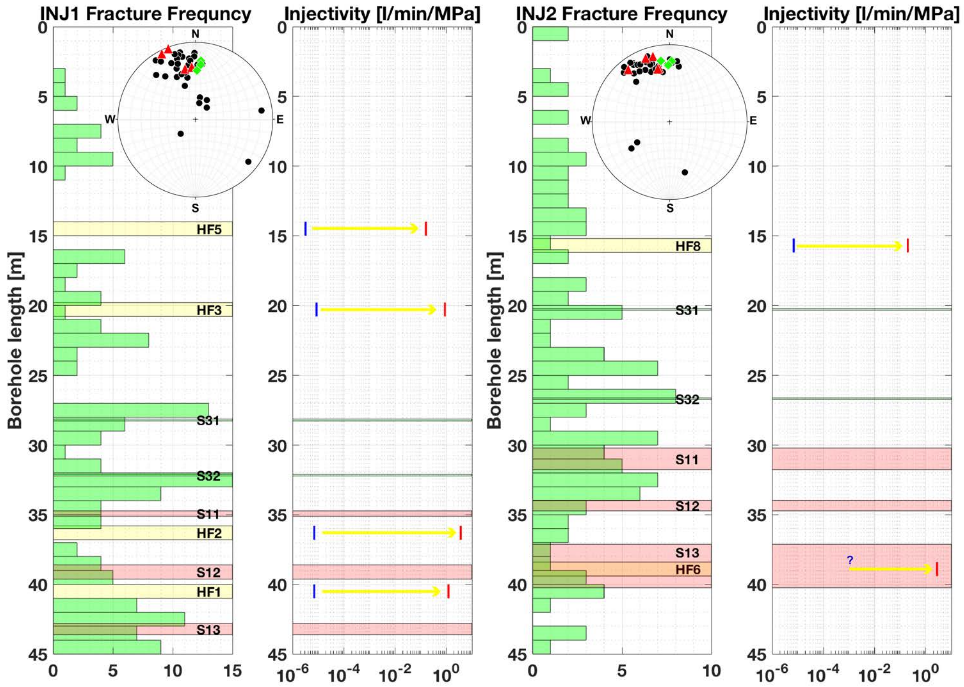

Fig. B.2 Fracture frequency incl. lower hemisphere equal-angle stereonet and injectivity for INJ1 and INJ2 borehole. The location of the shearzone S1 and S3 is shown with red respectively green bands and the polepoints are presented by red triangles respectively green diamonds in the stereonet. The yellow bands indicate the position of the hydraulic fractures. The value of the injectivity is indicated before (blue) and after (red) each HF.

minimal principal stress magnitude of 8.6-9.7 MPa and is sub-horizontal N-S oriented. The major principal stress magnitude ranges between 13.1 – 14.4 MPa and plunges with 30 to 40° to the East. The intermediate stress component ranges from 9.2 to 10.2 MPa. The S3 shear zone perturbs the stress field as the minimal stress component decline towards S3 to 3 MPa (Krietsch et al., 2019).

B.3 Hydraulic fracturing

From optical televiewer (OPTV) borehole logging intact intervals were identified for the HF locations in the two injection boreholes INJ1 and INJ2 (Fig. B.1C). HF3, HF5, and HF8 were located south of the S3 shear-zones and HF1, HF2, and HF6 were located north of S3 shear-zones. The initial transmissivity was measured by two pulse tests and ranged between $1.4 - 3.8 \cdot 10^{-13}$ m^2/s for all HF intervals. The initial injectivity was estimated from the transmissivity using the steady-state radial flow equation. An injectivity value of 1 (l/min)/MPa corresponds to the transmissivity of $4.42 \cdot 10^{-8}\ m^2/s$ for a wellbore of 0.07 m and a radius of influence of 0.4 m. The initial injectivity of the intact intervals ranged from $3.2 \cdot 10^{-6}$ to $8.6 \cdot 10^{-6}$ l/min/MPa. All HF experiments took place in intact rock without any fractures in the stimulated interval except HF6, which was accidentally stimulated three meters further down in the injection borehole at an interval with a pre-existing fracture.

B.3.1 HF procedure

The HF interval was packed off using a hydraulic double-packer system with a base length of 1 m to pressurize the interval with an injection pressure up to 30 MPa. Two different pumps were used to deliver a flow rate up to 100 l/min at a maximal pressure of 10 MPa and a pressure up to 30 MPa at a flow rate up to 35 l/min. A second double-packer system was installed to monitor the pore pressure response in a monitoring interval in the second injection borehole that was not used for active stimulation. Pore pressure was also monitored in the intervals beneath the injection and monitoring intervals. The injected fluid and the flow-back were measured with flowmeters. Once installed, all the packer intervals were saturated with water. To test the interval integrity and proper packer sealing a pulse test was performed (compare Fig. B.3). The actual hydraulic fracturing test started with a controlled rate fluid injection with a rate of approximately 5 l/min for half a minute to initiate a hydraulic fracture. The fracture propagation cycle had the aim to propagate the hydraulic fracture. This propagation cycle was executed in two cycles (C1 and C2) between which the pump was changed and reached a maximum flow rate of 100 l/min. For the tests during which xanthan-salt-water (XSW) was injected, a flushing cycle (C3) was added afterwards. The last cycle was a pressure-controlled cycle (C4) to evaluate the post-stimulation transmissivity of the created hydraulic fracture and to estimate the stress acting normal to the hydraulic fracture (jacking pressure). Figure 3 shows flow-rate versus injection pressure for the HF3 experiment during different injection cycles. The pressure was read at steady-state flow. During C2 the flow rate exceeds a maximum pressure of 6.8 MPa below 52 l/min. Above 52 l/min, the flow rate was ramped up faster as a consequence the pressure raised, instead keeping it at 6.8 MPa. Final injectivity and jacking pressure were measured during step-pressure cycle (C4). The final injectivity was extracted from the slope of the linear fit through the first six flow rate vs. pressure data points. The linear fit to the last three data points and solving the equation for y=0 gives the jacking pressure.

B.3.2 Variations along INJ1 and INJ2

The comparison of the injectivity increase, jacking pressure and injection recovery for the different tests (see Fig. B.4) indicate similar results for tests deep respectively shallow in the boreholes. The jacking pressure decreases and fluid recovery in the injection interval

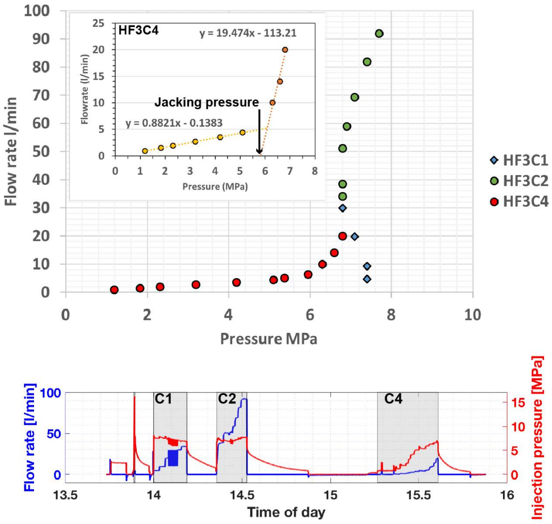

Fig. B.3 Flow-rate vs. pressure plot for HF3 experiment divided by fracture propagation cycle 1 (C1) and 2 (C2) and pressure step rate test (C4). The final injectivity and jacking pressure was taken from the pressure step rate cycle.

increases from the south (shallow borehole depth) to the north (near borehole end). It is noteworthy that the injectivity increase is highest for HF1 and HF2, which are located north of the S3 zone. Highest injectivity after stimulation was measured for HF2 and HF6 with 3.69 resp. 2.77 l/min/MPa. HF3 and HF8 showed similar jacking pressure and injection recovery, but different injectivity enhancement ratio. As there was no back-flow in the injection interval, the fracture near the borehole wall closed directly after shut-in. Note that the injection fluid for HF3 was water, whereas it was XSW for HF8. During these two tests, the fracture was drained to the AU-tunnel via zone S3.1, which consists to the southern boundary of S3 and at the end of propagation cycle 2 the fracture connected to the geophysical boreholes. HF5 behaved differently as we hit one of the seismic observation boreholes during the first propagation cycle.

The induced seismicity during hydraulic fracturing experiments was monitored with a dense monitoring network of highly sensitive sensors. The network consisted of 24 piezo-sensors and 6 accelerometers, which were connected to a 32-channel acquisition system with a sampling frequency of 200 kHz. The analysis of seismic data is still in progress and only preliminary results are presented. An initial seismic event count was established by detecting events with a recursive STA/LTA method. The number of recorded events (Fig. B.4) does not show a systematic pattern that depends on the injection below or above S3. The total number of recorded events for HF2, HF3 and HF5 range between 1969 and 2204. Only 94 respective 722 events were recorded for HF6 resp. HF8.

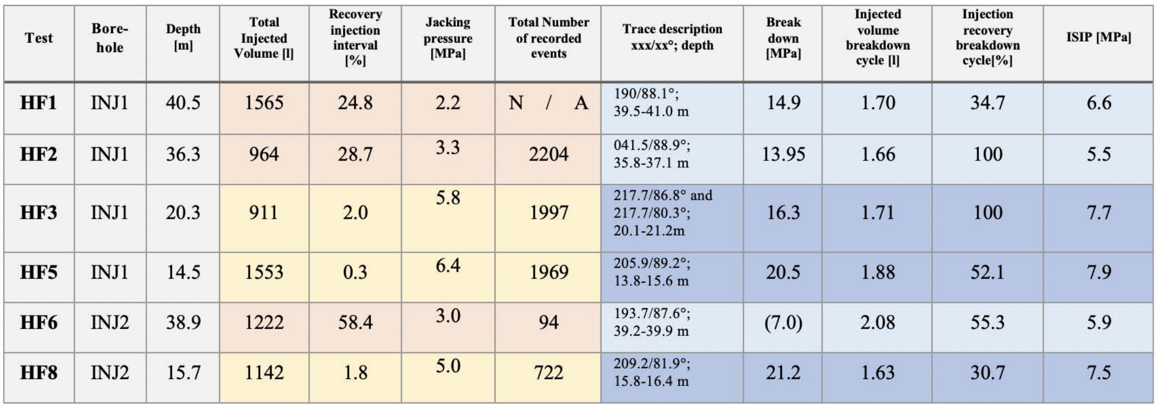

Test	Bore-hole	Depth [m]	Total Injected Volume [l]	Recovery injection interval [%]	Jacking pressure [MPa]	Total Number of recorded events	Trace description xxx/xx°; depth	Break down [MPa]	Injected volume breakdown cycle [l]	Injection recovery breakdown cycle[%]	ISIP [MPa]
HF1	INJ1	40.5	1565	24.8	2.2	N / A	190/88.1°; 39.5-41.0 m	14.9	1.70	34.7	6.6
HF2	INJ1	36.3	964	28.7	3.3	2204	041.5/88.9°; 35.8-37.1 m	13.95	1.66	100	5.5
HF3	INJ1	20.3	911	2.0	5.8	1997	217.7/86.8° and 217.7/80.3°; 20.1-21.2m	16.3	1.71	100	7.7
HF5	INJ1	14.5	1553	0.3	6.4	1969	205.9/89.2°; 13.8-15.6 m	20.5	1.88	52.1	7.9
HF6	INJ2	38.9	1222	58.4	3.0	94	193.7/87.6°; 39.2-39.9 m	(7.0)	2.08	55.3	5.9
HF8	INJ2	15.7	1142	1.8	5.0	722	209.2/81.9°; 15.8-16.4 m	21.2	1.63	30.7	7.5

Fig. B.4 Hydraulic and seismic characteristics of the 6 HF experiments with injection locations highlighted in red (north of S3) and yellow (south of S3) and break down characteristics highlighted in light blue (north of S3) and blue (south of S3).

B.3.3 Break down analysis

The break down pressure and the instantaneous shut-in pressure (ISIP) during breakdown cycle (Fig. B.4) range between 7.0 to 21.2 MPa respective between 5.5 to 7.9 MPa. The ISIP ranges between 7.5 and 7.9 MPa for HF locations south of S3 shear zones and decreased to 5.5 - 6.6 MPa toward the north. The behavior for the breakdown varied more in magnitude. Nevertheless, breakdown pressure north of S3 were smaller than 15 MPa and larger than 16 MPa south of S3. No real breakdown was observed during HF6 with a break down pressure of only 7.0 MPa. The total injected volume during breakdown cycle ranged between 1.63 and 2.78 l, with an injection recovery ranging between 30.7 to 100%. The full recovery during breakdown cycles can have two reasons. Either a natural, saturated fracture was hit during break down cycle or the saturation of the intervals or the tubing was inadequate.

The initialized fractures were identified along the borehole wall using acoustic televiewer (ATV) borehole logging. Most hydraulic fractures were initiated as axial fractures. A sinusoidal fit was used to estimate dip and dip direction. The fracture trace length ranged from 0.57 m to 1.8 m. The orientation of the new initiated hydraulic fractures are in good agreement i) with the observations from HF traces in SBH1 and ii) with the microseismic cloud. The normal point to the microseismic cloud corresponds to the minimal principal stress axis σ_3 at 005/15° (Gischig et al., 2018; Krietsch et al., 2017).

B.4 Fracture geometry

A comparison of the rock mass conditions and transient pressure response on HF2 (north of S3) and HF3 (south of S3) is done in the following, to study the geometry of the newly created fractures and the interaction of natural fractures. In total, 12 pressure observation intervals to observe pressure evolution and 60 fibre-Bragg grating (FBG) sensors with 1 m base length, high sampling rate (1 kHz) and high resolution (0.1 $\mu\varepsilon$) were installed to observe the rock mass deformation.

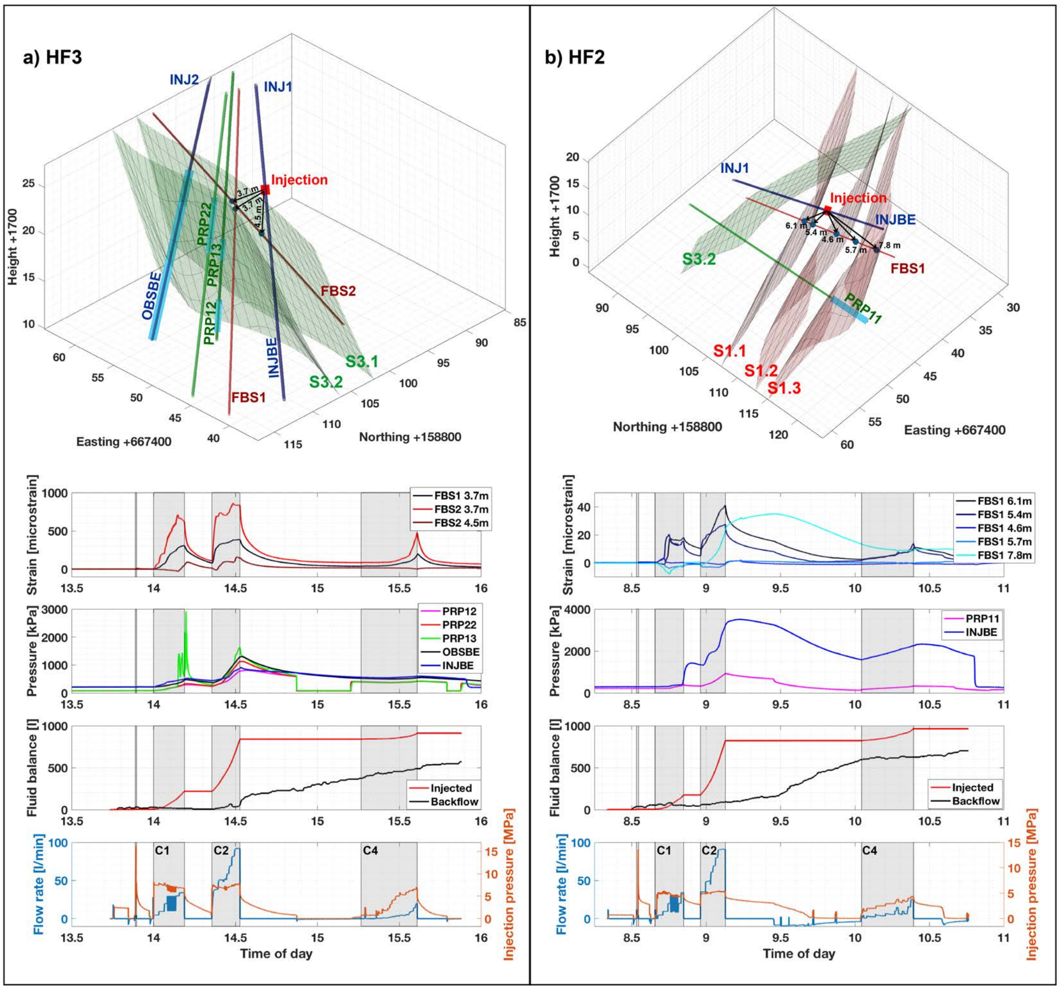

Fig. B.5 The comparison study between HF3 (south of S3) and HF2 (north of S2) compares most important rock mass response (strain plot), transient pressure propagation (pressure plot), fluid balance and flow rate (blue line) respective injection pressure (red line). The presented strain (tension is positive) and interval pressures respond positively to fluid injection (grey shaded areas). The 3D models include the boreholes with sensor/interval positions, injection point, and the major geological features.

B.4.1 HF3

The three FBG sensors presented in Fig. B.5a are positioned across pre-existing natural fractures. During break down cycle a small extensive strain response of approximately 5 was observed in the FBG sensor at a radial distance of 3.7 m in FBS2 to the injection point (Fig. B.5a, not visualized). The strain sensor at 3.7 m in FBS1 reached a magnitude of 300 $\mu\varepsilon$ and the sensor at 3.7 m in FBS2 a magnitude of 700 $\mu\varepsilon$ during the first propagation cycle. The sensor at 4.5 m started to show tension, where the sensor at 3.7 m (FBS2) indicated closing again. At the same time, the interval pressure in PRP13 showed strong variations. We interpret that these pressure oscillation are associated with an episodic stick-split mechanism as proposed by van Der Baan et al. (2016). Further analyses with the integration of the seismic data will give more insight into this response.

In the second propagation cycle (C2), the observed strain and pressure exceeded the values from the first propagation cycle. The pressure intervals shown in Fig. B.5a are known to be open flow path connections, as observed during the pre-characterization phase using conductivity logging (Jalali et al., 2018a). A direct connection exists between the pressure interval below injection (INJBE) and the pressure interval below observation (OBSBE). An increase in pressure was observed in interval PRP12, PRP13, and PRP22. This is either due to transient pressure response or direct flow path connection. The pressure observation during hydraulic fracturing indicated pressure increase in all of these intervals. We observed generally a short delay time, which is in agreement with the assumption of direct fluid flow, due to the hydraulic fractures. The interval react in the following order: PRP13, then PRP22 and OBSBE and finally PRP12 and INJBE. This is controlled by the flow path through the new created and connected fracture system and reflects pressure diffusion through this system. The small injection recovery of only 2.0% from the injection interval and the instantaneous pressure decay below jacking pressure after shut-in during propagation cycle 2 (C2) indicates that the injected fluid is not confined in the rock mass and found alternate escape way to the tunnels (zero pressure boundary) through the S3 shear zones. This also might explain the closing of the fracture near the injection borehole. In total, 840 l was injected until shut-in of C2. Before the shut-in of C2, 11% of total injection fluid was already drained toward the tunnel. This drained volume increased to 31% of total injected volume until bleed-off. We continued the HF protocol without waiting for full recovery. At the end of monitoring ($\sim$100 min after C2 shut-in), two third of the injected fluid had drained to the tunnel. This indicates that the densely fractured zone in S3 was able to drain most of the fluid towards the AU tunnel, which can be seen by the linear increase in the backflow volume.

B.4.2 HF2

The FBG strain sensor with a distance of 5.4 m in FBS1 to the injection point responded at a flow rate of 5 l/min (Fig. B.5b) during the first fracture propagation cycle (C1). The FBG sensors' responses next to the injection point are shown in the time-strain plot of Fig. B.5b. The maximum recorded strain is about 40 $\mu\varepsilon$ which is in comparison only about one-tenth of the maximum strain magnitude observed during HF3. During C1, the sensors at 6.1 and 5.4 m indicated opening while sensors at 5.7 and 7.8 m show closing. The pressure monitoring points in the rock mass do not show an increase during the first fracture propagation cycle. Only shortly before shut-in of C1, the INJBE interval starts to increase up to 1.4 MPa during the shut-in phase. During the second propagation cycle (C2), the FBG sensor at 7.8 m starts closing before it opens at the same time than the pressure in INJBE starts to increase. Open flow paths were investigated by conductivity logging before hydraulic fracturing with a low respond in pressure in the interval PRP11, injecting from the INJBE interval (Jalali et al., 2018a). This indicates a transient pressure change in the vicinity without any direct flow path to PRP11. In addition, the pressure interval INJBE exceeded pressure above 3 MPa with a response delay in shut-in and the PRP11 interval increased to a maximum value of 0.9 MPa without a delay in response during shut-in. About 30% of the injected fluid is recovered through the injection interval compared to 2% during the HF3 test. In total at the end of the test (100 min after C2 shut-in), 73% of the injected fluid was recovered. The other distinctive features of this test is a small jacking pressure and a large injectivity increase. We interpret these observations as reflecting 1) stress perturbation in the vicinity of the S1 shear zones and 2) connection of the HF with the S1.1 and S1.3 shear zones (Fig. B.5b) resulting in the stimulation of these pre-existing zones. The system, however, stayed almost closed, i.e. direct drainage to the tunnel was very limited.

B.4.3 Outlook

In our future work, we plan to quantify in more detail the fracture geometry in terms of fracture height and length, using the volume balance and AE localization. The localized AE events are necessary to evaluate the fracture geometry and to track the fluid flow. The response of transient pressure and FBG strain data will be compared to each flow rate step to investigate hydromechanical processes. Combining the 3D strain and pressure data allows estimating fracture aperture changes and transmissivity in the vicinity of the injection location. Additionally, longitudinal strain from FBG sensors along with recordings at three tiltmeters can be used to infer the fracture geometry.

B.5 Conclusion

The initial analysis of our HF tests shows two distinct responses in our suite of tests: a different behavior was observed in tests performed south of S3 compared to tests performed north of the S3 shear zone. The main differences are jacking, breakdown and ISIP pressures (low north of S3 and high south of it), fluid recovery through the injection hole (high north of S3, low south of S3), injectivity enhancement ratio (high north of S3 and low south of S3) and strain magnitude recorded during injection (low north of S3 and high south of S3). In the current state of our analyses, we assume that these differences are due to 1) different stress conditions north and south of S3 and 2) different pressure boundary conditions due to the flow path and links to the AU tunnel. For the experiments HF3 and HF8 (south of S3), the injected fluid was drained by the densely fractured S3 zone towards the AU tunnel. Due to this preferential flow path, the injections took place in an open system. This configuration also favored direct flow connections reflected by instantaneous responses of some pressure monitoring intervals to our injection and high-pressure levels recorded in the intervals. During the injection north of S3 (i.e. HF2) the FBG strain sensors showed only small magnitude responses. The reason for this is not fully understood at the moment and could be related to the stress conditions north of S3 reflected by smaller jacking pressure and ISIP. The stress perturbation can have various reasons, including effects of pre-existing fractures in the shear zones S1, stiffness difference of meta-basic dykes compared to the host rock in S3, and the combination of both effects. In addition, for the injections north of S3, it seems that the HF tests mostly interact with the S1 shear zones in a closed system as most of the injected fluid is recovered later on through the injection borehole. These differences in behavior seems also to affect the stimulation efficiency of the injections as the injection north of S3 lead to higher injectivity increase ratio. The reasons for this will be further investigated by integrating the microseismic data in our analyses.

Acknowledgement

Funding for this project was provided by the Swiss commission for technology and innovation (CTI), EKZ Zürich and Shell through the Swiss Competence Center for Energy Research – Supply of Electricity (SCCER - SoE). Additionally, this project was funded by the SNF-project 200021_165677/1. We are indebted to Nagra for hosting the ISC experiment in their GTS facility and to the Nagra technical staff for onsite support. We thank MeSy Solexperts, Bochum (Germany) for their good collaboration.

Appendix C

Observation of a repeated step-wise fracture growth during hydraulic fracturing experiment at the Grimsel Test Site

Please cite this section as: Dutler, N., Valley, B., Villiger, L., Gischig, V., Amann, F., Observation of a repeated step-wise fracture growth during hydraulic fracturing experiment at the Grimsel Test Site, Proceedings World Geothermal Congress, 21.5-26.5.2021, Reykjavik.

Abstract

Hydraulic fracturing (HF) experiments were conducted at the Grimsel Test Site (GTS), Switzerland, with the aim to improve our understanding of the seismo-hydro-mechanical processes associated with high-pressure fluid injection in a moderately fractured crystalline rock mass. Observations from one of these HF experiments indicate simultaneous propagation of multiple fractures during continuous fluid injection. The pressure measured in one observation interval show a cyclic response indicating repeated step-wise fracture growth. This is interpreted as a stick-split mechanism propagating fractures in an episodic manner and connecting them to the natural fracture network. In addition, transient partial closure and opening of fractures on the time-scale of seconds to minutes were observed from pressure and deformation monitoring. Our data set provides unprecedented insight in the complexity of hydraulic fracture propagation.

C.1 Introduction

Hydraulic fracturing is often used in reservoir engineering for shale gas/oil extraction and deep geothermal heat exploitation to increase the reservoir permeability and connectivity (Economides and Nolte, 2000; Evans et al., 2005). For deep enhanced geothermal systems (EGS), two prevalent concepts can be distinguished 1) hydraulic fracturing (HF) as the initiation and propagation of tensile fractures and 2) hydraulic shearing (HS) as the reactivation of pre-existing fractures in shear associated with dilation. These are end-members and a combination is possible i.e. primary fracturing with shear stimulation through leak-off or mixed-mechanism stimulation (McClure and Horne, 2014). The concepts for hydraulic fracturing for shale gas/oil extraction is generally similar but the objectives are different. For shale gas, establishing drainage of the formation from the production well is usually sufficient, while for an EGS a circulation between two or more boreholes need to be established. This is the crucial key process that depends on the target rock, the associated pre-existing fracture network, the temperature gradient and the stress field.

Current mathematical hydraulic fracture propagation models generally assume a single and continuous fracture growth (Adachi et al., 2007; Detournay, 2016). This kind of models simplify the complex nature of fracture propagation in-situ and are only valid in the context of single fracture propagation. Our experimental data sets challenge these simple assumptions as they show 1) multiple fracture growth and 2) intermittent fracture growth. Indeed, in low permeable rock mass with a pre-existing fracture network, the newly created hydraulic fracture will connect to the natural fracture network after a certain injection time (Dutler et al., 2019). This multi fracture extension mechanism is presented and discussed in this paper using the hydromechanical dataset from a hydraulic fracturing experiment. Concerning continuous fracture growth, a necessary condition is that the fluid flow speed at the crack tip matches the fracture propagation velocity. This interpretation is supported by the roughly constant fracture pressure propagation level (Zoback, 2007), which can be interpreted as continuous fracture growth by the absence of cyclic pressure fluctuation. Abundant geological evidence exist from outcrops that tensile fractures can grow in both continuous and episodic mode (Bahat and Engelder, 1984; Lacazette and Engelder, 1992). van Der Baan et al. (2016) proposed a new fracture growth mechanism during anthropogenic fluid injection, which is described in the following section.

Repeated brittle failure leads to microseismic events during hydraulic fracturing treatments (Cipolla et al., 2011; van der Baan et al., 2013). This repeated step-wise fracture growth is called stick-split mechanism proposed by van Der Baan et al. (2016). The model assumes that the fracture propagation is driven by tensile failure at the tip. The fluid pressure has to be sufficiently high so that the critical tensile fracture toughness value is exceeded. If local failure occurs the fracture extend and the fracture volume suddenly increases allowing fluid flow towards the new fracture tip. Therefore, a temporal local fluid pressure drop near the fracture tip can be observed so that the fracture partially closes there, until the fluid pressure builds up again due to continuous fluid injection. The repetition of these cycles leads to repeated step-wise fracture propagation. The repeated episodes of abrupt local opening of the hydraulic fracture walls, followed by partial closing is called hydraulic clapping mechanism. It occurs during the stick-split mechanism after pressure drop following tensile propagation. Seismic evidence from this short opening and closing cannot be observed directly due to the characteristic time of the clapping effect, which is estimated to be around milliseconds. Therefore, the modulation in the source spectrum was used (Eaton et al., 2014; Walter and Brune, 1993). Transient pressure analysis from geothermal well tests indicate that a closed fracture near the wellbore after shut-in results in a buildup of pressure in the remaining part of the fracture in contact. This can result in a partial re-opening of the fracture to allow fluid flow towards the open borehole interval driven by the pressure difference (Bakar and Zarrouk, 2018; Zarrouk and McLean, 2019). In this study, we present seismo-hydromechanical observations from a HF experiment (Dutler et al., 2019) providing evidence of the aforementioned fracturing mechanisms. The experiment is part of the In-situ stimulation and circulation project (Amann et al., 2018). The observations are discussed in term of 1) multiple fracture extension, 2) step-wise fracture growth and 3) hydraulic clapping mechanism.

C.2 Study site characterization and monitoring

The study site is located in the Central Alps of Switzerland, below (∼450 m) the Western flank of the Haslital valley in the southern part of the Grimsel Test Site. Prior to the hydraulic stimulation experiments, the rock mass of interest was characterized in great detail with respect to geology (Krietsch et al., 2018), geophysics (Doetsch et al., 2017), stress field (Gischig et al., 2018; Krietsch et al., 2019) and hydrogeology (Brixel et al., 2020a; Jalali et al., 2018a). The host rock consists of a moderately fractured and alpine overprinted granodiorite. Two sets of shear zones intersect the volume of interest. One set (S1.0, S1.1, S1.2 and S1.3) include four ductile shear zones characterized by a strong increase in the degree of foliation with an ENE-WSW strike and dip towards SSE. The most important shear zone is S1.0 next to the injection location (highlighted in Figure C.1a). It experienced retrograde brittle deformation and contain a prominent discrete brittle fracture. The other set (S3.1 and S3.2) contains two brittle-ductile shear zones coinciding with two biotite-rich meta-basic dykes with an E-W strike and dip towards S. These bound a densely fractured zone with 10 fractures per meter. The most prominent feature is the brittle-ductile S3.1 shear zone, which is intersected by S1.0 and show prominent brittle fractures for flow transport towards the AU-tunnel. Two fracture systems are associated with the densely fractured zone in between the two meta-basic dykes of the brittle-ductile shear zone S3, where one system is sub-vertical and strike towards E-W and the other system sub-vertically strikes in N-S direction The stress field has present strike-slip to thrust faulting conditions with a major principal stress axis towards E and dip of 40°. The magnitude of minimum and maximum principal stress is 8.6 MPa and 14.4 MPa, respectively. Approaching the brittle-ductile S3.1 shear zone from N, the stress field changes with a strike slip component, where the stress field is 30° rotated clockwise and intermediate and minimum principal stress axis switch place and the minimum principal stress magnitude reduces to 5.0 MPa (Dutler et al., view; Krietsch et al., 2020).

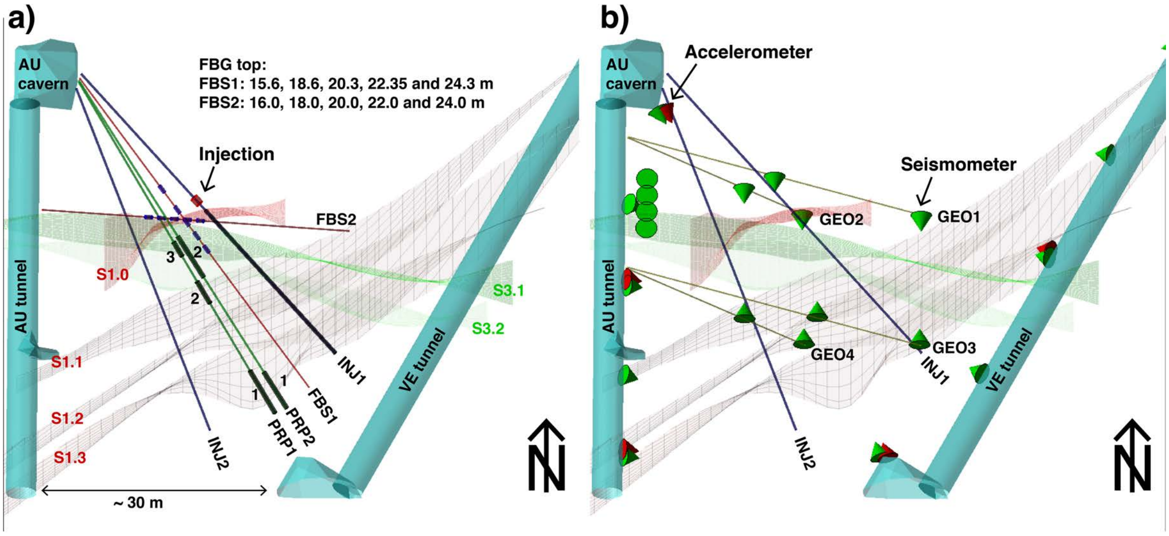

Fig. C.1 a) and b) present the geological model with AU- and VE-tunnels, AU cavern and brittle-ductile shear-zone S3 and ductile shear zone S1. The injection location, the FBG sensors in borehole FBS1 and FBS2 and the fracture pressure intervals in PRP1 and PRP2 are presented in a). b) The green and red cones indicate the location of the installed seismometers and accelerometers, respectively.

In this paper, we present the results from one of a series of six HF injection experiments. This is the tests referred as HF3 in the experimental report and other publications (Doetsch et al., 2018b; Dutler et al., 2019).The HF test was performed at the 16. May 2017 in the inclined borehole INJ1 using a 1 m long injection interval. The injection interval was placed from 19.8 to 20.8 m in the borehole INJ1, which was slightly north of the shear zone S1.0. Prior to stimulation this interval was free of visible discontinuities and transmissivity was in the order of 10^{-13} m^2/s indicating intact rock mass. During stimulation, injection pressure and flow rate were measured at the injection point. The fracture fluid pressure was also measured in the monitoring boreholes PRP1, PRP2 and INJ2. For the presented HF injection, data from intervals PRP1-2, PRP1-3 and PRP2-2 located in the brittle-ductile shear zone S3 are presented (location indicated as black cylinders in Figure C.1a). 20 Fiber-Bragg Grating (FBG) sensors recording longitudinal deformation were installed in three boreholes (labelled FBS); we present 6 deformation time series from around the injection location (blue cylinders in Figure C.1a). In addition, the time-strain plot from the Distributed Brillouin Strain Sensing (DSS) is presented for the sensor deployed along the PRP1 to track hydraulic connections. Positive strain indicate compression. The seismic monitoring network consists of total 26 uncalibrated piezo-electric acoustic emission (AE) sensors (green cones in Figure C.1b) and 5 calibrated accelerometers (red cones). Eight AE sensors were installed in 4 geophysical boreholes (GEO) in close proximity to the injection interval (3-25 m).

C.3 Results

The injection protocol of the HF experiment consists of three different cycles. The first injection cycle (F) aims to break down the formation and to initialize a new tensile crack. The two refracturing phases (RF1 and RF2) aim to propagate the fracture further into the pre-existing fracture network. The last cycle is a pressure-controlled step test (SR) to quantify final interval injectivity and jacking pressure based on the relationship of injection pressure and flow rate. The injection fluid was water and fracturing / refracturing are rate controlled cycles (Figure C.2c, top). In the following, we will mainly focus on the first refracturing cycle.

C.3.1 Hydraulic observations

The highest-pressure magnitude is observed during the breakdown cycle with a breakdown pressure of 16.3 MPa. The refracturing cycle RF1 reaches a maximum pressure of 8.3 MPa. With further fracture propagation the injection pressure stays below this maximum pressure. We observe a pressure limiting behavior at 6.8 MPa during cycle RF1 and RF2 for rates between 20 and 50 l/min. From the SR test, the final injectivity is 0.882 l/min/MPa and the jacking pressure is 5.1 MPa. The near wellbore transmissivity has increased to around 10^{-10} m^2/s. During the first refracturing cycle RF1, a small pressure signal starts to form (up to 0.35 MPa, see Fig. 2d) in the observation pressure intervals (PRP1-2 and PRP2-2 at 12.3 and 4.9 m from the injection point). At 1500 s, the PRP1-3 respond with a repeated pressure increase and drop. The first pressure increase is almost instantaneous and reaches a maximum pressure of 1.4 MPa until pressure drops. This cycle lasts for 56 s, until the repetition starts with an increase in pressure reaching a magnitude of 1.6 MPa. This cycle lasts for 87 s and show an erratic pressure increase and drop with small amplitude at the end of the larger cycle, before it drops to a value of 0.6 MPa until shut-in. During shut-in time we observe two more pressure increase and drop with highest peak pressure of 2.2 respective 2.9 MPa (66% of injection pressure). The cycles are shorter and lasts for 25 respective 50 s (Fig. C.2d). The selected observation pressure intervals indicate an increase in pressure during refracturing cycle RF2. The pressure signal reaches its peak pressure of 1.6 MPa in PRP1-3, 3 s after shut-in. PRP2-2 reaches a peak pressure of 1.1 MPa with a delay time of 51 s and PRP1-2 reach the smallest peak pressure of 0.8 MPa, with the longest delay time of 156 s after shut-in. Note, that PRP1-3 respond to each flow step with a change in slope, where the other two observation points only show a gradual increase during injection. Minor transient changes (<0.1 MPa) are related to the pressure step test (Fig. C.2c).

C.3.2 Mechanical observations

The six longitudinal FBG strain sensors located in borehole FBS1 and FBS2 cover the shortest radial distance (2.8 – 6.3 m) to the injection interval (Fig. C.2a + b). The selected data traces show either only extensional (at borehole depths of 18.6, 20.4, 22.35, 20 m) or mixed (22.0, 24.0 m) strain (Fig. C.2c). The peak strain measures 863.5 $\mu\varepsilon$ (during RF2 at 20 m). The same sensor responds by tension during the fracturing cycle, indicating a direct connection between injection interval and fracture intersecting the FBG sensor. Note that during RF1, the two sensors (at 22.35 and 20 m) with maximum tensional signal show direct response to the flow step during RF1 (Fig. C.2d). The FBG sensor in FBS1 at 20.4 m reacts in compression during refracturing cycle RF1 (Fig. C.2 d). The same sensor shows a compressional peak at 1217 s and reverse afterwards. The sensor next to it (18.6 m) shows a slight tensional reaction before reaching the peak tensional state, which is delayed (1237 s) compared with the sensor at 20.4 m. The FBG sensor at 24.3 m (in FBS1) show first a slight tensional signal and reverses at 1230 s and starts to be dominated by compression after 1282 s. At 1482 s, the sensor at 22.0 m (in FBS2) reaches a compressive peak and starts to reverse reaching a maximum change of -2.2 $\mu\varepsilon$/s. The sensor next to it (at 24.0 m) reaches the compressive peak at 1498 s and signals reverse as well, thereafter. The sensor at 20.0 m show peak tension of 713 µ at 1490 s. Then, it starts to slightly reverse until shut-in (623 $\mu\varepsilon$). The sensors at 22.0 and 24.0 m show a delayed tensional peak after pump shut-in (1639 s) at 1668 s and 1707 s for the sensor at 22.0 m respective 24.0 m. The other sensors presented in Fig. C.2 d do not show delayed peaks after pump shut-in. The Distributed Brillouin Strain Sensing in borehole FBS1 (Fig. C.2c) indicate two fractures intersecting at 20.0 (1268 s) and 17.9 m (1772 s). The temporal sampling is limited to 126 s. Thus, the interpretation of the precise timing of fracture formation is limited. The fracture at 20.0 m is related to the S1.0 brittle overprinted shear-zone. The fracture at 17.9 m is a new hydraulic fracture supported by the observations that the next observed pre-existing fractures are at 16.8 or 18.4 m.

C.3.3 Seismic observations

In total, 79 events were localized during this HF experiment. 77 events (97.5%) occur during fluid injection and only 2.5% during pump shut-off. The amplitude magnitude of the events range between -3.1 and -4.9 (Villiger et al., 2020). The event locations show a dispersed seismic pattern possibly related to the reactivation of two differently oriented fracture systems. The maximum radial distance between the injection interval and the seismic event observed is 15 m, where only two events have a bigger radial distance then 10 m. 26 events were localized during refracturing cycle RF1. Some events are located next to the boreholes and could possibly associated with the following effects: direct borehole effects including stress concentration, local change of pore water pressure, or compliance difference of concrete - rock mass and packer - rock mass. Another part is located in the targeted volume and show a dispersed pattern. The two fracture systems related with the S3 zone can probably explain this dispersed seismic pattern.

C.4 Discussion seismo-hydromechanics

C.4.1 Multiple fracture extension

We demonstrate multiple fracture extension by following the timeseries in Fig. C.2d and show three snapshots of the deformation labelled from a to f (Fig. C.2d) and the corresponding seismic events (Fig. C.4). Between time b and c, we observe two FBG sensors (18.6 and 20.4 m) which first show tensional increase and reverse during cyclic injection before the flow rate is ramped up. It seems that both sensors react to the dominant signal observed at 22.35 m, which first show compression and reverse to tension. This can be interpreted as the arriving fracture and fluid front, which reaches first the sensor at 18.6 m, then the one at 20.4 m and starts to open the fracture intersecting the base length of the sensor at 22.35 m. Note that the position of these fracture openings does not align with the predominant E-W striking seismicity cloud interpreted as the main hydraulic fracture orientation. Thus, we argue that not a single fracture but multiple strands of fractures propagate through the rock mass. This compressive front before the fluid arrives increases with injection volume and can be associated with the poro-elastic effect produced by the pressurized fluid-rock volume. In addition, the Distributed Brillouin Strain Sensing in FBS1 show a tensional signal at 20.0 m (lower blue circle in Fig. C.4) at the same time. The tensional signal does not go back to zero at the end of the experiment indicating a mismatch between the two fracture planes due to a shear component. At the time d (Fig. C.4), two FBG sensor (FBS1 at 22.35 m and FBS2 20.0 m) show abrupt tensional responses with reaching tensile strain of 386 and 862 microstrain, respective. The FBG sensor at 22.35 in FBS1 covers fractures associated with S3.1 zone. Since both sensors

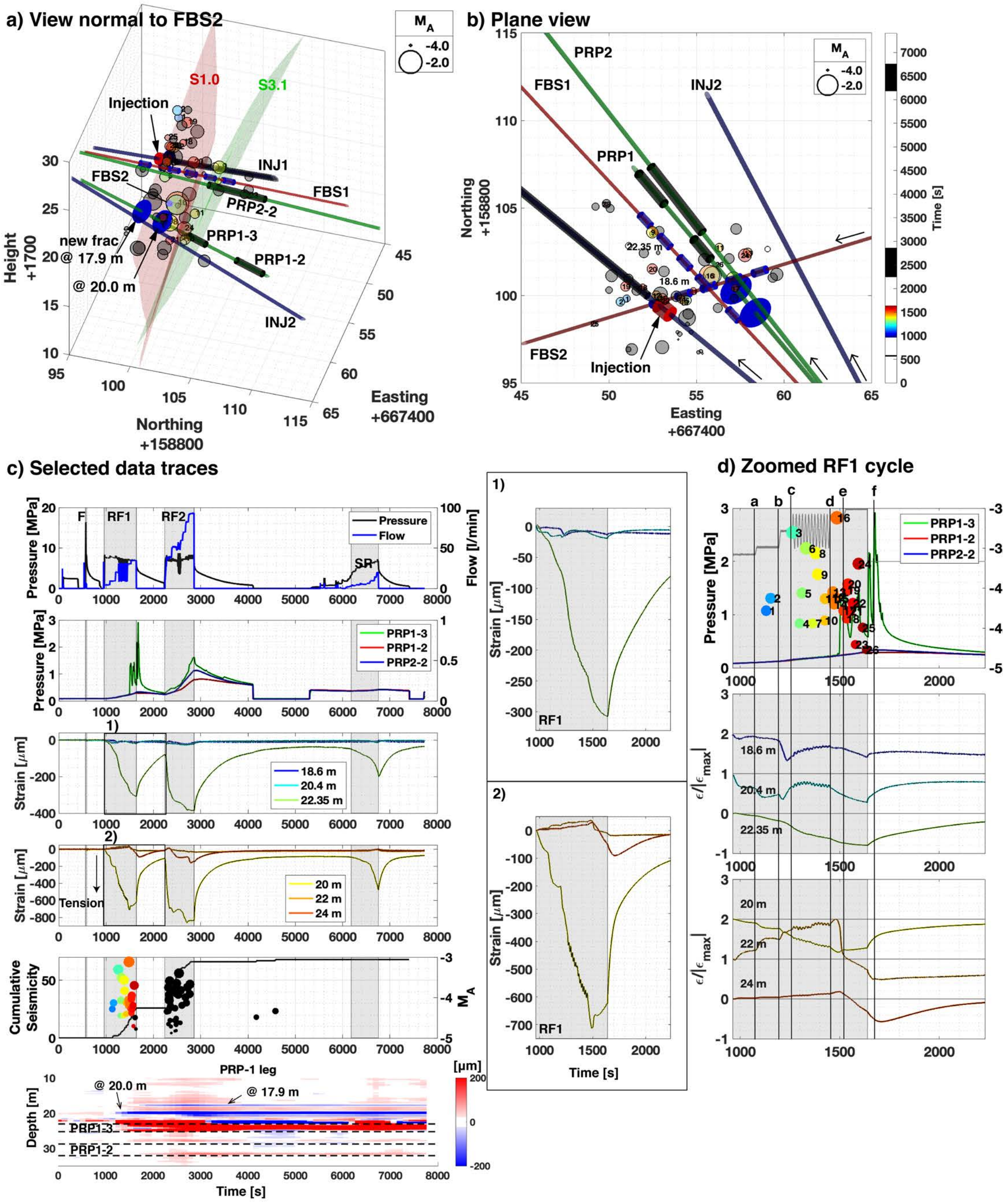

Fig. C.2 a) View normal to FBS2 inclusive S1.0 and S3.1 shear zone, boreholes, observation intervals and located seismic events (incl. color code) and fractures (blue ellipse); b) Plane view without shear zones; The black arrows indicate the plunge of the boreholes. c) Injection protocol; Timeseries of fracture fluid pressure interval PRP1-3, PRP1-2 and PRP2-2; Timeseries of strain multiplied (by the base length 1 m) data from the FBG sensors installed in FBS1 and FBS2; Amplitude magnitude of seismic events (highlighted for cycle RF1) and cumulative seismic; Timeseries of the Distributed Brillouin Strain Sensing (DSS) in PRP1 between 10 and 35 m borehole depth incl. highlighted PRP1-2 and PRP1-3 interval; d) Zoomed RF1 cycle for the transient pressure, seismic amplitude magnitude (incl. numbers) and strain curves. The numbers and color code of the seismic events correspond to the same numbers and color in a) and b). The flow rate is indicated in grey scaled between 2 and 3 MPa for 0 to 35 l/min.

respond in a similar way, it has to connected with the fractures intersecting the FBG sensor at 20 m in FBS2 (biggest tensional response). Also, the PRP1 observation at 20.0 m (blue circle in Fig. C.4) indicates connectivity to the same fracture system, showing continuously increasing pressure. Six of nine seismic events are located next to the sensors described before. The new fracture trace in the injection interval is presented by the blue disc (Fig. C.2a).

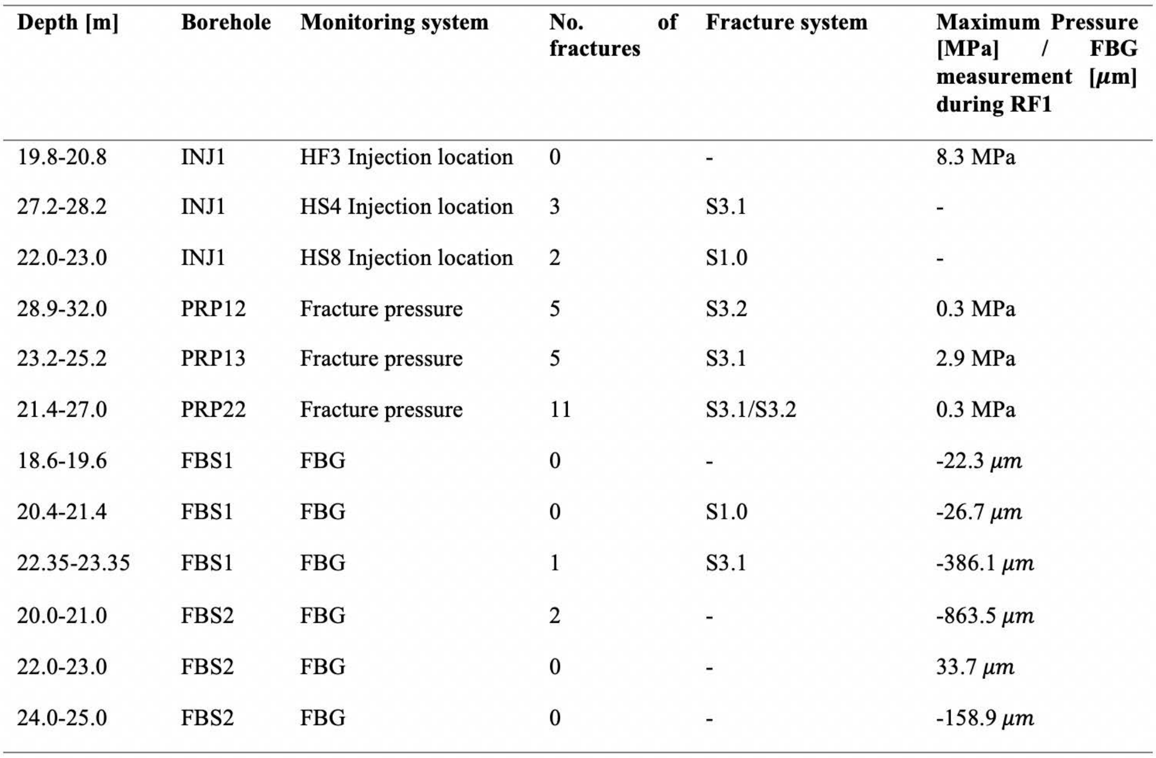

Depth [m]	Borehole	Monitoring system	No. of fractures	Fracture system	Maximum Pressure [MPa] / FBG measurement [μm] during RF1
19.8-20.8	INJ1	HF3 Injection location	0	-	8.3 MPa
27.2-28.2	INJ1	HS4 Injection location	3	S3.1	-
22.0-23.0	INJ1	HS8 Injection location	2	S1.0	-
28.9-32.0	PRP12	Fracture pressure	5	S3.2	0.3 MPa
23.2-25.2	PRP13	Fracture pressure	5	S3.1	2.9 MPa
21.4-27.0	PRP22	Fracture pressure	11	S3.1/S3.2	0.3 MPa
18.6-19.6	FBS1	FBG	0	-	-22.3 μm
20.4-21.4	FBS1	FBG	0	S1.0	-26.7 μm
22.35-23.35	FBS1	FBG	1	S3.1	-386.1 μm
20.0-21.0	FBS2	FBG	2	-	-863.5 μm
22.0-23.0	FBS2	FBG	0	-	33.7 μm
24.0-25.0	FBS2	FBG	0	-	-158.9 μm

Fig. C.3 Overview of the monitoring system response including number of fractures in the monitoring interval (prior to stimulation), related fracture system and maximum pressure or respectively FBG measurement magnitude during refracturing cycle RF1.

The FBG sensor at 20 m indicates fluid flow through the intersecting fractures due to direct strain change with each flow rate step increase (Fig. C.2c). From time d to e, the sensor at 22 and 24 m first show compression and start to reverse until tensional signals are observed, indicating existing fractures (Fig. C.2d). The number of fractures intersecting the base length of the FBG sensor (Fig. C.3) increases if new hydraulic fractures or sealed fractures are connected to the injection interval. Especially FBG sensors in intact rock (no intersecting natural fractures) should only show compression next to the injection location. Prior to the HF stimulation the HS stimulation took place. The HS4 injection stimulated the S3.1 zone. A strong instantaneous tensional signal was observed the FBG sensor in FBS2 at 24.0 m indicating that a new hydraulic fracture towards this sensor has been formed. The same fracture at this FBG sensor was reactivated during stimulation HS8 targeting the zone S1.0. During refracturing cycle RF1 from HF3, three FBG sensors (at 20, 22 and 24 m in FBS2), changed their behavior 2 s prior to the instantaneous pressure increase in the PRP1-3. These changes can be recognized in the snapshot at time e (Fig. C.4), 1) the bigger magnitude of pressure in PRP1-3 can be observed, 2) the FBG sensor at 22.0 m in FBS2 reverse (green->white) and 3) more seismic events are located, where the new events occur at the same patches similar to time d. The snapshot at time f (Fig. C.4) during pump shut–in time show only small changes compared to the snapshot at time e. 1) The magnitude for the interval PRP1-3 reaches its maximum, and 2) the strain sensor at 24 m in FBS2 is now tensional. The new seismic events occurring during Time e and Time f are located next to the previous events (grouped with black circles in Fig. C.4). Strain measured with Distributed Brillouin Strain Sensing in FBS1 starts showing a tensional signal at 17.9 m during this pump shut-off time. We assume that a new hydraulic connection is formed related to the fracturing processes around PRP1-3 at the end of RF1 and shut-in time. The FBG sensors at 22 and 24 m show an unusual long delay time between shut-in and reaching tensional peak (Fig. C.2d). The fluid path ways being blocked towards the injection borehole due to mechanical effects. Thus, fluid is pushed further into the reservoir resulting in delayed pressure peaks.

The cubic law in its simplest form ($T = a^3/12$) can be used to convert potential fracture opening measured with FBG sensors (a) into transmissivity (T). Assuming a single fracture has an initial aperture of 10 μm, then the transmissivity is in the order of 10^{-17} m^3. The largest observed tensional FBG measurement during the first refracturing cycle is 863.5 μm and leads to a transmissivity of 10^{-11} m^3. The local transmissivity change in the volume is at least in the order of 6 magnitudes.

C.4.2 Stick-split mechanism

The schematic representation of the stick-split mechanism (Fig. C.5a) is used to interpret the pressure observations in PRP1-3 (Figure C.5b). The process can be divided in four stages. 1) The fluid pressure builds up and the aperture near the tip increases (stick). 2) The effective pressure exceeds the tensile strength of the rock and local failure occurs (split). The abrupt increase in volume due to fracture extension allows the fluid to flow towards the new fracture tip location. 3) The volume increase is accompanied by a local and temporal pressure drop some distance from the fracture tip. Therefore, the fracture partially closes there. 4) Then, pressure start to build up again with continuous injection until a new stick-split cycle starts. During refracturing cycle RF1, we observed a cyclic variation in the fracture pressure interval PRP1-3. We relate the different stages from the stick-split mechanism with the pressure observation (Fig. C.5b) described in the section of hydraulic observations. The change in pressure is not related to changes in the flow

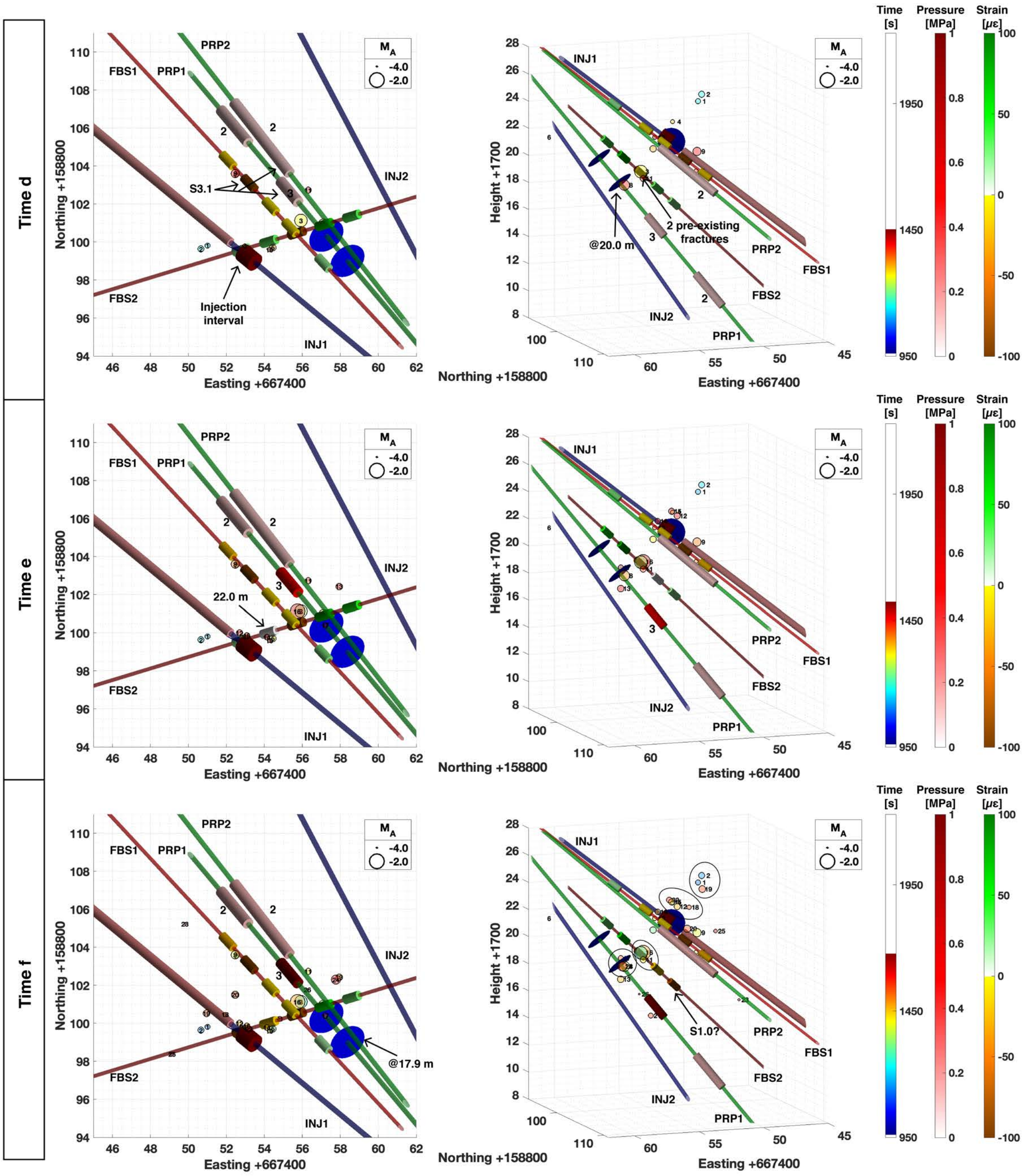

Fig. C.4 Seismo-hydromechanical observations visualized looking on plane view (left column) and parallel to the shear zones (right column). Each row represents a temporal resolved snapshot at time d, e and f presented in Figure C.2d.

rate in the injection borehole (except at 1525s). For conceptualization let us assume a parallel plate approximation with a laminar flow through it. This problem depends entirely on fluid velocity, pressure gradient, fluid viscosity and plate aperture. Assuming a constant viscosity and a given aperture leads to a correlation between fluid velocity (flow rate) and pressure gradient. However, the presented pressure observation from PRP1-3 and the injection rate contradicts this. We know from lab tests that the tensile strength of intact Grimsel Gneiss is at least 5.6 MPa (Dutler et al., 2018a). The time scale mentioned by van Der Baan et al. (2016) between opening and partial closing at the tip is in milliseconds. The pressure curve indicates different time scale with times of 56 and 87 s for a cycle. We explain this by the fact that the fracture is not initially created in intact rock and the volume to be filled is relatively big. Indeed, when of sealed fractures breaks and the fluid flows not only towards the new fracture tip but also to the associated new connected fracture volume and thus the time scale increases. It also dissipates the local pressure drop and the associated partial fracture closure near the fracture tip. An alternate explanation for the pressure signal of Fig. C.5b could be packer leakage. We can exclude this explanation because before we see the abrupt increase in PRP1-3, we see at 20 m a tensional signal in the Distributed Brillouin Strain Sensing. Therefore, we know that the water bearing fracture at 20 m is not changing the packer performance. We do see this cyclic change only during the refracturing cycle RF1 for experiment HF3. Cycle RF2 and all other experiments (especially the one performed later) do not indicate packer problems. Therefore, we assume these signals are in-situ evidence of the complex stick-split hydromechanical interaction and thus validate the existence of this process.

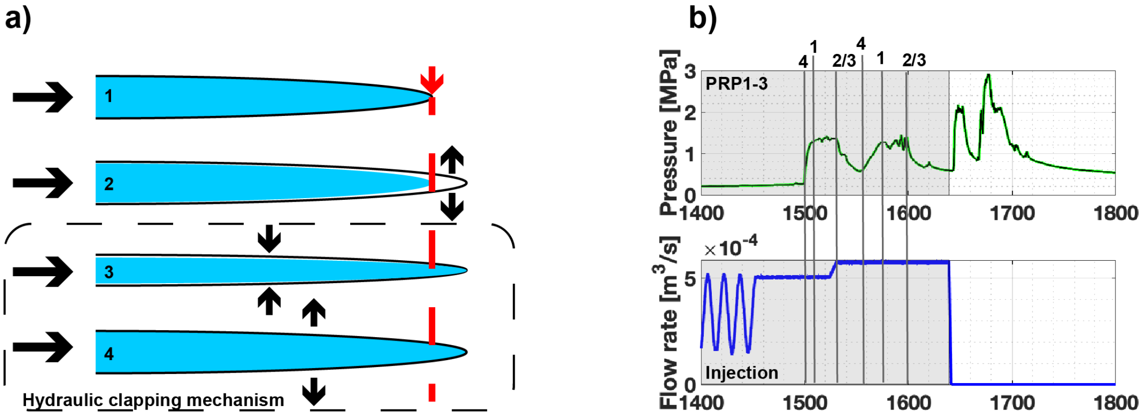

Fig. C.5 a) Schematic representation of the stick-split mechanism in four stages inclusive hydraulic clapping mechanism (last two stages) and b) applying the stages to the PRP1-3 pressure data from the HF3 experiment inclusive injection overview.

We interpret this in terms of the pressure diffusion equation that is based on coupling Darcy's law with the continuity equation:

$$\frac{\partial}{\partial x}(T_x\frac{\partial p}{\partial x})+\frac{\partial}{\partial y}(T_y\frac{\partial p}{\partial y})=\frac{1}{\rho_f}(S_f\frac{\partial p}{\partial t})$$

where p is the fluid pressure, T_i is the transmissivity, ρ_f is the fluid density (constant) and S_f is the storage coefficient of the fracture. If we assume constant transmissivity, an increase in the flow-rate at the injection interval (source) leads to change in the head for a cell next to the injection location. This agrees with our observation that the progressively increasing injection leads to an increase in the observation pressure. Considering the cyclic change in pressure in the observation interval PRP1-3, a fracture propagating in a stick-split manner may affect pressure (or head) in three ways: 1) by a change in the pressure (or head) gradient due to a pressure drop at the propagation front, 2) a change in the storage coefficient due to continued fracture opening as well as the void space created by the fracture propagation , 3) change in fracture aperture leading to a change in transmissivity. The three effects may act in concert to produce cyclic pressure behind a propagating fracture.

C.4.3 Hydraulic clapping mechanism

The last two cycles of PRP1-3 (Fig. C.5b) are most likely observations of the hydraulic clapping mechanism. These cycles occur during shut-in phase (pump is shut-off and injection line is closed), when fracture closure dominates.

The normalized drawdown for the injection curve for refracturing cycle RF2 show a dominant bilinear flow regime (slope 1/4 in both ΔH/Q and derivative in Fig. C.6a). At late time (600 s), the derivative reaches a peak, which can be interpreted as reaching a constant head boundary. We interpret this as fluid flow drained by the S3.1 or S1.0 towards the AU-tunnel. The drawdown observed in the monitoring intervals show strong pressure (head) variation for PRP1-2 and PRP2-2. Note that the time for the observation intervals is corrected by distance between the midpoint of the injection and observation intervals. The drawdown curve of PRP1-2 is slightly convex (1 s). The derivative of all these curves show slight hump for PRP2-2 and strong humps for PRP1-2 and PRP1-3. Bakar and Zarrouk (2018) showed that these humps are related to hydraulic fracture clapping. The difference to their study is that we observe these signals not at the injection interval, but in the observation intervals. The hydraulic clapping is observed at around 1 s (triangle Fig. C.6b), which is early compared with the observations of Bakar and Zarrouk (2018) at around 200 s for well test data from geothermal fields. It is an open question if our observation is also related to the poro-elastic wave driven by the instantaneous pressure loss in the injection interval.

Hydromechanical interaction

The observations from three FBG sensors at 20, 22 and 24 m in FBS2 presented in the result section are interpreted in Fig. 6. The hydromechanical interaction between two

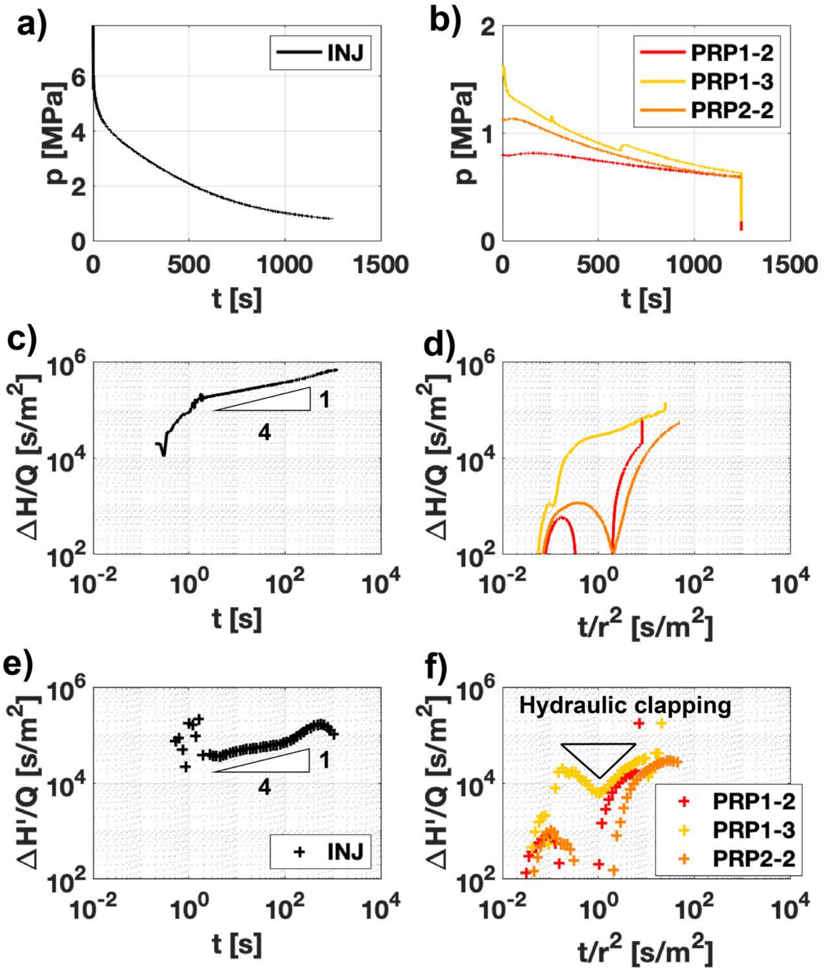

Fig. C.6 a) a+b) Timeseries of shut-in time for RF2 from the injection and observation pressure intervals. Log-log normalized hydraulic fracturing response (ΔH/Q) from the drawdown of refracturing cycle RF2 and Bourdet derivative (ΔH'/Q) for c+e) the injection curve and d+f) the observation curves with normalized distance.

fractures can explain the observed strain curves. We divided the normalized strain time series in four stages. 1) The fracture at 20 m respond with an increasing aperture by increasing flow rate. The fracture at 22 and 24 m reacts with compression. 2) The aperture for the fracture at 20 m reaches its maximum and then slightly decrease. The fractures at 24 m react with strain increase. We assume that we created a new hydraulic connection towards these two fractures. 3) At shut-in, the aperture of the fracture at 20 m decrease. The other two fractures show a time lag reaching its maximum fracture aperture. The time lag observed is dependent on the distance and the connectivity from the injection borehole

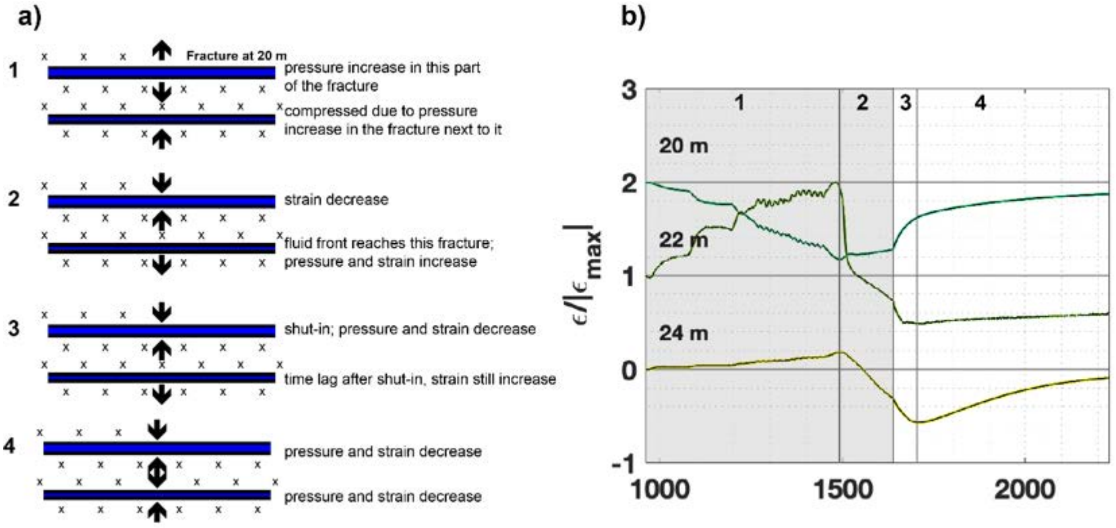

Fig. C.7 a) Scheme of a multiple-fracture system presented in b). The zoomed RF1 cycle for three FBG strain curves from borehole FBS2.

to this observation point, if we assume that these signals are related to fluid flow through the fractures. 4) After reaching the maximum fracture aperture, two of three FBG sensors indicate relaxation. The sensor at 22 m, indicate permanent strain change of -21.9 $\mu\varepsilon$ and therefore simple fracture opening and closing cannot explain this signal. We relate this permanent change to hydraulic shearing with dilation along the pre-existing fractures intersecting the base length of this FBG sensor.

C.5 Conclusion

The presented hydromechanical data from one hydraulic fracturing experiment indicate complex mechanisms between continuous fluid injection, episodic fracture propagation, interaction and connection of hydrofractures with the natural fracture system. We highlighted different responses of the FBG sensors during the experiment and related it to local transmissivity increase. The observed fracture pressure increases along with the variable spatial and temporal occurrence of seismicity indicates the new hydraulic fractures propagates as multiple fracture branches that connect to the pre-existing fracture network. Observed fracture pressure in observation intervals with pre-existing fractures show that rock mass stimulation occurs mainly through connecting pre-existing fractures and to a minor extend through the creation of new fractures in intact rock. Observed pressure indicate a non-uniform pressure distribution in the network during continuous fluid injection. Additionally, observed cyclic pressure observations during constant rate injection indicating an episodic fracture growth that is interpreted as stick-split mechanism breaking intact rock and connecting pre-existing fractures. We further observe post-shut-in pressure reversals during pressure decay. Normalized drawdown curves of these pressure decay curves may be interpreted as interaction of nearby fractures that close and open in response to spatially heterogeneous pressure diffusion to the far-field. Hydromechanical interaction between two fractures being formed and pressurized at different times is evident.

Acknoledgements

This study is part of the In-situ Stimulation and Circulation (ISC) project established by the Swiss Competence Center for Energy Research - Supply of Electricity (SCCER-SoE) with the support of Innosuisse. Funding for the ISC project was provided by the ETH Foundation with grants from Shell and EWZ and by the Swiss Federal Office of Energy through a P&D grant. Nathan Dutler is supported by SNF grant 200021_165677. The Grimsel Test Site is operated by Nagra, the National Cooperative for the Disposal of Radioactive Waste. We are indebted to Nagra for hosting the ISC experiment in their GTS facility and to the Nagra technical staff for onsite support.

Appendix D

Abstracts of related co-authored publications and reports

D.1 The seismo-hydromechanical behavior during deep geothermal reservoir stimulations: open questions tackled in a decameter-scale in situ stimulation experiment

Reference: *Amann, F., Gischig, V., Evans, K., Doetsch, J., Jalali, R., Valley, B., Krietsch, H., Dutler, N., Villiger, L., Brixel, B., Klepikova, M., Kittilä, A., Madonna, C., Wiemer, S., Saar, M. O., Loew, S., Driesner, T., Maurer, H., and Giardini, D. (2018), The seismo-hydromechanical behavior during deep geothermal reservoir stimulations: open questions tackled in a decameter-scale in situ stimulation experiment, Solid Earth, 9, 115-137, https://doi.org/10.5194/se-9-115-2018*

Abstract: In this contribution, we present a review of scientific research results that address seismo-hydromechanically coupled processes relevant for the development of a sustainable heat exchanger in low-permeability crystalline rock and introduce the design of the In situ Stimulation and Circulation (ISC) experiment at the Grimsel Test Site dedicated to studying such processes under controlled conditions. The review shows that research on reservoir stimulation for deep geothermal energy exploitation has been largely based on laboratory observations, large-scale projects and numerical models. Observations of full-scale reservoir stimulations have yielded important results. However, the limited access to the reservoir and limitations in the control on the experimental conditions during deep reservoir stimulations is insufficient to resolve the details of the hydromechanical processes that would enhance process understanding in a way that aids future stimulation design. Small-scale laboratory experiments provide fundamental insights into various processes relevant for enhanced geothermal energy, but suffer from (1) difficulties and uncertainties in upscaling the results to the field scale and (2) relatively homogeneous material and stress conditions that lead to an oversimplistic fracture flow and/or hydraulic fracture propagation behavior that is not representative of a heterogeneous reservoir. Thus, there is a need for intermediate-scale hydraulic stimulation experiments with high experimental control that bridge the various scales and for which access to the target rock mass with a comprehensive monitoring system is possible. The ISC experiment is designed to address open research questions in a naturally fractured and faulted crystalline rock mass at the Grimsel Test Site (Switzerland). Two hydraulic injection phases were executed to enhance the permeability of the rock mass. During the injection phases the rock mass deformation across fractures and within intact rock, the pore pressure distribution and propagation, and the microseismic response were monitored at a high spatial and temporal resolution.

D.2 Comprehensive geological data of a fractured crystalline rock mass analog for hydraulic stimulation experiments

Reference: *Krietsch, H., Doetsch, J., Dutler, N. O., Jalali, M., Gischig, V. S., Loew, S. & Amann, F. (2018). Comprehensive geological data of a fractured crystalline rock mass analog for hydraulic stimulation experiments, Scientific Data, 5, 180269, https://doi.org/10.1038/sdata.2018.269*

Abstract: High-resolution 3D geological models are crucial for underground development projects and corresponding numerical simulations with applications in e.g., tunneling, hydrocarbon exploration, geothermal exploitation and mining. Most geological models are based on sparse geological data sampled pointwise or along lines (e.g., boreholes), leading to oversimplified model geometries. In the framework of a hydraulic stimulation experiment in crystalline rock at the Grimsel Test Site, we collected geological data in 15 boreholes using a variety of methods to characterize a decameter-scale rock volume. The experiment aims to identify and understand relevant thermo-hydro-mechanical-seismic coupled rock mass responses during high-pressure fluid injections. Prior to fluid injections, we characterized the rock mass using geological, hydraulic and geophysical prospecting. The combination of methods allowed for compilation of a deterministic 3D geological analog that includes five shear zones, fracture density information and fracture locations. The model may serve as a decameter-scale analog of crystalline basement rocks, which are often targeted for enhanced geothermal systems. In this contribution, we summarize the geological data and the resulting geological interpretation.

D.3 Grimsel ISC Experiment description

Reference: *Doetsch, J. Gischig, V., Krietsch, H., Villiger, L., Amann, F., Dutler, N., Jalali, R., brixel, B., Roques, C., Giertzuch, P.L., Kittila, A., Hochreutener, R. (2018). Grimsel ISC Experiment description. ETH Zurich. doi:https://doi.org/10.3929/ethz-b-000310581*

Abstract: The In-situ Stimulation and Circulation (ISC) project was conducted at the Grimsel Test Site (GTS), Switzerland, between 2015 and 2018. The major goal of the project was to contribute to the understanding of seismo-hydromechanical-chemical coupled processes during hydraulic stimulations at the decameter scale. The major research question was, how the transmissivity of a fractured crystalline rock mass can be increased, while the induced seismicity is kept at an acceptable level. Besides the twelve main tests (6 Hydro-Shearing (HS) and 6 Hydro-Fracturing (HF) tests), various tests of new measurement and monitoring techniques were conducted, ranging from in-situ stress measurements, detailed hydrological characterization, geophysical measurements (including active and passive seismics) to the combination of different strain monitoring systems. Within this experiment description, we introduce our instrumentation, the rock mass characterization, and the hydro-shearing and hydro-fracturing tests. Note that this document is a technical report rather than a scientific publication. It contains relevant information required to process and interpret the recorded datasets that are to become publically available. Detailed results of the experiment will be published separately. The current list of all published results and datasets can be found at http://www.sccer-soe.ch/en/publications/grimsel-isc-project/. In addition the current list of publications is listed in Appendix B.

D.4 Stress measurements for an in-situ stimulation experiment: Integration of induced seismicity, stress relief and hydraulic methods in crystalline rock

Reference: *Krietsch, H., Gischig, V., Evans, K., Doetsch, J., Dutler, N., Valley, B. & Amann, F. (2019), Stress measurements for an in-situ stimulation experiment: Integration of induced seismicity, stress relief and hydraulic methods in crystalline rock, RMRE, 52(2), 517-542, https://doi.org/10.1007/s00603-018-1597-8*

Abstract: An extensive campaign to characterize rock stresses on the decameter scale was carried out in three 18–24 m long boreholes drilled from a tunnel in foliated granite at the Grimsel Test Site, Switzerland. The survey combined stress relief methods with hydrofracturing (HF) tests and concomitant monitoring of induced seismicity. Hydrofracture traces at the borehole wall were visualized with impression packer tests. The microseismic clouds indicate sub-vertical south-dipping HFs. Initial inversion of the overcoring strains with an isotropic rock model yielded stress tensors that disagreed with the HF and microseismic results. The discrepancy was eliminated using a transversely isotropic rock model, parametrized by a novel method that used numerical modelling of the in situ biaxial cell data to determine the requisite five independent elastic parameters. The results show that stress is reasonably uniform in the rock volume that lies to the south of a shear zone that cuts the NNW of the study volume. Stress in this volume is considered to be unperturbed by structures, and has principal stress magnitudes of 13.1–14.4 MPa for σ_1, 9.2–10.2 MPa for σ_2, and 8.6–9.7 MPa for σ_3 with σ_1 plunging to the east at 30–40°. To the NNW of the uniform stress regime, the minimum principal stress declines and the principal axes rotate as the shear zone is approached. The stress perturbation is clearly associated with the shear zone, and may reflect the presence of more fragmented rock acting as a compliant inclusion, or remnant stresses arising from slip on the shear zone in the past.

D.5 Running up the scales towards engineered geothermal systems: hydraulic stimulation and fluid circulation experiments in underground laboratories

Reference: *Gischig, V., Amann, F., Bethmann, F., Brixel, B., Doetsch, J., Doonechaly, N., Driesner, T., Dutler, N., Evans, K., Hertrich, M., Jalali, M., Kittilä, A., Krietsch, H., Loew, S., Ma X., Maurer, HR., Meier, P., Nejati, M., Obermann, A., Saar, M.O., Valley, B., Villiger, L., Wiemer, S. & Giardini, D. (2019), Running up the scales towards engineered geothermal systems: hydraulic stimulation and fluid circulation experiments in underground laboratories, Geomech Energy Envir, https://doi.org/10.1016/j.gete.2019.100175*

The history of reservoir stimulation to extract geothermal energy from low permeability rock (i.e. so-called petrothermal or engineered geothermal systems, EGS) highlights the difficulty of creating fluid pathways between boreholes, while keeping induced seismicity at an acceptable level. The worldwide research community sees great value in addressing many of the unresolved problems in down-scaled in-situ hydraulic stimulation experiments. Here, we present the rationale, concepts and initial results of ongoing stimulation experiments in two underground laboratories in the crystalline rocks of the Swiss Alps. A first experiment series at the 10 m scale was completed in 2017 at the Grimsel Test Site. Observations of permeability enhancement and induced seismicity show great variability between stimulation experiments in a small rock mass body. Monitoring data give detailed insights into the complexity of fault stimulation induced by highly heterogeneous pressure propagation, the formation of new fractures and stress redistribution. Future experiments at the Bedretto Underground Laboratory for Geoenergies are planned to be at the 100 m scale, closer to conditions of actual EGS projects, and a step closer to combining fundamental process-based research with testing techniques proposed by industry partners. Thus, effective and safe hydraulic stimulation approaches can be developed and tested, which should ultimately lead to an improved acceptance of EGS.

D.6 Influence of reservoir geology on seismic response during decameter scale hydraulic stimulations in crystalline rock

Reference: *Villiger, L., Gischig, V. S., Doetsch, J., Krietsch, H., Dutler, N. O., Jalali, M., Valley, B., Selvadurai, P. A., Mignan, A., Plenkers, K., Giardini, D., Amann, F., and Wiemer, S. (2020): Influence of reservoir geology on seismic response during decameter scale hydraulic stimulations in crystalline rock, Solid Earth, 11(2), 627-655, https://doi.org/10.5194/se-11-627-2020*

Abstract: We performed a series of 12 hydraulic stimulation experiments in a 20x20x20m foliated, crystalline rock volume intersected by two distinct fault sets at the Grimsel Test Site, Switzerland. The goal of these experiments was to improve our understanding of stimulation processes associated with high-pressure fluid injection used for reservoir creation in enhanced or engineered geothermal systems. In the first six experiments, pre-existing fractures were stimulated to induce shear dilation and enhance permeability. Two types of shear zones were targeted for these hydroshearing experiments: i) ductile ones with intense foliation and ii) brittle-ductile ones associated with a fractured zone. The second series of six stimulations were performed in borehole intervals without natural fractures to initiate and propagate hydraulic fractures that connect the wellbore to the existing fracture network. The same injection protocol was used for all experiments within each stimulation series so that the differences observed will give insights into the effect of geology on the seismo-hydro-mechanical response rather than differences due to the injection protocols. Deformations and fluid pressure were monitored using a dense sensor network in boreholes surrounding the injection locations. Seismicity was recorded with sensitive in-situ acoustic emission sensors both in boreholes and at the tunnel walls. We observed high variability in the seismic response in terms of seismogenic indices, b-values, spatial and temporal evolution during both hydroshearing and hydrofracturing experiments, which we attribute to local geological heterogeneities. Seismicity was most pronounced for injections into the highly conductive brittle-ductile shear zones, while injectivity increase on these structures was only marginal. No significant differences between the seismic response of hydroshearing and hydrofracturing was identified, possibly because the hydrofractures interact with the same pre-existing fracture network that is reactivated during the hydroshearing experiments. Fault slip during the hydroshearing experiments was predominantly aseismic. The results of our hydraulic stimulations indicate that stimulation of short borehole intervals with limited fluid volumes (i.e., the concept of

zonal insulation) may be an effective approach to limit induced seismic hazard if highly seismogenic structures can be avoided.

D.7 On the Variability in Pressure Propagation during Hydraulic Stimulation based on Seismic Velocity Observations

Reference: *Schopper F., Doetsch J., Villiger L., Krietsch H., Gischig. V.S., Jalali M., Amann F., Dutler N. & Maurer H. (2020): On the Variability in Pressure Propagation during Hydraulic Stimulation based on Seismic Velocity Observations, JGR Solid Earth, 2019JB018801, https://doi.org/10.1029/2019JB018801*

Abstract: Changes in crustal stress state caused by natural or human-induced subsurface fluid overpressures can lead to rock mass brittle damage, anywhere from the formation of grain-scale microcracks to the failure of kilometric-scale faults. Characterizing the timing and spatial extent of this type of deformation is critical both for industrial applications such as geothermal, oil and gas productions and to improve our ability to forecast earthquakes. Seismic and geodetic monitoring systems provide in general the vast majority of data collected in this perspective, even though authors have also proposed that geochemical anomalies may be used as proxy for rock deformation. These studies have reported changes in chemical compositions of surface waters, springs and groundwaters before, during or after earthquakes. It is generally assumed that these anomalies reflect changes in flow path connectivity involved during deformation which tends to remobilize and mix fluids with different sources, residence times and storage conditions6. While these studies have discussed this hypothesis based on geochemical and seismic signals monitored during natural earthquakes at the regional scale, a description of the mechanisms responsible for fluid remobilization and mixing at the scale of discrete fracture systems constrained from seismic, geodetic and geochemical signals is to our best knowledge still missing. Here we report transient helium (He) and argon (Ar) concentrations monitored during a series of decameter-scale reservoir stimulation experiments using an in-situ GE-MIMS9 (Gas Equilibrium Membrane Inlet Mass Spectrometer). Geodetic and seismic analyses revealed that the applied stimulation treatments lead to the formation of new fractures (hydraulic fracturing) as well as the reactivation of natural, pre-existing fractures (hydraulic shearing). The newly created fractures and flow paths remobilized (He, Ar)-enriched fluids originally trapped in the stimulated rock mass. We demonstrate that dissolved He and Ar are suitable tracers to track in-situ the evolution of rock deformation and damage. Such geochemical monitoring may provide critical insights when seeking the characterization of the evolution of the fracture network connectivity and evaluation of stimulation efficiency, while also providing critical process-understanding linking in-situ fluid migration to rock deformation and seismicity.

D.8 In-situ observation of helium and argon release during fluid-pressure-triggered rock deformation

Reference: *Roques, C., Weber, U. W., Brixel, B., Krietsch, H., Dutler, N., Brennwald, M. S., Villiger, L., Doetsch, J., Jalali, M., Gischig, V., Amann, F., Valley, B., Klepikova, M., & Kipfer, R. (2020). In-situ observation of helium and argon release during fluid-pressure-triggered rock deformation, Sci Rep 10, 6949, https://doi.org/10.1038/s41598-020-63458-x*

Abstract: Permeability enhancement of a reservoir through hydraulic stimulation is ever so often accompanied by potentially hazardous induced seismicity. Monitoring of in-situ pressure propagation remains an important step in understanding the underlying seismo-hydro mechanical processes during hydraulic stimulation and mitigating hazardous induced seismicity. In an effort to monitor pressure propagation remotely, active seismic monitoring was performed during deca-meter scale hydraulic stimulation experiments at the Grimsel Test Site (GTS) in Switzerland. Using cross-correlation schemes, subtle traveltime variations that correlate well with the high-pressure fluid injections during hydraulic stimulation become apparent. The 4D seismic tomograms obtained through time-lapse differential traveltime inversion reveal transient changes in the seismic velocity within the stimulated volume that depend on the effective stress. In-depth comparison of the seismic velocity variations and measured pressure data indicates that the seismic velocity variations can be used as a proxy for pressure propagation within an equilibrated system. Observations show that traveltime tomography is insensitive to isolated, high pressure variations such as a breakthrough within the fracture network. Joint interpretation of the 4D seismic tomograms with geological and hydro-mechanical data reveals fundamental differences between the different experiments due to a large variability in the rock mass response to the hydraulic stimulation. Using the observed velocity variations as a proxy for pressure propagation we can infer characteristics of the shear zones and the rock volume at the GTS. The observed velocity variations not only provide information on the characteristics of the reservoir itself, but also its response to different stimulation techniques.